

AIX-MARSEILLE UNIVERSITÉ  
UNIVERSITÀ DEGLI STUDI DI MILANO-BICOCCA  
ECOLE DOCTORALE DES SCIENCES CHIMIQUES  
LABORATOIRE DE BIOÉNERGÉTIQUE ET INGÉNIERIE DES PROTÉINES /  
UMR 7281 CNRS-AMU

SCUOLA DI DOTTORATO IN SCIENZE CHIMICHE,  
GEOLOGICHE E AMBIENTALI  
DIPARTIMENTO DI BIOTECNOLOGIE E BIOSCIENZE / UNIMIB

Thèse présentée pour obtenir le grade universitaire de docteur  
Tesi di dottorato

**Matteo SENSI**

## **Reactivity and photochemistry of the active site of FeFe-hydrogenase**

Soutenance prévue le 8 novembre 2017 devant le jury composé de:  
Difesa prevista l'8 novembre 2017 di fronte alla seguente commissione:

Emilia SICILIA	Rapportrice
Cédric TARD	Rapporteur
Jochen BLUMBERGER	Examineur
Christophe LÉGER	Directeur de thèse
Luca DE GIOIA	Directeur de thèse
Carole BAFFERT	Invitée
Luca BERTINI	Invité



*Nothing in life is to be feared, it is only to be understood. Now is the time to understand more, so that we may fear less.*

---

Marie Curie



# Acknowledgments

Many people have played an important role during my PhD and I feel the need to thank them. First of all, I would like to thank my two supervisors, Christophe Léger and Luca De Gioia for their trust in me, for all the opportunities they gave me and all the knowledge that they shared with me. I am grateful to my co-supervisors Carole Baffert and Luca Bertini, for the constant support and for all I've learned from them. I am grateful to Vincent Fourmond, Maurizio Bruschi, Sebastien Dementin, Claudio Greco for the scientific discussions and the nice time spent together. A special thank to Martino, who arrived in Marseilles with me three years ago and has always been a good friend and colleague. I want to thank Meriem, who has always been very kind with me and she has been a great PhD colleague since the beginning. Thanks to all the members of the two teams, which have been very important in these three years from a personal and scientific point of view: Giuseppe, Jacopo, Federica, Giulia, Tommaso, Andrea, Daniele, Ilaria, Francesco, Pierre, Christophe, Jessica, Maryam, Laura, Melisa, Marco, Arianna.

I want to thank my parents because they supported me, helped me in difficult moments and they always believed in me. I am grateful to my brother because he was always near me, although we were in different countries. Thanks to all my relatives and friends who supported me.

And last but not least, I want to say thank you to my girlfriend Silvia for the constant support and the sacrifices that she did for me. We were far, but you were always there for me.



# Contents

<b>1</b>	<b>Introduction</b>	<b>1</b>
1.1	Hydrogenases	2
1.2	FeFe hydrogenases enzyme structure	4
1.3	Gas diffusion channels	7
1.4	Proton transfer	8
1.5	States of the H-cluster	9
1.5.1	$H_{\text{ox}}$ and $H_{\text{ox}}\text{CO}$	9
1.5.2	$H_{\text{red}}$	11
1.5.3	$H_{\text{inact}}$	11
1.5.4	$H_{\text{ired}}$	13
1.5.5	$H_{\text{hyd}}$	14
1.6	Electronic structure of the H-cluster from DFT	15
1.7	Aerobic oxidative inactivation	17
1.8	Anaerobic oxidative inactivation	20
1.9	Reductive inactivation	22
1.10	The catalytic cycle	25
1.10.1	Which states of the H-cluster are involved in the catalytic cycle?	25
1.10.2	Proposed catalytic cycles	28
1.11	Inhibition of FeFe hydrogenases by CO	33
1.12	The effect of light on the CO-inhibited state of FeFe hydrogenases	34
1.12.1	Early studies of the effect of light on hydrogenases	34
1.12.2	Spectroscopic studies	35
1.12.3	Photodissociation of CO studied by X-ray crystallography	38

1.12.4 Kinetic studies . . . . .	39
1.13 Photoinhibition . . . . .	40
1.14 Objective of my thesis . . . . .	45
<b>2 Introduction to the methods</b>	<b>47</b>
2.1 Theoretical methods . . . . .	48
2.1.1 Density Functional Theory . . . . .	48
2.1.2 Broken Symmetry approach . . . . .	50
2.1.3 Time-Dependent Density Functional Theory . . . . .	53
2.1.4 Excited states radiationless deactivation . . . . .	55
2.1.5 Potential energy surface (PES) . . . . .	57
2.1.6 Exploration of excited states PES with TDDFT . . . . .	57
2.1.7 TDDFT optimizations . . . . .	58
2.1.8 Level of theory used for DFT and TDDFT calculations . . . . .	60
2.2 Direct electrochemistry . . . . .	61
2.2.1 New perspectives in hydrogenases direct electrochemistry . . . . .	64
<b>3 Aerobic oxidative inactivation in FeFe hydrogenases</b>	<b>73</b>
3.1 Summary . . . . .	74
3.2 Résumé . . . . .	76
3.3 Mechanism of oxygen diffusion and reduction in FeFe hydrogenases . . . . .	78
<b>4 Effect of light on FeFe hydrogenases inhibited by CO</b>	<b>87</b>
4.1 Summary . . . . .	88
4.2 Résumé . . . . .	90
4.3 Reactivity of the excited states of the H-cluster of FeFe hydrogenases . . . . .	92
4.4 Supporting Information . . . . .	99
<b>5 Effect of light on the active forms of FeFe hydrogenases</b>	<b>133</b>
5.1 Summary . . . . .	134
5.2 Résumé . . . . .	136
5.3 Photoinhibition of FeFe hydrogenase . . . . .	138
5.4 Supporting Information . . . . .	158



5.5	Effect of Cl <sup>-</sup> on photoinhibition . . . . .	186
5.5.1	The effect of Cl <sup>-</sup> on the shape of the CV of CrHydA1 . . . . .	186
5.5.2	The effect of irradiation on the CV of CrHydA1 recorded in potassium phosphate or mixed buffer . . . . .	187
5.5.3	Is UV light responsible of the characteristic shape of the CVs under of irradiation? . . . . .	189
5.5.4	Effect of temperature and scan rate on the CV shape in mixed buffer . . . . .	190
5.5.5	Chronoamperograms recorded in mixed buffer . . . . .	194
5.5.6	Discussion . . . . .	195
<b>6</b>	<b>Effect of light on other metalloenzymes</b>	<b>197</b>
6.1	Summary . . . . .	198
6.2	Résumé . . . . .	199
6.3	NiFe hydrogenases photo-activation . . . . .	200
6.3.1	Introduction . . . . .	200
6.3.2	Results . . . . .	202
6.3.3	Discussion . . . . .	204
6.4	Effect of light on Ni-CODH . . . . .	206
6.4.1	Introduction . . . . .	206
6.4.2	Results . . . . .	207
6.4.3	Discussion . . . . .	211
<b>7</b>	<b>Conclusions and perspectives</b>	<b>213</b>
	<b>Bibliography</b>	<b>219</b>



# Chapter 1

## Introduction

## 1.1 Hydrogenases

Hydrogenases are metalloproteins capable of catalyzing both the oxidation and production of molecular hydrogen. Discovered in bacteria in 1931,<sup>1</sup> hydrogenases are widely present in archaea, bacteria and in some eukaryotes, where they are involved in several metabolic pathways. The presence of specific metals cofactors in the active site of these enzymes suggested their classification as FeFe, NiFe and Fe hydrogenases<sup>2-4</sup> (see figure 1.1). While NiFe and FeFe hydrogenases catalyze the production/oxidation of  $H_2$ , Fe hydrogenases catalyze the reversible reaction of reduction of methenyl- $H_4MPT^+$  to methylene- $H_4MPT$  and are found only in methanogenic archaea. The heteromultimeric NiFe hydrogenase from *Ralstonia eutropha* couples the oxidation of  $H_2$  with the reduction of  $NAD^+$ . FeFe hydrogenases exist also in multimeric complexes that bifurcate electrons, like for example the FeFe hydrogenase from *Thermatoga maritima* that couples the protons reduction to form molecular hydrogen with the oxidation of NADH (endergonic) and the oxidation of ferredoxin (exergonic).<sup>5</sup>

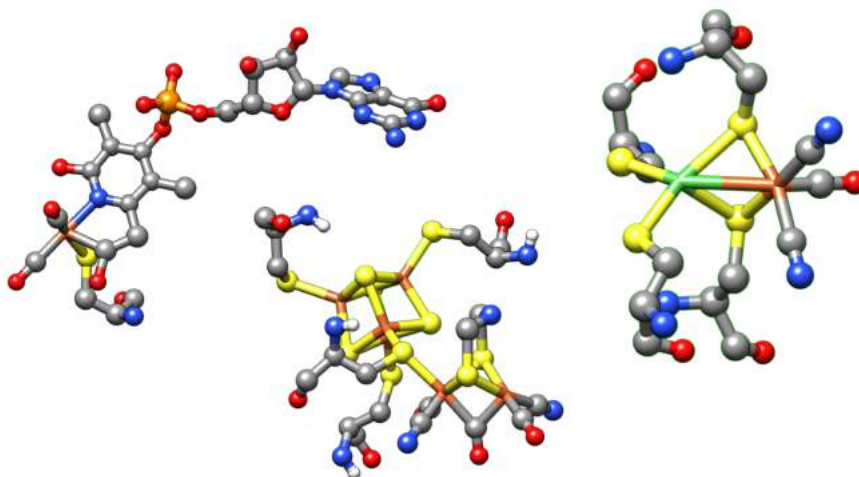


Figure 1.1: From left to right, active sites of Fe-Hydrogenases (PDB code 4JJG), FeFe-hydrogenases (PDB code 4XDC) and NiFe-hydrogenases (PDB code 3MYR). Color code: gray C, red O, blue N, brown Fe, green Ni, yellow S, white H.

The high turnover rate of hydrogenases ( $H_2$  production maximum TOF = 10000  $s^{-1}$  for FeFe hydrogenases)<sup>6</sup> has driven the study of these enzymes, since hydrogen

could be exploited as an electron carrier to produce energy without the polluting and unhealthy emissions produced by the combustion of carbon fuels (like CO, NO, NO<sub>2</sub>, SO<sub>2</sub> and benzene).

	H <sub>2</sub> uptake (U)		H <sub>2</sub> evolution (U)	
	as isolated	activated	as isolated	activated
<i>D. desulfuricans</i>				
aerobic purification	19300	62200	8200	8200
anaerobic purification	60000	nd	nd	nd
<i>C. reinhardtii</i>				
anaerobic purification	nd	nd	935	nd
<i>C. pasteurianum I</i>				
anaerobic purification	24000	nd	5500	nd
<i>C. pasteurianum II</i>				
anaerobic purification	34000	nd	10	nd
<i>M. elsdenii</i>				
anaerobic purification	9000	nd	7000	nd

Table 1.1: Specific activity of FeFe hydrogenases, table from ref. 4. U =  $\mu\text{mol of H}_2 \cdot \text{min}^{-1} \cdot \text{mg of enzyme}$ .

H<sub>2</sub> is an efficient electron carrier and it is oxidized in fuel cells to produce electricity, for example in hydrogen vehicles or even power plants. The principle of fuel cells, shown in figure 1.2 is to generate an electric current from the electron transfer between a metallic anode, where H<sub>2</sub> is oxidized, and a metallic cathode, where oxygen is reduced. The presence of a proton exchange membrane between the two electrodes allows the transfer of the protons generated by hydrogen oxidation toward the oxygen atoms on the cathode and the formation of water molecules, which, with heat, are the only byproducts.

Nowadays, this technology is used, for example, to power hydrogen cars but it requires hydrogen, which is actually mainly produced from hydrocarbons by a polluting process that produces 9-12 tons of CO<sub>2</sub> for each ton of H<sub>2</sub>.<sup>7</sup> Alternatively hydrogen can be obtained by water splitting, which requires energy mainly produced by carbon fuels and platinum as a catalyst, which is rare and expensive. The production or photo-production of hydrogen *in vivo* or *in vitro* employing hydrogenases or synthetic catalysts that mimic the active site of the enzyme, constitutes a possible solution to produce high amounts of H<sub>2</sub> reducing the polluting emissions.

Hydrogenases are employed also in biofuel cells where their H<sub>2</sub> oxidation activity

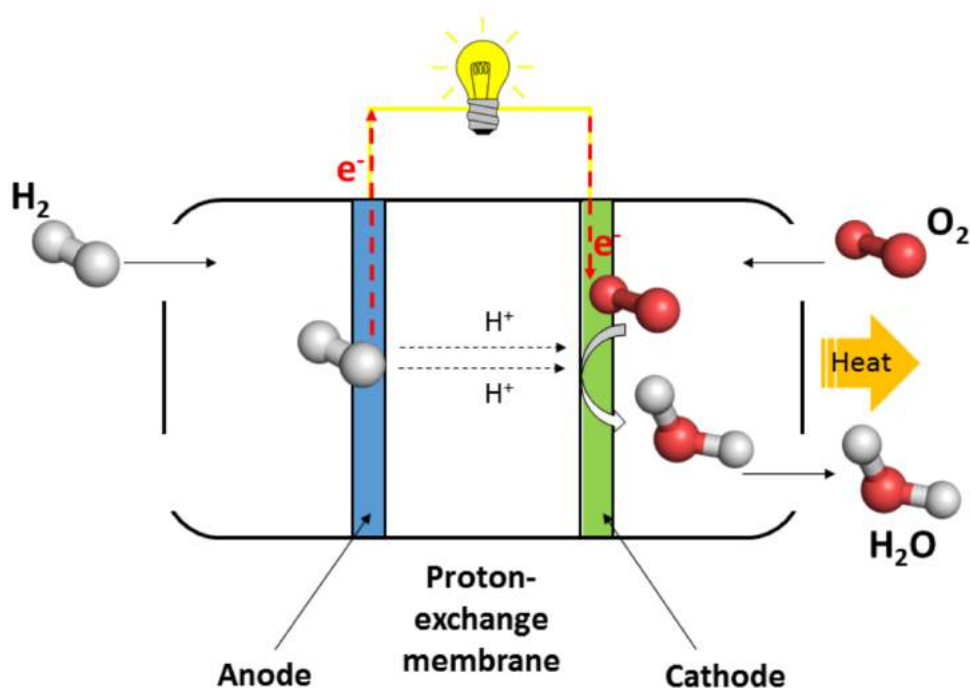


Figure 1.2: Principle of an hydrogen fuel cell.

is exploited replacing the expensive metal anode (for example platinum) in a fuel cells.<sup>8-10</sup> Actually all these technologies have to face the limits of hydrogenases, in particular the oxygen sensitivity, the reductive and oxidative anaerobic inactivation and the photoinhibition.

## 1.2 FeFe hydrogenases enzyme structure

During my PhD, I studied mainly FeFe-hydrogenases. FeFe hydrogenases can be monomeric, dimeric or multimeric and with a specific domains composition, which depends on the microorganism from which the enzyme originates. The crystals and the protein sequences showed that the binding domain of the active site, called H-cluster, is highly conserved in all FeFe hydrogenases and is characterized by three binding motifs P1, P2 and P3, reported in table 1.2.<sup>11</sup> The highest variability is located at the N-terminus, where we find different combinations of ferredoxin-like domains.

The H-cluster consists of a  $[4Fe4S]_H$  cluster bound to the protein matrix by three

## 1.2. FEFE HYDROGENASES ENZYME STRUCTURE

Motif name	Pattern
P1	[FILT][ST][SCM] <b>C</b> [CS] <b>P</b> [AGSMIV][FWY]
P2	[FILV][MGTV] <b>PC</b> [xx] <b>K</b> [DKQRS][x][EV]
P3	<b>E</b> [x] <b>M</b> [x] <b>C</b> [xx] <b>GC</b> [xx] <b>G</b> [ <b>AGP</b> ]

Table 1.2: H-cluster binding motifs shown in PROSITE format: the residues in brackets are present in a single position, "x" means any residue, the bold letters are amino acids that occur in the 80% of the sequences. Adapted from figure 12 in reference 11.

cysteines and by the thiolate group of a cysteine to a  $[2\text{Fe}]_{\text{H}}$  site (figure 1.3). The latter consists of two iron atoms, proximal ( $\text{Fe}_{\text{P}}$ ) and distal ( $\text{Fe}_{\text{D}}$ ) with respect to the  $[4\text{Fe}4\text{S}]_{\text{H}}$  cluster and each iron atom is coordinated by one CO and one  $\text{CN}^-$  ligand.<sup>12</sup> The iron atoms are bridged by a further CO and an azadithiolate group (ADT).<sup>13–16</sup> The distal iron presents a free coordination site in apical position, which is the binding site for  $\text{H}_2$  and the inhibitors CO<sup>17</sup> and  $\text{O}_2$ .<sup>18</sup> The presence of gas channels, which connect the surface to the H-cluster, allows the access of the substrate to the active site, which is deeply buried inside the protein<sup>18–20</sup> (see section 1.2).

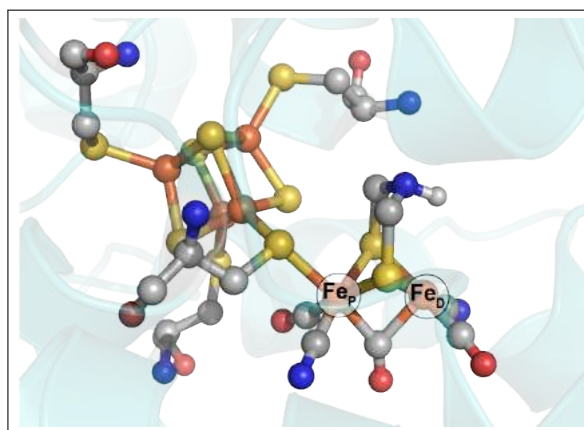


Figure 1.3: Structure of the H-cluster (extracted from the PDB file 4XDC) of FeFe hydrogenases. Color code: Fe brown, N blue, O red, S yellow, C grey, H white.

Peters et al.<sup>21</sup> obtained the first X-ray structure of a FeFe hydrogenase (CpHydA1) from the obligate anaerobe bacterium *Clostridium pasteurianum* in 1998 (PDB code: 1FEH)(fig. 1.1). CpHydA1 is a 64 kDa monomer, characterized by several domains: the H-cluster domain, which harbors the active site of the enzyme, two ferredoxin-

like [4Fe4S] binding domains, one histidine-coordinated [4Fe4S] binding domain and one ferredoxin-like [2Fe2S] binding domain, all involved in electron transfer to a ferredoxin (the redox partner).

The FeFe hydrogenase from the sulfate-reducing obligate anaerobe bacterium *Desulfovibrio desulfuricans* (DdHydAB) is a 53 kDa dimeric enzyme (42 kDa + 11 kDa) and its structure was resolved by Nicolet et al.<sup>22</sup> in 1999 (PDB code: 1HFE); in this case the enzyme presented only the H-cluster domain and two ferredoxin-like [4Fe4S] binding domains.

As shown in figure 1.4, the FeFe hydrogenase (CrHydA1) from the alga *Chlamydomonas reinhardtii*<sup>23</sup> has the H-cluster domain and no accessory FeS clusters. The crystallographic structure of CrHydA1 has been resolved only without in the apo-form (without a full H-cluster) expressed in absence of the maturases (PDB code: 3LX4<sup>24</sup>) or damaged by oxygen (PDB code: 4R0V<sup>25</sup>).

The structural diversity between the FeFe hydrogenases from different microorganisms, in particular the presence of accessory FeS cluster, could be related to the specific cellular localization of the enzyme and its role in the metabolic pathways. In particular, CpHydA1 is localized in the cytoplasm and it is involved in H<sub>2</sub> evolution, DdHydAB function is H<sub>2</sub>-uptake and it is contained in the periplasm,<sup>26</sup> while CrHydA1 evolves H<sub>2</sub><sup>27</sup> in the stroma of chloroplasts.

These three enzymes, classified among FeFe hydrogenases in the group A1 (prototypical) by Greening et al.,<sup>28</sup> are the most studied and they exchange electrons with ferredoxins (Fd), small proteins that harbor FeS clusters. The redox partner of CrHydA1 is the ferredoxin PetF, which transfers electrons from the photosystem-I to the H-cluster, where protons are reduced to molecular hydrogen. This process is transient, since the oxygen produced by photosynthesis inhibits the enzyme and suppresses the expression of the gene for CrHydA1.<sup>29</sup> CpHydA1 is involved in the elimination of the electron surplus produced during fermentation,<sup>30</sup> while DdHydAB oxidizes molecular hydrogen to produce a proton gradient through the membrane coupled to ATP synthesis in the cytoplasm.

In this thesis, I describe experiments performed on the already cited CrHydA1, but also on the FeFe hydrogenases from the anaerobic bacteria *Megasphaera elsdenii*



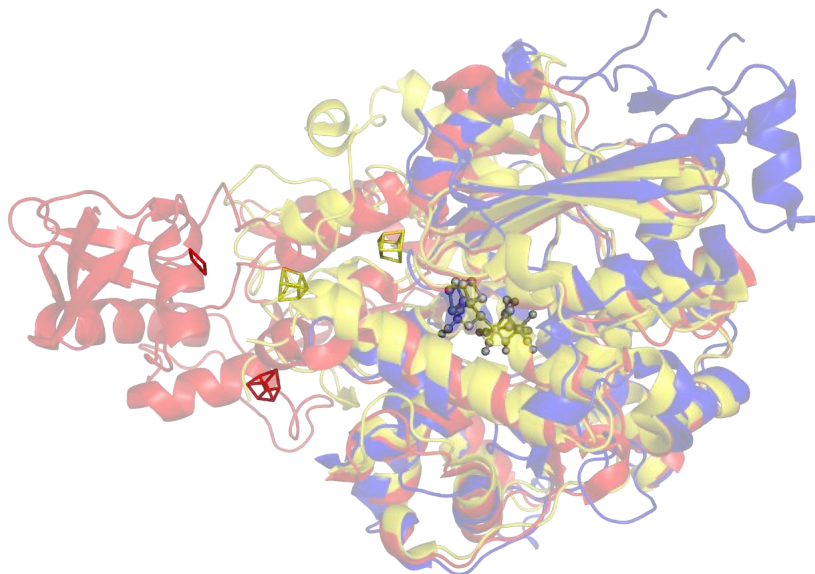


Figure 1.4: Superimposition of the crystallographic structure of the FeFe hydrogenase from *Chlamydomonas reinhardtii* (blue, PDB code: 3LX4<sup>24</sup>), *Desulfovibrio desulfuricans* (yellow, PDBcode:1HFE<sup>22</sup>) and *Clostridium pasteurianum* (red, PDB code: 3C8Y<sup>31</sup>). The FeS clusters and the active site of the enzyme are shown as sticks.

(MeHydA) and *Clostridium acetobutylicum* (CaHydA). At the present time, the X-ray crystallographic structures of these two enzymes have not been resolved, but we can observe from sequence alignments that MeHydA is a monomer and has the H-cluster binding domain and two ferredoxin-like [4Fe4S] binding domains<sup>32</sup> (42.4% sequence identity with CpHydA1 and 42.8% with DdHydAB) while CaHydA has the same structural domains as CpHydA1 (71.7% of sequence identity).

### 1.3 Gas diffusion channels

H<sub>2</sub> and the inhibitors of FeFe hydrogenases (carbon monoxide, molecular oxygen and also formaldehyde<sup>33</sup>) are all small molecules and they use intramolecular gas channels to reach the active site buried in the protein.

The investigation of gas channels has been performed analyzing the X-ray crystallographic structures,<sup>22</sup> *in silico*<sup>19,20</sup> and by kinetic studies on enzymes with mutations along the gas channels combined with MD simulations.<sup>18</sup> Nicolet, studying

the diffusion of xenon in DdHydAB with crystallography and molecular dynamics, observed an hydrophobic channel with a diameter of around  $0.75 \text{ \AA}$  that connects the surface of the protein to the H-cluster. Cohen and collaborators used molecular dynamics advanced techniques to simulate the diffusion of  $\text{H}_2$  and  $\text{O}_2$  in the crystallographic structure of CpHydA1 (PDB code: 1FEH<sup>21</sup>). As shown in figure 1.5, the authors found two main gas channels called pathway A and B which are not permanent but are cavities generated by the natural flexibility of the protein, independently of the presence of gas molecules.

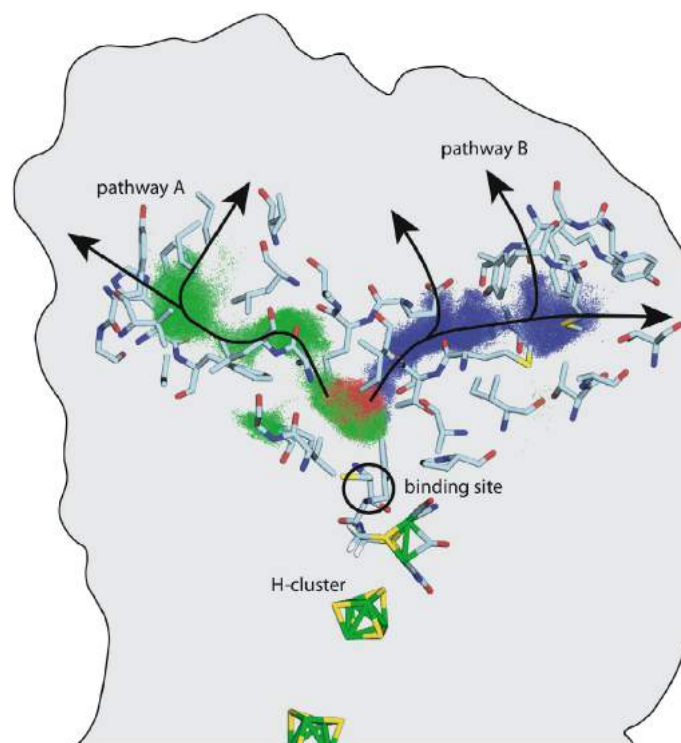


Figure 1.5:  $\text{O}_2$  channels identified by Cohen and colleagues<sup>20</sup> with Temperature-controlled Locally Enhanced Sampling (TLES).

## 1.4 Proton transfer

The existence of a proton transfer pathway is fundamental for the turnover of the enzyme. The analyses of the crystallographic structures of DdHydAB and CpHydA1, together with site-direct mutagenesis,<sup>34–39</sup> molecular dynamics and QM/MM computational studies<sup>40–43</sup> elucidate the presence of at least one proton pathway from the surface of the enzyme to the H-cluster, composed by highly conserved residues.

In DdHydAB and CpHydA1 the proton pathway starts from a glutamate (159 in DdHydAB, 282 in CpHydA1) on the surface of the protein, followed by protonation of a serine (198 in DdHydAB, 319 in CpHydA1). Successively one proton is transferred to the lateral chain of a glutamate (156 in DdHydAB and 279 in CpHydA1) and, through a water molecule, to a cysteine (178 in DdHydAB and 299 in CpHydA1), which is able to transfer protons directly to the amine of the ADT.

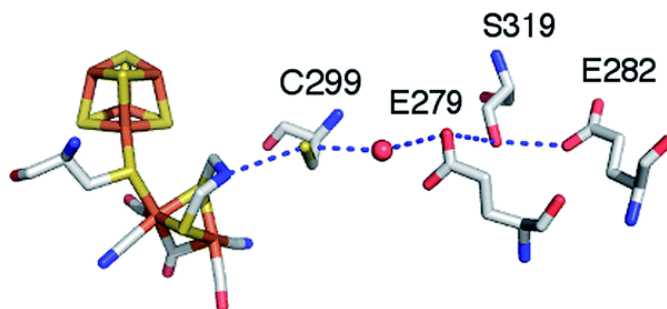


Figure 1.6: Residues involved in the proton transfer from the protein surface to the active site of the FeFe-hydrogenase of *C. pasteurianum* (PDB code: 3C8Y). Figure from ref. 43.

In CrHydA1 the pathway has not been defined yet, but the mutant Cys169Ser (homologous of DdHydAB Cys178 and CpHydA1 Cys299) has no activity,<sup>36</sup> meaning that the mutation probably affects the catalysis (this residue is near the  $[2\text{Fe}]_{\text{H}}$  site and has also a role in inhibition by  $\text{O}_2$ , as discussed in 1.7).

## 1.5 States of the H-cluster

In the following subsections, I will describe the redox-states of the H-cluster that have been identified by spectroscopic techniques:  $\text{H}_{\text{ox}}$ ,  $\text{H}_{\text{ox}}\text{CO}$ ,  $\text{H}_{\text{red}}$ ,  $\text{H}_{\text{inact}}$ ,  $\text{H}_{\text{sred}}$  and  $\text{H}_{\text{hyd}}$ .

### 1.5.1 $\text{H}_{\text{ox}}$ and $\text{H}_{\text{ox}}\text{CO}$

The electronic structure of the H-cluster has been investigated with spectroscopy and theoretical methods since the 1970's but it is still debated. The EPR spectra of oxidized CpHydA1 recorded in 1975 by Erbes et al.<sup>44</sup>(fig. 1.7, left) showed for

the first time the EPR rhombic signal with  $g$  values 2.098, 2.040, 2.001 (the so-called rhombic 2.10 signal) which is the "fingerprint" of the  $H_{ox}$  state of the H-Cluster ( $S=1/2$ ). The inhibition by CO of the oxidized enzyme, generates an axial signal with  $g$ -values 2.074 and 2.011 (the so-called "axial 2.07 signal", right spectrum in figure 1.7), attributed to  $H_{ox}CO$  state.

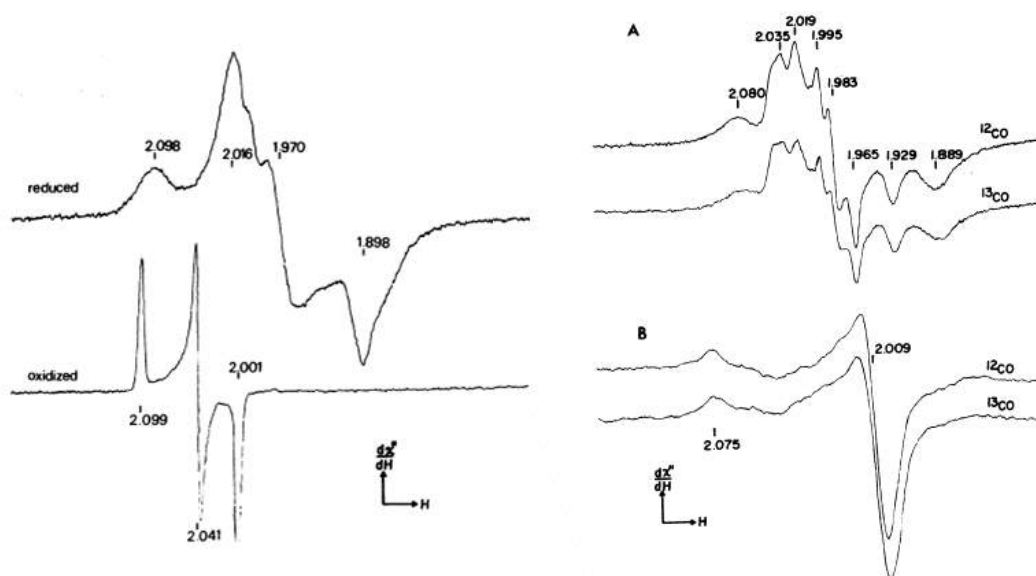


Figure 1.7: EPR spectra of CpHydA1 hydrogenase, adapted from figure 3 and 5 in reference 44. Conditions: 20 K, 50 mM Tris-HCl buffer pH 8.0, oxidized anaerobically with thionine and frozen in  $N_2$ .

The Mössbauer spectra by Rusnak et al.<sup>45</sup> and Popescu et al.<sup>46</sup> indicated that the  $[4Fe4S]$  in the H-cluster is in the  $2^+$  state and it is composed by 2  $Fe^{2+}$  and 2  $Fe^{3+}$ . The  $[4Fe4S]_H$  cluster consists of two high-spin  $[2Fe2S]$  subclusters, antiferromagnetically coupled to form an overall low spin state. The iron atoms of the  $[2Fe]_H$  site, in both  $H_{ox}$  and  $H_{ox}CO$  states of the H-Cluster, are in the  $Fe^I Fe^{II}$  redox configuration. The attribution of the redox state to  $Fe_P$  and  $Fe_D$  is not trivial: FTIR spectroelectrochemistry,<sup>47,48</sup> EPR<sup>49</sup> and DFT<sup>50</sup> studies suggest that  $Fe_D$  is the  $Fe^I$  while ENDOR, HYSCORE<sup>51</sup> and FTIR<sup>2,52,53</sup> data support the paramagnetic  $Fe^I$  nature of  $Fe_P$ .

Fourier transform infrared spectroscopy (FTIR) evidenced the presence of intrinsic CO and  $CN^-$  ligands bound to the active site.<sup>12,54</sup> The FTIR spectra of oxidized CpHydA1,<sup>47</sup> shown on the left of figure 1.8 in panel A, is characterized by two bands

arising from  $\text{CN}^-$  at 2086 and 2072  $\text{cm}^{-1}$ , two terminal CO bands at 1971 and 1948  $\text{cm}^{-1}$  and a bridging CO band at 1802  $\text{cm}^{-1}$ . The addition of CO induces a shift of all the bands at higher wavenumbers (panel B in figure 1.8) and the appearance of the band at 2017  $\text{cm}^{-1}$  assigned to the exogenous CO.

Since CO and  $\text{CN}^-$  are high field ligands, they maintain the iron atoms of the  $[\text{2Fe}]_{\text{H}}$  site in a low spin state.<sup>12</sup> Furthermore, the formation of hydrogen bonds between the two  $\text{CN}^-$  and the residues Ala109, Lys237 and Ile204 (Ddh numbering) lowers the basicity of the cyanide ligands, preventing their protonation.<sup>55</sup> DFT studies<sup>56</sup> underlined that the cyanide ligands have also a role in the tuning of the electronic properties of the H-cluster and the electron transfer between the  $[\text{4Fe4S}]$  cluster and the  $[\text{2Fe}]_{\text{H}}$  site.

### 1.5.2 $\text{H}_{\text{red}}$

The  $\text{H}_{\text{red}}$  state is the one electron reduced form of  $\text{H}_{\text{ox}}$  state.  $\text{H}_{\text{red}}$  is diamagnetic<sup>45</sup> (EPR silent), both irons in the  $[\text{2Fe}]_{\text{H}}$  site are considered as  $\text{Fe}^{\text{I}}$ ,<sup>58</sup> while the  $[\text{4Fe4S}]_{\text{H}}$  cluster is in the oxidized state (2+), as in the  $\text{H}_{\text{ox}}$  and  $\text{H}_{\text{ox}}\text{-CO}$  states.

The CO bands in the spectroelectrochemical FTIR spectra of CrHydA1 in the  $\text{H}_{\text{red}}$  state (on the bottom in figure 1.8) are shifted to lower wavenumbers compared to  $\text{H}_{\text{ox}}$  (1935, 1891 and 1780  $\text{cm}^{-1}$ ). The FTIR spectrum of DdHydAB in the  $\text{H}_{\text{red}}$  state is different from that of CrHydA1, since the bridging CO band (around 1800  $\text{cm}^{-1}$ ) is absent and another band appears in the terminal CO region (panel C, on the right of figure 1.8), suggesting that the geometry of the ligands in the reduced DdHydAB is all-terminal, without bridging CO.

### 1.5.3 $\text{H}_{\text{inact}}$

The  $\text{H}_{\text{inact}}$  state has been observed only in FeFe hydrogenases from *D. desulfuricans*, *D. vulgaris* (DvH)<sup>59</sup> and recently also in the FeFe hydrogenase from *Clostridium beijerinckii* (CbA5H).<sup>60</sup> The FTIR spectra of aerobically purified DdHydAB revealed the presence of a new state called  $\text{H}_{\text{inact}}$ .<sup>61,62</sup> The spectrum of  $\text{H}_{\text{inact}}$  (A on the right of fig.1.8) is similar to that of  $\text{H}_{\text{ox}}$  but all bands are shifted to higher wavenumbers,

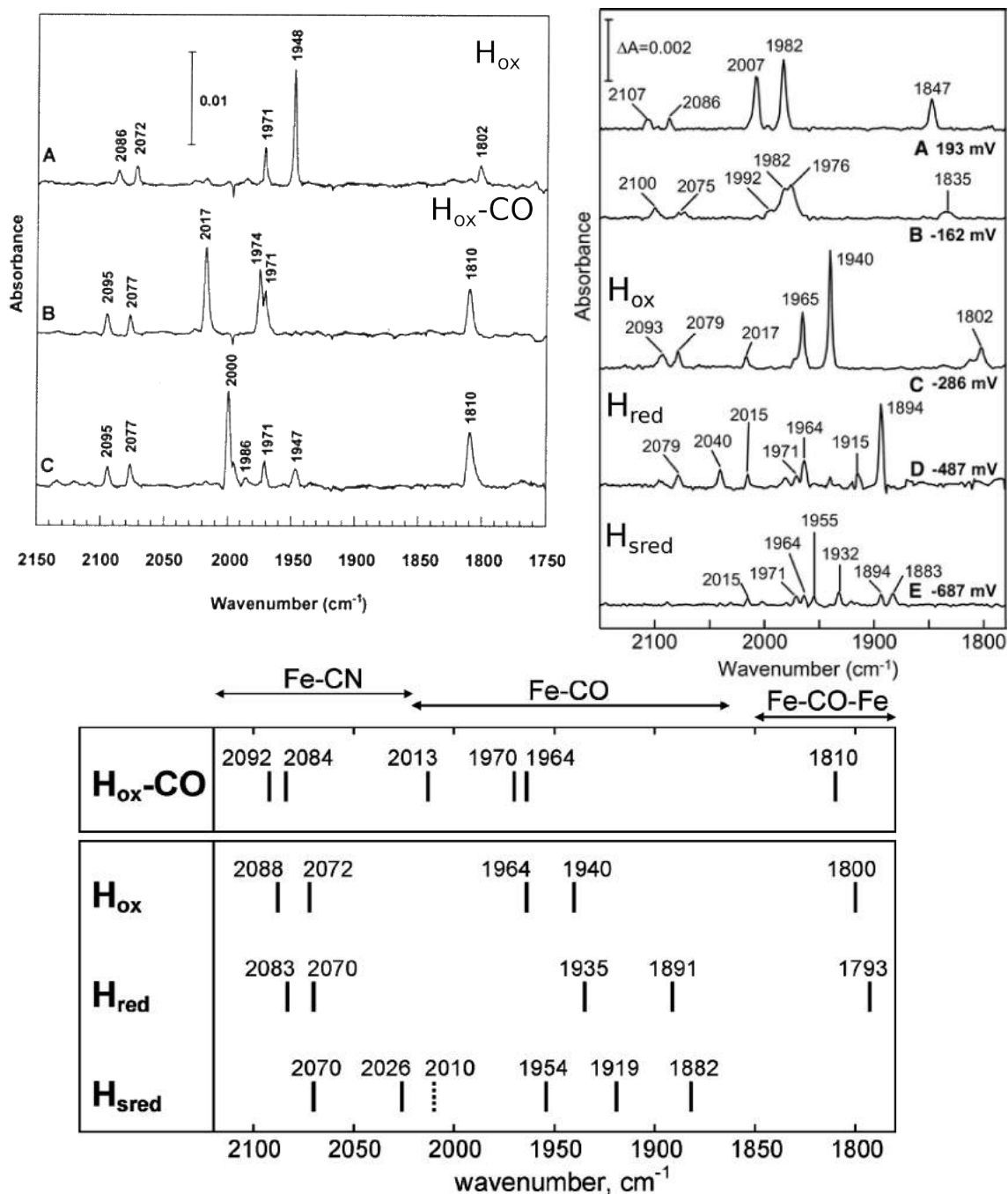


Figure 1.8: Vibrational frequencies of CO and CN<sup>-</sup> in FeFe hydrogenases. On the left (figure 2 from 47) is shown the spectra of CpHydA1 in the H<sub>ox</sub> (A), H<sub>ox</sub>-CO (B) and H<sub>ox</sub>-CO<sup>13</sup> (C) states at 20 K. On the right are shown the spectra at different potentials of DdHydAB (figure 2 from 48) recorded at 298 K. On the bottom (scheme 1 from 57) are shown the vibrational bands of CrHydA1 in different redox states, observed with spectroelectrochemistry at 277 K.

in particular the CO bands show a redshift of 40 cm<sup>-1</sup>. This state is inactive but it is oxygen resistant. It can be irreversibly converted to the transient state H<sub>trans</sub>

upon reduction by  $H_2$  or dithionite and to  $H_{ox}$  after further reduction. Only the FTIR spectra of the FeFe hydrogenase from *Clostridium beijerinckii* (CbA5H)<sup>60</sup> show that the  $H_{ox}/H_{inact}$  transition is reversible. In CbA5H  $H_{inact}$  can be obtained by exposure to air without inducing any damage by oxygen, then the enzyme can be reduced by  $H_2$  to obtain a  $H_{ox}/H_{red}$  mixture. EPR spectra suggest that the  $H_{inact}/H_{trans}$  transition is a one electron reduction of the  $[4Fe_4S]_H$  cluster.<sup>62</sup>  $H_{inact}$  is EPR silent<sup>63</sup> and the H-cluster is in a super-oxidized state, where both irons in the  $[2Fe]_H$  site are  $Fe^{II}$ . Liu et al.,<sup>64</sup> using DFT calculations, proposed that in  $H_{inact}$  the  $[2Fe]_H$  site is in a diferrous state but with a hydroxy group bound to the distal iron. The group of Michael B. Hall optimized with DFT the active site of CpHydA1 obtained by Peters.<sup>21</sup> The crystallographic structure of CpHydA1 presents an oxygen bound to the distal iron. Hall considered in the calculations the  $[2Fe]_H$  site in the  $Fe^{II}Fe^{II}$  state and the oxygen as  $OH^-$  or  $OOH^-$ , obtaining a distance  $d(Fe_D-O_{HO^-}) = 2 \text{ \AA}$ , which is what we would expect if the two atoms were bound. Hall and colleagues proposed that in  $H_{inact}$  the  $Fe_D$  is bound to  $OH^-$  or  $OOH^-$  since the IR computed spectra of these species well reproduce the experimental one. The presence of an exogenous ligand bound to the distal iron in the  $H_{inact}$  state would explain its oxygen resistance, but actually there is no real experimental evidence supporting this hypothesis.

To date, the reason why this state has been observed only in DdHydAB, DvHydAB and CbA5H is not clear; we can speculate that it is related to the presence of two accessory  $[4Fe_4S]$  clusters in these enzymes but the FeFe-hydrogenase from *M. elsdenii*, which has two accessory  $[4Fe_4S]$  clusters, can be purified only anaerobically.<sup>65–67</sup> We don't know if the presence of the 11 kDa secondary subunit in DdHydAB and of the SLBB (soluble-ligand-binding  $\beta$ -grasp fold) domain in CbA5H could also be somehow related to the formation of  $H_{inact}$  state.

#### 1.5.4 $H_{sred}$

Roseboom and colleagues observed with FTIR that at very low redox potentials (panel E on the right in figure 1.8) the spectrum of DdHydAB is characterized by weak bands.<sup>48</sup> The formation of this super reduced state, that they called  $H_{sred}$ ,

is irreversible, suggesting the destruction of the  $[2\text{Fe}]_{\text{H}}$  site. The FTIR spectrum of CrHydA1 obtained with spectroelectrochemistry under very reducing conditions, shown on the bottom of figure 1.8, is considered by the authors as  $\text{H}_{\text{sred}}$ . The band of the bridging CO is not observed in the super reduced state, suggesting the all-terminal geometry of the ligands. As said before, Roseboom<sup>48</sup> show that the formation of the  $\text{H}_{\text{sred}}$  state in DdHydAB is irreversible and the spectrum is characterized by low intensity bands, in contrast Silakov<sup>68</sup> observed that the  $\text{H}_{\text{sred}}$  state is reversibly formed in CrHydA1 and the spectrum presents intense bands. Silakov and colleagues<sup>68</sup> observed also that the  $\text{H}_{\text{ox}}/\text{H}_{\text{red}}$  redox transition takes place at -400 mV in both DdHydAB and CrHydA1 while the  $\text{H}_{\text{red}}/\text{H}_{\text{sred}}$  transition is observed at -540 mV in DdHydAB and -460 mV in CrHydA1. The authors proposed that this difference is due to the presence of accessory FeS clusters in DdHydAB. Considering the EPR data<sup>52</sup> of CrHydA1 the super reduced H-cluster can be described as a  $[4\text{Fe}4\text{S}]^{1+} \text{Fe}^{\text{I}} \text{Fe}^{\text{I}}$  state.

### 1.5.5 $\text{H}_{\text{hyd}}$

The groups of Hall and De Gioia, based on DFT studies, proposed the existence of an intermediate hydride-bound state in the catalytic cycle.<sup>14,58,69</sup> The hydride was considered either bound in apical position on the distal iron<sup>70</sup> or bound in bridging position between the distal and the proximal iron.<sup>71</sup> The detection of the hydride-bound species is difficult since the turnover frequency is high. To face this issue Mulder and Reijerse slowed the proton transfer to accumulate the hydride bound species. Mulder used mutated forms of the enzyme (*Cr* Cys169Ser)<sup>72</sup> and detected by EPR,<sup>42</sup> FTIR, Mössbauer<sup>72</sup> one hydride-bound species called  $\text{H}_{\text{hyd}}$ . In  $\text{H}_{\text{hyd}}$  state the  $[4\text{Fe}4\text{S}]_{\text{H}}$  is reduced (1+), the distal and proximal irons are  $\text{Fe}^{\text{II}}$ , the  $\text{Fe}_{\text{D}}$  is bound to an hydride in apical position and the bridging CO is terminal on the distal iron (see figure 1.15). Reijerse produced a synthetically matured CrHydA1 where the  $[2\text{Fe}]_{\text{H}}$  site has an ODT (oxadithiolate) group instead of ADT and used Raman spectroscopy<sup>73</sup> and Nuclear resonance vibrational spectroscopy (NRVS)<sup>74</sup> to detect in the spectra three different hydride-bound species. Using DFT, Reijerse assigned one species to  $\text{H}_{\text{hyd}}$  and the other two to protonation states of  $\text{H}_{\text{hyd}}$ :  $\text{H}^*_{\text{hyd}}\text{H}^+$ , which



has the same electronic structure as  $H_{\text{hyd}}$  but the ODT is protonated, and  $H_{\text{hyd}}H^+$ , which is characterized by an oxidized  $[4\text{Fe}4\text{S}]_{\text{H}}$  ( $2+$ ), a distal iron in  $\text{Fe}^{\text{I}}$  state and a protonated ODT.

## 1.6 Electronic structure of the H-cluster from DFT

At the beginning of this century, the availability of FTIR spectra,<sup>12</sup> EPR spectra<sup>75</sup> and X-ray crystallographic structures of  $\text{CpHydA1}$ <sup>21</sup> and  $\text{DdHydAB}$ <sup>22</sup> in conjunction with the increase in computing power of supercomputer facilities, encouraged the *in silico* modeling of the active site of FeFe-hydrogenases. Density functional theory (DFT) is the main method used for the study of metalloenzymes because it is a good compromise between the computational resources needed to perform the calculations and the accuracy of the results. The functionals that give the best results in DFT calculations of metal cofactors are BP86, B3LYP and PBE0.<sup>76</sup> The first calculations were performed on models of the  $[2\text{Fe}]_{\text{H}}$  site because the implementation of the electronic structure of the full H-cluster is not trivial. The  $[2\text{Fe}]_{\text{H}}$  site was modeled with PDT ( $\text{S}_2(\text{CH}_2)_3$ ) instead of ADT,<sup>58,64,77</sup> because the presence of the pendant amine was not confirmed yet and synthetic models with PDT were already available.<sup>78-80</sup> The  $[4\text{Fe}4\text{S}]_{\text{H}}$  cluster consists of two  $[2\text{Fe}2\text{S}]$  layers coupled antiferromagnetically, each formed by one  $\text{Fe}^{2+}$  and one  $\text{Fe}^{3+}$  high spin ions coupled ferromagnetically, giving an overall low spin state.<sup>50,69</sup> As shown in figure 1.9, the H-cluster in the  $H_{\text{ox}}$  and  $H_{\text{ox}}\text{-CO}$  states can be described as a three spin system: the  $[2\text{Fe}]$  site has  $S = 1/2$ , each layer of the  $[4\text{Fe}4\text{S}]_{\text{H}}$  cluster has  $S = S(2)+S(5/2) = 9/2$ .

The treatment of the resulting wave function would require multiconfigurational methods but this is actually impossible because of the extremely high amount of computational resources required. Fortunately, Noodleman developed the Broken Symmetry (BS)<sup>81,82</sup> approach to treat antiferromagnetical coupling with DFT. Adam Fiedler and Thomas Brunold in 2005 were the first to use BS with DFT to calculate the geometrical and electronic properties of the full H-cluster.<sup>50</sup> The authors were able to fairly reproduce the g-values and the ligand hyperfine coupling

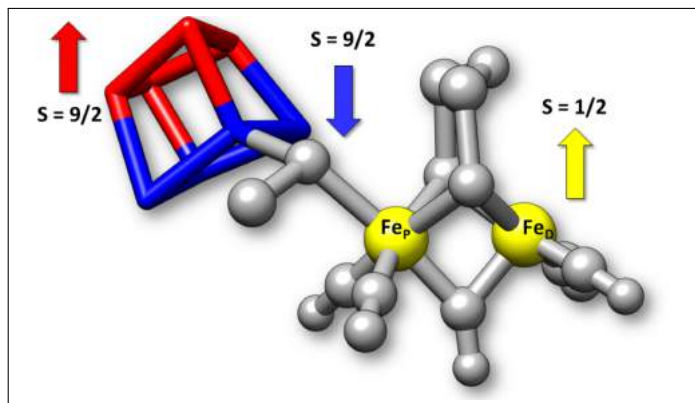


Figure 1.9: Three-spin model of the H-cluster in the  $H_{ox}$ . The atoms in blue and red represent the two  $2Fe_2S$  layers coupled antiferromagnetically. The distal and proximal iron are colored in yellow. The spin of the three layers are indicated near the corresponding arrows.

constants of experimental EPR spectra of  $H_{ox}$ . Furthermore, Brunold observed from Mulliken population analysis that in the  $H_{ox}$  state the spin density is localized on the distal iron, suggesting a  $Fe_P^{II}-Fe_D^I$  configuration, while the binding of a CO in apical position on the  $Fe_D$ , to form the  $H_{ox}-CO$  state, moves the spin density toward the proximal iron. Bruschi et al.<sup>69</sup> systematically studied reduced and oxidized states of the full H-cluster with DFT and BS. The results from the calculations showed that the optimized geometry of the  $[2Fe]_H$  site is not affected by the presence of the  $[4Fe_4S]_H$  cluster in all redox states, as shown by the geometrical equivalence between the small  $Fe_2S_2$  models and the  $Fe_6S_6$  full H-cluster models (using BP86 functional and the def-TZVP basis set). In all the redox states, the  $[4Fe_4S]_H$  cluster was in the oxidized state (+2), except for the super reduced state that presented a reduced (+1) iron-sulfur cluster. The atomic charges of the distal and proximal irons are almost symmetrical. The presence of spin density on the distal iron is clearly visible when the active site is in the  $H_{ox}$  state (as observed by Brunold). The binding of a CO,  $H_2$  or a proton on the  $Fe_D$  shifts the unpaired electron toward the proximal iron. Bruschi et al.<sup>56</sup> calculated the molecular orbitals of the full H-cluster. The determination of the highest-occupied molecular orbital (HOMO) and the lowest unoccupied molecular orbital (LUMO) is important because those are frontier orbitals mainly involved in the reactivity. The authors observed that in the  $H_{red}$  state the HOMO is localized on the  $[2Fe]_H$  cluster, while the LUMO is localized on the

$[4\text{Fe}4\text{S}]_{\text{H}}$  site. This means that upon oxidation one electron is removed from the  $[2\text{Fe}]_{\text{H}}$  site.

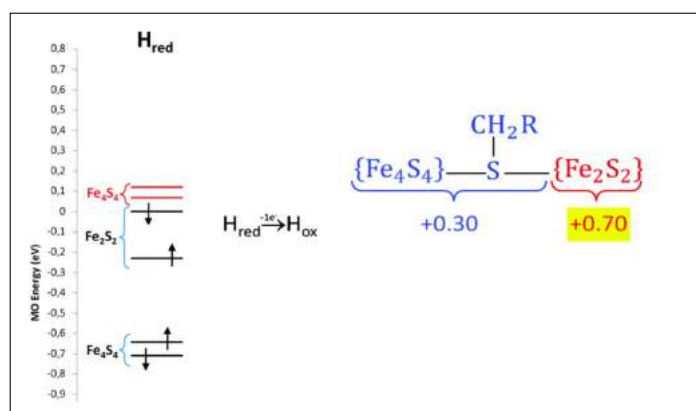


Figure 1.10: Localization of the molecular orbitals in  $\text{H}_{\text{red}}$  state on the left. On the right are reported the values of the Mulliken population upon oxidation of  $\text{H}_{\text{red}}$  to  $\text{H}_{\text{ox}}$ . In yellow is marked the fragment that is oxidized. Adapted from ref. 56.

The same authors, performed QM/MM calculations<sup>83</sup> with the structure of the full DdHydAB enzyme, observed that the binding of hydrogen on the distal iron when the active site is in the  $\text{H}_{\text{ox}}$  state decreases the HOMO-LUMO gap. In this large model, the HOMO is localized on the H-cluster and the LUMO on the  $[4\text{Fe}4\text{S}]$  cluster localized on the surface of the protein ( $\text{F}'$ -Cluster), so the decrease in the energy difference between the two orbitals favors long-range electron transfer between the H-cluster and the accessory FeS clusters.

## 1.7 Aerobic oxidative inactivation

FeFe hydrogenases have to be purified fully anaerobically to be active (except for DdHydAB, DvHydAB and CbA5H which reversibly form an inactive state, see subsection 1.5.3) because exposure to oxygen destroys the enzyme. Kowal observed with EPR that upon treatment of DdHydAB with oxygen and without CO<sup>84</sup> the  $\text{H}_{\text{ox}}$ -CO signal appeared and Adams initially assigned this signal to an  $\text{O}_2$ -bound active form.<sup>85</sup> In PFV experiments DdHydAB is irreversibly inactivated by exposure to low concentrations of oxygen<sup>86</sup> at potentials where the dominant species is  $\text{H}_{\text{ox}}$  (while  $\text{H}_{\text{red}}$  state is more resistant toward oxygen inhibition<sup>87</sup>). At least two

steps are involved in the process of inhibition by oxygen: at first the oxygen diffuses towards the active site and binds the H-cluster, then the active site is irreversibly damaged. The initial binding site for oxygen is the  $\text{Fe}_D$ , since we know that the competitive inhibitor CO, which in the crystal of CpHydA1 is bound to the distal iron,<sup>17</sup> protects the enzyme against  $\text{O}_2$  inhibition.<sup>88,89</sup> Conversely the irreversible inactivation process is still matter of debate. Two main mechanisms have been proposed:

- a. Haumann et al.<sup>90,91</sup> based on XAS (X-ray absorption spectroscopy) spectra of CrHydA1 concluded that the  $[\text{4Fe4S}]_H$  cluster is destroyed by oxygen. The authors proposed a three steps mechanism that starts with the interaction between the distal iron and oxygen that causes an elongation of the  $\text{Fe}_D$ - $\text{Fe}_P$  distance and fast generation of a reactive oxygen species (ROS). The ROS converts the  $[\text{4Fe4S}]_H$  cluster into a  $[\text{3Fe4S}]$  cluster and finally, in the third phase, most of the Fe-Fe and Fe-S interactions disappear and iron oxidation is detected, meaning that the H-cluster is completely degraded.
- b. Peters et al. published in 2015<sup>25</sup> a crystallographic structure of CrHydA1 (PDB code 4R0V) treated with  $\text{O}_2$  that shows the absence of the  $[\text{2Fe}]_H$  site in the H-cluster and the oxidation of a conserved cysteine (169 in Cr, 178 in DdHydAB, 299 in CpHydA1), while the  $[\text{4Fe4S}]_H$  cluster is still intact. The FTIR analysis of CrHydA1 treated with oxygen showed a decrease of  $\text{H}_{\text{ox}}$  bands and the appearance of the typical bands of  $\text{H}_{\text{ox}}\text{-CO}$ , as observed by EPR. Peters proposed that the  $\text{H}_{\text{ox}}\text{CO}$  signal observed after exposure to oxygen arises from the so-called "cannibalization" process. This process consists in the inhibition of the undamaged enzymes by the CO released from the degraded  $[\text{2Fe}]_H$  sites.

The group of Reiher deeply studied *in silico* the possible effect of oxygen on the H-cluster with density functional theory (DFT).<sup>93</sup> In a recent paper<sup>94</sup> his group investigated all the possible pathways to activate oxygen bound to the distal iron and calculated the energy barriers for the formation of intermediates, considering different states of the H-cluster. They showed that proton transfer to  $\text{O}_2$  bound to  $\text{H}_{\text{ox}}$  has low activation barriers, which decrease further if the H-cluster is reduced. This

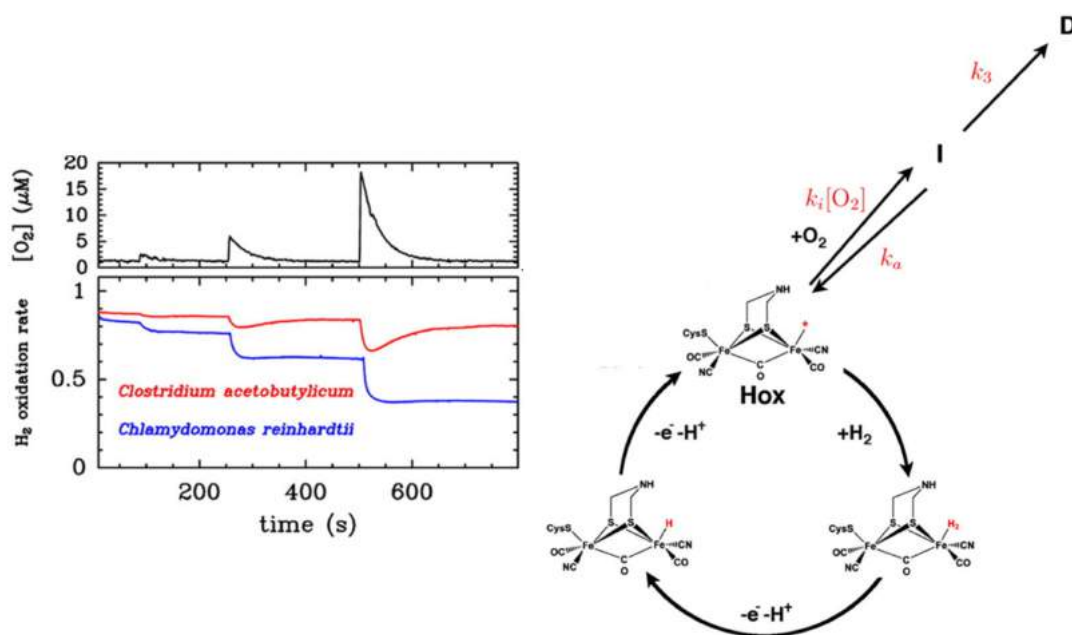


Figure 1.11: Figure from ref 92. On the left is shown in a chronoamperogram (current vs time) the effect of successive exposure to oxygen at 100s, 250s and 500s (final concentration of  $O_2$  are shown in the top panel) of CrHydA1 (blue) and CaHydA (red). The partial recovery of current after the initial inhibition shows that CaHydA is more resistant to oxygen than CrHydA1. Conditions:  $E = 40$  mV vs SHE,  $\Omega = 3000$  rpm, 1 bar  $H_2$ ,  $T = 12^\circ\text{C}$ ,  $pH = 7$  (mixed buffer). On the right is shown the scheme of the species generated by aerobic oxidative inactivation.

means that oxygen reduction is possible if there are enough electrons and protons but it requires the formation of an  $H_2O_2$  intermediate. During this process ROS can be formed and they have low energy barriers for dissociation. If the protonations are fast and coupled to electron transfer, water formation is exothermic. When the H-cluster is in the  $H_{\text{red}}$  state, the process is faster and so less ROS should be formed. Starting from these results, Reiher and colleagues suggest that the differences in resistance to oxygen between the FeFe-hydrogenases from different microorganisms could be due to the more efficient electron transfer, needed for the water formation, in the enzymes that harbor a FeS clusters chain. This hypothesis would explain the higher resistance to oxygen of CaHydA, that has 3 accessory  $[4Fe4S]$  clusters and one  $[2Fe2S]$  cluster, compared to CrHydA1, that has no accessory clusters.

In protein film electrochemistry experiments the inactivation by  $O_2$  of CaHydA<sup>88</sup>

and CrHydA1<sup>92</sup> is partially reversible. Baffert suggests that the process should start with the reversible formation of a species bound to O<sub>2</sub> that then can irreversibly evolve towards a dead-end species (see scheme in figure 1.11).<sup>88</sup> As shown in figure 1.11, the FeFe hydrogenase from *Clostridium acetobutylicum* is more resistant toward oxygen than the enzyme from *Chlamydomonas reinhardtii*. The higher sensitivity to O<sub>2</sub> of CrHydA1 is not related to the reactivation process, since the rate of reactivation is the same as CaHydA1 ( $k_a$  in fig.1.11), but it is related to the higher rate of formation of the dead-end species ( $k_3$  in fig.1.11) in CrHydA1 than in CaHydA1.

To better understand the aerobic oxidative inactivation we studied the FeFe-hydrogenase from *C. reinhardtii* using protein film electrochemistry and theoretical methods (MD and DFT). We identified the diffusion channels for oxygen and carbon monoxide and we obtained the pathways of ROS generation and water formation with DFT calculations supported by direct electrochemistry data, as reported in chapter 3.

## 1.8 Anaerobic oxidative inactivation

All FeFe hydrogenases inactivate under anaerobic oxidative conditions. The H<sub>inact</sub> state of DdHydAB, described in the subsection 1.5.3, is an inactive over-oxidized and oxygen resistant form of the H-cluster obtained by aerobic purification. In 1983 van Dijk et al. showed that the H<sub>2</sub> reduced DvHydAB can be anaerobically converted to the inactive oxygen resistant form of the enzyme<sup>59</sup> by oxidation with DCIP(2-6-dichlorophenol-indophenol) in presence of sulfide, iron and EDTA, followed by addition of Tris-EDTA at pH 9. The possibility to obtain the H<sub>inact</sub> state of DvHydAB under anaerobic conditions, suggests that oxygen is not directly involved in the generation of this state. Van Dijk was not able to obtain the same result with the FeFe hydrogenase from *M. elsdenii*<sup>59</sup> and Roseboom<sup>48</sup> was not able to reproduce it with DdHydAB, which has the same sequence as DvH. Recently F. Valetti showed with FTIR that it is possible to oxidize H<sub>ox</sub> to H<sub>inact</sub> with DCIP or air and to reduce it back to H<sub>ox</sub> without any damage by oxygen in the FeFe hydrogenase

from *Clostridium beijerinckii*.<sup>60</sup>

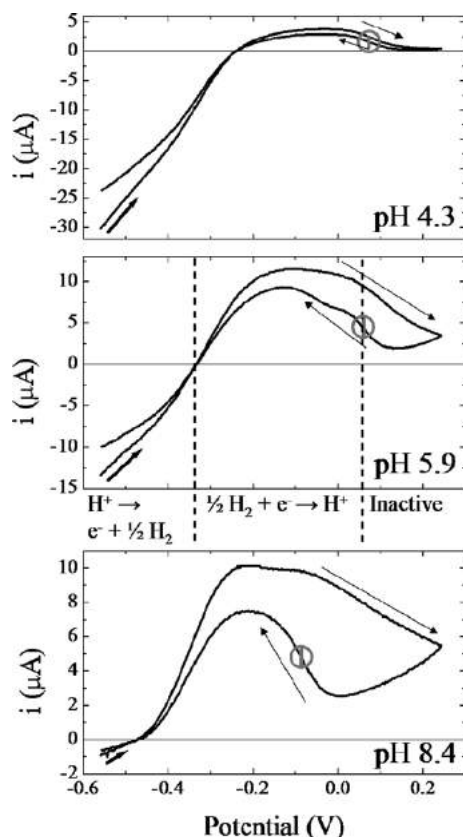


Figure 1.12: Figure from ref. 95. Cyclic voltammograms of DdHydAB at different pH. Conditions:  $\Omega = 2500$  rpm,  $\nu = 10$  mV/s, 1 bar  $\text{H}_2$ ,  $T = 10^\circ\text{C}$ , gray circles indicate the  $E_{\text{switch}}$ .

Parkin et al.<sup>95</sup> observed with protein film voltammetry that cyclic voltammograms (current against potential) of DdHydAB showed at high potential the appearance of an hysteresis (see figure 1.12), due to inactivation on the forward scan (from low to high potential) and reactivation on the reverse scan. The same authors observed also the oxygen stability of the oxidized inactive enzyme, so they suggested that at high potential the enzyme is in the  $\text{H}_{\text{inact}}$  state. However, the  $\text{H}_{\text{inact}}$  state has been observed with FTIR only in the FeFe hydrogenases from *Desulfovibrio desulfuricans* and *Clostridium beijerinckii* purified aerobically but the cyclic voltammograms of FeFe hydrogenases from CaHydA and CrHydA1 show clearly the presence of anaerobic oxidative inactivation, denying the identity between  $\text{H}_{\text{inact}}$  and the inactive state(s) produced at high potential. To clarify the oxidative inactivation mechanism, in 2014, the groups of Christophe Léger and Luca De Gioia studied

CrHydA1 and CaHydA combining protein film voltammetry, molecular dynamics and density functional theory calculations.<sup>96</sup> The data show that at high potential at least two inactive species are reversibly formed and one inactive species is irreversibly formed. The rate of inactivation of the reversibly formed inactive species is dependent of  $H_2$  pressure, while the rate of reactivation strongly depends on potential and pH. Each reversibly formed inactive state exists in two redox states, one is a minor isomer of  $H_{ox}$  where  $H_2$  is bound to an unusual position (bridging or bound equatorial to the  $Fe_D$ ) and an over-oxidized form,  $H_{overox}$ , where the  $[2Fe]_H$  site is an hydride-bound diferrous state after deprotonation (called **1H** and **2H**). **1H** and **2H** are reactivated by slow direct reduction to  $H_{ox}$  or by a reduction followed by a fast chemical reaction (scheme 1.13). Both inactive species are protected from oxygen, because there are no available binding sites on the 6-coordinated irons. The formation of minor isomers of  $H_{ox}$  is possible because the COs on the distal iron can isomerize, as showed by FTIR,<sup>48,97</sup> and MD simulation suggested that the flexibility of a phenylalanine residue (F290 in CrHydA1) near the distal iron allows the isomerization. To confirm this, the authors replaced this phenylalanine with a tyrosine and observed that the mutation induces an increase of the proportion of irreversible inactivation in CVs and almost no reactivation, because the formation of the isomers is hindered. The study of Fourmond et al. shows that the oxidative inactivation at high potential is more complex than the formation of an  $H_{inact}$  state and involves reversible and irreversible processes.

## 1.9 Reductive inactivation

In 1982 Fernandez performed activity assays at different potentials with CpHydA1 and observed that the  $H_2$  evolution activity of the enzyme decreases greatly at very low potential.<sup>98</sup> Roseboom et al.<sup>48</sup> (as said before in subsection 1.5.4) observed with FTIR that, under strong reductive conditions, the spectrum of DdHydAB shows low intensity bands. The authors assigned these bands to the  $H_{sred}$  state. Roseboom suggested that the weakness of the bands and the impossibility to oxidize the sample, to obtain the  $H_{red}$  spectrum, indicate the destruction of the active site at very low



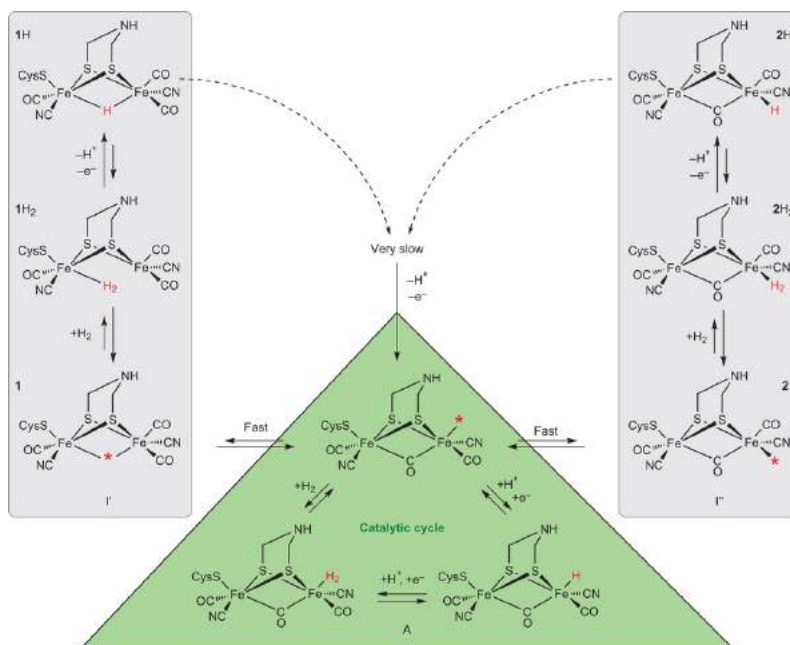


Figure 1.13: Scheme of the species formed by anaerobic oxidative inactivation from ref 96.

potential, in agreement with the great decrease of activity observed by Fernandez.<sup>98</sup>

Adamska et al.<sup>52</sup> studied the super-reduced state in DdHydAB, CrHydA1 and CaHydA with EPR, FTIR spectroelectrochemistry and PFV and were able to oxidize samples mainly in the  $H_{\text{sred}}$  state to  $H_{\text{red}}$ . In the same paper the authors showed chronoamperograms with steps at low potential and claimed that no irreversible inactivation on DdHydAB and CaHydA1 is present. The data of CrHydA1 showed a decrease of current, which the authors attributed to film-loss, meaning desorption of the enzyme from the electrode. The absence of inactivation at low potential in PFV was considered as a confirmation that  $H_{\text{sred}}$  is involved in the catalytic cycle. But in 2014 Hajj et al.<sup>99</sup> showed electrochemical data similar to those of Adamska, obtained using CrHydA1, where inactivation at low potential is clearly visible. The experiments of Hajj<sup>99</sup> revealed that under turnover conditions, at very low potentials, species are reversibly and irreversibly formed.

The CV of CrHydA1 shown in figure 1.14 was recorded starting from a potential where the enzyme performs  $H_2$  oxidation (at that potential  $H_{\text{ox}}$  should be the major species) and going at low potential. The backward sweep presents a hysteresis at low potential. The 30% of current is lost at low potential but the enzyme partially

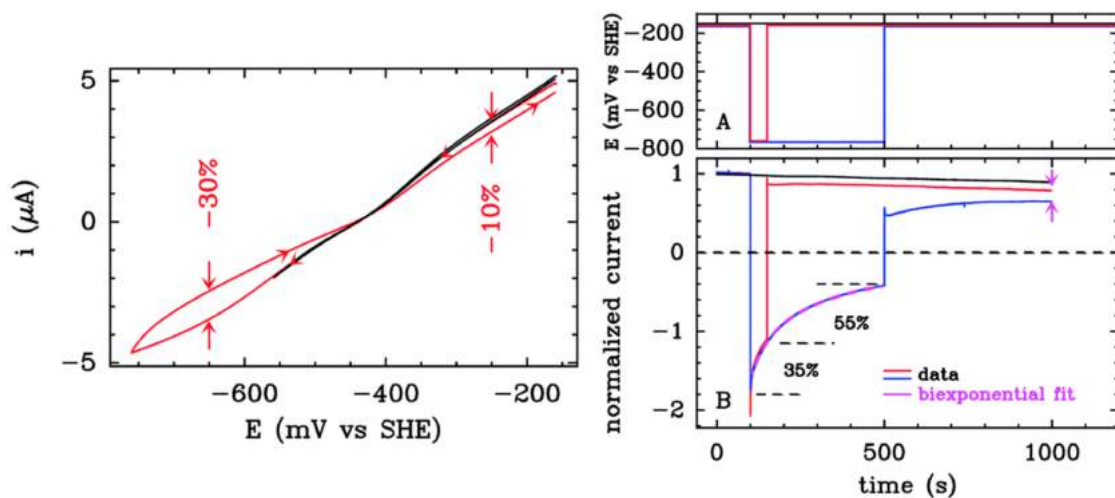


Figure 1.14: Figure from ref. 99. On the left, cyclic voltammogram of CrHydA1. Conditions:  $\Omega = 3000$  rpm,  $\nu = 20$  mV/s, 1 bar  $\text{H}_2$ ,  $T = 30^\circ\text{C}$ ,  $p\text{H} = 7$ . On the right panel A shows the potential steps as function of time applied in the chronoamperograms of CrHydA1 in panel B. The black line is a control experiment where no potential steps were applied, the dashed magenta line is the fit of a biexponential function. Conditions:  $\Omega = 3000$  rpm, 1 bar  $\text{H}_2$ ,  $T = 30^\circ\text{C}$ ,  $p\text{H} = 7$ .

reactivates increasing the potential, so at  $\text{H}_2$  oxidation potential only 10% of current is lost. The chronoamperograms recorded with a CrHydA1 film shown in panel B of figure 1.14 were performed by Hajj et al. stepping the potential up and down for different windows of time. When the step at low potential is short (red trace) the current decrease by 35% but the 90% of the lost current is recovered stepping back at high potential. If the step at low potential is longer (blue trace), the inactivation is biphasic (the best fit of the data is a biexponential function). The subsequent step at high potential produces a monoexponential increase of current but the overall loss of current (pink arrows) indicate the presence of irreversible inactivation. The data suggest that at least two species are formed at low potential and that one of them is a species that is less active in  $\text{H}_2$  production but still active in  $\text{H}_2$  oxidation. The inactivation observed is not due to film loss, since the enzyme was covalently immobilized on the electrode.<sup>100</sup> The time scale of the inactivation (minutes) is faster than that needed for the preparation of samples in the  $\text{H}_{\text{sred}}$  state for spectroscopy,

that, as a consequence, are probably composed by a fraction of inactive enzyme and a fraction of active enzyme that still produces hydrogen. Considering the results of Fernandez, Albracht, Hajj and the PFV data of Adamska, we can conclude that at very low potential FeFe-hydrogenases irreversibly form, at least, one inactive species.

## 1.10 The catalytic cycle

Many states of the H-cluster has been isolated by spectroscopy, as shown in section 1.5, but are they all involved in the catalytic cycle? Electrochemistry under turnover conditions show us that, for example, an inactive species is irreversibly formed under the reducing conditions at which  $H_{\text{sred}}$  has been detected by FTIR. Why should an accumulating inactive species be involved in the catalytic cycle? In the following subsections I discuss the current opinions about the inclusion or not of the states of the H-cluster observed with spectroscopy as intermediates of the catalytic cycle and the currently proposed mechanisms.

### 1.10.1 Which states of the H-cluster are involved in the catalytic cycle?

As mentioned in previous sections, three states of the H-cluster have been identified so far in all FeFe hydrogenases:  $H_{\text{ox}}$ ,  $H_{\text{red}}$  and  $H_{\text{sred}}$ . As shown in figure 1.15, the  $H_{\text{ox}}$  state is considered by every group as part of the catalytic cycle. The main issue about this state, as reported in subsection 1.5.1, is the formal redox state of the distal and proximal irons.

$H_{\text{ox}}$  can bind hydrogen and the  $H_{\text{ox}}-H_2$  state has been described theoretically in two different forms:  $[4\text{Fe}4\text{S}]^{1+}-\text{Fe}^{\text{II}}-\text{Fe}^{\text{II}}-H_2$ <sup>72</sup> or  $[4\text{Fe}4\text{S}]^{2+}-\text{Fe}^{\text{I}}-\text{Fe}^{\text{II}}-H_2$ .<sup>74</sup> As underlined in section 1.6, DFT calculations show that the binding of  $H_2$  to  $H_{\text{ox}}$  generates a diferrous intermediate state which is essential for the splitting of hydrogen. Also  $H_{\text{red}}$  is a key state in the catalytic cycle since DFT showed that ADT can be protonated only in the reduced state.  $H_{\text{red}}$  is usually represented in the form  $[4\text{Fe}4\text{S}]^{2+}-\text{Fe}^{\text{I}}-\text{Fe}^{\text{I}}$  with a protonated ADT ( $= (\text{SCH}_2)_2\text{NH}_2^+$ ).

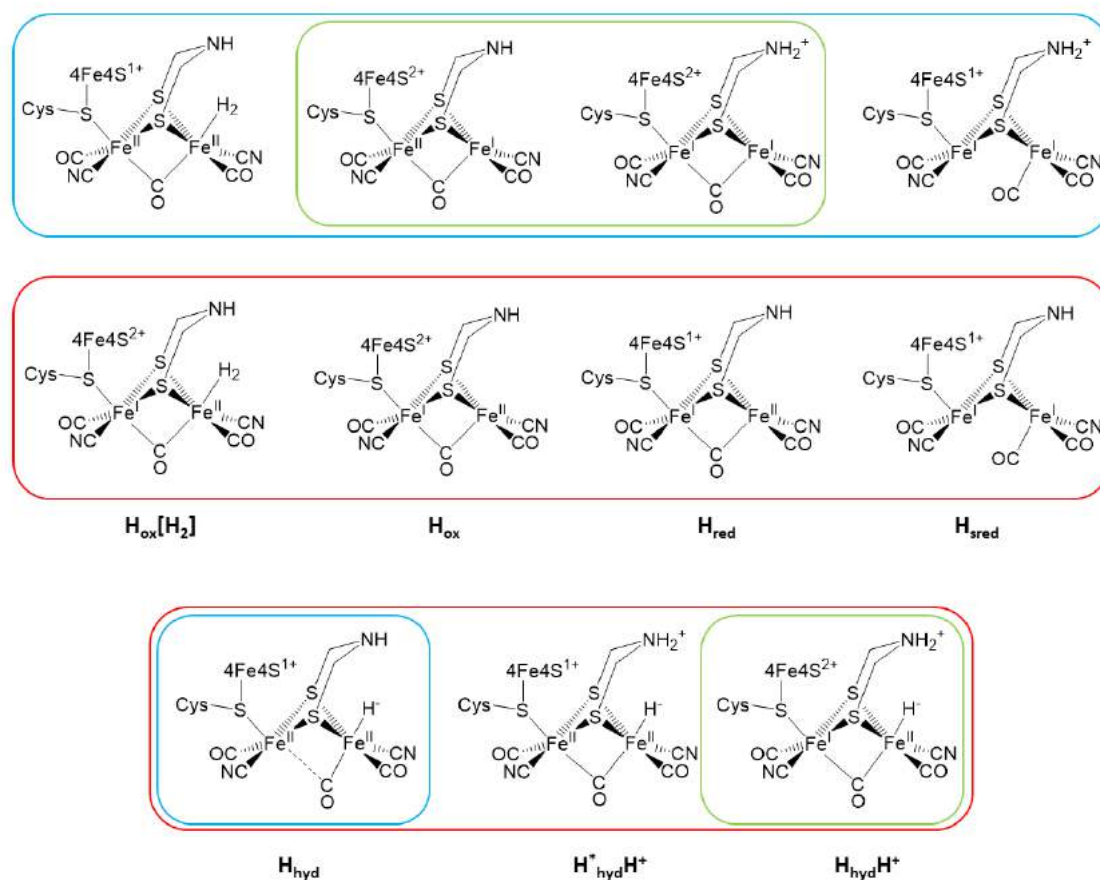


Figure 1.15: States of the H-cluster. The color of the boxes indicates the paper where the intermediates were included in the catalytic cycle: green is ref. 99, (figure 1.17), blue is ref. 72 (top scheme in figure 1.18) and red is ref. 74 (bottom cycle in figure 1.18).

Recently Reijerse et al.,<sup>74</sup> using spectroelectrochemistry, proposed that in the  $H_{red}$  state the  $[4Fe_4S]_H$  cluster is reduced (1+) and the  $[2Fe]_H$  site is in the  $Fe^I-Fe^{II}$  state as in  $H_{ox}$  (ADT is not protonated). Considering only the three states that are commonly considered as part of the catalytic cycle  $H_{ox}$ ,  $H_{ox}-H_2$  and  $H_{red}$ , we can write the simplified form of the catalytic cycle showed in figure 1.16.

The  $H_{red}/H_{ox}-H_2$  transition requires an intermediate with an hydride bound on the distal iron, which then forms a bond with the proton on the ADT and finally an hydrogen molecule is released. Computational calculations on the  $[2Fe]_H$  site models suggested the energetic feasibility of hydrogen production either from a bridging hydride (observed in mimic models of the  $[2Fe]_H$  site<sup>101</sup>) and a proton on a sulfide<sup>71</sup>

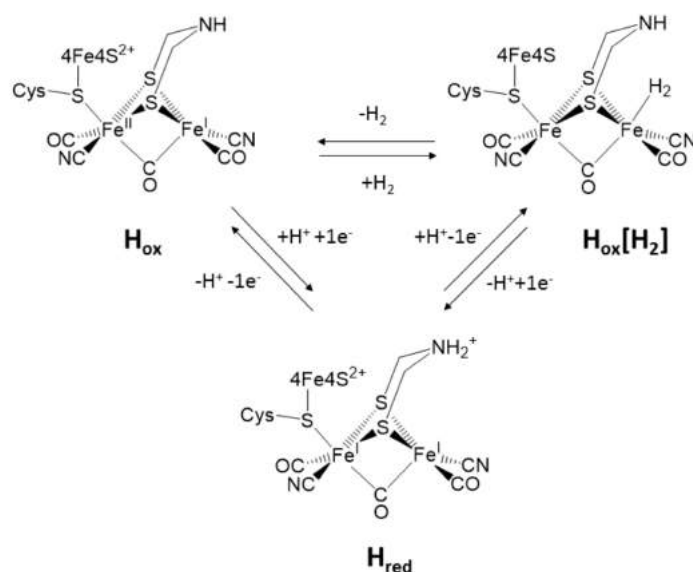


Figure 1.16: Simplified catalytic cycle including only the widely accepted intermediates  $H_{ox}$ ,  $H_{ox}-H_2$  and  $H_{red}$ .

of the ADT, or from an apical hydride on the distal iron and a proton on the amine of the ADT.<sup>70</sup> The presence of one or more intermediates where a hydride is bound on  $Fe_D$  in the catalytic cycle is actually supported by all the main groups that study FeFe-hydrogenases, although the existence of  $H_{hyd}$  has been proved only recently in mutated CrHydA1 (subsection 1.5.5). The proposed hydride-bound states are in the form  $[4Fe_4S]^{2+}-Fe^I-Fe^{II}-H^-$  with protonated ADT or  $[4Fe_4S]^{1+}-Fe^{II}-Fe^{II}-H^-$ .

The  $H_{sred}$  state observed with FTIR has been included by spectroscopists as an intermediate state between  $H_{red}$  and  $H_{hyd}$ . The super-reduced state (see section 1.5.4) is characterized by the shift of the bridging CO to the terminal position, the reduction of the  $[4Fe_4S]_H$  cluster and Reijerse et al. proposed also the presence of protonated ADT. The inclusion of this state in the catalytic cycle is controversial because PFV showed reductive inactivation (see subsection 1.9) at the potential where  $H_{sred}$  has been observed by FTIR spectroelectrochemistry, making the inclusion in the catalytic cycle of this specific super reduced form unlikely. Anyway, we cannot exclude the presence in the catalytic cycle of a species more reduced than  $H_{red}$ .

One still open question about the cycle arises from the analysis of the states: is the  $[4Fe_4S]_H$  redox active in the catalytic cycle? We know from Mössbauer stud-

ies<sup>46,61</sup> that in the main states ( $H_{\text{ox}}$ ,  $H_{\text{ox-CO}}$  and  $H_{\text{red}}$ ) the  $[4\text{Fe}4\text{S}]_{\text{H}}$  cluster is always in the oxidized state (+2) and so it seems not redox active. From DFT calculations<sup>69</sup> and EPR/FTIR spectra<sup>42,49</sup> we know that the binding of  $\text{H}_2$  to the oxidized H-cluster shifts electron density toward the  $[4\text{Fe}4\text{S}]$  clusters, forming a diferrous state. The active site in this state splits the hydrogen molecule and upon deprotonation of the ADT forms the  $H_{\text{hyd}}$ , which however has been observed clearly only using mutated forms of the enzyme. The splitting of hydrogen requires an intermediate where one electron is transferred from the  $[2\text{Fe}]_{\text{H}}$  site to the  $[4\text{Fe}4\text{S}]_{\text{H}}$  cluster, which is strongly electronically connected to the  $[2\text{Fe}]_{\text{H}}$  site.<sup>56</sup> If we include the  $H_{\text{sred}}$  state, where the  $[4\text{Fe}4\text{S}]_{\text{H}}$  cluster is reduced (+1), we imply that the  $[4\text{Fe}4\text{S}]_{\text{H}}$  cluster is redox active and its transient reduction/oxidation is essential for catalysis, but we have no evidence that this state could be involved in the catalytic cycle.

### 1.10.2 Proposed catalytic cycles

In this subsection I will describe the most recently proposed catalytic cycles (see figure 1.18).

#### C. Léger and colleagues

The group of Christophe Léger proposed a catalytic cycle (see figure 1.17) in a paper discussing the reductive inactivation of CrHydA1.<sup>99</sup>  $H_{\text{sred}}$  is not included in the catalytic cycle, since the authors showed with PFV that inactive states are formed at low potential. Following the  $\text{H}_2$  evolution in the scheme the  $H_{\text{ox}}$  state  $[4\text{Fe}4\text{S}]^{2+}\text{-Fe}^{\text{II}}\text{-Fe}^{\text{I}}\text{-ADT}$  is reduced and protonated on the ADT (PCET) to form the  $H_{\text{red}}$  state  $[4\text{Fe}4\text{S}]^{2+}\text{-Fe}^{\text{I}}\text{-Fe}^{\text{I}}\text{-ADTH}^+$ . A further protonation generates an hydride-bound state  $[4\text{Fe}4\text{S}]^{2+}\text{-Fe}^{\text{II}}\text{-Fe}^{\text{II}}\text{-H}^-\text{-ADTH}^+$ , which is reduced to form the  $[4\text{Fe}4\text{S}]^{2+}\text{-Fe}^{\text{II}}\text{-Fe}^{\text{I}}\text{-H}^-\text{-ADTH}^+$  state, releases  $\text{H}_2$  and goes back to  $H_{\text{ox}}$ . The authors include two possible hydride-bound intermediate states, one of which has been observed recently by FTIR<sup>74</sup> on CrHydA1 with a modified  $[2\text{Fe}]_{\text{H}}$  site and called  $H^{\text{hyd}}\text{-H}^+$ , while the other has not been observed with spectroscopy. The  $[4\text{Fe}4\text{S}]_{\text{H}}$  cluster preserves the oxidized state (+2) in all the intermediates included in the cycle; only the iron atoms of the  $[2\text{Fe}]_{\text{H}}$  site are redox active.

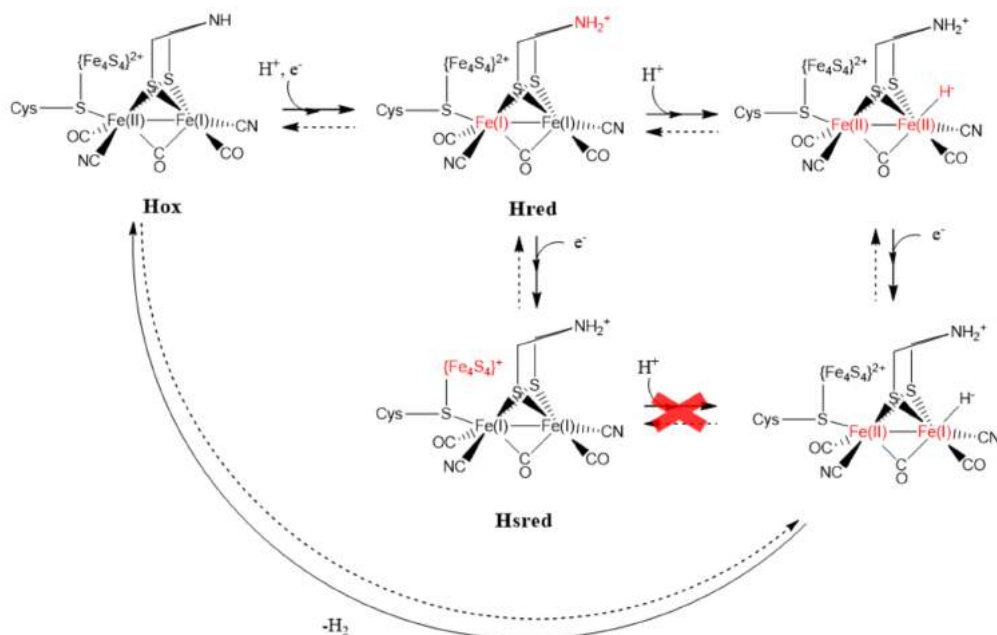


Figure 1.17: Scheme of the catalytic cycle proposed by Hajj et al. adapted from ref. 99

## P. King and colleagues

In the catalytic cycle proposed by the group of Paul King,<sup>72</sup> in the direction of H<sub>2</sub> evolution, the H<sub>ox</sub> state [4Fe<sub>4</sub>S]<sup>2+</sup>-Fe<sup>II</sup>-Fe<sup>I</sup>-ADT is reduced and protonated on the ADT (PCET) to form the H<sub>red</sub> state [4Fe<sub>4</sub>S]<sup>2+</sup>-Fe<sup>I</sup>-Fe<sup>I</sup>-ADT<sup>+</sup>. A further reduction generates the H<sub>hyd</sub> state [4Fe<sub>4</sub>S]<sup>1+</sup>-Fe<sup>II</sup>-Fe<sup>II</sup>-H<sup>-</sup>-ADT, which is protonated to form the [4Fe<sub>4</sub>S]<sup>1+</sup>-Fe<sup>II</sup>-Fe<sup>II</sup>-H<sub>2</sub>-ADT state, releases H<sub>2</sub> and goes back to H<sub>ox</sub> state. In the cycle proposed by P. King the [4Fe<sub>4</sub>S]<sub>H</sub> cluster is redox active and the authors consider unnecessary the presence of a super-reduced intermediate. The authors used FTIR, EPR<sup>49,72</sup> and Mössbauer spectroscopy<sup>72</sup> with DFT<sup>42</sup> calculations by Bruschi to define the H<sub>hyd</sub> state, but only using a mutated form of CrHydA1. There is no experimental evidence of the existence of the H<sub>hyd</sub> state in the WT enzyme. No experimental data about the electronic structure of H<sub>ox</sub>-H<sub>2</sub> state are available because it is probably a short life intermediate, however the authors define it from DFT calculations. King demonstrates that it is possible to fully describe the catalytic cycle of FeFe hydrogenases using just H<sub>ox</sub>, H<sub>red</sub> and an hydride bound intermediate.

## T. Happe and colleagues

Thomas Happe and collaborators proposed a catalytic cycle that includes the  $H_{\text{sred}}$  state and two different forms of  $H_{\text{red}}$ .<sup>73</sup> In the direction of  $H_2$  production, the  $H_{\text{ox}}$  state  $[4\text{Fe4S}]^{2+}\text{-Fe}^{\text{I}}\text{-Fe}^{\text{II}}\text{-ADT}$  is reduced on the  $[4\text{Fe4S}]_{\text{H}}$  cluster to form the  $H_{\text{red}}'$  state  $[4\text{Fe4S}]^{1+}\text{-Fe}^{\text{I}}\text{-Fe}^{\text{II}}\text{-ADT}$ .  $H_{\text{red}}'$  is protonated and one electron is transferred from the  $[4\text{Fe4S}]_{\text{H}}$  cluster to the proximal iron to form the  $H_{\text{red}}$  state  $[4\text{Fe4S}]^{2+}\text{-Fe}^{\text{I}}\text{-Fe}^{\text{I}}\text{-ADTH}^+$ . Then the  $[4\text{Fe4S}]_{\text{H}}$  cluster is reduced and an  $H_{\text{sred}}$  or  $H_{\text{sred}}'$  protonated state is formed. Then the addition of a proton generates an hydride-bound state, which is the same state as that called  $H_{\text{hyd}}\text{-H}^+$  by W. Lubitz and colleagues, previously included in the cycle by C. Léger and collaborators. Finally the hydrogen molecule is formed and released to give back the  $H_{\text{ox}}$  state. The cycle proposed by T. Happe and colleagues is characterized by a strong role of the  $[4\text{Fe4S}]_{\text{H}}$  cluster, which is redox active and reduced in both the  $H_{\text{red}}'$  and  $H_{\text{sred}}$  states. Using Raman and FTIR spectroscopy the authors define the  $H_{\text{red}}'$  state which is essentially the  $H_{\text{ox}}$  state but with a reduced (+1)  $[4\text{Fe4S}]_{\text{H}}$  cluster and they also claim that it is possible to convert  $H_{\text{red}}$  to  $H_{\text{red}}'$  by irradiation with a laser beam, but it is not clear why the  $H_{\text{ox}}/H_{\text{red}}$  transition should pass through this intermediate. As said before, the inclusion of  $H_{\text{sred}}$  is problematic, since PFV showed that at low potential inactive states are formed. The group gives no explanation about the mechanism of the transition from the hydride-bound state to  $H_{\text{ox}}$ , followed by release of  $H_2$ .

## W. Lubitz and colleagues

W. Lubitz and colleagues using mainly FTIR and spectroelectrochemistry<sup>74,102</sup> defined a catalytic cycle which is essentially the same as that described by T. Happe but with two hydride bound states included between the super reduced state and the  $H_{\text{ox}}\text{-H}_2$  state. The protonate super-reduced state  $[4\text{Fe4S}]^{1+}\text{-Fe}^{\text{I}}\text{-Fe}^{\text{I}}\text{-ADTH}^+$  is converted to the  $H_{\text{hyd}}$  state  $[4\text{Fe4S}]^{1+}\text{-Fe}^{\text{II}}\text{-Fe}^{\text{II}}\text{-H}^-$  which, after protonation on the ADT, becomes the  $H_{\text{hyd}}\text{H}^+$  state. Then the cycle proceeds as described in the previous subsection. The Lubitz group was the first to include the super reduced state in the catalytic cycle.<sup>52</sup> The criticism about this cycle are the same as those described



the scheme of Happe and colleagues in the previous subsection. In this scheme it is not clear why after formation of the  $H_{\text{hyd}}$  state, the cycle should not proceed as described by P. King with the formation of the  $[4\text{Fe4S}]^{1+}\text{-Fe}^{\text{II}}\text{-Fe}^{\text{II}}\text{-H}_2$  state as observed by DFT calculations.

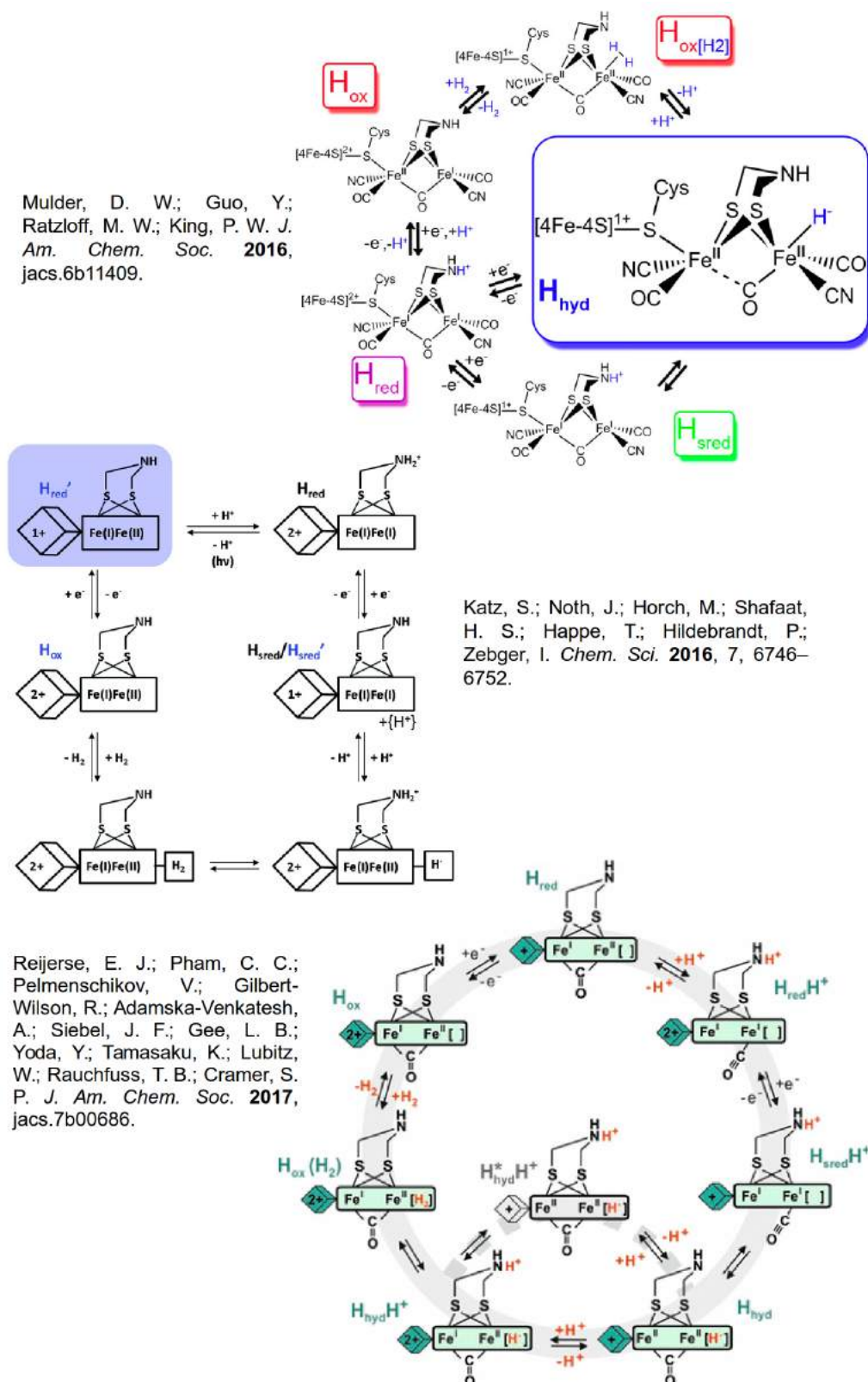


Figure 1.18: Summary of the most recently proposed schemes for the catalytic cycle of FeFe hydrogenases.

## 1.11 Inhibition of FeFe hydrogenases by CO

Soon after the discovery of hydrogenases, Kempner and Kubowitz<sup>103</sup> observed that CO inhibits the hydrogen production by bacterial cells. Kinetic studies<sup>104</sup> showed that inhibition of CpHydA1 by CO is competitive with respect to H<sub>2</sub> and Peters showed with X-ray crystallography that CO binds the distal iron in apical position (PDB code: 1C4C<sup>17</sup>). As said before, infrared spectroscopy and EPR showed in all FeFe hydrogenases the existence of the oxidized state inhibited by carbon monoxide called H<sub>ox</sub>CO (see section 1.5.1). DFT calculations showed that the binding of CO to H<sub>ox</sub> increases the distance d(Fe<sub>P</sub>-Fe<sub>D</sub>). In H<sub>ox</sub>CO the spin is delocalized, meaning that the two irons in the [2Fe]<sub>H</sub> site can be formally considered in the Fe<sup>+1.5</sup> state.<sup>105</sup> The rates of inhibition by CO at oxidizing potentials have been measured with PFV on FeFe-hydrogenases from various microorganisms.<sup>88,95,106</sup>

CO inhibits also the reduced enzyme but the reaction is different from the formation of H<sub>ox</sub>CO. PFV experiments<sup>107</sup> showed that, at reducing potential, CO does not behave as a simple competitive inhibitor, since it damages the enzyme. The results of DFT calculations suggested the following explanation of the damage: the binding of CO to the H-cluster in the H<sub>red</sub> state breaks the bond between the [4Fe4S]<sub>H</sub> cluster and the [2Fe]<sub>H</sub> site.<sup>105,107</sup> No one was able to obtain a FTIR spectra of H<sub>red</sub>CO until 2014, when Adamska et al.<sup>53</sup> observed it with FTIR spectroelectrochemistry using CrHydA1. The signal of H<sub>red</sub>CO was obtained in the presence of CO either during reductive titration of H<sub>ox</sub>CO or oxidative titration of H<sub>sred</sub>. Adamska described this new state as H<sub>ox</sub>CO but with the [4Fe4S]<sub>H</sub> cluster reduced. This state has not been obtained yet for other FeFe-hydrogenases, in agreement with the presence of damage observed by PFV and DFT.

## 1.12 The effect of light on the CO-inhibited state of FeFe hydrogenases

In this section I review the studies that investigated the photo-dissociation of the inhibitor CO from FeFe-hydrogenases, using various methods and under different conditions. The early studies on this process were performed to understand the composition of the active site and the binding site of hydrogen. Recently the investigations on this topic have focused on understanding the properties and the dynamics of the active site.

### 1.12.1 Early studies of the effect of light on hydrogenases

In 1933 Kempner and Kubowitz<sup>103</sup> showed that the production of H<sub>2</sub> in cells of *Clostridium butyricum* is inhibited by CO and illumination reverses the inhibition. At that time neither the structure of the enzyme nor the presence of nickel and/or iron in the active site was known. The flash photolysis of CO had been used to study the reactivity of myoglobin with small ligands.<sup>108,109</sup> In myoglobin CO binds an iron atom, so the inhibition by CO of hydrogenases was considered as a hint of the presence of an iron atom as binding site of hydrogen. The reversal of CO inhibition by white light was observed also in cells from other bacteria.<sup>110–114</sup> We have to underline that in those studies the inhibition by CO and the irradiation affected both FeFe and NiFe hydrogenases in the cells. The effect of light on the cells was probably also modulated by the permeability of the cellular and intracellular membranes and the photon harvesting by pigments and flavins.

Thauer<sup>104</sup> performed the first kinetic study of FeFe hydrogenases inhibition by CO in vitro and also observed the reversal of the inhibition by light. The author qualitatively observed that during the illumination with a 250 W halogen lamp, after exposure to CO, the rate of reduction of Methyl-viologen (and therefore, the H<sub>2</sub> oxidation activity of the enzyme) is ten times greater than in the dark, as a consequence of the photolysis of the CO-enzyme complex. The effect was fully reversible upon removal of the light source. The rate of binding and release of CO

under illumination was not measured.

### 1.12.2 Spectroscopic studies of CO-photodissociation from FeFe-hydrogenases

As said before, EPR and FTIR are very informative techniques for the study of the properties of the H-cluster. The modification of the geometry or the release of a CO ligand from the H-cluster results in a change in the spectrum. For this reason EPR and FTIR are good methodologies to study the topic of this section. I analyze in two different subsections the experiments performed at cryogenic and room temperatures. In the cryogenic range of temperatures, in FTIR and EPR experiments, the illumination of CpI and DdHydAB in the  $H_{ox}CO$  state induces the photodissociation of CO. In the  $H_{ox}CO$  state four CO ligands are bound to the  $[2Fe]_H$  site and temperature (in the cryogenic range) defines which CO is photodissociated. At room temperature the illumination allows the isotope exchange between CO and  $^{13}CO$  and this process has been used to study the dynamics of the  $[2Fe]_H$  site.

#### Cryogenic temperature

In the late 1980's, Patil et al.<sup>115</sup> and Kowal et al.<sup>84</sup> performed electron paramagnetic resonance studies of the hydrogenases from *D. vulgaris* and *C. pasteurianum*, respectively, to detect the light-sensitivity of the enzyme inhibited by CO. Patil<sup>115</sup> and Kowal<sup>84</sup> recorded EPR spectra, after irradiation of an enzyme sample inhibited by CO, at cryogenic temperatures. Patil and colleagues observed that the EPR  $g = 2.06$  signal, assigned to  $H_{ox}CO$ , after irradiation at 9 K with a mercury arc lamp (200 W), is converted to the rhombic  $g = 2.10$  signal, assigned to  $H_{ox}$ . Increasing the temperature from 9 K to 200 K induces the return of the  $H_{ox}CO$  signal. This result was explained by the persistence of the CO ligand in the enzyme matrix and the requirement of high temperatures to overcome an energy barrier to recombine with the H-cluster.

Kowal and colleagues observed that illuminating the FeFe-hydrogenase inhibited by CO, at different temperatures, led to different photo-products. At 8 K the

illumination induces the appearance of the  $H_{ox}$  signal. At 30 K the authors observed a dominant photo-product with EPR signals  $g = 2.26, 2.12$  and  $1.89$ , suggesting the presence of low spin  $Fe^{III}$  center (the structure of the active site of the enzyme was unknown at that time). The photodissociation of the inhibitor CO, in CpHydA1 and DdHydAB, was studied also by FTIR by Chen and Roseboom.

Chen et al.<sup>47</sup> (Peters and Bagley groups) studied the light sensitivity of the oxidized CO-inhibited form of CpHydA1 at cryogenic temperature as Kowal but with infrared spectroscopy. The irradiation of the CO-inhibited enzyme at cryogenic temperatures with a Xenon lamp (300W), simultaneously with the infrared beam, generates two species. One species obtained after irradiation at 6-14 K has the IR spectrum of  $H_{ox}$ , which decays back to the  $H_{ox}CO$  spectrum at temperatures above 150 K, because of CO rebinding. Above 20 K, the irradiation induces the appearance of the second species, which decays above 80 K and is characterized by loss of the bridging CO band ( $1809\text{ cm}^{-1}$ ). The species without the bridging CO was assigned by the authors to the  $g = 2.26$  rhombic signal observed by Kowal et al.<sup>84</sup> Chen and collaborators proposed for the first time a structural description of the photo-dissociation mechanism, suggesting that the process involves the bridging or apical CO depending on temperature (see fig. 1.19).

Albracht and Roseboom performed a study of the effect of light on DdHydAB at cryogenic temperatures with EPR<sup>63</sup> as Patil, but also with FTIR<sup>48</sup> spectroscopy. As previously detected by Chen<sup>47</sup> with CpHydA1, the authors observed in the spectra of DdHydAB that at 8 K a moderate intensity illumination of  $H_{ox}CO$  induces the dissociation of the extrinsic CO and the signal goes back to the  $H_{ox}$  state. In contrast with Chen results, illumination of  $H_{ox}CO$  at 15–30 K and/or with a more intense light (Xenon lamp) causes the disappearance of both the bands of extrinsic CO and of the bridging CO (or only of the bridging CO in molecules where the extrinsic CO is already photo-dissociated). The removal of the bridging CO from  $H_{ox}CO$  at cryogenic temperatures has no effect on the frequencies of the other intrinsic COs and on the charge densities of the irons, again in contrast with the results of Chen.<sup>47</sup> The different observations by Chen and Albracht could be also related to the fact that they studied different FeFe-hydrogenases (Chen used the FeFe-

## 1.12. THE EFFECT OF LIGHT ON THE CO-INHIBITED STATE OF FEFE HYDROGENASES

hydrogenase from *C. pasteurianum*, while Albracht and Roseboom used the enzyme from *D. desulfuricans*), the different irradiations times (Chen:10 minutes, Albracht: from 20 minutes to hours) or light power (300 W vs 150 W). All the signals obtained by irradiation were reversed upon warming the sample in the dark at 150 K.

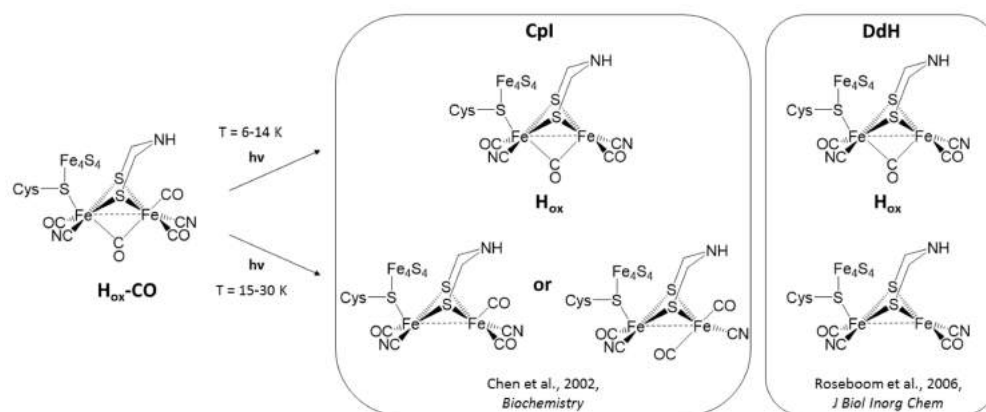


Figure 1.19: Species formed by irradiation of FeFe hydrogenases inhibited by CO at cryogenic temperatures proposed by Chen and Roseboom

The photo-induced states of  $H_{ox}\text{-CO}$  in DdHydAB were studied also by Silakov et al.<sup>116</sup> with EPR and ENDOR. The authors proposed, as Chen,<sup>47</sup> the formation of two different possible states after illumination at cryogenic temperatures:  $H_{ox}$  (photodissociation of the apical CO) and  $H_{LI}$  (photodissociation of the bridging CO). Both states revert to  $H_{ox}\text{-CO}$  above 150 K, as observed by Chen and Roseboom. The  $H_{LI}$  state is characterized by an unpaired spin density localized on the diiron site, in particular over the  $\text{CN}^-$  ligands. Silakov and colleagues underlined that the presence of the unpaired spin density should arise from structural rearrangements in the geometry of  $[2\text{Fe}]_H$ , not fully explainable only with the dissociation of the bridging CO but they do not offer further explanations.

### Room temperature

At room temperature Albracht<sup>63</sup> and Roseboom<sup>48</sup> observed, with EPR and FTIR, that  $H_{ox}\text{-CO}$  and  $H_{inact}$  spectra are not affected by irradiation, however illumination induces a shuffling of the COs on the  $\text{Fe}_D$ , in samples prepared with  $^{13}\text{CO}$ .

The light-induced CO shuffling was employed by Senger et al.<sup>97</sup> to study the

dynamics of the  $[2\text{Fe}]_{\text{H}}$  site by isotope exchange with real-time attenuated total reflection FTIR (ATR-FTIR). The exposure of CrHydA1, DdHydAB and CpHydA1 in the  $\text{H}_{\text{ox}}\text{CO}$  state to  $^{13}\text{C}$  shows a shift in the frequencies ascribed to the exchange of one of the CO on  $\text{Fe}_{\text{D}}$  with the isotope. With sufficient hydration the irradiation of CrHydA1 with red light (640 nm) induces the exchange of the other CO on  $\text{Fe}_{\text{D}}$  with  $^{13}\text{C}$  and the subsequent exposure to blue light (460 nm) produces the isotopic exchange of the CO bound to  $\text{Fe}_{\text{P}}$ . The isotopic exchange of both intrinsic CO in CpHydA1 and DdHydAB requires only red light irradiation. With this procedure the authors obtained 8  $\text{H}_{\text{ox}}$  and 16  $\text{H}_{\text{ox}}\text{CO}$  species labeled with  $^{13}\text{C}$  at specific positions. The numerous spectra were interpreted by DFT, using a model of the H-cluster with truncated cysteines or larger models that include amino acids around the active site. The authors underline that the best match between experimental and calculated spectra for the  $\text{H}_{\text{ox}}$  and  $\text{H}_{\text{ox}}\text{CO}$  was obtained considering the  $\text{CN}^-$  ligand on the  $\text{Fe}_{\text{D}}$  in apical position instead of the equatorial position observed in all the crystallographic structures. The  $\text{CN}^-$  in apical position forms an hydrogen bond with the ADT, as calculated before.<sup>117</sup> In contrast, previous DFT studies<sup>55,118,119</sup> already considered and excluded the movement of the distal  $\text{CN}^-$  in apical position. These studies showed that the distal cyanide ligand in equatorial position forms an hydrogen bond with an alanine and a strong salt bridge with a lysine,<sup>55,118,119</sup> which forms a further salt bridge with a glutamate. Those interactions keeps the  $\text{CN}^-$  in equatorial position and prevent the movement of the ligand in apical position, making unlikely the formation of the structure used for the calculations by Senger et al.<sup>97</sup>

### 1.12.3 Photodissociation of CO studied by X-ray crystallography

Peters and Lemon resolved the first crystallographic structure of the FeFe-hydrogenase of *Clostridium pasteurianum* (CpHydA1).<sup>21</sup> The same authors made the first study irradiating with light at specific wavelength, using X-ray diffraction to investigate the effect of a helium/neon laser at 635.8 nm on CO-inhibited CpHydA1.<sup>122</sup> The



authors observed that the difference between the electron density maps of the illuminated and non-illuminated enzyme, shows a peak of negative electron density in the position of the exogenous carbon monoxide molecule, which indicates the loss of CO. The maps show also an incomplete cleavage which indicates the presence of a small amount of CO that is still bound, or the presence of a water molecule in the CO binding-site. The difference between the electron density maps evidences an increased distance between the S $\delta$  of a conserved methionine residue and the bridging CO in the illuminated model, due to the increased electron density on the bridging CO after the photolysis of the CO in apical position.

#### 1.12.4 Kinetic studies

The photodissociation of CO from the enzyme inhibited and irradiated under turnover conditions has been studied by direct protein electrochemistry. Experiment performed with this method showed qualitatively that upon irradiation the rate of release of CO increases, but only at H<sub>2</sub> oxidation potential. Time-resolved spectroscopy was also used to determine the kinetics of rebinding of CO after irradiation.

The Armstrong group investigated for the first time with direct protein electrochemistry the photodissociation of CO from FeFe-hydrogenases. Parkin et al.<sup>95</sup> studied the recovery of activity of the enzyme after exposure to CO, under conditions of H<sub>2</sub> oxidation or H<sup>+</sup> reduction (figure 1.20). The illumination, with an Halogen lamp, of the enzyme at H<sub>2</sub> oxidation potential causes a faster recovery of activity than in the dark. In the same experiments the authors stepped down the potential and they observed that the illumination has no effect on the CO inhibition under H<sub>2</sub> production conditions. Goldet et al.<sup>106</sup> observed the same effect under conditions of H<sub>2</sub> oxidation with the FeFe-hydrogenases from *Clostridium acetobutylicum* and *Chlamydomonas reinhardtii*. In both cited papers there are no measurements of the kinetics of the process.

Mirmohades et al.<sup>120</sup> recently studied the photodissociation of CO in the artificially matured<sup>16</sup> FeFe hydrogenase from *Chlamydomonas reinhardtii* (CrHydA1) with time-resolved nanosecond mid-infrared spectroscopy. The enzyme sample was exposed to 10 laser flashes (10 ns, lambda = 355 nm), at room temperature under

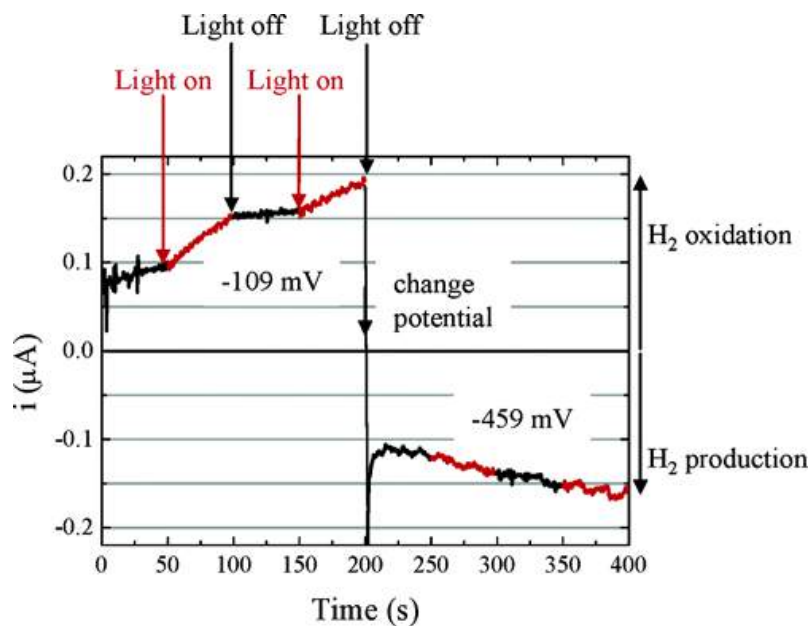


Figure 1.20: Figure from ref. 95. Chronoamperometric experiments of DdHydAB exposed to CO under H<sub>2</sub> oxidation conditions until  $t = 200$  s and H<sup>+</sup> reduction conditions after  $t = 200$  s. During the experiments an halogen lamp directed on the surface of the electrode was turned on (red line and red arrows) and off (black line and black arrows) for time windows of 50 s.

anaerobic conditions, to obtain the kinetics of release and rebinding of CO with TRIR. Only 8% of the sample was converted to H<sub>ox</sub> upon irradiation and the half life of the rebinding process of the geminate CO (near the binding site, not diffused away) measured from the kinetic traces is  $13 \pm 5$  ms.

### 1.13 Photoinhibition

FTIR and EPR measurements with DdHydAB showed that sunlight damages the enzyme. Irradiating the enzyme at room temperature with a Xenon lamp, to mimic the sunlight, caused the destruction of the active site of the enzyme, which was not observed using a Halogen lamp. No inactivation was observed upon illumination with a Halogen lamp also in PFV experiments with CrHydA1 and CaHydA. In contrast, recent PFV and FTIR studies on DdHydAB showed that irradiation with a Halogen lamp damages the enzyme at H<sub>2</sub> oxidation potential.

Albracht et al.,<sup>63</sup> performing EPR measurements on the FeFe hydrogenase from

*D. Desulfuricans*, unexpectedly observed that daylight degraded the enzyme. At room temperature and upon irradiation with a Xenon lamp (UV-filtered), which mimics the sunlight, the EPR and FTIR<sup>48</sup> spectra of DdHydAB in H<sub>ox</sub> state are characterized by the appearance of signals typical of H<sub>ox</sub>CO. The presence of enzymes in the H<sub>ox</sub>CO state was attributed by Albracht to the inhibition of active enzymes by CO released from the [2Fe]<sub>H</sub> degraded by light (the so-called “cannibalization” observed also upon exposure to oxygen<sup>25</sup>). DdHydAB in the H<sub>red</sub> state was less sensitive to light.

At cryogenic temperatures illumination of the DdHydAB samples in H<sub>ox</sub>CO state with a Xenon lamp leads to the disappearance of both the extrinsic and bridging CO bands from the FTIR spectra (see fig. 1.19), while only the release of the extrinsic CO is observed using a Halogen lamp. The specific effect of the two lamps suggests that the differences between the emission spectra of the Halogen and Xenon lamp are fundamental to determine the damage. Xenon lamps have a UV component, which is almost completely absent in Halogen lamps, but the authors used a “glass light guide” that eliminated “most of the UV contribution”.<sup>48</sup> We can speculate that the different effects of the lamps are due to the higher intensity of the emission of the Xenon lamp in the visible range or to a small fraction of UV light not filtered.

In 2016 Rodriguez-Macia et al.<sup>87</sup> studied the light sensitivity of the same enzyme as that studied by Albracht and Roseboom, DdHydAB, at room temperature with protein film voltammetry and FTIR. The authors illuminated the protein film with a halogen lamp (50 W) positioned under an electrochemical glass cell which blocks UV light. As shown in figure 1.21, in chronoamperometric experiments at H<sub>2</sub> oxidation potential, the illumination of the protein film induced an inactivation followed by a recovery of part of the activity while the enzyme was still under light. Another partial reactivation was observed by the authors upon removal of the light source. The same experiment performed at reducing potential showed that light has no effect on the H<sub>2</sub> evolution process. The FTIR spectra of DdHydAB after irradiation presented the typical H<sub>ox</sub>CO bands observed also by Albracht and Roseboom.<sup>48,63</sup> Combining electrochemistry and FTIR, Rodriguez-Macia et al.<sup>87</sup> proposed that the inactivation by light observed in the chronoamperograms is due to the inhibition

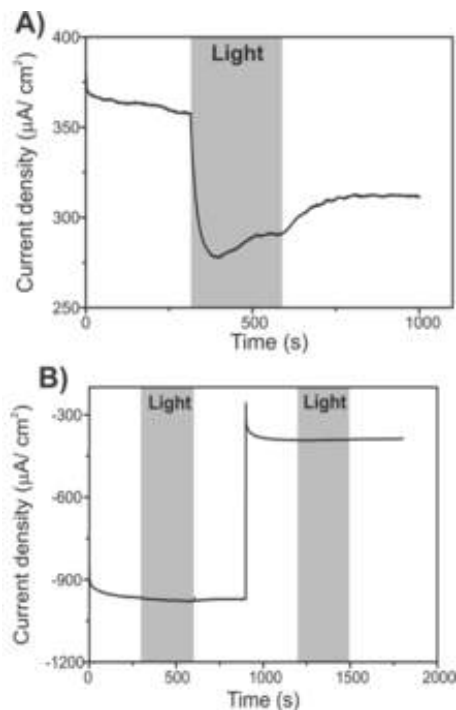


Figure 1.21: Figure from ref. 87. Chronoamperometric experiments of DdHydAB irradiated by an halogen lamp under A) H<sub>2</sub> oxidation conditions and B) H<sup>+</sup> reduction conditions (at two different potentials).

by CO released from the damaged [2Fe]<sub>H</sub> cluster, followed by reactivation due to the dissociation of the inhibitor CO. This interpretation is unconvincing, since the concentration of CO released by the damaged enzymes in the electrochemical cell should be in the picomolar range and the constant flow of N<sub>2</sub> and H<sub>2</sub> should remove it from the surface of the electrode and from the solution, as stated also by the authors themselves. The authors offer no explanation for the presence of a two step reactivation, under illumination and after light removal.

The role of the emission spectra of the lamp is not clear. Albracht and Roseboom observed the photodamage mainly on DdHydAB in H<sub>ox</sub> state with FTIR using a Xenon lamp and no photoinhibition was observed irradiating with an halogen lamp. In contrast, Rüdiger and collaborators observed the inactivation of the same enzyme only in H<sub>ox</sub> state using an halogen lamp. In direct electrochemistry experiments by Rüdiger et al.,<sup>87</sup> the inactivation of DdHydAB under turnover conditions induced by halogen lamp is present only at oxidizing potential and is mostly reversible. In contrast Parkin et al.,<sup>95</sup> using the same enzyme and a similar lamp with lower power, observed that “in the presence of light, the rate of film loss decreases” both at proton

reduction and hydrogen oxidation potential. Different results were obtained studying FeFe-hydrogenases from other organisms (CrHydA1 and CaHydA) by Goldet and collaborators,<sup>106</sup> since they observed that “irradiation [with an halogen lamp] slightly increased the rate of catalysis, though to a much lesser degree than it increases the rate of recovery from CO inhibition”.

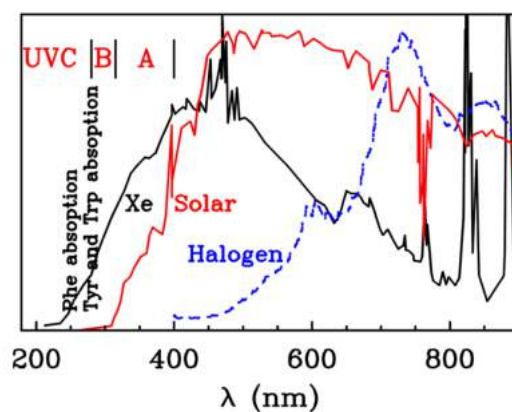


Figure 1.22: Emission spectra of Sunlight (red), Xenon lamp (black) and Halogen lamp (blue)

Comparing the emission spectra of the Xenon and Halogen lamps in figure 1.22, we can observe two main differences that could be determinant in the experiments. First, the halogen lamp spectra as an overall higher emission in the visible range above 600 nm compared to the Xenon lamp but the latter has some emission peaks in the near-infrared. Second, the Xenon lamp has higher emission UVA component compared to the halogen lamp and in the Xenon lamp spectrum there are also UVB that are completely absent in that of the halogen lamp. Also the power of the lamp could affect the effect of light, as observed in the photodissociation of CO, but no data are available about this issue.

Ref.	Topic	Method	Enzyme	Light source	Wavelength	Power	T
104	CO+light	Activity assays	CpHydA1	Halogen	Visible	250 W	Room
115	CO+light	EPR	DvHydAB	Halogen	Visible	300 W	Cryogenic
84	CO+light	EPR	CpHydA1	Xenon	Visible	200 W	Cryogenic
17	CO+light	XRD	CpHydA1	HeNe laser	632.8 nm		
47	CO+light	IR	CpHydA1	Xenon	Visible	300 W	Cryogenic
63	CO+light	EPR	DdHydAB	Halogen	Visible	150 W	Cryogenic/Room
63	CO+light	EPR	DdHydAB	Xenon	Visible	150 W	Cryogenic/Room
48	CO+light	IR	DdHydAB	Halogen	Visible	150 W	Cryogenic/Room
48	Photoinhibition	IR	DdHydAB	Xenon	Visible	150 W	Cryogenic/Room
95	CO+light	PFV	DdHydAB	Halogen	Visible	10 W	Room
116	CO+light	EPR/ENDOR	DdHydAB	Laser	355 nm		Cryogenic
73	CO+light	FTIR/Raman	DdHydAB	LED	460 nm		Cryogenic
97	CO+light	TR-IR	DdHydAB, CpHydA1, CrHydA1	Laser	460/640 nm		Room
120	CO+light	TR-IR	CrHydA1	Laser	355 nm		Room
121	CO+light	PFV/TDDFT	MeHydA, CaHydA, CrHydA1	Laser	405/450/532/635 nm	10 mW	Room
87	Photoinhibition	PFV/FTIR	DdHydAB	Halogen	Visible	50 W	Room
Chapter 5	Photoinhibition	PFV/TDDFT	CaHydA, CrHydA1	Xenon	UV-Visible	150 W	Room

Table 1.3: Summary of the literature about FeFe hydrogenases and light

## 1.14 Objective of my thesis

In my thesis I study mainly FeFe hydrogenases, which are enzymes that catalyze reversibly the production of hydrogen. These enzymes has been discovered almost ninety years ago but many of their properties are still obscure, like for example the oxidative and reductive inactivations or the catalytic cycle. Oxygen sensitivity is generally considered as a major obstacle in the use of hydrogenases to produce hydrogen in a hydrogen economy context. In this thesis I present in chapter 3 the results about the mechanism of oxygen diffusion and reduction in FeFe-hydrogenases, where I perform experiments on enzymes with mutations in the gas channels. Another possible obstacle to the employment of FeFe-hydrogenases is their possible sensitivity to solar light, as observed by spectroscopy. I investigate this issue in two phases. In the first phase, in chapter 4, I develop a new technique to study the effect of light on the enzyme, alternative to the classical spectroscopic methods. I combine this technique, which we call direct photoelectrochemistry, with theoretical chemistry calculations and I test this approach investigating the photodissociation of CO from the CO-inhibited enzyme. In the second phase, in chapter 5, I study the photoinhibition process with the same approach. Most of the presented results has been published as articles or have been recently submitted to journals. In chapter 6 I present some unpublished preliminary results about the effect of light on NiFe-hydrogenases and CO-dehydrogenase, studied by direct photoelectrochemistry.





## Chapter 2

### Introduction to the methods

## 2.1 Theoretical methods

In this thesis, we carry out DFT and TDDFT calculations to study the electronic and structural properties of the ground state and the excited states of the H-cluster. In the following subsections, we shall describe the theory of DFT and TDDFT. We shall also illustrate the approach that we use in our calculations.

### 2.1.1 Density Functional Theory

Density Functional Theory (DFT) is a ground-state theory based on the use of functionals of the electron density.<sup>123,124</sup> With this approach we can describe the structural and electronic properties of many-body systems, from atoms and molecules to crystals and complex extended systems. DFT calculations require relatively low computational resources, compared to post-Hartree-Fock methods. For these reasons DFT is widely used to describe and predict the properties of molecular systems, in particular organometallic complexes.

The Hohenberg-Kohn theorems<sup>125</sup> are the theoretical foundation of density functional theory. In a system with  $N$  interacting electrons, subject to an external potential  $V(\mathbf{r})$  (usually the Coulomb potential of the nuclei), the total energy of the system, in the Born-Oppenheimer approximation (nuclei are considered as fixed since they are slower than the electrons), is given by a many-electron Hamiltonian operator:

$$H = T + U + V, \quad (2.1)$$

with ground state wavefunction  $\Psi$ . Where  $T$  is the kinetic energy,  $U$  the electron-electron interaction,  $V$  the external potential. The first theorem demonstrates that there is only one  $V(\mathbf{r})$  that gives the ground-state electron density  $\rho(\mathbf{r})$ :

$$\rho(\mathbf{r}) = N \int |\Psi(\mathbf{r}, \mathbf{r}_2, \mathbf{r}_3, \dots, \mathbf{r}_N)|^2 d\mathbf{r}_2 \dots d\mathbf{r}_N \quad (2.2)$$

where  $\mathbf{r}$  are the spatial coordinates. The second theorem is a direct consequence of the first one and states that the ground-state electron density determine a unique

ground-state energy  $E$ , which is a functional  $E[\rho(\mathbf{r})]$  of  $\rho(\mathbf{r})$ :

$$E[\rho(\mathbf{r})] = \langle \Psi | T + U + V | \Psi \rangle = \langle \Psi | T + U | \Psi \rangle + \langle \Psi | V | \Psi \rangle = F[\rho(\mathbf{r})] + \int \rho(\mathbf{r})V(\mathbf{r})d\mathbf{r} \quad (2.3)$$

$F[\rho(\mathbf{r})]$  is a universal functional of the electron density  $\rho(\mathbf{r})$ . Using this functional the ground-state electron density minimize the ground-state energy (variational principle). This simplifies the calculation because the  $N$  electron system is reduced to the determination of a the three-dimensional function  $\rho(\mathbf{r})$ , which minimizes  $E[\rho(\mathbf{r})]$ . The universal functional  $F[\rho(\mathbf{r})]$  is unknown and due to the problems in the computation of kinetic energy term, the DFT approach is reformulated within the Kohn and Sham (KS)<sup>126</sup> framework. The KS approach introduces a reference system of non-interacting electrons, where the electron-electron repulsion is not considered. In this system the ground-state electron density can be calculated as the sum of the one-electron orbitals  $\psi_i(\mathbf{r})$  (called KS orbitals):

$$\rho(\mathbf{r}) = 2 \sum_i |\psi_i(\mathbf{r})|^2 \quad (2.4)$$

where  $i$  goes from 1 to  $N/2$ , assuming a double occupancy and the KS orbitals are the solution of the Schrödinger equation:

$$\left( -\frac{\hbar^2}{2m} \nabla^2 + V_{KS}(\mathbf{r}) \right) \psi_i(\mathbf{r}) = \epsilon_i \psi_i(\mathbf{r}) \quad (2.5)$$

where  $m$  is the electron mass and  $\epsilon_i$  are the energies of the  $\psi_i$  KS molecular orbitals (MO). The MOs are expanded in a basis set of functions representing the atomic orbitals  $\varphi_i$ , given by a linear combination of gaussian functions. The quality of the basis set is determined by the number of functions. We can define the KS Hamiltonian as:

$$H_{KS} = -\frac{\hbar^2}{2m} \nabla^2 + V_H(\mathbf{r}) + V_{xc}(\mathbf{r}) + V(\mathbf{r}) \equiv -\frac{\hbar^2}{2m} \nabla^2 + V_{KS}(\mathbf{r}) \quad (2.6)$$

where  $V_H$  is the Hartree potential (electrostatic interactions) and  $V_{xc}$  is the exchange-correlation potential which is the functional derivative of the exchange-correlation

energy  $E_{xc}[\rho(\mathbf{r})]$ :

$$E_{xc}[\rho(\mathbf{r})] = (T[\rho(\mathbf{r})] - T_S[\rho(\mathbf{r})]) + (U[\rho(\mathbf{r})] - J[\rho(\mathbf{r})]) \quad (2.7)$$

where  $T$  and  $T_S$  are respectively the kinetic energies of the real and reference system,  $U[\rho(\mathbf{r})]$  is the electron-electron interaction energy, which considers also the classical contribution given by  $J[\rho(\mathbf{r})]$ . The exchange-correlation term is essential to take into account the differences between the real and the reference systems. To estimate the exchange-correlation energy, Kohn and Sham introduced the local density approximation (LDA), where  $\epsilon_{xc}$  is function only of the density in an homogeneous electron gas. In the generalized gradient approximation (GGA) functionals, the approximation is improved adding explicit dependence on  $\nabla\rho(\mathbf{r})$  in the  $E_{xc}[\rho(\mathbf{r})]$  exchange-correlation energy term. Beside the GGA approach, the hybrid method is also commonly used to build the exchange-correlation energy term. Starting from the so-called adiabatic connection formula, the exact exchange-correlation energy term is approximated by adding a variable portion of the Hartree-Fock exact exchange energy to that of GGA.

### 2.1.2 Broken Symmetry approach

Studying the H-cluster is challenging because the cluster  $[4\text{Fe4S}]_{\text{H}}$  consists of two layers of high spin irons, coupled each other antiferromagnetically in order to obtain a global low spin state. This type of spin-coupled systems is difficult to treat using DFT, since the fundamental state wavefunctions correspond to a linear combination of more determinant. To determine the energies and properties of the H-cluster is important to describe the weak antiferromagnetic coupling at the same level of theory as strong metal-metal and metal-ligand bonds. It is reasonably possible to deal better with these exchange interactions, using the broken symmetry approach (BS) developed by Noodleman et al.<sup>82</sup> The BS approach consists in the localization of opposite spin in different fragments of the molecule, in order to use a mono-determinant representation of the interaction of exchange within it. The BS wave function is not in a pure spin state (it is a self-function of  $S_z$ , but not of  $S^2$ ). In

this context, the BS wave function can be considered as a low spin wave function with high spin contamination. Despite this restriction, Noodlemann showed that BS states are a weighted average of pure spin wave functions. The "weights" are the Clebsch-Gordan's coefficients, relative to the quantum number of spin of the subunits, aligned in opposite direction. The BS energy can then be related to the energies of spin states derived from the Hamiltonian of Heisenberg, which for two spin centers is:

$$H = J(S_A S_B) \quad (2.8)$$

Where  $S_A$  and  $S_B$  are the spin operators with center  $A$  and  $B$  respectively and  $J$  is the constant of exchange and correlation, which represents the strength of the interaction of exchange between the two spin centers. It is assumed that  $J$  has a negative value for anti-ferromagnetic interactions and positive for ferromagnetic interactions. In this case, from the Hamiltonian of Heisenberg, we can obtain the following expression for the energies of spin states:

$$E(S_{tot}) = \frac{1}{2} J [S_{tot}(S_{tot} + 1)] \quad (2.9)$$

where  $S_{tot}$  is the total spin from  $|S_A - S_B|$  to  $|S_A + S_B|$ . The difference of the energies in two successive spin states is:

$$E(S_{tot}) - E(S_{tot} - 1) = JS_{tot} \quad (2.10)$$

The determination of  $J$  by the previous equation allows to construct the whole scale of energies of spin states. Specifically, the value of  $J$  can be determined by the BS wave function and the high spin wave function, which is easily calculated by aligning ferromagnetically the spin of the iron atoms. Noodlemann<sup>82</sup> showed that the expectation values of the products of the previously defined spin operators, can be calculated for HS and BS states such as:

$$\langle S_A S_B \rangle_{HS} = +S_A S_B \quad (2.11)$$

$$\langle S_A S_B \rangle_{BS} = -S_A S_B \quad (2.12)$$

Then we can calculate the difference between the HS and BS energy states as:

$$E(HS; S_{max} = S_A + S_B) - E(BS; M_S = |S_A - S_B|) = 2J(S_A S_B) \quad (2.13)$$

We use this equation to find  $J$  which, in turn, can be used to project BS states on pure spin states and then to determine the energy correction. In particular, the difference in energy between high and low spin states can be calculated as follows:

$$E(S_{max}) - E(S_{min}) = \frac{1}{2}J[S_{max}(S_{max} + 1)] - \frac{1}{2}J[S_{min}(S_{min} + 1)] \quad (2.14)$$

The difference between this equation and the eq. 1.20 gives  $\Delta E_{spin} = E(BS) - E(S_{min})$ , which represents the BS energy correction to the energy of the pure spin fundamental state. The use of the Hamiltonian of Heisenberg is restricted to weakly interacting dimers, for which loose electrons are located on one of the two metal centers. In the case of a strong interaction, the electrons that are loose are more delocalized on the ligands and therefore  $E(BS) = E(S_{min})$ . The description of BS approach for two-spin systems can be easily generalized for systems with more than two spin centers. This is possible by introducing the Hamiltonian spin operator:

$$H = \sum_{ij} J_{ij}(S_{ij} S_{ij}) \quad (2.15)$$

The summation is extended on all pairs of spin centers  $i$  and  $j$ , having spin  $S_i$  and  $S_j$ .  $J_{ij}$  is the constant of exchange and correlation associated with the spin centers. In these multiple spin centers systems, many BS states can be calculated by aligning ferromagnetically or antiferromagnetically the spin of the different centers. For  $N$  spin centers, we can define  $2^N/2$  non-equivalent spin combinations to obtain BS states. The  $J_{ij}$  parameters can be determined by the HS state and a large number of BS states, by applying the spin algebra previously described. In order to reduce the number of coupling constants to be determined, the summing is generally approximated by considering only the adjacent spin centers.

### 2.1.3 Time-Dependent Density Functional Theory

DFT cannot be used to evaluate the excitation energies and therefore the photochemistry of a system, since the Hohenberg-Kohn theorems are valid only in the ground-state. Runge and Gross,<sup>127</sup> using the time-dependent response theory, extended the first theorem of Hohenberg-Kohn to the time-dependent case, reducing the electronic excitation to ground state properties in time-dependent DFT (TDDFT). In the Runge-Gross theorem the hamiltonian assumes the following form:

$$H = T + U + V_{ext}(t), \quad (2.16)$$

where  $V_{ext}(t)$  is the time-dependent external potential that mimics the applied field. In TDDFT the action is the unique functional of the density, while in DFT was the total energy (equation 2.3). The stationary points of the action give the exact value of the time-dependent electron density. The Runge-Gross time-dependent electron density is defined as follows:

$$\rho(\mathbf{r}, t) = \sum_{i=1}^N |\psi_i(\mathbf{r}, t)|^2 \quad (2.17)$$

The equation 2.5 can be rewritten, for the time dependent case, as:

$$H_{KS}(\mathbf{r}, t)\psi_i(\mathbf{r}, t) = i\frac{\partial}{\partial t}\psi_i(\mathbf{r}, t) \quad (2.18)$$

The linear-response theory can be applied to TDDFT if the external perturbation is small and the ground-state structure is not completely changed. The possibility to study the linear response of the system is an advantage, since any variation of the system will depend only on the ground-state wavefunction. This allows to use the ground state approximate wave-function obtained from DFT to compute the excitation energies. The time-dependent linear response theory electron density is:

$$\rho(\mathbf{r}, \omega) = \sum_{ia} [X_{ia}(\omega)\phi_a^*(\mathbf{r})\phi_i(\mathbf{r}) + Y_{ai}(\omega)\phi_a(\mathbf{r})\phi_i^*(\mathbf{r})] \quad (2.19)$$

where  $\omega = E_{ex} - E_0$  is the excitation energy at which the electronic transition occurs ( $E_{ex}$  and  $E_0$  are, respectively, the total energy of the excited state and that of the ground state), the  $i$  and  $a$  terms are, respectively, the occupied and virtual KS ground-state molecular orbitals. The coefficients  $X_{ia}(\omega)$  are frequency dependent and associated to the single excitations  $\phi_i \rightarrow \phi_a$ .  $Y_{ai}(\omega)$  are also frequency dependent and associated to the non-physical de-excitation excitations  $\phi_a \rightarrow \phi_i$ , which is necessary to describe the correlation effects. The linear response of the ground-state Kohn-Sham molecular orbitals to the external time-dependent potential is given by the the  $\mathbf{X}$  and  $\mathbf{Y}$  matrices. The external time-dependent KS potential  $V_{KS}(\mathbf{r}, t)$  is given by the TDKS equation:

$$V_{KS}(\mathbf{r}, t) = V(t) + \int \frac{\rho(\mathbf{r}', t)}{|\mathbf{r} - \mathbf{r}'|} d\mathbf{r}' + V_{xc}(\mathbf{r}, t) \quad (2.20)$$

where  $V(t)$  is the applied external potential and  $\rho(\mathbf{r}, t)$  is the Fourier transform of  $\rho(\mathbf{r}, \omega)$ . In the adiabatic approximation (the potential is applied gradually)  $V_{xc}(\mathbf{r}, t)$  is computed as the functional derivative of the static  $[E_{xc}(\rho(\mathbf{r}))_t]$  with respect to the time-dependent electron density calculated at a fixed time  $t$ . To determine the  $\mathbf{X}$  and  $\mathbf{Y}$  coefficients we can rewrite the TD electron density as follows:

$$\rho(\mathbf{r}, \omega) = \int \chi_{KS}(\mathbf{r}\mathbf{r}', \omega) V_{xc} + (\mathbf{r}', \omega) d\mathbf{r} d\mathbf{r}' \quad (2.21)$$

where  $\chi_{KS}(\mathbf{r}\mathbf{r}', \omega)$  is defined as:

$$\chi_{KS}(\mathbf{r}\mathbf{r}', \omega) = \sum_{ia} \left[ \frac{\phi_i^*(\mathbf{r}) \phi_a(\mathbf{r}) \phi_i(\mathbf{r}') \phi_a^*(\mathbf{r}')}{\omega - (\epsilon_a - \epsilon_i)} + \frac{\phi_i(\mathbf{r}) \phi_a^*(\mathbf{r}) \phi_i^*(\mathbf{r}') \phi_a(\mathbf{r}')}{\omega + (\epsilon_a - \epsilon_i)} \right] \quad (2.22)$$

To calculate the excitation energy we need just to find the poles of  $\chi_{KS}(\mathbf{r}\mathbf{r}', \omega)$  function solving a non-hermitian eigenvalues-eigenvectors problem. The first derivative of the excited state energy with respect to the nuclear positions can be computed within a Langragian approach. [128](#)



### 2.1.4 Excited states radiationless deactivation

An electronic excited state of a molecular system is a new state of the system populated upon absorption of light in the UV-visible region. The fate of an electronic excited state is the loss of the excess of energy and consequently it undergoes deactivation. The process of deactivation can be radiative, a photon is emitted, or radiationless (no photon emission). In this thesis, we investigate the fate of the electronic excitations of the H-cluster, to characterize in a better detail its photochemical processes upon irradiation with near-UV and visible light. Since it is known from literature that FeFe-hydrogenases do not show any fluorescence or phosphorescence, we are interested in radiationless deactivation, which is schematized in figure 1.

As shown in fig. 1, upon absorption of light a molecular system in the initial singlet ground state ( $S_0$ ) is excited to a  $S_n$  singlet state. The excitation to a state with a different spin multiplicity is in principle forbidden, since the integral of the initial and final spin functions would be 0, although the effect of spin-orbit coupling can be significant for transition metal atoms. Upon vertical Franck-Condon excitation, the system is in the electronic and vibrational excited states and undergoes a vibrational relaxation (red arrows) to the lowest vibrational state. If the system is in the  $S_n$  state it decays to the  $S_{n-1}$  state by internal conversion (IC, blue arrows) or to a state with a different spin multiplicity, for example  $T_1$ , by intersystem crossing (ISC, orange arrows). The ISC or IC transitions take place between isoenergetic vibrational levels of two states. The radiationless transitions are irreversible because the vibrational relaxations are very fast (picosecond time scale) and cause an entropy increase. According to the Fermi's golden rule we can define the rate constant of the radiationless transitions as:

$$K_{nr} = \frac{2\pi}{\hbar} \langle \phi_i S_i | \hat{H}' | \phi_f S_f \rangle^2 \sum_n \langle \theta_{i,0} | \theta_{f,n} \rangle^2 \quad (2.23)$$

Index  $i$  and  $f$  refers to the initial and final states, while  $\phi$  and  $S$  refers to the spatial and spin part of the wavefunctions. The perturbation that induces the transition ( $\hat{H}'$ ) is the nuclear kinetic energy operator ( $\hat{H}_{ic}$ ) in the case of IC and the spin-orbit operator ( $\hat{H}_{SO}$ ) for ISC. In eq. 1 is also considered the vibrational coupling

(or vibrational overlap) between the vibrational states  $\theta$  of the two electronic excited states under consideration. This contribution is maximum when there is a crossing between the PES of the two states, which correspond to the molecular geometry at which the two vibrational states are equal in energy. The deactivation continues with the same sequence of events described above until the ground state is reached by ISC or IC from a vibrational level of, respectively, T1 or S1 isoenergetic to a high vibrational level of the ground state S0. Then a vibrational relaxation restores the initial state of the system. The energy difference between two excited states is in general lower than the difference between the lowest energy excited states and the ground state. This determines the rates of the transitions: IC is in the order of picoseconds, ICS in the sub-nanoseconds to nanoseconds and the deactivation from the lowest excited state to the ground state is the nanoseconds to microseconds region.

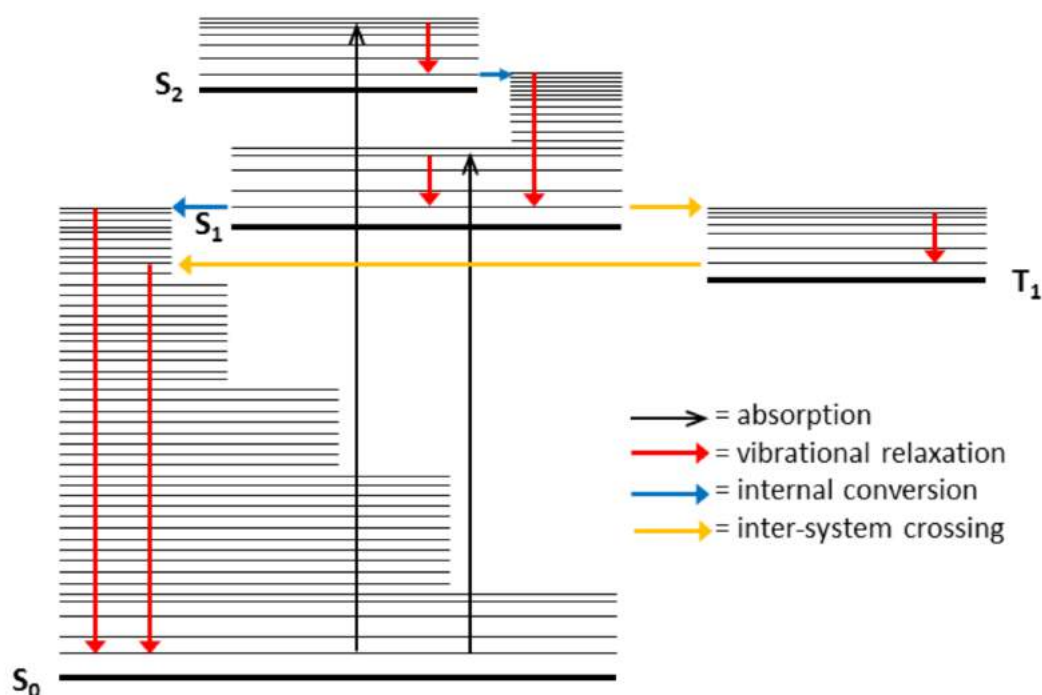


Figure 2.1: Jablonski diagram of the radiationless deactivation processes.

### 2.1.5 Potential energy surface (PES)

We can consider the potential energy surface (PES) of a molecular system as an energetic profile of one of its electronic states in the Born-Oppenheimer (BO) approximation. A potential energy surface shows the evolution of the energy of a system as a function of changes in the nuclear coordinates. The potential energy surfaces of two electronic states of a system (like two excited state, for example) can be *adiabatic* or *diabatic* (called also *non-adiabatic*), depending respectively on the presence of avoided-crossings or crossings between the surfaces. Within the BO approximation (slow motion of the nuclei), two electronic states do not cross unless they have different spin-multiplicity. In this case, the actual crossing between two PES is described as avoided-crossing. When the nuclei are sufficiently fast a conical intersection occurs in correspondence of an avoided-crossing. In the conical intersection, there is a single point with a degenerate wave function that makes possible a fast transition between the two surfaces.<sup>129</sup>

### 2.1.6 Exploration of excited states PES with TDDFT

In this thesis, we studied the excited states of models of the  $[2\text{Fe}]_{\text{H}}$  site of the active site of FeFe-hydrogenases and we investigated the process of photodissociation of the CO ligands from the iron atoms. We performed an exploration of the PES of the ground state and of the excited states of our system. In this procedure, we calculated the variation of total energy of the ground state and of the excited states as a function of the Fe-C bond distance between an iron atom and the carbon of the dissociating CO ligand. The procedure that we used is shown in the left panel of figure 2. Starting from the geometry of the system optimized by DFT in the ground state (first black circle on the black curve), we calculated the excitation energies of many excited states (in the figure is shown as a red circle only the lowest energy excited state). Then, We increased the length of the selected bond by 0.05 Å and we optimized the ground state geometry of this system, keeping fixed the distance that we previously modified. The energy obtained from this optimization is represented by the second black dot on the ground state in the left panel of figure 2. Then we

calculated the energy of many excited states starting from this new ground state geometry. In the left panel of figure 2 the energy of the lowest energy excited state computed on the new geometry is represented by the second red circle. We repeated each step of this procedure until we reached a bond length where the ligand is for sure dissociated. By connecting the various excitation energies along the scan for a given excited state, we obtain an approximated Fe-C dissociation pathway computed from the minimum energy pathway on the  $S_0$ . Indeed, the constrained geometry optimization on the ground state identifies a minimum energy pathway whose maximum energy point is a transition state. This pathway is then projected on the excited PES, yielding an approximated description of that process for the excited state.

During the exploration of the PES, we can find points where two excited states have almost the same energy and conical intersections are possible. Furthermore, the calculation stops when there is a crossing point between the potential energy surface of the lowest energy excited state and that of the ground state.

The exploration of the PES is informative because the presence of a sequence of crossings between the PES of the excited states that ends near the ground state PES shows possible energy paths that the system can follow to deactivate the excited state, which ends up with a bond stretching or breaking.

### 2.1.7 TDDFT optimizations

The exploration of the PES of the excited states is an approach that allows to explore regions of the surfaces far from the ground state geometry, as reported in literature, for instance in the case of the photodissociation of the CO ligand bound to the heme group.<sup>130</sup> However in this approach we are moving on a projection of ground state pathway instead of the actual excited surface.

The optimization of the system with time-dependent DFT is an approach complementary to the exploration of the PES to study the evolution of a system upon irradiation. This approach allows to identify excited state stationary points on the excited PES by TDDFT geometry optimizations, using the ground state geometry as starting point. TDDFT optimization give a more detailed characterization of the

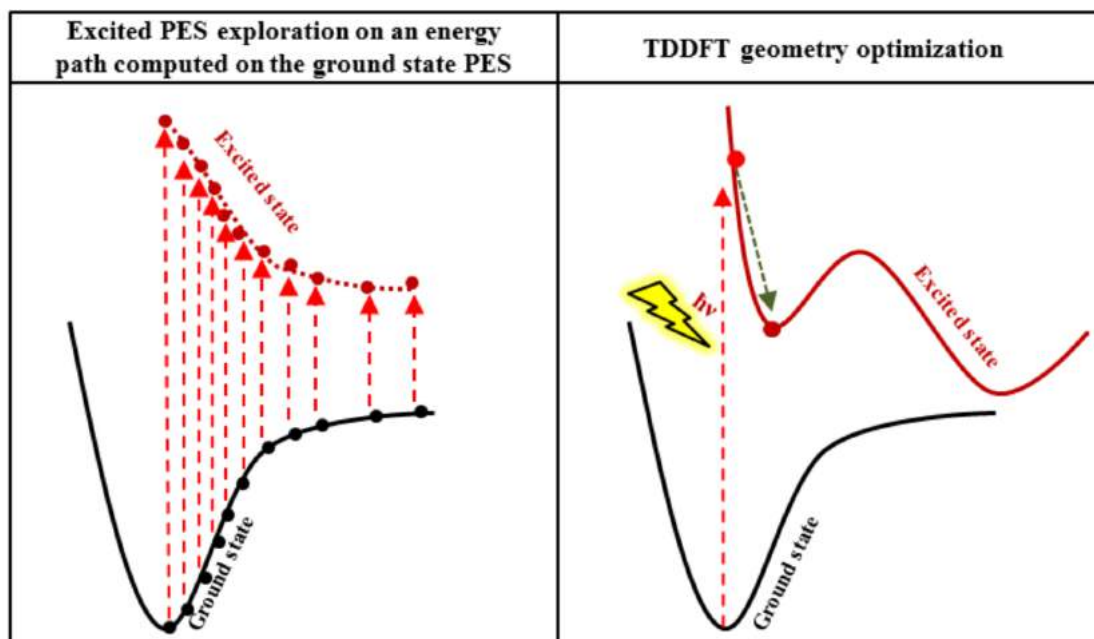


Figure 2.2: Schematization of PES exploration (left) and TDDFT optimization (right) procedures. This figure is a modified version of an unpublished figure realized by Dr. L. Bertini.

initial steps of the photodynamic processes of a system. This approach is essentially equal to an ordinary ground state geometry optimization, in which the analytical first derivatives of the excitation energy as a function of the nuclei position are used.<sup>128,131</sup> In TDDFT optimizations, schematized in the right panel of figure 2, we calculated the energy of an excited state generated by absorption of light of a specific wavelength, starting from the initial geometry of the ground state. Then the calculation ends when the software finds the best local minimum on the PES of the excited state or in presence of a crossing between the PES of the excited state and that of the ground state. The result of a TDDFT optimization is the local minimum on the excited state surface closest to the ground state geometry. We can analyze the geometrical and electronic structure of the excited system to observe for example the tendency of bonds to elongate or brake upon excitation.

These two approaches have been successfully adopted to characterize the CO photolysis from 2Fe binuclear small models of the H-cluster in the  $\text{Fe}^{\text{I}}\text{Fe}^{\text{I}}$  state.<sup>132–134</sup>

### 2.1.8 Level of theory used for DFT and TDDFT calculations

We used the software Turbomole 7.0 to perform all the calculations. In the calculations presented in this thesis we adopted the triple-zeta valence polarized (def-TZVP) basis set,<sup>135</sup> characterized by the use of three functions for each valence atomic orbital and functions to describe the polarization of the electron density. We adopted the GGA functional Becke-Perdew (BP86), composed by an exchange<sup>136</sup> and a correlation<sup>137</sup> terms. We used also the hybrid functional PBE0,<sup>138</sup> where the exchange energy is composed by 25% of Hartree-Fock exact exchange energy and 75% of PBE (GGA) exchange energy. These hybrid functional such as PBE0 are known to better describe the charge-transfer excitation within the time-dependent DFT approach for excitation energy evaluation (vide infra). The Resolution of Identity (RI) technique was adopted for pure functionals in order to save CPU time.<sup>139</sup> The optimization of transition state (TS) structures on the ground state PES was carried out according to a procedure based on a pseudo-Newton-Raphson method. Analytic excited state energy gradients were recently implemented within the Turbomole suite of programs also in combination with the RI technique.<sup>128,131</sup>

## 2.2 Direct electrochemistry

In this thesis, we perform direct electrochemistry experiments to study the kinetics of FeFe-hydrogenases. This method and its application in the study of hydrogenases are illustrated in the following review.



ELSEVIER

Available online at [www.sciencedirect.com](http://www.sciencedirect.com)

ScienceDirect

Current Opinion in  
Electrochemistry

## Review Article

## New perspectives in hydrogenase direct electrochemistry

Matteo Sensi, Melisa del Barrio, Carole Baffert, Vincent Fourmond and Christophe Léger<sup>1,\*</sup>

Electrochemical studies of hydrogenases, the biological catalysts of H<sub>2</sub> oxidation and production, have proven wrong the old saying that enzymes do not easily transfer electrons to electrodes in the absence of mediators. Many distinct hydrogenases have actually been directly connected to electrodes or particles, for studying their catalytic mechanism or for designing solar-fuels catalysts. In this review, we list the electrodes that have proved successful for direct electron transfer to hydrogenases, and we discuss recent results which illustrate new directions in this research field: the study of the biosynthesis of FeFe hydrogenase, the electrochemical characterization of non-standard NiFe or FeFe hydrogenases, the general discussion of what makes a catalyst better in one particular direction of the reaction, and the elucidation of the molecular mechanisms of hydrogenase catalysis by combining electrochemistry and theoretical chemistry, spectroscopy or photochemistry. The electrochemical methods described herein will probably prove useful for studying or using other redox enzymes.

## Address

Laboratoire de Bioénergétique et Ingénierie des Protéines, Aix Marseille Univ, CNRS, UMR7281, Marseille, France

\*Corresponding author: Léger, Christophe ([leger@imm.cnrs.fr](mailto:leger@imm.cnrs.fr))<sup>1</sup> [bip06.fr](mailto:bip06.fr), [@BIP6\\_Marseille.cnrs.fr](mailto:@BIP6_Marseille.cnrs.fr)

Current Opinion in Electrochemistry 2017, XX:XX–XX

This review comes from a themed issue on Bioelectrochemistry

Edited by Nicolas Plumeré

For a complete overview see the [Issue](#) and the [Editorial](#)

Available online XX XXXX 2017

<http://dx.doi.org/10.1016/j.coelec.2017.08.005>

2451-9103/© 2017 Elsevier B.V. All rights reserved.

## Introduction

Hydrogenases are the enzymes that oxidize and produce H<sub>2</sub>. They are classified as NiFe and FeFe hydrogenases based on the metal content of their active site. The NiFe active site (Figure 1A) consists of pair of metal ions bridged by the sulfur atoms of two cysteine residues; the Ni ion is also attached to the protein by either two cysteines or one cysteine and one selenocysteine. The Fe ion binds carbonyl and cyanide ligands which also occur at the active site of FeFe hydrogenases, the “H cluster”, shown in Figure 1C.

The NiFe hydrogenases that have been crystallized so far all look like the heterodimeric enzyme from *D. fructosovorans*, whose structure is shown in Figure 1B. A chain of three FeS clusters (whose exact nature varies) wires the active site to the soluble redox partner or the electrode. The FeFe hydrogenase from *C. reinhardtii* whose structure is shown in Figure 1D has no other cofactor than the surface-exposed H cluster, but other FeFe hydrogenases embed accessory FeS clusters for long range electron transfer (ET).

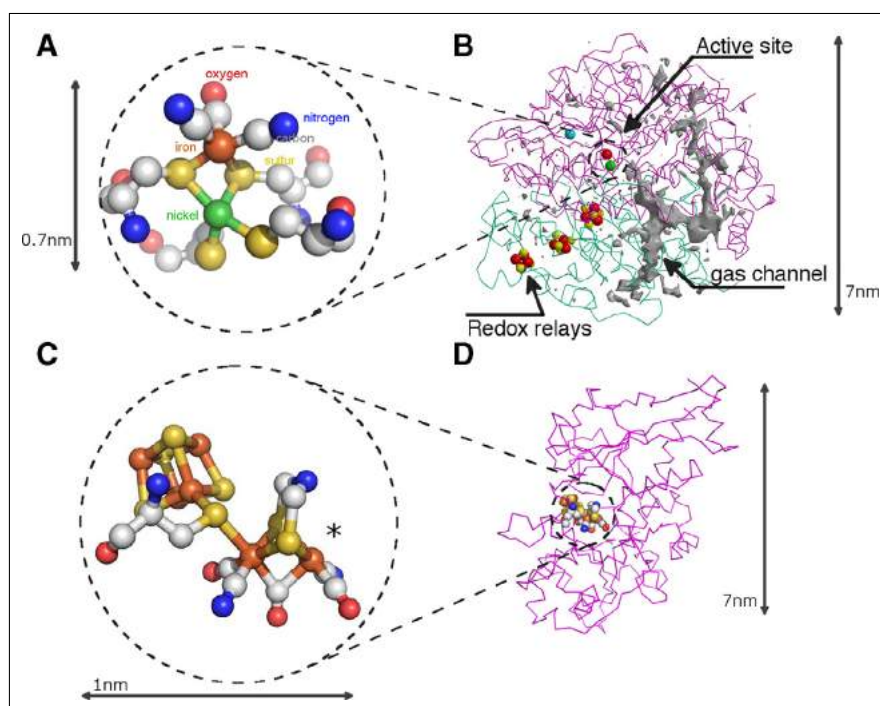
Evidence for direct electron transfer between electrodes and hydrogenases goes all the way back to the 1980s [10,35,71], and the research in this field has expanded enormously over the last 10 years, driven by the objective of using hydrogenases in solar-fuels devices. When direct electrochemistry is used in the context of enzyme kinetics, it provides unequalled redox control, time resolution and accuracy of the activity measurement, together with flexibility in terms of transient exposures to inhibitors and/or substrate. If such kinetic information is combined with that obtained from other methods, the potential for gaining original information becomes enormous.

## Electrodes for direct electron transfer

Hydrogenases are easily wired to electrodes because they all have at least one surface-exposed redox center, either the active site (e.g. Figure 1D) or the final redox relay (e.g. Figure 1B), which allows fast electron entry/exit. (This is unlike other redox enzymes such as glucose oxidase where the active site is buried and isolated in the protein matrix.) Many hydrogenases oxidize and produce hydrogen at very high rates (in excess of thousands per second, Table 4 in ref. [75]), and therefore a catalytic current may be detected even if the amount of enzyme that is attached to the electrode is very low. This explains the diversity of electrode materials that have proven useful in this context, listed in Table 1 (see also refs. [76–78] for reviews). Finely designed architectures for embedding membrane-bound hydrogenases have also been developed [79–81].



Fig. 1



The X-ray structures of two hydrogenases. Panel A shows the active site of NiFe hydrogenases. Panel B shows the backbones of the heterodimeric enzyme from *D. fructosovorans* (pdb 1YQW). Panel C shows the H cluster of FeFe hydrogenases (a star marks the H<sub>2</sub> binding site), and panel D shows the backbone of the enzyme from *Chlamydomonas reinhardtii* (pdb 3LX4).

### Heterogeneous reconstitution

In the natural biosynthetic pathway of FeFe hydrogenase, a 2Fe fragment of the H cluster is delivered to the “apo” form of the enzyme. The recent discovery that a *synthetic* 2Fe fragment can be directly incorporated into apo-hydrogenase has revolutionized hydrogenase research [82,83]. The use of direct electrochemistry to probe the kinetics of such artificial maturation of the enzyme is one of the most recent and exciting developments: the apo-enzyme can be adsorbed onto an electrode and can incorporate the 2Fe synthetic subcluster when the latter is added to the solution. The reconstitution of a holo-active enzyme results in an increase in H<sub>2</sub>-oxidation current which reports on the rate of reconstitution [84]. (This is reminiscent of the recent evidence by Limoges and coworkers that the PQQ cofactor of glucose dehydrogenase can bind the apo-enzyme anchored on an electrode surface [85].) Armstrong and coworkers could design potential-steps PFV experiments to detect the formation of an intermediate that is probably relevant to the final stage of biological H cluster maturation.

### Electrochemical studies of exotic hydrogenases

The electrochemical literature does not accurately reflect the biodiversity of hydrogenases. Indeed, most of the hy-

drogenases that have been studied in electrochemistry are very similar to each other. They are relatively small (60–100 kDa), and consist of a small number of proteins subunits, most often one or two. In contrast, some hydrogenases are part of very large enzymatic systems (e.g. 18 subunits and 600 kDa in the formate hydrogen lyase complex of *Thermococcus*). These complex hydrogenases use the same active sites as those shown in Figure 1, but their protein sequences, quaternary structure and cofactor content make them unique.

Recent electrochemical studies of hydrogenases whose structures are out of the ordinary [19,22,23,73] have revealed unprecedented properties. For example, the NiFe hydrogenase of the hyperthermophilic bacterium *P. furiosus* remains active upon exposure to O<sub>2</sub> at 80 °C, and its mechanism of O<sub>2</sub> tolerance is uncommon [23]. The FeFe hydrogenase of *A. woodii* is part of a large complex which reduces CO<sub>2</sub> to formate; it has high affinity for H<sub>2</sub> and is reversibly inhibited by CO under all redox conditions [73], unlike other FeFe hydrogenases, for which the inhibition is only partly reversible under reducing conditions [70].

Together with site-directed mutagenesis (SDM) studies, the characterization of these non-standard hydrogenases

Table 1

The hydrogenases that have been directly connected to electrodes, and the natures of the electrodes used in these studies. bSi: nanoporous black silicon, CC/CB: carbon black on carbon cloth, CDC: carbodiimide coupling, CF: carbon felt, NC: nanocrystals, NP: nanoparticles, GC: glassy carbon, GC/KB: Ketjen black-modified GC, CNT: carbon nanotubes, CNF: carbon nanofibers, MPDB: electropolymerized pyrrol, PGE: pyrolytic graphite edge [74], PGB: basal plane of PG, PGP: PG particles, QD: quantum dots, SAM: self-assembled monolayers.

Type	Source	Attachment methods
NiFe	<i>A. vinosum</i>	PGE/polymyxin [1,2], Au/polymyxin [3,4], PGP [5]
	<i>D. gigas</i>	Au/SAM/CDC [6], GC [7], PGE/CDC [8], CNT/CDC [9]
	<i>D. vulgaris</i> Hildenborough	PGE/polylysine [10], basal PGE [11]
	<i>D. fructosovorans</i>	PGE [12], PGE/CDC [13], CNT [14]
	<i>E. coli</i> (Hyd-1)	PGE [15], pyrenyl carbon nanostructures [16]
	<i>E. coli</i> (Hyd-2)	PGE [17], PGP [18]
	<i>E. coli</i> (Hyd-3)	PGE/CNT/polymyxin [19]
	<i>E. coli</i> membrane fractions	TiO <sub>2</sub> [20]
	<i>Citrobacter</i> sp. S-77	CC/CB [21]
	<i>Synechocystis</i> sp. PCC 6803	PGE [22]
	<i>P. furiosus</i> (hydrogenase I)	PGE [23]
	<i>A. aeolicus</i>	PGB [24], PGE [25], Au/SAM [26], CNT [27], CNF [28], SWCNT/CDC [29]
	<i>R. eutropha</i> (MbH)	PGE(FAA), AU/SAM [30,31]
	<i>R. eutropha</i> (RH)	CB [32]
	<i>R. metallidurans</i> CH34 (Rm)	PGE [33]
	<i>R. eutropha</i> (SH)	PGE [34]
<i>T. roseopersicina</i>	CB [35], CNT [36], CNF [37], CNF/MPDB [38]	
<i>H. marinus</i>	Au/CDC [39], GC & Gc/KB [40]	
NiFeSe	<i>D. vulgaris</i> Hildenborough	Au/SAM/CDC [6,41,42], PGE [43]
	<i>D. baculatum</i>	PGE [44], TiO <sub>2</sub> NP [45], mesoporous TiO <sub>2</sub> [46], SiTiO <sub>2</sub> [47]
FeFe	<i>C. acetobutylicum</i>	TiO <sub>2</sub> [48], CF [49], Au/SAM [50], CNT [51,52], PGE [53–57], PGE/CDC [58–60], CdS [61–63], CdTe NC [64], CdTe QD [65], bSi [66]
	<i>C. perfringens</i>	TiO <sub>2</sub> [67]
	<i>D. desulfuricans</i>	PGE [54,55,68], PGE/CDC [59]
	<i>C. reinhardtii</i>	Au/SAM [69], PGE [54,59,70], PGE/CDC [58]
	<i>M. elsdenii</i>	GC [71], PGE [72]
	<i>A. woodii</i>	PGE [73]

demonstrates that the catalytic properties depend on the environment of the active site, but also on structural elements that are remote from the conserved active site.

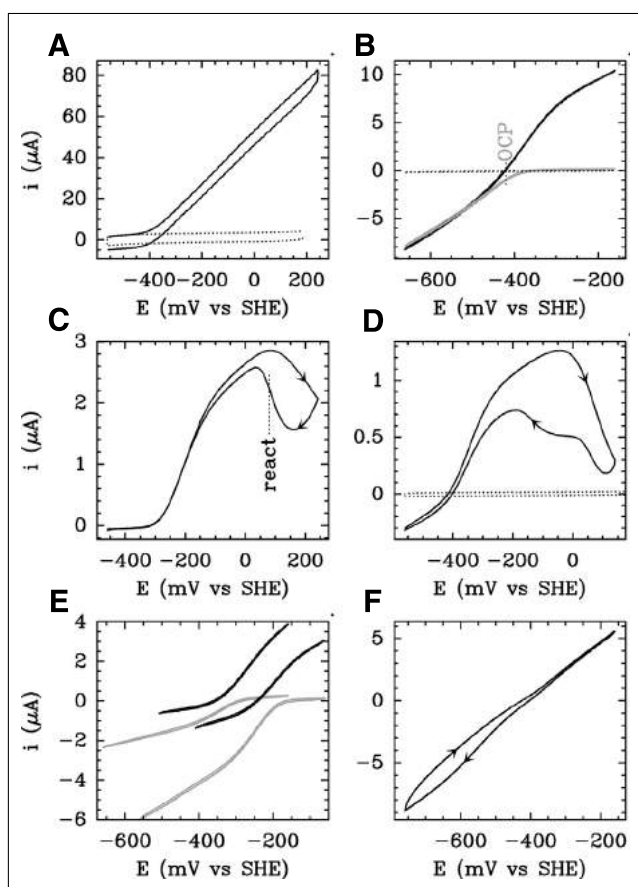
### The catalytic bias

Studies of hydrogenases have recently encouraged discussions on an important and often neglected aspect of enzyme catalysis: the question of what makes a particular enzyme a better catalyst in one direction of the reaction than in the other [91]. Answering this question is very important in the context of solar-fuels research, for the ra-

tional design of either synthetic catalysts [92] or bacterial strains [93] that either produce or oxidize H<sub>2</sub>.

One defines the catalytic bias of a hydrogenase as the ratio of the H<sub>2</sub>-oxidation and H<sub>2</sub>-production rates, which have to be measured under two different sets of experimental conditions. In PFV experiments, sweeping the potential makes it possible to probe the enzymatic response on either side of the equilibrium potential (OCP) in a single experiment. Any predisposition for oxidizing or producing H<sub>2</sub> is thus qualitatively observed as a larger current

Fig. 2



Cyclic voltammograms obtained with hydrogenases undergoing direct ET with a rotating electrode, recorded under an atmosphere of either  $N_2$  (gray lines) or  $H_2$  (black lines). The oxidation current is counted as positive. Arrows mark the directions of the potential sweeps. The dotted lines are blanks. A:  $H_2$  oxidation and evolution by *A. vinosum* NiFe hydrogenase (the fast scan rate used here prevents oxidative inactivation) [86]. B:  $H_2$  oxidation and evolution by *C. acetobutlicum* FeFe hydrogenase [53]. C: high potential inactivation of *A. aeolicus* NiFe hydrogenase [25]. D: high potential inactivation of a site-directed mutant of *C. reinhardtii* FeFe hydrogenase [56]. E:  $H_2$  oxidation and evolution by *D. fructosovorans* NiFe hydrogenase at pH 4 or 6 (signals at higher or lower potential, respectively), all other things being equal [87]. F: low potential reversible inactivation of *C. reinhardtii* FeFe hydrogenase at pH 7 [88]. In all cases here, the absence of current plateau results from the distribution of interfacial ET rate constants [86,89,90].

in one particular direction (Figure 2) [94]. (Of course, the rate of  $H_2$  evolution is likely to be larger under more acidic conditions because the proton is the substrate [87,95], and  $H_2$  production is also faster when  $H_2$  is removed [95,96]; see Figure 2E.)

A standardized method for measuring the bias (either in solution assays or on an electrode) is lacking, but the comparison between various results such as those in

Figure 2 suggested that NiFeSe [43,44,100] and FeFe hydrogenases are better  $H_2$ -production catalysts than their NiFe counterparts (see however ref [22]). The  $O_2$ -resistant NiFe hydrogenases are essentially unidirectional  $H_2$ -oxidation enzymes whereas the standard ( $O_2$ -sensitive) enzymes are bidirectional catalysts [101], and certain mutations that strongly increase the  $O_2$  tolerance of standard NiFe hydrogenase also selectively slow  $H_2$  evolution [12,102–104]. Other mutations of amino acids that are remote from the active site also alter the bias of NiFe hydrogenases [105–107].

There is much interest in understanding the bias in relation to the shape of the catalytic signal and the properties of the catalytic intermediates. The ratio of oxidative and reductive currents is inevitably related to the difference between the two-electron “catalytic potential”  $E_{cat}$  and the OCP by Equation (1) in Box 1, but various models give distinct answers to the question of what defines  $E_{cat}$ . Emphasis was often on the role of the redox relays [89,97,107] (Box 1), but there is one clear example from our group where the bias is defined by the  $H_2$  diffusion rates along the gas channel [104].

The observed rate of catalysis in either direction is also affected by any redox-driven inactivation of the enzyme, unmistakably detected as a hysteresis in cyclic voltammetry at a rotating disk electrode (RDE) [90]. NiFe hydrogenases reversibly inactivate under oxidative conditions [12,25,43,108], whereas FeFe hydrogenases inactivate in a complex manner both at high [56,68,73] and low potential [84,88] (see e.g. Figure 2C, D and F, respectively).

### Combining electrochemistry and theoretical chemistry

(Electro)kinetic measurements alone most often cannot give the molecular mechanism of a reaction whose rate is being measured. An approach that has recently gained popularity is to combine electrochemistry and theoretical chemistry [109]. In this context, a seminal PFV paper addressed the mechanism of electron/proton transfer to a buried FeS cluster in a small protein [110]: electrochemical experiments identified the “kinetic mechanism” (sequential, rather than concerted), and the results of molecular dynamics (MD) simulations and SDM experiments could be used to describe the molecular details of the reaction.

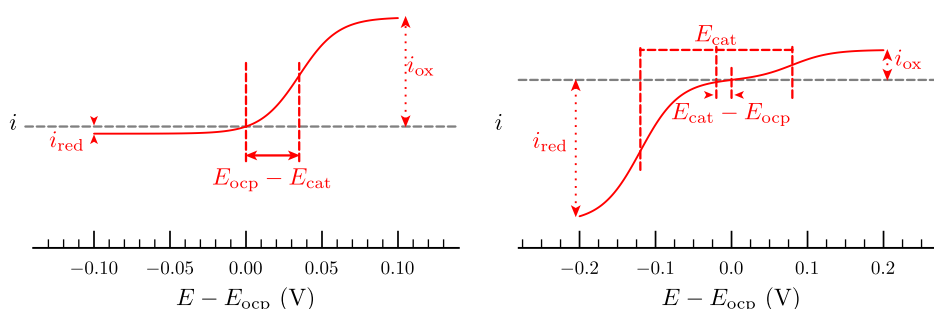
More recently, the approach that combines PFV and theoretical calculations (DFT and/or MD) proved powerful to decipher the mechanism of inhibition of FeFe hydrogenases by formaldehyde [111–113], CO [57,70],  $O_2$  [57], or under anaerobic oxidative conditions [56]. These studies concern the active site mechanism, but also the diffusion along gas channels and binding at the active site of

**Box 1: The relation between catalytic overpotential and the catalytic bias, when the catalytic signal is sigmoidal.**

If the steady-state catalytic wave shape is sigmoidal, as observed in the case of hydrogenases, a simple equation relates the two-electron “catalytic potential”  $E_{\text{cat}}$ , the open circuit potential (Nernst potential of the  $\text{H}^+/\text{H}_2$  couple), and the catalytic bias:

$$\frac{i_{\text{ox}}}{i_{\text{red}}} = \exp \left[ \frac{2F}{RT} (E_{\text{cat}} - E_{\text{OCP}}) \right] \quad (1)$$

The value  $n = 2$  comes from the stoichiometry of the redox reaction, and Eq. (1) results from the condition that  $i = 0$  at the OCP.



For a two-electron redox reaction, if the catalytic signal is a two-electron sigmoid,  $E_{\text{cat}}$  is the mid-wave potential; if the wave consists of two one-electron waves,  $E_{\text{cat}}$  is the average value of the two mid-wave potentials. In intermediates cases or if the signal is broadened by slow interfacial ET,  $E_{\text{cat}}$  must be determined by fitting [90].

Verifying Eq. (1) in a particular case does not give an explanation for the bias. What matters is the reason  $E_{\text{cat}}$  takes a particular value. According to models that only take into account one relay (no active site, no redox chain, no kinetics of intramolecular ET),  $E_{\text{cat}}$  can only equate the potential of the unique redox center in the model, the relay [97]; this was taken as evidence that the difference between the potential of the entry/exit relay and the OCP defines the catalytic bias [98]. In contrast, according to models that take into account reversible catalysis, one-electron mediation, and two-electron active-site chemistry, the two-electron potential  $E_{\text{cat}}$  cannot strictly equate the one-electron potential of any of the redox relays [89];  $E_{\text{cat}}$  tends to the potential of the active site if intramolecular ET is very fast, but its value is influenced by the kinetics and thermodynamics of intramolecular ET, and the kinetics of all steps in the catalytic cycle that are coupled to active site redox chemistry [89,90,99].

small molecules: the rates of these reactions can be measured using electrochemistry and sometimes calculated—this was achieved with both NiFe [55,109,114,115] and FeFe hydrogenases [54,57].

**Direct spectroelectrochemistry**

The vibrations of the carbonyl and cyanide ligands at the active sites of hydrogenases result in IR absorptions in the 1800–2100  $\text{cm}^{-1}$  region, which is devoid of other absorption bands, allowing selective detection of the active site. Spectroelectrochemical titrations followed by FTIR spectroscopy have identified various states of the active sites, some of which are probably catalytic intermediates. The caveat of this approach is that a system that reduces protons can only reach equilibrium under a certain pressure of hydrogen that becomes much too large at poten-

tials below  $E^0 = -0.06 \times \text{pH}$ . For instance, equilibration at  $-450$  mV at pH 7 requires a  $\text{H}_2$  pressure of 10 bars, much too high for a spectroelectrochemical cell to withstand. Recently, various groups have gone beyond equilibrium titrations by combining standard catalytic protein film voltammetry with the simultaneous detection of the active site spectroscopic signatures of NiFe hydrogenases; this made it possible to correlate the features of the catalytic response and specific states of the active site, as illustrated below.

Surface-enhanced infrared absorption spectroscopy, with NiFe hydrogenases adsorbed onto modified gold electrodes, has been used to relate the appearance of the NiB active site signature to the disappearance of activity at high potentials [116,117].

A significant breakthrough came from the Vincent group in Oxford, who combined an attenuated total reflection cell with a volumic carbon black electrode [118], giving electrochemical signals strongly resembling those obtained with a “flat” PGE electrode, with enough sensitivity to characterize species that had previously escaped detection. Vincent and coworkers showed that the Ni-L state, long thought to be an artifact of illumination at cryogenic temperatures, is one of the possible intermediates of the oxidation of Ni-C [32], with which it is in acid–base equilibrium [119]. They could also detect for the first time the presence of Ni-R, the most reduced state in the catalytic cycle, in *R. eutropha* regulatory hydrogenase [120].

### Direct photoelectrochemistry

The active sites of hydrogenases bearing Fe-carbonyl bonds, it is no surprise that these enzymes are sensitive to light in the UV–vis range. It has long been known that exposure to white light reactivates the FeFe hydrogenase bound to extrinsic CO, but until recently the photochemistry of hydrogenases was much less studied than that of hydrogenase synthetic mimics.

In spectroscopic investigations, information on the electronic structure of the active site is obtained from the knowledge of which wavelengths are absorbed by the cluster; in contrast, with the enzyme wired to an electrode, one can detect light absorption by monitoring wavelength-dependent light-induced changes in turnover rate. This is possible even when the protein or chromophores hide the weak absorption that triggers the change in activity. By monitoring changes in turnover rate, one is certain to focus on light absorption events that impact the catalytic intermediates.

Regarding FeFe hydrogenases, the first direct photoelectrochemistry experiments focused on the inhibited form of the active site and the enhancement of the rate of release of extrinsic CO by white light [68]. More recently, we could observe that this enhancement only occurs in the blue part of the visible spectrum, and it is proportional to light power; the effect is small because the H cluster has very low absorption in the visible range, but the quantitative analysis of the electrochemical data demonstrates that every photon that is absorbed by the inhibited H cluster induces CO release [72].

It had also been reported that day-light destroys the H cluster of *D. desulfuricans* FeFe hydrogenase [121], which certainly raises questions as to whether FeFe hydrogenases can be coupled to photosensitizers for solar H<sub>2</sub> production. White light photoelectrochemistry experiments with *D. desulfuricans* FeFe hydrogenase gave a less dramatic picture [122]. In the case of the enzymes from *C. acetobutylicum* and *C. reinhardtii*, recent results demonstrate that photoinhibition only occurs upon UV irradiation, which triggers the release of an *intrinsic* CO ligand

followed by irreversible isomerization of the H cluster [123].

Lojou and coworkers also discovered that irradiation at 405 nm *activates* the O<sub>2</sub>-tolerant NiFe hydrogenase from *A. aeolicus* under turnover conditions [124]. The mechanism and action spectrum of this unprecedented reaction and the implications regarding the nature of the inactive states of NiFe hydrogenases must be explored.

### Conclusion

The abundant literature in the field of hydrogenase electrochemistry reflects the ease with which catalytic currents are obtained, the variety of the mechanistic questions that these studies can answer, the large number of applications which rely on wiring hydrogenases to electrodes, nanoparticles or photosensitizers [77,125–128] and, of course, the creativity and combined talent of many biochemists and electrochemists. The implications of these results are wide, from the understanding of fundamental concepts in electrocatalysis to implications for the design of solar-fuel catalysts. We hope that they will also prove inspirational in other, related fields of research.

### Funding

Our work is supported by CNRS, Aix Marseille Université, Agence Nationale de la Recherche (ANR-12-BS08-0014, ANR-14-CE05-0010, ANR-15-CE05-0020), and Excellence Initiative of Aix-Marseille University—A\*MIDEX, a French “Investissements d’Avenir” programme (ANR-11-IDEX-0001-02). The authors are part of the FrenchBIC network ([www.frenchbic.cnrs.fr](http://www.frenchbic.cnrs.fr)).

### References and recommended reading

Papers of particular interest, published within the period of review, have been highlighted as:

- Paper of special interest
- Paper of outstanding interest

1. Pershad HR, Duff JL, Heering HA, Duin EC, Albracht SP, Armstrong FA: **Catalytic electron transport in *Chromatium vinosum*[NiFe]-hydrogenase: application of voltammetry in detecting redox-active centers and establishing that hydrogen oxidation is very fast even at potentials close to the reversible H<sup>+</sup>/H<sub>2</sub> value.** *Biochemistry* 1999, **38**(28):8992–8999. <http://dx.doi.org/10.1021/bi990108v>.
2. Jones AK, Sillery E, Albracht SPJ, Armstrong FA: **Direct comparison of the electrocatalytic oxidation of hydrogen by an enzyme and a platinum catalyst.** *Chem Commun* 2002(8):866–867. <http://dx.doi.org/10.1039/b201337a>.
3. Hoeben FJM, Heller I, Albracht SPJ, Dekker C, Lemay SG, Heering HA: **Polymyxin-coated Au and carbon nanotube electrodes for stable [NiFe]-hydrogenase film voltammetry.** *Langmuir* 2008, **24**(11):5925–5931. <http://dx.doi.org/10.1021/la703984z>.
4. Hoeben FJM, Meijer FS, Dekker C, Albracht SPJ, Heering HA, Lemay SG: **Toward single-enzyme molecule electrochemistry: [NiFe]-hydrogenase protein film voltammetry at nanoelectrodes.** *ACS Nano* 2008, **2**(12):2497–2504. <http://dx.doi.org/10.1021/nm800518d>.

5. Vincent KA, Li X, Blanford CF, Belsey NA, Weiner JH, Armstrong FA: **Enzymatic catalysis on conducting graphite particles.** *Nat Chem Biol* 2007, **3**(12):761–762. <http://dx.doi.org/10.1038/nchembio.2007.47>.
6. Rüdiger O, Gutiérrez-Sánchez C, Olea D, Pereira IA, Vélez M, Fernández VM, De Lacey AL: **Enzymatic anodes for hydrogen fuel cells based on covalent attachment of Ni-Fe hydrogenases and direct electron transfer to SAM-modified gold electrodes.** *Electroanalysis* 2010, **22**(7–8):776–783. <http://dx.doi.org/10.1002/elan.200880002>.
7. Cordas CM, Moura I, Moura JGG: **Direct electrochemical study of the multiple redox centers of hydrogenase from *Desulfovibrio gigas*.** *Bioelectrochemistry* 2008, **74**(1):83–89. <http://dx.doi.org/10.1016/j.bioelechem.2008.04.019>.
8. Rüdiger O, Abad JM, Hatchikian EC, Fernandez VM, De Lacey AL: **Oriented immobilization of *Desulfovibrio gigas* hydrogenase onto carbon electrodes by covalent bonds for nonmediated oxidation of H<sub>2</sub>.** *J Am Chem Soc* 2005, **127**(46):16008–16009. <http://dx.doi.org/10.1021/ja0554312>.
- The first paper showing covalent (hence long term) attachment of NiFe hydrogenase to a graphite electrode. This method proved useful later for quantifying the various inactive forms of the enzyme that are produced upon oxidative inactivation [13] and could be adapted to attach FeFe hydrogenase [58].
9. Alonso-Lomillo MA, Rüdiger O, Maroto-Valiente A, Velez M, Rodríguez-Ramos I, Muñoz FJ, Fernández VM, De Lacey AL: **Hydrogenase-coated carbon nanotubes for efficient H<sub>2</sub> oxidation.** *Nano Lett* 2007, **7**(6):1603–1608. <http://dx.doi.org/10.1021/nl070519u>.
10. Bianco P, Haladjian J: **Electrocatalytic hydrogen evolution at the pyrolytic graphite electrode in the presence of hydrogenase.** *J Electrochem Soc* 1992, **139**(9):2428–2432. <http://dx.doi.org/10.1149/1.2221244>.
11. Guiral-Brugna M, Giudici-Ortoni MT, Bruschi M, Bianco P: **Electrocatalysis of the hydrogen production by [Fe] hydrogenase from *Desulfovibrio vulgaris* Hildenborough.** *J Electroanal Chem* 2001, **510**(1–2):136–143. [http://dx.doi.org/10.1016/S0022-0728\(01\)00502-2](http://dx.doi.org/10.1016/S0022-0728(01)00502-2).
12. Hamdan AA, Liebgott P-P, Fourmond V, Gutiérrez-Sanz O, De Lacey AL, Infossi P, Rousset M, Dementin S, Léger C: **Relation between anaerobic inactivation and oxygen tolerance in a large series of NiFe hydrogenase mutants.** *Proc Natl Acad Sci USA* 2012, **109**(49):19916–19921. <http://dx.doi.org/10.1073/pnas.1212258109>.
13. Abou Hamdan A, Burlat B, Gutiérrez-Sanz O, Liebgott P-P, Baffert C, De Lacey AL, Rousset M, Guigliarelli B, Léger C, Dementin S: **O<sub>2</sub>-independent formation of the inactive states of NiFe hydrogenase.** *Nat Chem Biol* 2012, **9**(1):15–17. <http://dx.doi.org/10.1038/nchembio.1110>.
14. Lojou E, Luo X, Brugna M, Candoni N, Dementin S, Giudici-Ortoni MT: **Biocatalysts for fuel cells: efficient hydrogenase orientation for H<sub>2</sub> oxidation at electrodes modified with carbon nanotubes.** *J Biol Inorg Chem* 2008, **13**(7):1157–1167. <http://dx.doi.org/10.1007/s00775-008-0401-8>.
15. Lukey MJ, Roessler MM, Parkin A, Evans RM, Davies RA, Lenz O, Friedrich B, Sargent F, Armstrong FA: **Oxygen-tolerant [NiFe]-hydrogenases: the individual and collective importance of supernumerary cysteines at the proximal Fe-S cluster.** *J Am Chem Soc* 2011, **133**(42):16881–16892. <http://dx.doi.org/10.1021/ja205393w>.
16. Krishnan S, Armstrong FA: **Order-of-magnitude enhancement of an enzymatic hydrogen-air fuel cell based on pyrenyl carbon nanostructures.** *Chem Sci* 2012, **3**(4):1015–1023. <http://dx.doi.org/10.1039/c2sc01103d>.
17. Lukey MJ, Parkin A, Roessler MM, Murphy BJ, Harmer J, Palmer T, Sargent F, Armstrong FA: **How *Escherichia coli* is equipped to oxidize hydrogen under different redox conditions.** *J Biol Chem* 2010, **285**(6):3928–3938. <http://dx.doi.org/10.1074/jbc.m109.067751>.
18. Lazarus O, Woolerton TW, Parkin A, Lukey MJ, Reisner E, Seravalli J, Pierce E, Ragsdale SW, Sargent F, Armstrong FA: **Water-gas shift reaction catalyzed by redox enzymes on conducting graphite platelets.** *J Am Chem Soc* 2009, **131**(40):14154–14155. <http://dx.doi.org/10.1021/ja905797w>.
19. McDowall JS, Murphy BJ, Haumann M, Palmer T, Armstrong FA, Sargent F: **Bacterial formate hydrogenlyase complex.** *Proc Natl Acad Sci USA* 2014, **111**(38):E3948–E3956. <http://dx.doi.org/10.1073/pnas.1407927111>.
20. Schlicht S, Assaud L, Hansen M, Lickleder M, Bechelany M, Perner M, Bachmann J: **An electrochemically functional layer of hydrogenase extract on an electrode of large and tunable specific surface area.** *J Mater Chem A* 2016, **4**(17):6487–6494. <http://dx.doi.org/10.1039/c6ta00392c>.
21. Matsumoto T, Eguchi S, Nakai H, Hibino T, Yoon K-S, Ogo S: **[NiFe]hydrogenase from *Citrobacter* sp. s-77 surpasses platinum as an electrode for H<sub>2</sub> oxidation reaction.** *Angew Chem Int Ed* 2014, **53**(34):8895–8898. <http://dx.doi.org/10.1002/anie.201404701>.
22. McIntosh CL, Germer F, Schulz R, Appel J, Jones AK: **The [NiFe]-hydrogenase of the cyanobacterium *Synechocystis* sp. PCC 6803 works bidirectionally with a bias to H<sub>2</sub> production.** *J. Am. Chem. Soc.* 2011, **133**(29):11308–11319. <http://dx.doi.org/10.1021/ja203376y>.
23. Kwan P, McIntosh CL, Jennings DP, Hopkins RC, Chandrayan SK, Wu C-H H, Adams MW, Jones AK: **The [NiFe]-hydrogenase of *Pyrococcus furiosus* exhibits a new type of oxygen tolerance.** *J Am Chem Soc* 2015, **137**(42):13556–13565. <http://dx.doi.org/10.1021/jacs.5b07680>.
- Electrochemical characterization of an oxygen-tolerant, group 3, soluble, thermophilic [NiFe]-hydrogenase. The mechanism of oxygen resistance is shown to differ from that of group 1 enzymes.
24. Lojou E, Giudici-Ortoni M-T, Bianco P: **Hydrogenases from the hyperthermophilic bacterium *Aquifex aeolicus*: electrocatalysis of the hydrogen production/consumption reactions at carbon electrodes.** *J Electroanal Chem* 2005, **577**(1):79–86. <http://dx.doi.org/10.1016/j.jelechem.2004.11.016>.
25. Fourmond V, Infossi P, Giudici-Ortoni M-T, Bertrand P, Léger C: **“Two-step” chronoamperometric method for studying the anaerobic inactivation of an oxygen tolerant NiFe hydrogenase.** *J Am Chem Soc* 2010, **132**(13):4848–4857. <http://dx.doi.org/10.1021/ja910685j>.
26. Ciaccafava A, Infossi P, Ilbert M, Guiral M, Lecomte S, Giudici-Ortoni MT, Lojou E: **Electrochemistry, AFM, and PM-IRRA spectroscopy of immobilized hydrogenase: role of a hydrophobic helix in enzyme orientation for efficient H<sub>2</sub> oxidation.** *Angew Chem Int Ed* 2012, **51**(4):953–956. <http://dx.doi.org/10.1002/anie.201107053>.
27. Luo X, Brugna M, Tron-Infossi P, Giudici-Ortoni M, Lojou E: **Immobilization of the hyperthermophilic hydrogenase from *Aquifex aeolicus* bacterium onto gold and carbon nanotube electrodes for efficient H<sub>2</sub> oxidation.** *J Biol Inorg Chem* 2009, **14**(8):1275–1288. <http://dx.doi.org/10.1007/s00775-009-0572-y>.
28. Poulpouquet A, Marques-Knopf H, Wernert V, Giudici-Ortoni MT, Gadiou R, Lojou E: **Carbon nanofiber mesoporous films: efficient platforms for bio-hydrogen oxidation in biofuel cells.** *Phys Chem Chem Phys* 2014, **16**(4):1366–1378. <http://dx.doi.org/10.1039/c3cp54631d>.
29. Ciaccafava A, De Poulpouquet A, Techer V, Giudici-Ortoni MT, Tingry S, Innocent C, Lojou E: **An innovative powerful and mediatorless H<sub>2</sub>/O<sub>2</sub> biofuel cell based on an outstanding bioanode.** *Electrochem Commun* 2012, **23**:25–28. <http://dx.doi.org/10.1016/j.elecom.2012.06.035>.
30. Sezer M, Frielingsdorf S, Millo D, Heidary N, Utesch T, Mroginski M-A, Friedrich B, Hildebrandt P, Zebger I, Weidinger IM: **Role of the HoxZ subunit in the electron transfer pathway of the membrane-bound [NiFe]-hydrogenase from *Ralstonia eutropha* immobilized on electrodes.** *J Phys Chem B* 2011, **115**(34):10368–10374. <http://dx.doi.org/10.1021/jp204665r>.
31. Heidary N, Utesch T, Zerball M, Horch M, Millo D, Fritsch J, Lenz O, von Klitzing R, Hildebrandt P, Fischer A, Mroginski MA, Zebger I: **Orientation-controlled electrocatalytic efficiency of an adsorbed oxygen-tolerant hydrogenase.** *PLOS ONE* 2015, **10**(11):e0143101+. <http://dx.doi.org/10.1371/journal.pone.0143101>.

## 8 Bioelectrochemistry

32. Hidalgo R, Ash PA, Healy AJ, Vincent KA: **Infrared spectroscopy during electrocatalytic turnover reveals the Ni-L active site state during H<sub>2</sub> oxidation by a NiFe hydrogenase.** *Angew Chem Int Ed Engl* 2015, **54**(24):7110–7113. <http://dx.doi.org/10.1002/anie.201502338>.
- This article is the first demonstration of the potential of the use of the concomitant monitoring of catalytic activity using PFV and detection of IR spectra to show the catalytic relevance of the Ni-L state.
33. Cracknell JA, Vincent KA, Ludwig M, Lenz O, Friedrich B, Armstrong FA: **Enzymatic oxidation of H<sub>2</sub> in atmospheric O<sub>2</sub>: the electrochemistry of energy generation from trace H<sub>2</sub> by aerobic microorganisms.** *J Am Chem Soc* 2007. <http://dx.doi.org/10.1021/ja078299+>.
34. Lauterbach L, Liu J, Horch M, Hummel P, Schwarze A, Haumann M, Vincent KA, Lenz O, Zebger I: **The hydrogenase subcomplex of the NAD<sup>+</sup>-reducing [NiFe] hydrogenase from *Ralstonia eutropha*—insights into catalysis and redox interconversions.** *Eur J Inorg Chem* 2011, **2011**(7):1067–1079. <http://dx.doi.org/10.1002/ejic.201001053>.
35. Yaropolov AI, Karyakin AA, Varfolomeev SD, Berezin IV: **Mechanism of H<sub>2</sub>-electrooxidation with immobilized hydrogenase.** *Bioelectrochem Bioenerg* 1984, **12**(3–4):267–277. [http://dx.doi.org/10.1016/0302-4598\(84\)87009-9](http://dx.doi.org/10.1016/0302-4598(84)87009-9).
36. Kihara T, Liu X-Y, Nakamura C, Park K-M, Han S-W, Qian D-J, Kawasaki K, Zorin NA, Yasuda S, Hata K, Wakayama T, Miyake J: **Direct electron transfer to hydrogenase for catalytic hydrogen production using a single-walled carbon nanotube forest.** *Int J Hydrogen Energy* 2011, **36**(13):7523–7529. <http://dx.doi.org/10.1016/j.ijhydene.2011.03.135>.
37. Karyakin AA, Morozov SV, Karyakina EE, Varfolomeyev SD, Zorin NA, Cosnier S: **Hydrogen fuel electrode based on bioelectrocatalysis by the enzyme hydrogenase.** *Electrochem Commun* 2002, **4**(5):417–420. [http://dx.doi.org/10.1016/s1388-2481\(02\)00335-1](http://dx.doi.org/10.1016/s1388-2481(02)00335-1).
38. Karyakin AA, Morozov SV, Voronin OG, Zorin NA, Karyakina EE, Fateyev VN, Cosnier S: **The limiting performance characteristics in bioelectrocatalysis of hydrogenase enzymes.** *Angew Chem Int Ed* 2007, **46**(38):7244–7246. <http://dx.doi.org/10.1002/anie.200701096>.
39. So K, Hamamoto R, Takeuchi R, Kitazumi Y, Shirai O, Endo R, Nishihara H, Higuchi Y, Kano K: **Bioelectrochemical analysis of thermodynamics of the catalytic cycle and kinetics of the oxidative inactivation of oxygen-tolerant [NiFe]-hydrogenase.** *J Electroanal Chem* 2016, **766**:152–161. <http://dx.doi.org/10.1016/j.jelechem.2016.02.009>.
40. Sugimoto Y, Kitazumi Y, Shirai O, Kano K: **Effects of mesoporous structures on direct electron transfer-type bioelectrocatalysis: facts and simulation on a three-dimensional model of random orientation of enzymes.** *Electrochemistry* 2017, **85**:82–87. <http://dx.doi.org/10.5796/electrochemistry.85.82>.
41. Gutiérrez-Sánchez C, Olea D, Marques M, Fernández VM, Pereira IAC, Vélez M, De Lacey AL: **Oriented immobilization of a membrane-bound hydrogenase onto an electrode for direct electron transfer.** *Langmuir* 2011, **27**(10):6449–6457. <http://dx.doi.org/10.1021/la200141t>.
42. Gutiérrez-Sanz O, Tapia C, Marques MC, Zacarias S, Vélez M, Pereira IAC, De Lacey AL: **Induction of a proton gradient across a gold-supported biomimetic membrane by electroenzymatic H<sub>2</sub> oxidation.** *Angew Chem Int Ed* 2015, **54**(9):2684–2687. <http://dx.doi.org/10.1002/anie.201411182>.
43. Ceccaldi P, Marques MC, Fourmond V, Pereira IC, Léger C: **Oxidative inactivation of NiFeSe hydrogenase.** *Chem Commun* 2015, **51**(75):14223–14226. <http://dx.doi.org/10.1039/c5cc05930e>.
44. Parkin A, Goldet G, Cavazza C, Fontecilla-Camps JC, Armstrong FA: **The difference a Se makes? oxygen-tolerant hydrogen production by the [NiFeSe]-hydrogenase from *Desulfomicrobium baculatum*.** *J Am Chem Soc* 2008, **130**(40):13410–13416. <http://dx.doi.org/10.1021/ja803657d>.
45. Reisner E, Powell DJ, Cavazza C, Fontecilla-Camps JC, Armstrong FA: **Visible light-driven H<sub>2</sub> production by hydrogenases attached to dye-sensitized TiO<sub>2</sub> nanoparticles.** *J Am Chem Soc* 2009, **131**(51):18457–18466. <http://dx.doi.org/10.1021/ja907923r>.
46. Mersch D, Lee C-Y, Zhang JZ, Brinkert K, Fontecilla-Camps JC, Rutherford AW, Reisner E: **Wiring of photosystem II to hydrogenase for photoelectrochemical water splitting.** *J Am Chem Soc* 2015, **137**(26):8541–8549. <http://dx.doi.org/10.1021/jacs.5b03737>.
- Here the authors describe a photoelectrochemical cell that is based on direct electron transfer. Photosystem II absorbs light and oxidizes water on anode electrode; a hydrogenase produces H<sub>2</sub> on the other. The electron transport chain is simpler than the Natural "Z scheme" of photosynthesis, but the price to pay for having a single photosynthetic enzyme is the small bias that has to be applied to drive photoelectrolysis with this semiartificial system.
47. Lee C-Y, Park HS, Fontecilla-Camps JC, Reisner E: **Photoelectrochemical H<sub>2</sub> evolution with a hydrogenase immobilized on a TiO<sub>2</sub>-protected silicon electrode.** *Angew Chem Int Ed* 2016, **55**(20):5971–5974. <http://dx.doi.org/10.1002/anie.201511822>.
48. Morra S, Valetti F, Sadeghi SJ, King PW, Meyer T, Gilardi G: **Direct electrochemistry of an [FeFe]-hydrogenase on a TiO<sub>2</sub> electrode.** *Chem Commun* 2011, **47**(38):10566–10568. <http://dx.doi.org/10.1039/c1cc14535e>.
49. Hamburger M, Gervaldo M, Svedruzic D, King PW, Gust D, Ghirardi M, Moore AL, Moore TA: **[FeFe]-hydrogenase-catalyzed H<sub>2</sub> production in a photoelectrochemical biofuel cell.** *J Am Chem Soc* 2008, **130**(6):2015–2022. <http://dx.doi.org/10.1021/ja077691k>.
50. Madden C, Vaughn MD, Díez-Pérez I, Brown KA, King PW, Gust D, Moore AL, Moore TA: **Catalytic turnover of [FeFe]-hydrogenase based on single-molecule imaging.** *J Am Chem Soc* 2012, **134**(3):1577–1582. <http://dx.doi.org/10.1021/ja207461t>.
- Direct observation of the single enzyme distribution on the Au-SAM surface (*Clostridium acetobutylicum*) FeFe hydrogenase).
51. McDonald TJ, Svedruzic D, Kim Y-H, Blackburn JL, Zhang SB, Heben MJ, Heben MJ: **Wiring-up hydrogenase with single-walled carbon nanotubes.** *Nano Lett* 2007, **7**(11):3528–3534. <http://dx.doi.org/10.1021/nl072319o>.
52. Svedružić D, Blackburn JL, Tenent RC, Rocha J-D D, Vinzant TB, Heben MJ, King PW: **High-performance hydrogen production and oxidation electrodes with hydrogenase supported on metallic single-wall carbon nanotube networks.** *J Am Chem Soc* 2011, **133**(12):4299–4306. <http://dx.doi.org/10.1021/ja104785e>.
53. Baffert C, Demuez M, Cournac L, Burlat B, Guigliarelli B, Bertrand P, Girbal L, Léger C: **Hydrogen-activating enzymes: activity does not correlate with oxygen sensitivity.** *Angew Chem Int Ed* 2008, **47**(11):2052–2054. <http://dx.doi.org/10.1002/anie.200704313>.
54. Goldet G, Brandmayr C, Stripp ST, Happe T, Cavazza C, Fontecilla-Camps JC, Armstrong FA: **Electrochemical kinetic investigations of the reactions of [FeFe]-hydrogenases with carbon monoxide and oxygen: comparing the importance of gas tunnels and active-site electronic/redox effects.** *J Am Chem Soc* 2009, **131**(41):14979–14989. <http://dx.doi.org/10.1021/ja905388j>.
55. Liebgott P-P, Leroux F, Burlat B, Dementin S, Baffert C, Lautier T, Fourmond V, Ceccaldi P, Cavazza C, Meynial-Salles I, Soucaille P, Fontecilla-Camps JC, Guigliarelli B, Bertrand P, Rousset M, Léger C: **Relating diffusion along the substrate tunnel and oxygen sensitivity in hydrogenase.** *Nat Chem Biol* 2009, **6**(1):63–70. <http://dx.doi.org/10.1038/nchembio.276>.
56. Fourmond V, Greco C, Sybirna K, Baffert C, Wang P-H, Ezanno P, Montefiori M, Bruschi M, Meynial-Salles I, Soucaille P, Blumberger J, Bottin H, De Gioia L, Léger C: **The oxidative inactivation of FeFe hydrogenase reveals the flexibility of the H-cluster.** *Nat Chem* 2014, **6**(4):336–342. <http://dx.doi.org/10.1038/nchem.1892>.

57. Kubas A, Orain C, De Sancho D, Saujet L, Sensi M, Gauquelin C, Meynial-Salles I, Soucaille P, Bottin HA, Baffert C, Fourmond V, Best RB, Blumberger J, Léger C: **Mechanism of O<sub>2</sub> diffusion and reduction in FeFe hydrogenases.** *Nat Chem* 2017, **9**(1):88–95. <http://dx.doi.org/10.1038/nchem.2592>.

This article is an illustration of the power of combining kinetic techniques from PFV and theoretical chemistry approaches, here to elucidate all steps in the reaction of O<sub>2</sub> with FeFe hydrogenases.

58. Baffert C, Sybirna K, Ezanno P, Lautier T, Hajj V, Meynial-Salles I, Soucaille P, Bottin H, Léger C: **Covalent attachment of FeFe hydrogenases to carbon electrodes for direct electron transfer.** *Anal Chem* 2012, **84**(18):7999–8005. <http://dx.doi.org/10.1021/ac301812s>.
59. Adamska A, Silakov A, Lambert C, Rüdiger O, Happe T, Reijerse E, Lubitz W: **Identification and characterization of the “super-reduced” state of the H-Cluster in [FeFe] hydrogenase: a new building block for the catalytic cycle?** *Angew Chem Int Ed* 2012, **51**(46):11458–11462. <http://dx.doi.org/10.1002/anie.201204800>.
60. Orain C, Saujet L, Gauquelin C, Soucaille P, Meynial-Salles I, Baffert C, Fourmond V, Bottin H, Léger C: **Electrochemical measurements of the kinetics of inhibition of two FeFe hydrogenases by O<sub>2</sub> demonstrate that the reaction is partly reversible.** *J Am Chem Soc* 2015, **137**(39):12580–12587. <http://dx.doi.org/10.1021/jacs.5b06934>.
61. Brown KA, Wilker MB, Boehm M, Dukovic G, King PW: **Characterization of photochemical processes for H<sub>2</sub> production by CdS nanorod-[FeFe] hydrogenase complexes.** *J Am Chem Soc* 2012, **134**(12):5627–5636. <http://dx.doi.org/10.1021/ja2116348>.
62. Utterback JK, Wilker MB, Brown KA, King PW, Eaves JD, Dukovic G: **Competition between electron transfer, trapping, and recombination in CdS nanorod-hydrogenase complexes.** *Phys Chem Chem Phys: PCCP* 2015, **17**(8):5538–5542. <http://dx.doi.org/10.1039/c4cp05993j>.
63. Wilker MB, Shinopoulos KE, Brown KA, Mulder DW, King PW, Dukovic G: **Electron transfer kinetics in CdS nanorod-[FeFe]-hydrogenase complexes and implications for photochemical H<sub>2</sub> generation.** *J Am Chem Soc* 2014, **136**(11):4316–4324. <http://dx.doi.org/10.1021/ja413001p>.
64. Brown KA, Dayal S, Ai X, Rumbles G, King PW: **Controlled assembly of hydrogenase-CdTe nanocrystal hybrids for solar hydrogen production.** *J Am Chem Soc* 2010, **132**(28):9672–9680. <http://dx.doi.org/10.1021/ja101031r>.
65. Brown KA, Song Q, Mulder DW, King PW: **Diameter dependent electron transfer kinetics in semiconductor-enzyme complexes.** *ACS Nano* 2014, **8**(10):10790–10798. <http://dx.doi.org/10.1021/nn504561v>.
66. Zhao Y, Anderson NC, Ratzloff MW, Mulder DW, Zhu K, Turner JA, Neale NR, King PW, Branz HM: **Proton reduction using a hydrogenase-modified nanoporous black silicon photoelectrode.** *ACS Appl Mater Interf* 2016, **8**(23):14481–14487. <http://dx.doi.org/10.1021/acsami.6b00189>.
67. Morra S, Valetti F, Sarasso V, Castrignanò S, Sadeghi SJ, Gilardi G: **Hydrogen production at high Faradaic efficiency by a bio-electrode based on TiO<sub>2</sub> adsorption of a new [FeFe]-hydrogenase from *Clostridium perfringens*.** *Bioelectrochemistry* 2015, **106**:258–262. <http://dx.doi.org/10.1016/j.bioelechem.2015.08.001>.
68. Parkin A, Cavazza C, Fontecilla-Camps JC, Armstrong FA: **Electrochemical investigations of the interconversions between catalytic and inhibited states of the [FeFe]-hydrogenase from *Desulfovibrio desulfuricans*.** *J Am Chem Soc* 2006, **128**(51):16808–16815. <http://dx.doi.org/10.1021/ja064425i>.
69. Krassen H, Stripp S, von Abendroth G, Ataka K, Happe T, Heberle J: **Immobilization of the [FeFe]-hydrogenase CrHydA1 on a gold electrode: design of a catalytic surface for the production of molecular hydrogen.** *J Biotechnol* 2009, **142**(1):3–9. <http://dx.doi.org/10.1016/j.jbiotec.2009.01.018>.
70. Baffert C, Bertini L, Lautier T, Greco C, Sybirna K, Ezanno P, Etienne E, Soucaille P, Bertrand P, Bottin H, Meynial-Salles I, De Gioia L, Léger C: **CO disrupts the reduced H-cluster of FeFe hydrogenase. A combined DFT and protein film voltammetry study.** *J Am Chem Soc* 2011, **133**(7):2096–2099. <http://dx.doi.org/10.1021/ja110627b>.
71. Butt JN, Filipiak M, Hagen WR: **Direct electrochemistry of *Megasphaera elsdenii* iron hydrogenase—definition of the enzyme’s catalytic operating potential and quantitation of the catalytic behaviour over a continuous potential range.** *FEBS J* 1997, **245**(1):116–122. <http://dx.doi.org/10.1111/j.1432-1033.1997.00116.x>.
72. Sensi M, Baffert C, Greco C, Caserta G, Gauquelin C, Saujet L, Fontecave M, Roy S, Artero V, Soucaille P, Meynial-Salles I, Bottin H, de Gioia L, Fourmond V, Léger C, Bertini L: **Reactivity of the excited states of the H-cluster of FeFe hydrogenases.** *J Am Chem Soc* 2016, **138**(41):13612–13618. <http://dx.doi.org/10.1021/jacs.6b06603>.
73. Ceccaldi P, Schuchmann K, Muller V, Elliott SJ: **The hydrogen dependent CO<sub>2</sub> reductase: the first completely CO tolerant FeFe-hydrogenase.** *Energy Environ Sci* 2017, **10**(2):503–508. <http://dx.doi.org/10.1039/c6ee02494g>.
- This article is one of the demonstrations that studying “non-standard” enzymes, here the FeFe hydrogenase module of the hydrogen dependent carbon dioxide reductase from *Acetobacterium woodii*, can reveal unusual properties, such as higher resistance to irreversible damage by CO in reducing conditions.
74. Blanford C, Armstrong F: **The pyrolytic graphite surface as an enzyme substrate: microscopic and spectroscopic studies.** *J Solid State Electrochem* 2006, **10**(10):826–832. <http://dx.doi.org/10.1007/s10008-006-0183-2>.
75. Fontecilla-Camps JC, Volbeda A, Cavazza C, Nicolet Y: **Structure/function relationships of [NiFe]- and [FeFe]-hydrogenases.** *Chem Rev* 2007, **107**(10):4273–4303. <http://dx.doi.org/10.1021/cr050195z>.
76. Lojou E: **Hydrogenases as catalysts for fuel cells: strategies for efficient immobilization at electrode interfaces.** *Electrochim Acta* 2011, **56**(28):10385–10397. <http://dx.doi.org/10.1016/j.electacta.2011.03.002>.
77. King PW: **Designing interfaces of hydrogenase-nanomaterial hybrids for efficient solar conversion.** *Biochim Biophys Acta* 2013, **1827**(8–9):949–957. <http://dx.doi.org/10.1016/j.bbabi.2013.03.006>.
78. Saboe PO, Conte E, Farrell M, Bazan GC, Kumar M: **Biomimetic and bioinspired approaches for wiring enzymes to electrode interfaces.** *Energy Environ Sci* 2017, **10**(1):14–42. <http://dx.doi.org/10.1039/c6ee02801b>.
79. Radu V, Frielingsdorf S, Evans SD, Lenz O, Jeuken LJC: **Enhanced oxygen-tolerance of the full heterotrimeric membrane-bound [NiFe]-hydrogenase of *Ralstonia eutropha*.** *J Am Chem Soc* 2014, **136**(24):8512–8515. <http://dx.doi.org/10.1021/ja503138p>.
- The oligomeric form of *Ralstonia eutropha* membrane-bound hydrogenase embedded in a planar bilayer lipid membranes tethered to a gold electrode. Electron transfer is mediated by the quinone pool in the membrane. The results of the electrochemical investigation contrast with those obtained with the same enzyme undergoing direct electron transfer with a graphite electrode. In particular, the authors observe a greater resistance to oxidative inactivation.
80. Radu V, Frielingsdorf S, Lenz O, Jeuken LJC: **Reactivation from the Ni-B state in [NiFe] hydrogenase of *Ralstonia eutropha* is controlled by reduction of the superoxidized proximal cluster.** *Chem Commun* 2016, **52**(12):2632–2635. <http://dx.doi.org/10.1039/c5cc10382g>.
81. Jeuken LJ: **Structure and modification of electrode materials for protein electrochemistry.** *Adv Biochem Eng/Biotechnol* 2016. [http://dx.doi.org/10.1007/10\\_2015\\_5011](http://dx.doi.org/10.1007/10_2015_5011).
82. Esselborn J, Lambert C, Adamska-Venkatesh A, Simmons T, Berggren G, Noth J, Siebel J, Hemschemeier A, Artero V, Reijerse E, Fontecave M, Lubitz W, Happe T: **Spontaneous activation of [FeFe]-hydrogenases by an inorganic [2Fe] active site mimic.** *Nat Chem Biol* 2013, **9**(10):607–609. <http://dx.doi.org/10.1038/nchembio.1311>.



83. Khanna N, Esmieu C, Meszaros LS, Lindblad P, Berggren G: **In vivo activation of an [FeFe] hydrogenase using synthetic cofactors.** *Energy Environ Sci* 2017. <http://dx.doi.org/10.1039/c7ee00135e>.
84. Megarity CF, Esselborn J, Hexter SV, Wittkamp F, Apfel U-P, Happe T, Armstrong FA: **Electrochemical investigations of the mechanism of assembly of the active-site H-cluster of [FeFe]-hydrogenases.** *J Am Chem Soc* 2016, **138**(46):15227–15233. <http://dx.doi.org/10.1021/jacs.6b09366>.  
A very original and insightful electrochemical study of H cluster insertion in FeFe hydrogenase.
85. Zhang L, Miranda-Castro R, Stines-Chaumeil C, Mano N, Xu G, Mavr e F, Limoges B: **Heterogeneous reconstitution of the PQQ-dependent glucose dehydrogenase immobilized on an electrode: a sensitive strategy for PQQ detection down to picomolar levels.** *Anal Chem* 2014, **86**(4):2257–2267. <http://dx.doi.org/10.1021/ac500142e>.
86. L ger C, Jones AK, Albracht SP, Armstrong FA: **Effect of a dispersion of interfacial electron transfer rates on steady state catalytic electron transport in [NiFe]-hydrogenase and other enzymes.** *J Phys Chem B* 2002, **106**(50):13058–13063. <http://dx.doi.org/10.1021/jp0265687>.
87. L ger C, Dementin S, Bertrand P, Rousset M, Guigliarelli B: **Inhibition and aerobic inactivation kinetics of *Desulfovibrio fructosovorans* NiFe hydrogenase studied by protein film voltammetry.** *J Am Chem Soc* 2004, **126**(38):12162–12172. <http://dx.doi.org/10.1021/ja046548d>.
88. Hajj V, Baffert C, Sybirna K, Meynial-Salles I, Soucaille P, Bottin H, Fourmond V, Leger C: **FeFe hydrogenase reductive inactivation and implication for catalysis.** *Energy Environ Sci* 2014, **7**(2):715–719. <http://dx.doi.org/10.1039/c3ee42075b>.
89. Fourmond V, Baffert C, Sybirna K, Lautier T, Abou Hamdan A, Dementin S, Soucaille P, Meynial-Salles I, Bottin H, L ger C: **Steady-state catalytic wave-shapes for 2-electron reversible electrocatalysts and enzymes.** *J Am Chem Soc* 2013, **135**(10):3926–3938. <http://dx.doi.org/10.1021/ja311607s>.
90. Fourmond V, L ger C: **Modelling the voltammetry of adsorbed enzymes and molecular catalysts.** *Curr Opin Electrochem* 2017, **1**(1):110–120. <http://dx.doi.org/10.1016/j.coelec.2016.11.002>.  
Comprehensive description of all models proposed to quantitatively interpret the voltammetry of adsorbed enzymes, including hydrogenases.
91. **Cornish-Bowden A, Wiley J: *Fundamentals of Enzyme Kinetics*.** Wiley-Blackwell; 2014.  
A rare textbook to debunk the idea that catalysts must work both ways: “some enzymes are much more effective catalysts for one direction than the other, [although] even after a thorough discussion of this type of behavior [in the 1970s] many biochemists remain rather uneasy about it, suspecting that it may violate the laws of thermodynamics”
92. Gentil S, Lalaoui N, Dutta A, Nedellec Y, Cosnier S, Shaw WJ, Artero V, Le Goff A: **Carbon-nanotube-supported bio-inspired nickel catalyst and its integration in hybrid hydrogen/air fuel cells.** *Angew Chem* 2017, **129**(7):1871–1875. <http://dx.doi.org/10.1002/ange.201611532>.
93. Raleiras P, Khanna N, Miranda H, Meszaros LS, Krassen H, Ho F, Battchikova N, Aro E-M, Magnuson A, Lindblad P, Styring S: **Turning around the electron flow in an uptake hydrogenase. EPR spectroscopy and in vivo activity of a designed mutant in HupSL from *Nostoc punctiforme*.** *Energy Environ Sci* 2016, **9**(2):581–594. <http://dx.doi.org/10.1039/c5ee02694f>.
94. L ger C, Bertrand P: **Direct electrochemistry of redox enzymes as a tool for mechanistic studies.** *Chem Rev* 2008, **108**(7):2379–2438. <http://dx.doi.org/10.1021/cr0680742>.
95. L ger C, Jones AK, Roseboom W, Albracht SP, Armstrong FA: **Enzyme electrokinetics: hydrogen evolution and oxidation by *Allochroamatium vinosum* [NiFe]-hydrogenase.** *Biochemistry* 2002, **41**(52):15736–15746. <http://dx.doi.org/10.1021/bi026586e>.
96. Fourmond V, Baffert C, Sybirna K, Dementin S, Abou-Hamdan A, Meynial-Salles I, Soucaille P, Bottin H, Leger C: **The mechanism of inhibition by H<sub>2</sub> of H<sub>2</sub>-evolution by hydrogenases.** *Chem Commun* 2013, **49**(61):6840–6842. <http://dx.doi.org/10.1039/c3cc43297a>.
97. Hexter SV, Grey F, Happe T, Climent V, Armstrong FA: **Electrocatalytic mechanism of reversible hydrogen cycling by enzymes and distinctions between the major classes of hydrogenases.** *Proc Natl Acad Sci USA* 2012, **109**(29):11516–11521. <http://dx.doi.org/10.1073/pnas.1204770109>.
98. Murphy BJ, Sargent F, Armstrong FA: **Transforming an oxygen-tolerant [NiFe] uptake hydrogenase into a proficient, reversible hydrogen producer.** *Energy Environ Sci* 2014, **7**(4):1426–1433. <http://dx.doi.org/10.1039/c3ee43652g>.
99. L ger C, Lederer F, Guigliarelli B, Bertrand P: **Electron flow in multicenter enzymes: theory, applications, and consequences on the natural design of redox chains.** *J Am Chem Soc* 2006, **128**(1):180–187. <http://dx.doi.org/10.1021/ja055275z>.
100. Wombwell C, Caputo CA, Reiser E: **[NiFeSe]-hydrogenase chemistry.** *Acc Chem Res* 2015, **48**(1):2858–2865. <http://dx.doi.org/10.1021/acs.accounts.5b00326>.
101. Flanagan LA, Parkin A: **Electrochemical insights into the mechanism of NiFe membrane-bound hydrogenases.** *Biochem Soc Trans* 2016, **44**(1):315–328. <http://dx.doi.org/10.1042/BST20150201>.
102. Dementin S, Leroux F, Cournac L, Lacey AL, Volbeda A, L ger C, Burlat B, Martinez N, Champ S, Martin L, Sanganas O, Haumann M, Fern andez VM, Guigliarelli B, Fontecilla-Camps JC, Rousset M: **Introduction of methionines in the gas channel makes [NiFe] hydrogenase aero-tolerant.** *J Am Chem Soc* 2009, **131**(29):10156–10164. <http://dx.doi.org/10.1021/ja9018258>.
103. Liebgott P-P, de Lacey AL, Burlat B, Cournac L, Richaud P, Brugna M, Fernandez VM, Guigliarelli B, Rousset M, L ger C, Dementin S: **Original design of an oxygen-tolerant [NiFe] hydrogenase: major effect of a valine-to-cysteine mutation near the active site.** *J Am Chem Soc* 2011, **133**(4):986–997. <http://dx.doi.org/10.1021/ja108787s>.
104. Abou Hamdan A, Dementin S, Liebgott P-P, Gutierrez-Sanz O, Richaud P, De Lacey AL, Rousset M, Bertrand P, Cournac L, L ger C: **Understanding and tuning the catalytic bias of hydrogenase.** *J Am Chem Soc* 2012, **134**(20):8368–8371. <http://dx.doi.org/10.1021/ja301802r>.
105. Dementin S, Belle V, Bertrand P, Guigliarelli B, Adryanczyk-Perrier G, De Lacey AL, Fernandez VM, Rousset M, L ger C: **Changing the ligation of the distal [4Fe4S] cluster in NiFe hydrogenase impairs inter- and intramolecular electron transfers.** *J Am Chem Soc* 2006, **128**(15):5209–5218. <http://dx.doi.org/10.1021/ja060233b>.
106. Flanagan LA, Wright JJ, Roessler MM, Moir JW, Parkin A: **Re-engineering a NiFe hydrogenase to increase the H<sub>2</sub> production bias while maintaining native levels of O<sub>2</sub> tolerance.** *Chem Commun* 2016, **52**(58):9133–9136. <http://dx.doi.org/10.1039/c6cc00515b>.
107. Adamson H, Robinson M, Wright JJ, Flanagan LA, Walton J, Elton D, Gavaghan DJ, Bond AM, Roessler MM, Parkin A: **Re-tuning the catalytic bias and overpotential of a [NiFe]-hydrogenase via a single amino acid exchange at the electron entry/exit site.** *J Am Chem Soc* 2017. <http://dx.doi.org/10.1021/jacs.7b03611>.  
Fourier transformed alternating current voltammetry is used to detect and measure the potential of the distal FeS cluster in *E. coli* hydrogenase.
108. Jones AK, Lamle SE, Pershad HR, Vincent KA, Albracht SP, Armstrong FA: **Enzyme electrokinetics: electrochemical studies of the anaerobic interconversions between active and inactive states of *Allochroamatium vinosum* [NiFe]-hydrogenase.** *J Am Chem Soc* 2003, **125**(28):8505–8514. <http://dx.doi.org/10.1021/ja035296y>.
109. Greco C, Fourmond V, Baffert C, Wang P-h, Dementin S, Bertrand P, Bruschi M, Blumberger J, de Gioia L, Leger C: **Combining experimental and theoretical methods to learn**

- about the reactivity of gas-processing metalloenzymes.** *Energy Environ Sci* 2014, **7**(11):3543–3573. <http://dx.doi.org/10.1039/c4ee01848f>.
110. Chen K, Hirst J, Camba R, Bonagura CA, Stout CD, Burgess BK, Armstrong FA: **Atomically defined mechanism for electron-coupled proton transfer to a buried redox centre in a protein.** *Nature* 2000, **405**:814–817. <http://dx.doi.org/10.1038/35015610>.
111. Wait AF, Brandmayr C, Stripp ST, Cavazza C, Fontecilla-Camps JC, Happe T, Armstrong FA: **Formaldehyde—a rapid and reversible inhibitor of hydrogen production by [FeFe]-hydrogenases.** *J Am Chem Soc* 2011, **133**(5):1282–1285. <http://dx.doi.org/10.1021/ja110103p>.
112. Foster CE, Krämer T, Wait AF, Parkin A, Jennings DP, Happe T, McGrady JE, Armstrong FA: **Inhibition of [FeFe]-hydrogenases by formaldehyde and wider mechanistic implications for biohydrogen activation.** *J Am Chem Soc* 2012, **134**(17):7553–7557. <http://dx.doi.org/10.1021/ja302096r>.
113. Bachmeier A, Esselborn J, Hexter SV, Krämer T, Klein K, Happe T, McGrady JE, Myers WK, Armstrong FA: **How formaldehyde inhibits hydrogen evolution by [FeFe]-hydrogenases: determination by <sup>13</sup>C ENDOR of direct Fe–C coordination and order of electron and proton transfers.** *J Am Chem Soc* 2015, **137**(16):5381–5389. <http://dx.doi.org/10.1021/ja513074m>.
114. Leroux F, Dementin S, Burlat B, Cournac L, Volbeda A, Champ S, Martin L, Guigliarelli B, Bertrand P, Fontecilla-Camps J, Rousset M, Léger C: **Experimental approaches to kinetics of gas diffusion in hydrogenase.** *Proc Natl Acad Sci USA* 2008, **105**(32):11188–11193. <http://dx.doi.org/10.1073/pnas.0803689105>.
115. Wang P-H, Blumberger J: **Mechanistic insight into the blocking of CO diffusion in [NiFe]-hydrogenase mutants through multiscale simulation** 2012, **109**(17):6399–6404. <http://dx.doi.org/10.1073/pnas.1121176109>.
116. Millo D, Hildebrandt P, Pandelia M-E, Lubitz W, Zebger I: **SEIRA spectroscopy of the electrochemical activation of an immobilized [NiFe] hydrogenase under turnover and non-turnover conditions.** *Angew Chem Int Ed* 2011, **50**(11):2632–2634. <http://dx.doi.org/10.1002/anie.201006646>.
117. Sezer M, Millo D, Weidinger IM, Zebger I, Hildebrandt P: **Analyzing the catalytic processes of immobilized redox enzymes by vibrational spectroscopies.** *IUBMB Life* 2012, **64**(6):455–464. <http://dx.doi.org/10.1002/iub.1020>.
118. Ash PA, Hidalgo R, Vincent KA: **Proton transfer in the catalytic cycle of [NiFe] hydrogenases: insight from vibrational spectroscopy.** *ACS Catal* 2017, **7**(4):2471–2485. <http://dx.doi.org/10.1021/acscatal.6b03182>.
119. Murphy BJ, Hidalgo R, Roessler MM, Evans RM, Ash PA, Myers WK, Vincent KA, Armstrong FA: **Discovery of dark pH-dependent H<sup>+</sup> migration in a [NiFe]-hydrogenase and its mechanistic relevance: mobilizing the hydrido ligand of the Ni–C intermediate.** *J Am Chem Soc* 2015, **137**(26):8484–8489. <http://dx.doi.org/10.1021/jacs.5b03182>.
120. Ash PA, Liu J, Coutard N, Heidary N, Horch M, Gudim I, Simler T, Zebger I, Lenz O, Vincent KA: **Electrochemical and infrared spectroscopic studies provide insight into reactions of the NiFe regulatory hydrogenase from *Ralstonia eutropha* with O<sub>2</sub> and co.** *J Phys Chem B* 2015, **119**(43):13807–13815. <http://dx.doi.org/10.1021/acs.jpcc.5b04164>.
121. Roseboom W, De Lacey A, Fernandez V, Hatchikian, Albracht S: **The active site of the [FeFe]-hydrogenase from *Desulfovibrio desulfuricans*. II. Redox properties, light sensitivity and CO-ligand exchange as observed by infrared spectroscopy.** *J Biol Inorg Chem* 2006, **11**(1):102–118. <http://dx.doi.org/10.1007/s00775-005-0040-2>.
122. Rodríguez-Maciá P, Birrell JA, Lubitz W, Rüdiger O: **Electrochemical investigations on the inactivation of the [FeFe] hydrogenase from *desulfovibrio desulfuricans* by O<sub>2</sub> or light under hydrogen-producing conditions.** *ChemPlusChem* 2017, **82**(4):540–545. <http://dx.doi.org/10.1002/cplu.201600508>.
123. Sensi M, Baffert C, Fradale L, Gauquelin C, Soucaille P, Meynial-Salles I, Bottin H, de Gioia L, Bruschi M, Fourmond V, Léger C, Bertini L: **Photoinhibition of FeFe hydrogenase.** *ACS Catalysis* 2017 in press. <http://dx.doi.org/10.1021/acscatal.7b02252>.
- The comparison herein of the available data show that not all FeFe hydrogenases can actually be combined with photosensitizers that utilise the solar spectrum: further investigations of the compatibility of hydrogenases or hydrogenase mimics with light-harvesting systems should also consider the possibility of irreversible photoinhibition.
124. Ciaccafava A, Hamon C, Infossi P, Marchi V, Giudici-Ortoniconi M-T, Lojou E: **Light-induced reactivation of O<sub>2</sub>-tolerant membrane-bound [Ni–Fe] hydrogenase from the hyperthermophilic bacterium *Aquifex aeolicus* under turnover conditions.** *Phys Chem Chem Phys* 2013, **15**(39):16463–16467. <http://dx.doi.org/10.1039/c3cp52596a>.
- This article demonstrates that purple light activates the oxidized, inactive forms of an O<sub>2</sub>-tolerant NiFe hydrogenase.
125. Hambourger M, Moore GF, Kramer DM, Gust D, Moore AL, Moore TA: **Biology and technology for photochemical fuel production.** *Chem Soc Rev* 2009, **38**(1):25–35. <http://dx.doi.org/10.1039/b800582f>.
126. Reisner E: **Solar hydrogen evolution with hydrogenases: from natural to hybrid systems.** *Eur J Inorg Chem* 2011, **2011**(7):1005–1016. <http://dx.doi.org/10.1002/ejic.201000986>.
127. Woolerton TW, Sheard S, Chaudhary YS, Armstrong FA: **Enzymes and bio-inspired electrocatalysts in solar fuel devices.** *Energy Environ Sci* 2012, **5**(6):7470–7490. <http://dx.doi.org/10.1039/c2ee21471g>.
128. Reeve HA, Ash PA, Park H, Huang A, Posidias M, Tomlinson C, Lenz O, Vincent KA: **Enzymes as modular catalysts for redox half-reactions in H<sub>2</sub>-powered chemical synthesis: from biology to technology.** *Biochem J* 2017, **474**(2):215–230. <http://dx.doi.org/10.1042/bcj20160513>.
- A very recent review that describes the applications of hydrogenases. See also refs. [77, 125–127].

## Chapter 3

# Aerobic oxidative inactivation in FeFe hydrogenases

### 3.1 Summary

The aerobic oxidative inactivation has always been one of the main topics of hydrogenase research (section 1.7). The reason for this is that the sensitivity to oxygen impedes the exploitation of hydrogenases for the production of  $H_2$ , which is an energy carrier. The group of Christophe Léger previously demonstrated that the inhibition of FeFe-hydrogenases by  $O_2$  is partially reversible.<sup>88,92</sup> The aerobic inactivation begins with the diffusion of oxygen within the enzyme, then near the active site a geminate state is formed (oxygen is not bound to distal iron, yet) and finally oxygen binds to the active site, forming an inactive state. This state can reactivate or irreversibly form an inactive species. Two hypothesis have been proposed to explain the mechanism of irreversible inactivation at the active site. In both mechanisms the first step is the binding of oxygen to the distal iron. The proposed second steps are the formation of ROS that destroys the  $[4Fe4S]_H$  cluster<sup>90,91</sup> or the degradation of the  $[2Fe]_H$  site.<sup>25</sup> No hypothesis has been made on the nature of the reversibly formed species. To fully explain all the steps of the inhibition of FeFe-hydrogenases by  $O_2$ , we used PFV experiments, MD simulations and DFT calculations.

Atomistic molecular dynamics allowed to simulate the diffusion of oxygen from the surface to the active site of CpI. We found two putative gas channels, which converge near the distal iron. Using a Markov state model, we estimated the rate constant of oxygen diffusion in the channels, which, combined with the rate constants of binding and release of  $O_2$  calculated by DFT, showed a good agreement with the values measured by protein film voltammetry. From the analysis of MD simulations, we suggested that modifications of the lateral chains of some residues in the gas channels could affect the rate of gas diffusion. Indeed, we observed that their mutation results in a decrease in the rate of binding and release of CO in PFV experiments. We performed MD simulations with a model of CpI with the same mutations as above and we showed that the mutated residues slow down the formation of the geminate state, explaining the experimental data. PFV experiment showed that the rate of reactivation depends on potential and pH, demonstrating that this process involves protons and electrons and cannot consist in the simple release of

O<sub>2</sub> from the active site. With DFT calculations we obtained a mechanism for both reversible and irreversible aerobic inactivations. We proposed that the reactivation consists in the reduction of oxygen to water and that this reaction depends on the availability of electrons. We finally proposed that the irreversible inactivation is due to the oxidation of a cysteine involved in the proton transfer chain and/or to the release of free hydroxyl radicals, which damage the active site.

This study paves the way to the design and study of new O<sub>2</sub>-resistant FeFe-hydrogenases mutants.

My contributions to this study are the PFV experiments performed on the mutants of CrHydA1 and shown in panels d, e and f of figure 2.

## 3.2 Résumé

L'inactivation aérobie a toujours été l'un des principaux sujets de recherche sur l'hydrogénase (sous-section 1.7). La raison en est que la sensibilité à l'oxygène empêche l'utilisation des hydrogénases pour la production de  $H_2$ , qui est un vecteur d'énergie. Le groupe de Christophe Léger a précédemment démontré que l'inhibition de hydrogenases-FeFe par  $O_2$  est partiellement réversible.<sup>88,92</sup> L'inactivation aérobie commence par la diffusion de l'oxygène dans l'enzyme, puis, à proximité du site actif, un état geminé est formé (l'oxygène n'est pas lié au fer distal) et enfin l'oxygène se lie au site actif, conduisant à un état inactif. Cet état peut se réactiver ou former irréversiblement une espèce inactive. Deux hypothèses ont été proposées pour expliquer le mécanisme d'inactivation aérobie du site actif. Dans les deux mécanismes, la première étape est la liaison de l'oxygène sur le fer distal. Les deuxièmes étapes proposées sont la formation de ROS qui détruisent le cluster  $[4Fe4S]_H$ <sup>90,91</sup> ou la dégradation du site  $[2Fe]_H$ .<sup>25</sup> Aucune hypothèse n'a été faite sur la nature des espèces formées réversiblement. Pour expliquer complètement toutes les étapes de l'inhibition des hydrogenases-FeFe par  $O_2$ , nous avons réalisé des expériences PFV, des simulations MD et des calculs DFT pour étudier cette réaction.

Des calculs de dynamique moléculaire atomique ont permis de simuler la diffusion de l'oxygène de la surface de la protéine jusqu'au le site actif de CpI. Nous avons trouvé deux canaux de gaz putatifs, qui convergent vers le fer distal. En utilisant un modèle de Markov, nous avons estimé la constante de vitesse de la diffusion de l'oxygène dans les canaux, ce qui, combiné avec les constantes de vitesse de liaison et de libération de  $O_2$  calculé par DFT, a montré un bon accord avec les valeurs mesurées par électrochimie directe. Les simulations de MD ont suggéré que les modifications des chaînes latérales de certains résidus dans les canaux de gaz pourraient affecter la vitesse de diffusion du gaz. Nous avons observé que leur remplacement effectivement a entraîné en une diminution du vitesse de liaison et de libération de  $CO$  dans des expériences de PFV avec les deux mutants. Nous avons effectué des simulations de MD avec un modèle de CpI avec les mêmes mutations que ci-dessus et nous avons montré que les mutations ralentissaient la formation

de l'état geminé, en expliquant les données expérimentales. Les expériences de PFV ont montré que les vitesses de réactivation dépendent du potentiel et du pH, ce qui démontre que ce processus implique des protons et des électrons et ne peut pas être dû simplement à la libération de l' $O_2$  du site actif. À partir des calculs DFT, nous avons déterminé un mécanisme pour les inactivations aérobies réversibles et irréversibles. Nous avons proposé que la réactivation implique la réduction du dioxygène en eau et que cette réaction dépend de la disponibilité des électrons. Nous avons finalement proposé que l'inactivation irréversible est due à l'oxydation d'une cystéine impliquée dans la chaîne de transfert de protons et/ou à la libération de radicaux hydroxylés qui endommagent le site actif.

Cette étude ouvre la voie à la conception et à l'étude de nouveaux mutants FeFe-hydrogenases résistant à  $O_2$ .

Mes contributions à cette étude sont les expériences de PFV effectuées sur les mutants de CrHydA1 et montrées dans les panneaux d, e et f de la figure 2.

# Mechanism of O<sub>2</sub> diffusion and reduction in FeFe hydrogenases

Adam Kubas<sup>1,2†</sup>, Christophe Orain<sup>3†</sup>, David De Sancho<sup>4,5,6†</sup>, Laure Saujet<sup>7,8</sup>, Matteo Sensi<sup>3</sup>, Charles Gauquelin<sup>9</sup>, Isabelle Meynial-Salles<sup>9</sup>, Philippe Soucaille<sup>9</sup>, Hervé Bottin<sup>7,8</sup>, Carole Baffert<sup>3</sup>, Vincent Fourmond<sup>3</sup>, Robert B. Best<sup>10</sup>, Jochen Blumberger<sup>1\*</sup> and Christophe Léger<sup>3\*</sup>

**FeFe hydrogenases are the most efficient H<sub>2</sub>-producing enzymes. However, inactivation by O<sub>2</sub> remains an obstacle that prevents them being used in many biotechnological devices. Here, we combine electrochemistry, site-directed mutagenesis, molecular dynamics and quantum chemical calculations to uncover the molecular mechanism of O<sub>2</sub> diffusion within the enzyme and its reactions at the active site. We propose that the partial reversibility of the reaction with O<sub>2</sub> results from the four-electron reduction of O<sub>2</sub> to water. The third electron/proton transfer step is the bottleneck for water production, competing with formation of a highly reactive OH radical and hydroxylated cysteine. The rapid delivery of electrons and protons to the active site is therefore crucial to prevent the accumulation of these aggressive species during prolonged O<sub>2</sub> exposure. These findings should provide important clues for the design of hydrogenase mutants with increased resistance to oxidative damage.**

One of the grand scientific challenges facing society is the design of cheap catalysts for the efficient production and oxidation of carbon-neutral energy carriers such as molecular hydrogen. A very promising perspective in this regard is to harness the catalytic power of NiFe and FeFe hydrogenases, the enzymes that have evolved over millions of years to produce and oxidize H<sub>2</sub> (ref. 1). Living microorganisms that express hydrogenases, or purified hydrogenases, could be used in this context. These highly efficient enzymes are also an invaluable source of inspiration for inorganic chemists to design synthetic mimics.

However, a major obstacle to using either type of hydrogenase is their sensitivity to oxidation, and the characterization of their inactivation by O<sub>2</sub> has become a major field of research<sup>2</sup>. NiFe hydrogenases that naturally resist O<sub>2</sub> have recently been identified<sup>3,4</sup>, and attempts to increase the resistance of O<sub>2</sub>-sensitive NiFe hydrogenases have been partially successful<sup>5</sup>. A different solution is to incorporate the enzyme into a redox polymer film that provides a self-activated O<sub>2</sub> shield<sup>6,7</sup>, but it is unknown whether this strategy can protect the enzyme under conditions of reductive catalysis.

This Article deals with FeFe hydrogenases, which are more active for H<sub>2</sub> production and less inhibited by H<sub>2</sub> than NiFe hydrogenases<sup>8</sup>. Their active site, the 'H-cluster', consists of a [Fe<sub>2</sub>(CO)<sub>3</sub>(CN)<sub>2</sub>(dithiomethylamine)] subsite<sup>9–12</sup> covalently bound to a 4Fe4S subcluster. Figure 1a shows the structure of the bidirectional FeFe hydrogenase 1 from *Clostridium pasteurianum* (*Cp*), a structural homologue of the FeFe hydrogenase from *Clostridium acetobutylicum* (*Ca*)<sup>9</sup>, which covalently binds four FeS clusters in addition to the H-cluster. The enzyme from the photosynthetic organism *Chlamydomonas reinhardtii* (*Cr*) has no cofactor other

than the H-cluster<sup>13</sup>. Due to the sensitivity of FeFe hydrogenases to molecular oxygen, understanding the mechanism of O<sub>2</sub> inhibition is a prerequisite for using genetic engineering to increase their O<sub>2</sub> tolerance. This is crucial in the case of the enzyme from *Cr*, because this green alga could be used for biological H<sub>2</sub> photoproduction<sup>14</sup> if its hydrogenases were less inhibited by the O<sub>2</sub> produced by photosynthesis.

Aerobic inhibition of FeFe hydrogenase involves the diffusion of O<sub>2</sub> through the protein<sup>15</sup> and its initial attack on the vacant site on the Fe that is remote from the cubane (the so-called distal iron, Fe<sub>d</sub>; Fig. 1b)<sup>16–20</sup>. Quantum chemical calculations rule out outer-sphere electron transfer to O<sub>2</sub> (ref. 20), but what happens after O<sub>2</sub> attachment is unclear. According to X-ray absorption measurements, exposing the enzyme from *Cr* to O<sub>2</sub> damages the 4Fe4S subcluster; this suggests that O<sub>2</sub> binding to Fe<sub>d</sub> results in the formation of a reactive oxygen species (ROS) that diffuses towards the 4Fe4S subcluster and destroys it<sup>18,21</sup>. According to the density functional theory (DFT) studies of Reiher<sup>22,23</sup> and Pachter<sup>24</sup>, this ROS could be the OOH radical or H<sub>2</sub>O<sub>2</sub>. However, the mechanism in refs 18 and 21 conflicts with a recent report, according to which the O<sub>2</sub>-damaged enzyme from *Cr* harbours an intact 4Fe4S subsite and no 2Fe subcluster, and the observation that the O<sub>2</sub>-damaged enzyme is repaired on insertion of a synthetic analogue of the 2Fe subcluster<sup>25</sup>.

Protein film electrochemistry (whereby the enzyme is adsorbed onto an electrode and electron transfer is direct) has been useful for characterizing the kinetics of aerobic inhibition of hydrogenases, because the activity can be recorded as a current while the enzyme is exposed to controlled 'bursts' of oxygen<sup>16,17</sup>. Figure 1c shows the response of *Ca* and *Cr* hydrogenases to pulses of O<sub>2</sub>. The activity

<sup>1</sup>Department of Physics and Astronomy, University College London, Gower Street, London WC1E 6BT, UK. <sup>2</sup>Institute of Physical Chemistry, Polish Academy of Science, ul. Kasprzaka 44/52, 01-224 Warsaw, Poland. <sup>3</sup>Aix Marseille Univ, CNRS, Laboratoire de Bioénergétique et Ingénierie des Protéines, Institut de Microbiologie de la Méditerranée, Marseille, France. <sup>4</sup>Department of Chemistry, University of Cambridge, Lensfield Road, Cambridge CB2 1EW, UK.

<sup>5</sup>CIC nanoGUNE, Tolosa Hiribidea 76, 20018 Donostia-San Sebastián, Spain. <sup>6</sup>IKERBASQUE; Basque Foundation for Science, María Díaz de Haro 3, 48013 Bilbao, Spain. <sup>7</sup>Institut de Biologie et de Technologies de Saclay IBITECS, SB2SM, F-91191 Gif sur Yvette, France. <sup>8</sup>Institut de Biologie Intégrative de la Cellule I2BC, UMR 9198, CEA, CNRS, Université Paris Sud, F-91191 Gif sur Yvette, France. <sup>9</sup>Université de Toulouse, INSA, UPS, INP, LISBP, INRA:UMR792, CNRS: UMR 5504, 135 avenue de Rangueil, Toulouse 31077 Cedex 04, France. <sup>10</sup>Laboratory of Chemical Physics, National Institute of Diabetes and Digestive and Kidney Diseases, National Institutes of Health, Bethesda, Maryland 20892-0520, USA; <sup>†</sup>These authors contributed equally to this work.

\*e-mail: j.blumberger@ucl.ac.uk; christophe.leger@imm.cnrs.fr



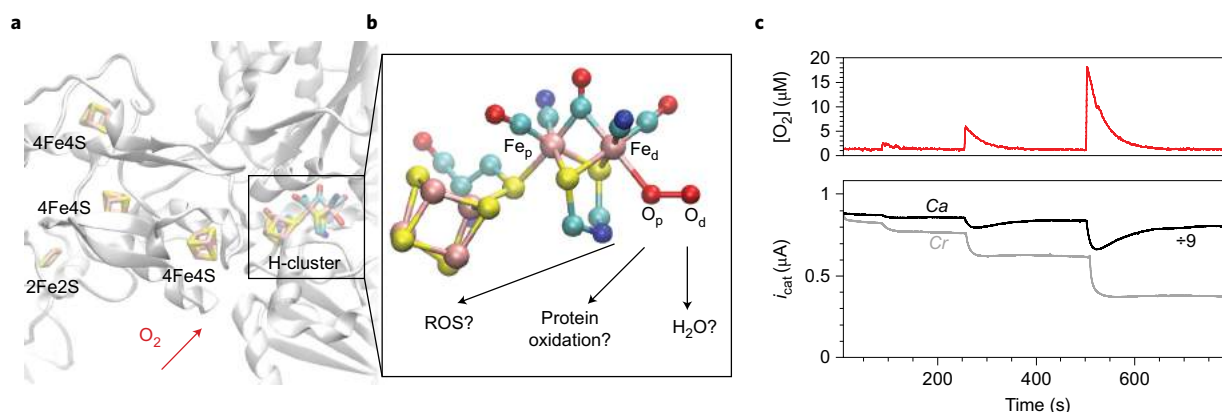


**Figure 1 | FeFe hydrogenase and its inhibition by O<sub>2</sub>.** **a**, Crystal structure of FeFe hydrogenase from *Clostridium pasteurianum* (*Cp*, PDB 3C8Y), a structural homologue of *Ca* FeFe hydrogenase. The protein backbone is shown in cartoon representation and the FeS- and H-clusters in licorice representation. Colour code: Fe, pink; S, yellow; O, red; N, blue; C, cyan. **b**, Enlarged view of the H-cluster with O<sub>2</sub> bound to the distal iron, Fe<sub>d</sub> and a nitrogen atom in the dithiomethyl bridge<sup>9–12</sup>. Possible reaction products are indicated, ROS: reactive oxygen species (for example, O<sub>2</sub>H, H<sub>2</sub>O<sub>2</sub> or OH). **c**, *Ca* and *Cr* FeFe hydrogenase behaviour on exposure to O<sub>2</sub>. Top: instantaneous O<sub>2</sub> concentration. Bottom: catalytic H<sub>2</sub>-oxidation current versus time for *Ca* (black) and *Cr* (grey) FeFe hydrogenases (*T* = 12 °C, 1 bar H<sub>2</sub>, pH 7, data reproduced from ref. 16).

of *Ca* hydrogenase is mostly recovered after a brief exposure to O<sub>2</sub>, but the enzyme is irreversibly inactivated by prolonged exposure to O<sub>2</sub>. The enzyme from *Cr* is inhibited more strongly and less reversibly than that from *Ca*, but we have recently demonstrated that the mechanism of inhibition for both enzymes is described by the same kinetic scheme<sup>16</sup>:



The active enzyme **A** reacts with O<sub>2</sub> (second-order rate constant  $k_i$ ) to form an inactive species **I** that either reverses to **A** (first-order rate constant  $k_a$ ) or irreversibly transforms into a dead-end, irreversibly inactivated species **D** ( $k_3$ ).

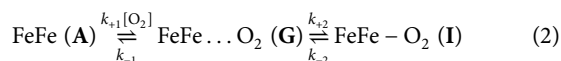
Here, we examine how the above-defined rate constants depend on electrode potential, pH, replacement of H<sub>2</sub>O with D<sub>2</sub>O, and protein mutations. We combine this experimental information with the results of theoretical chemistry calculations<sup>26</sup>—molecular dynamics (MD) simulation and Markov state modelling of O<sub>2</sub> diffusion in the enzyme to the active site, as well as DFT calculations for the characterization of the reaction products—to deduce the molecular mechanism of each step in the above kinetic scheme.

## Results

We used the method described in ref. 16 to examine how the kinetics of the inhibition of FeFe hydrogenase by O<sub>2</sub> depends on the experimental conditions. Figure 2 presents raw electrochemical data, and Fig. 3 summarizes the changes in  $k_i$ ,  $k_a$  and  $k_3$  (defined in equation (1)) against electrode potential  $E$ , for experiments performed in H<sub>2</sub>O at three pH values and one set of experiments performed with the enzyme oxidizing D<sub>2</sub> in D<sub>2</sub>O at pD 7.

### Initial O<sub>2</sub> attack (rate constant $k_i$ )

Figure 3a shows that the second-order rate constant of O<sub>2</sub> binding,  $k_i$ , is independent of  $E$  and pH (it increases less than twofold over two pH units), with no significant isotope effect, consistent with  $k_i$  simply describing the diffusion of O<sub>2</sub> through the protein and its binding at the active site. The rate  $k_i$  of conversion from **A** to **I** in equation (1) can be calculated from the rate constants in the following scheme<sup>27,28</sup>:



Above,  $k_{+1}$  is the second-order rate constant for the diffusion of O<sub>2</sub> from the solvent to the active site, and  $k_{-1}$  is the first-order rate constant for diffusion in the opposite direction. In the resulting state **G** (for ‘Geminate’), O<sub>2</sub> is in the active site pocket but it is not yet chemically bound to the active site. The formation and breaking of the chemical bond is described by the first-order rate constants  $k_{+2}$  and  $k_{-2}$ , respectively. As shown in Supplementary Section 1 and refs 26 and 27, the measured rate constant  $k_i$  is related to the rate constants in equation (2) by

$$k_i = \frac{k_{+1}k_{+2}}{k_{-1} + k_{+2}} \quad (3)$$

We have previously investigated the chemical binding of O<sub>2</sub> to the H-cluster and determined a binding free energy of  $-7.1 \text{ kcal mol}^{-1}$  and an activation free energy of  $12.9 \text{ kcal mol}^{-1}$  from quantum chemical calculations<sup>20</sup>; this gives  $k_{+2} = 2.2 \times 10^3 \text{ s}^{-1}$  and  $k_{-2} = 1.4 \times 10^{-2} \text{ s}^{-1}$  at  $T = 298 \text{ K}$ . The value of  $k_{+2}$  is three orders of magnitude larger than the experimental (pseudo-first order) inhibition rate at typical ligand concentrations of 1 mM,  $k_i \times 1 \text{ mM}$ , indicating that intraprotein diffusion is an essential part of the binding kinetics.

We obtained the pathways of intraprotein O<sub>2</sub> diffusion from atomistic MD simulations of *Cp* FeFe hydrogenase (for which a high-quality X-ray structure is available<sup>9</sup>) in the presence of O<sub>2</sub> molecules. We calculated the corresponding diffusion rate constants  $k_{\pm 1}$  by careful analysis of the atomistic dynamics based on a Markov state model (MSM)<sup>29,30</sup>. In the MSM, the access of O<sub>2</sub> to the H-cluster is described as a series of discrete jumps, from the solvent to protein cavities and between protein cavities. The dynamics of hopping between these cavities is given by a kinetic master equation with transition rate constants obtained from the MD data (see Methods and Supplementary Section 2 for details). Figure 4a shows the structure of the *Cp* FeFe hydrogenase, the microstates obtained from the MSM and the two pathways (1 and 2) with the highest diffusive flux towards the active site. The dominant path (1) was also identified by Schulten and co-workers as the most important access tunnel (‘pathway A’ in ref. 15). Diffusion along pathway 2 is less likely to occur, as the gas molecule needs to get around the sidechain of F417 (Fig. 4b and Supplementary Fig. 3). The bottleneck for ligand diffusion along the dominant pathway 1 is the last transition, involving the jump from site 7 to the geminate site. Only when thermal fluctuations increase the distance between Cys299–Pro324 and Cys299–F417 is the passage of O<sub>2</sub> into

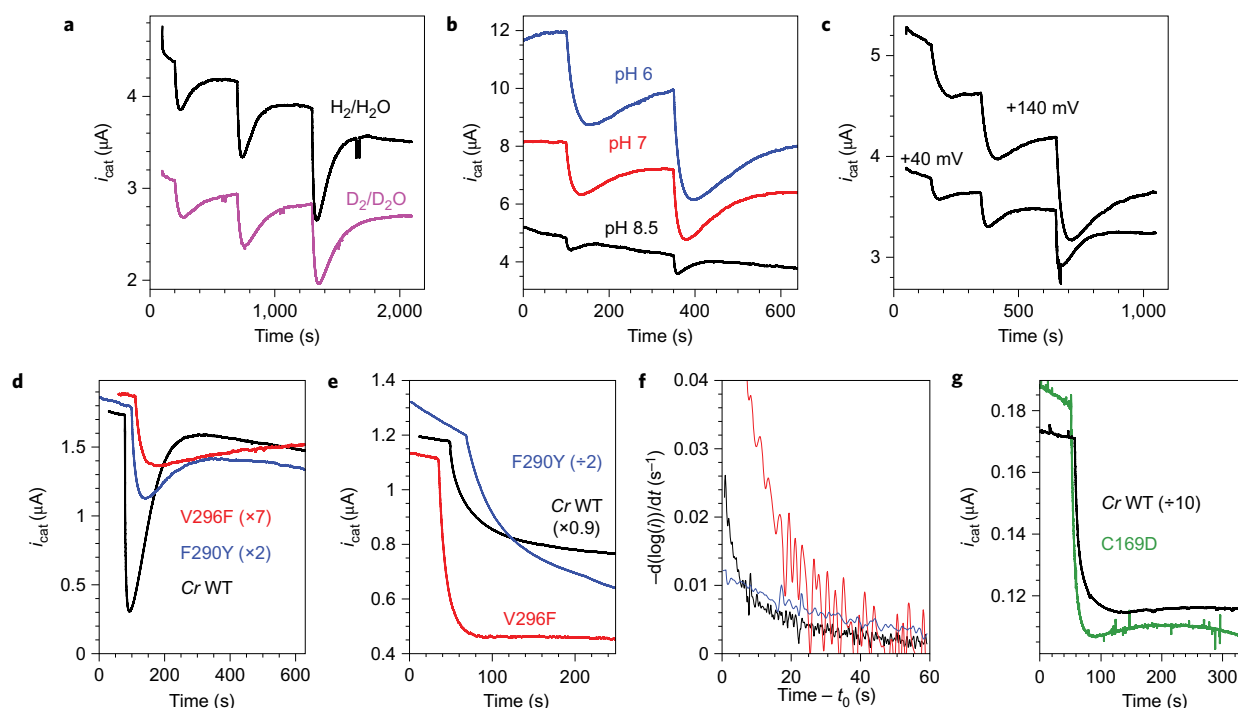


**Figure 2 | Change in catalytic H<sub>2</sub>-oxidation current versus time. a–g,** *Ca* (a–c) or *Cr* (d–g) FeFe hydrogenases were exposed to ‘bursts’ of CO (d) or O<sub>2</sub> (all other panels). Data were not corrected. ‘×’ and ‘÷’ indicate normalization factors. In these experiments, the absolute magnitude of the current should not be interpreted because it depends on the electroactive coverage, which is both unknown and variable. **a**, Effect of H/D exchange on the inhibition of WT *Ca* FeFe hydrogenase by O<sub>2</sub> at pH or pD 7.1. **b**, Effect of pH on the inhibition of WT *Ca* FeFe hydrogenase by O<sub>2</sub>. **c**, Effect of electrode potential on the inhibition of WT *Ca* FeFe hydrogenase by O<sub>2</sub>. **d**, Effect of F290Y and V296F substitutions on the inhibition of *Cr* FeFe hydrogenase by CO. **e**, Effect of F290Y and V296F substitutions on the inhibition of *Cr* FeFe hydrogenase by O<sub>2</sub>. **f**, The same data as in **e**, but in a plot of  $-d(\log(i))/dt$  against time after injection of O<sub>2</sub>, giving the instantaneous rate constant of inactivation at the time of injection of O<sub>2</sub> (ref. 33). **g**, Effect of C169D substitution on inhibition of *Cr* FeFe hydrogenase by O<sub>2</sub>. See Supplementary Section 5.1 for detailed experimental conditions.

the active site possible (Fig. 4c), but these events are rare. From the MSM we obtain the values  $k_{+1} = 3.0 \pm 1.8 \times 10^3 \text{ s}^{-1} \text{ mM}^{-1}$  and  $k_{-1} = 7.7 \pm 0.3 \times 10^7 \text{ s}^{-1}$  (Supplementary Fig. 6b). Combining  $k_{+1}$ ,  $k_{-1}$  and  $k_{+2}$  according to equation (3), we calculate  $k_i = 8.6 \pm 5.1 \times 10^{-2} \text{ s}^{-1} \text{ mM}^{-1}$ . The 13-fold difference from the measured  $k_i$  ( $1.1 \text{ s}^{-1} \text{ mM}^{-1}$ ) represents good agreement, considering that besides the statistical uncertainties quoted, each of the contributing rate coefficients  $k_{+1}$ ,  $k_{-1}$  and  $k_{+2}$  includes systematic errors due to approximations in the underlying computational models.

The molecular-scale picture of the diffusion process obtained from MD simulation of the *Cp* hydrogenase is supported by the experimental results in Fig. 2d, showing the binding of the competitive inhibitor CO to wild-type (WT) and mutant forms of the structurally homologous *Cr* hydrogenase. (CO binds reversibly to Fe<sub>d</sub> under oxidizing conditions<sup>31</sup>.) Replacing V423 (*Cp* numbering, *Cr* V296) (Fig. 4b) with a phenylalanine, or F417 (*Cp* numbering, *Cr* F290) with a tyrosine, significantly decreases the rates of CO binding and release: from  $k_i^{\text{CO}} = 60 \pm 15 \text{ s}^{-1} \text{ mM}^{-1}$  and  $k_a^{\text{CO}} = 0.025 \pm 0.006 \text{ s}^{-1}$  in the WT, to  $6 \pm 2 \text{ s}^{-1} \text{ mM}^{-1}$  and  $0.0014 \pm 0.0002 \text{ s}^{-1}$  ( $n = 3$  independent determinations) in *Cr* V296F and  $7 \pm 2 \text{ s}^{-1} \text{ mM}^{-1}$  and  $0.008 \pm 0.001 \text{ s}^{-1}$  ( $n = 3$ ) in *Cr* F290Y, all at 30 °C, pH 7,  $E = -158 \text{ mV}$ . Note that *Cr* F290 was mistakenly numbered F234 in ref. 32. We also observed that the *Cr* F290W mutant has no activity. Explicit MD simulations of the *Cp* V423F and *Cp* F417Y mutants (Fig. 4b and Supplementary Section S2.6) predict a slowdown in the last transition into the geminate site, resulting, respectively, in an approximately twofold and 100-fold decrease in the  $k_{+1}$  rate. Hence, experiment and simulation concur that the transition from site 7 to the geminate site is a key step in ligand diffusion to the active site.

The CO data in Fig. 2d inform on O<sub>2</sub> intramolecular diffusion because there is evidence that, at least in the case of NiFe hydrogenase, CO and O<sub>2</sub> use the same pathway to access the active site<sup>27</sup>. However, equation (3) shows that intramolecular diffusion is not the only factor that determines the rate of reaction with O<sub>2</sub>. Figure 2e shows the reaction of *Cr* WT FeFe hydrogenase and the two mutants with oxygen. Figure 2f shows the corresponding plot of  $d(\log(i))/dt$  against time, which can be extrapolated to the time of O<sub>2</sub> injection to estimate the pseudo-first-order rate constant of reaction with O<sub>2</sub> (ref. 33). The reaction of F290Y with O<sub>2</sub> is half as fast as for the WT, consistent with the observation in Fig. 2d that the F290Y mutation slows access to the active site. Surprisingly, the reaction of the V296F mutant with O<sub>2</sub> is about 2.5 times faster than with the WT, despite CO access to the active site being slower (Fig. 2d). However, Supplementary Fig. 12 shows that the anaerobic oxidative inactivation mechanism of the V296F mutant is qualitatively different from that of the WT (the chemistry is different, not just the rates), suggesting that the mutation affects not only the diffusion kinetics, but also the reactivity of the active site in a manner that appears to increase the rate of reaction with O<sub>2</sub> and compensates for slower intramolecular diffusion.

### Reactivation ( $k_a$ )

The rate constant  $k_a$  in equation (1) corresponds to the transformation of the O<sub>2</sub> adduct into an active form of the enzyme. As shown in the following, this reaction is more complex than the mere release of bound O<sub>2</sub>. Indeed, reactivation is slowed by replacing H<sub>2</sub>O and H<sub>2</sub> with D<sub>2</sub>O and D<sub>2</sub> (Fig. 2a, kinetic isotope effect (KIE) in the range 2.4–4 at  $T = 12 \text{ °C}$ , depending on the potential), and the value of  $k_a$  is strongly dependent on pH and electrode

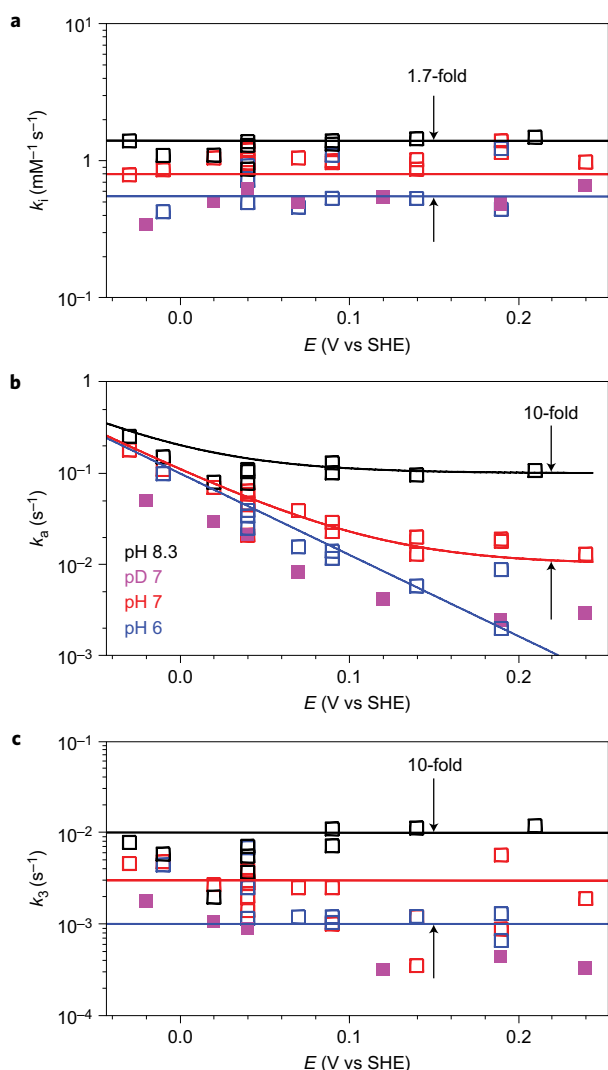


**Figure 3 | Potential dependence of the three rate constants defined in equation (1).** Rates constants were measured in experiments where *Ca* FeFe hydrogenase is inhibited by  $O_2$  at pH 6 (blue), 7 (red) and 8.3 (black) and pD 7 (pink, see Methods).  $T = 12^\circ C$ , 1 bar  $H_2$  or  $D_2$ . The bimolecular rate constant of the initial  $O_2$  binding step,  $k_i$ , is independent of  $E$  and pH, and the rate of formation of the dead-end species,  $k_3$ , only depends on pH. Horizontal lines in **a** and **c** are a guide to the eye at  $k_i = 1.4$ , 0.8 and 0.55 (**a**) and  $k_3 = 0.01$ , 0.003 and 0.001 (**c**). Two pathways (the rate constants of which add up) contribute to reactivation. Lines in **b** are the sum of a pH-dependent constant (0.1 at pH 8.3 and 0.01 at pH 7) and a pH-independent function that is proportional to  $\exp(-FE/2RT)$ .

potential  $E$  (Fig. 2b,c). Moreover, the observation in Fig. 3b that  $k_a$  decreases exponentially as  $E$  increases and then levels off at high  $E$  provides unambiguous evidence that two distinct processes contribute to the reactivation: one that is triggered by a reduction (hence the sigmoidal increase in  $k_a$  as  $E$  decreases, the observed exponential variation being the foot of this sigmoid) and one that is non-redox and predominates at high  $E$  and high pH. The value of  $k_a$  in Fig. 3b is the sum of the two corresponding reactivation rates.

We first consider the non-redox reactivation, the rate of which is independent of potential and increases tenfold per pH unit between pH 6 and 8 (Fig. 3b). This shows that the non-redox reactivation occurs only from the basic form of a species whose protonation/deprotonation is fast compared to  $k_a$ . Theoretical calculations (Supplementary Section 3) suggest that the two protonation states

are  $Fe_d-O_2H^+$  and  $Fe_d-O_2$  and that protonation occurs via a neighbouring Cys that is part of a proton transfer chain connecting the active site to the solvent (Cys299 in *Cp* hydrogenase, Cys169 in the *Cr* enzyme)<sup>23,34–37</sup>. In the alkaline limit where  $[Fe_d-O_2H^+] \ll [Fe_d-O_2]$ , the computed  $k_a = k_{-2} = 1.4 \times 10^{-2} s^{-1}$ , compares favourably with the experimental estimate of  $k_a > 1.0 \times 10^{-1} s^{-1}$  (see Supplementary Section 3 for further discussion).

We now turn our attention to reductive reactivation, which dominates at low  $E$  (Fig. 3b). We propose that the reactivation process is the reduction of bound oxygen to a species whose dissociation from the active site gives back the active state. This hypothesis is confirmed by extensively validated theoretical calculations (Supplementary Section 4) for consecutive electron transfer/proton transfer (ET/PT) coupled reduction of  $O_2$  bound to the active site (Fig. 5). Calculations suggest that the four-electron/four-proton reduction of  $O_2$  is possible without formation of high-energy intermediates, and the species dissociating from the active site is indeed water. During the first ET/PT step ( $2 \rightarrow 3$ ,  $-2.7 kcal mol^{-1}$ ) the O–O bond length is elongated from 1.30 to 1.46 Å, which is best interpreted as a change from a superoxide to a hydro-peroxide species (see inset 3 in Fig. 5). The second step may proceed via two pathways. The proton can attach either to the proximal Fe-bound oxygen to form hydrogen peroxide ( $3 \rightarrow 5$ ) or to the distal oxygen atom, upon which the O–O bond breaks and the first water molecule is formed ( $3 \rightarrow 4$ ). We found that the formation of water is highly exothermic ( $-34.9 kcal mol^{-1}$ ) and strongly preferred over the endothermic formation of hydrogen peroxide ( $+8.6 kcal mol^{-1}$ ). The proximal oxygen atom easily abstracts the hydrogen atom from Cys299, which results in a shift of electron spin density from oxygen to sulfur. The same proton transfer reaction is discussed in ref. 23. The sulfur atom of Cys299 now serves as a hydrogen-bond acceptor, while the newly formed water molecule stabilizes the Fe-bound hydroxy group by hydrogen bonding (see inset 4 in Fig. 5). In the third step ( $4 \rightarrow 6$ ), which is mildly uphill ( $+0.7 kcal mol^{-1}$ ), the sulfur atom is re-protonated and the Fe-bound hydroxy radical is reduced to  $OH^-$ . Finally, in the fourth step ( $6 \rightarrow 7$ ,  $-12.9 kcal mol^{-1}$ ) the Fe-bound hydroxide is reduced to water and the di-iron site returns to its initial redox state.

### The irreversible formation of dead-end species ( $k_3$ )

In the kinetic model, the partial irreversibility of the reaction with  $O_2$  is accounted for by the irreversible transformation of the  $O_2$  adduct, with a first-order rate constant  $k_3$ . Figure 3c shows that the value of  $k_3$  is independent of  $E$  and increases about tenfold over two pH units (Fig. 2b shows that the inhibition is more reversible at high pH, but that is because  $k_a$  is greater (cf. Fig. 3b) and the  $O_2$  adduct is therefore short-lived). Replacing  $H_2O$  with  $D_2O$  decreases  $k_3$  fivefold. These observations suggest that  $k_3$  is the rate of a non-redox transformation of one of the species shown in Fig. 5.

The conversion of **4** to **6** is the least exergonic step in the reduction of  $O_2$ ; state **4** may therefore be a bottleneck for water reduction and the starting point for the irreversible formation of various dead-end products. Indeed, calculations reveal that the Fe-bound hydroxy radical can readily attack the deprotonated sulfur atom of Cys299 to form sulfenic acid (inset 9 in Fig. 5,  $-14.0 kcal mol^{-1}$ ). The latter is strongly stabilized by a hydrogen bond to the  $CN^-$  ligand. Alternatively, the dissociation of the OH radical from the distal iron into the active site pocket is also energetically favourable by  $-14.7 kcal mol^{-1}$ ; this highly reactive species could readily oxidize either the H-cluster or surrounding protein residues<sup>23</sup>.

Our proposal that Cys299-SOH and/or free OH radicals are involved in the irreversible inactivation is further supported by the following observations. First, the formation of Cys299-SOH requires Cys299 to be deprotonated, consistent with the observed increase in  $k_3$  when the pH is increased and the observed KIE. Besides, an increase in pH makes the third ET/PT step even more endothermic,

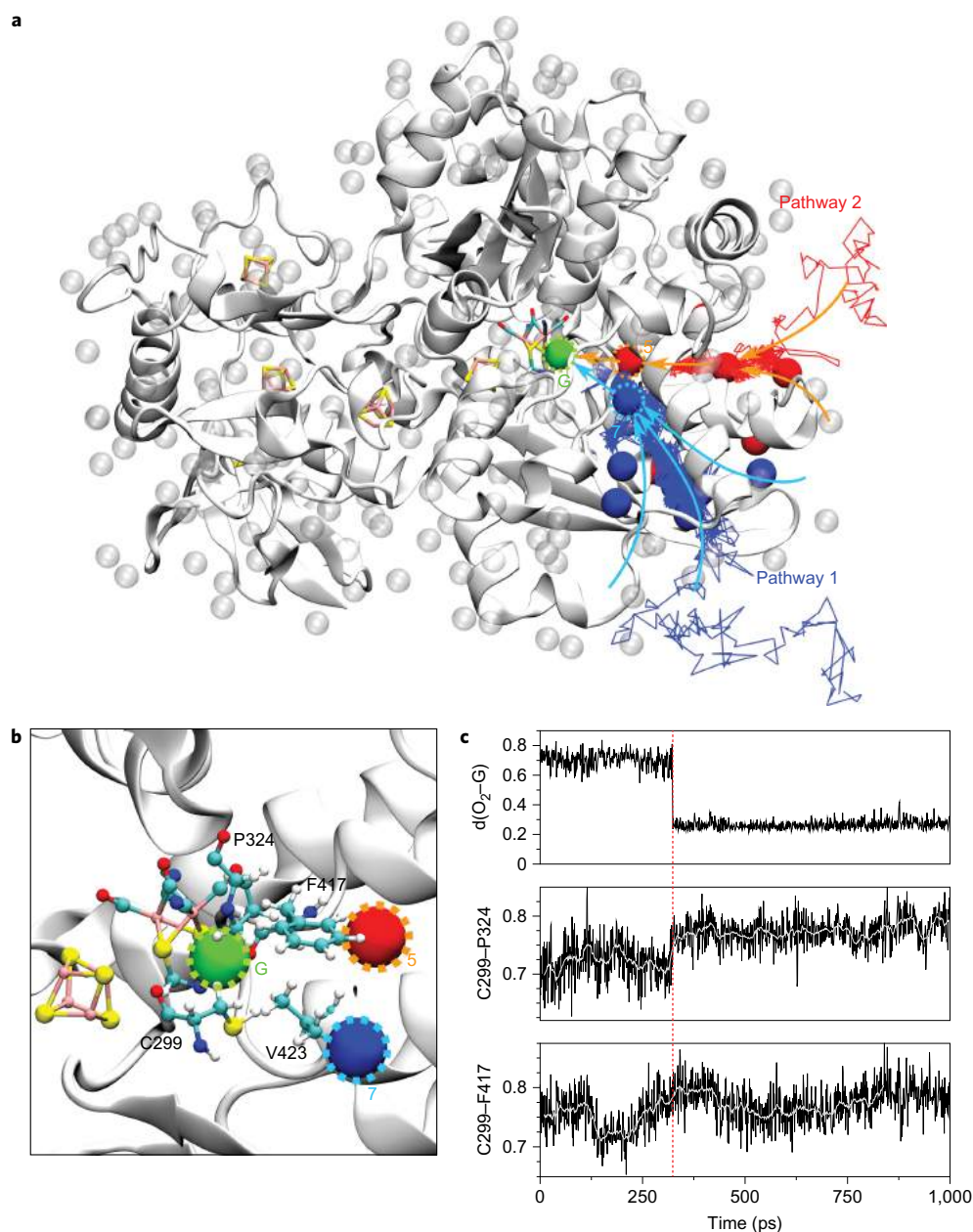


**Figure 4 | Markov state model for O<sub>2</sub> diffusion into Cp hydrogenase.** **a**, Location of gas molecule microstates identified from the MD simulations (transparent spheres) overlaid on the structure of Cp hydrogenase (white). Atomic detail is shown only for the inorganic clusters. Red and blue solid spheres mark the microstates that are involved in the two paths (1 and 2, in blue and red) to the H-cluster. Microstates 5 (red with orange dotted line) and 7 (blue, with cyan dotted line) are those directly connected to the geminate site (G, green), as derived from flux calculations. Example paths arriving through pathways 1 and 2 are shown as blue and red lines, respectively. **b**, Zoom into the vicinity of the H-cluster. The geminate, 5 and 7 sites are colour-coded as in **a**. **c**, Distance between key residues (shown in **b**), that block access to the active site, as obtained from low force pulling simulations. Note the increase in distance between the sidechains of Cys299 and those of Pro324 (middle) and Phe417 (bottom) at ~320 ps (red dashed line), facilitating the transition of an O<sub>2</sub> molecule from microstate 7 to geminate site G.

leading to an increase in the concentration of **4** and eventually of the dead-end product. Second, Swanson *et al.* have observed the oxidation of Cys169 (Cys299 in the enzyme from Cp)<sup>25</sup>. Third, the replacement of Cys169 with Asp in the Cr enzyme<sup>38</sup>, which has no effect on the spectroscopic signatures of the H-cluster<sup>39</sup>, decreases the value of  $k_3$  about tenfold, from  $k_3 = 24 \pm 3 \times 10^{-3} \text{ s}^{-1}$  in the WT to  $21 \pm 8 \times 10^{-4} \text{ s}^{-1}$  in the C169D mutant (ref. 16 and Supplementary Fig. 11; see Supplementary Section 5 for details). Figure 2d confirms that the inhibition of the C169D mutant is significantly more reversible than that of the WT enzyme.

## Discussion

Figure 6 summarizes our proposed mechanism of aerobic inactivation of FeFe hydrogenase, including diffusion of O<sub>2</sub> from the solvent, O<sub>2</sub> binding at the active site and the reactions that follow.

Our conclusion from MD calculations that amino-acid side chains along the pathway shown in Fig. 4a determine the rates of diffusion of O<sub>2</sub> to the active site is supported by the observation that the V296F and F290Y mutations in Cr hydrogenase strongly decrease the rates of binding and release of the competitive inhibitor

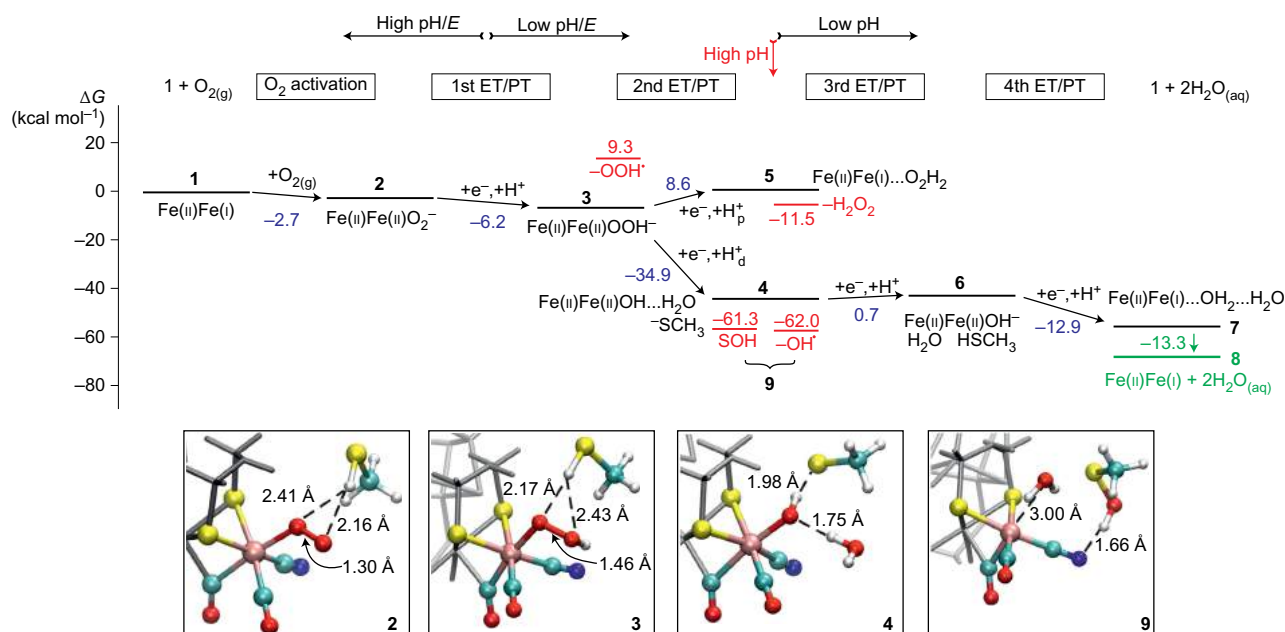


**Figure 5 | Graphical representation of the relative free energies of the most important states (1-9) involved in oxygen reduction to water at the active site of the FeFe hydrogenase.** The free energies, shown for pH 7 relative to the SHE, were obtained from DFT calculations on large active site models, as explained in detail in Supplementary Section 4. State 1 is equivalent to species A in equation (1). For structures 2, 3, 4 and 9, the most important interatomic distances are shown in the respective insets. The first coordination sphere of the distal iron atom is presented in ball and stick representation (Fe, pink; O, red; C, turquoise; N, dark blue; S, yellow; H, white).

CO. We found that the rate of inhibition by O<sub>2</sub> of WT FeFe hydrogenase ( $k_i$ ) is the product of two parameters, the ratio  $k_{+1}/k_{-1}$  and the chemical binding rate  $k_{+2}$  (cf. equation (3),  $k_{-1} \gg k_{+2}$ ). Both ligand diffusion into the active site ( $k_{+1}$ ) and chemical bond formation ( $k_{+2}$ ) occur on the 0.1–1 ms timescale, but the observed inhibition rate is about four orders of magnitude slower, because  $k_{+1}/k_{-1} \approx 10^{-4} \text{ mM}^{-1}$ . This also means that a mutation that decreases both  $k_{+1}$  and  $k_{-1}$  is expected to slow O<sub>2</sub> inhibition only

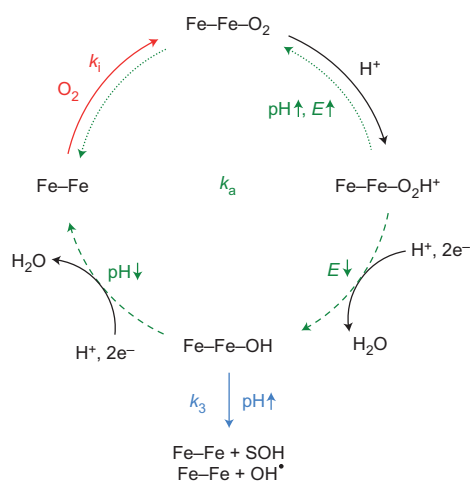


**Figure 6 | Proposed mechanism for aerobic inhibition of FeFe hydrogenase.** The binding of O<sub>2</sub> with rate constant  $k_i \times [\text{O}_2]$  is indicated in red, and the two paths that contribute to the rate constant of reactivation  $k_a$  are shown in green. The reactivation path that dominates at high pH and high electrode potential  $E$  is indicated by dotted arrows and the reactivation that dominates at low pH and low potential is indicated by dashed arrows. The reaction with rate constant  $k_3$ , which makes the inhibition partly irreversible, is depicted in blue.

if it makes  $k_{-1}$  lower than  $k_{+2}$  (cf. equation (3)), as observed previously in a series of NiFe hydrogenase channel mutants<sup>27</sup>.

The partial reversibility of the reaction with O<sub>2</sub> (Fig. 2 and ref. 16) could not be detected in experiments where the enzyme was exposed to a constant concentration of O<sub>2</sub> (refs 18 and 40) and, as a consequence, all previous computational studies of the inhibition of hydrogenase have placed their emphasis on explaining the irreversibility of the reaction. In the light of experimental results showing that O<sub>2</sub> inhibition is reversible (this work and refs 16 and 17), a major change of paradigm is required as well as new theoretical calculations that can explain our results on a molecular scale. We have shown that the reactivation results from the combined effects of the release of O<sub>2</sub> and its four-electron four-proton reduction to water (Fig. 6), consistent with recent evidence for O<sub>2</sub> reduction by synthetic analogues of the H-cluster<sup>41</sup>. However, with less than 1 pmol of enzyme on the electrode and a rate constant of reactivation (O<sub>2</sub> reduction) of  $\sim 3 \times 10^{-2} \text{ s}^{-1}$ , only a few pmol of H<sub>2</sub>O are formed during a 100 s exposure to O<sub>2</sub>. The use of mass spectrometry to detect the reduction of O<sub>2</sub> to H<sub>2</sub>O (as, for example, in refs 6 and 42) is therefore not possible.

According to our calculations, no high-energy intermediate is formed en route to water formation. By contrast, the formation of hydrogen peroxide requires an endothermic ET/PT step and is therefore unlikely. The two-electron, two-proton reduced state (4 in Fig. 5) can readily interconvert to produce harmful OH radicals, which could be responsible for H-cluster degradation as observed previously<sup>18,25</sup>, or to hydroxylate the neighbouring cysteine residue, consistent with recent crystallographic evidence<sup>25</sup>. Because this residue is involved in proton transfer from the active site<sup>43,44</sup>, its oxidation alone should be enough to make the enzyme inactive. That irreversible damage follows the two-electron/two-proton reduction of O<sub>2</sub> is consistent with the observation that enzyme lyophilization (which suppresses the source of protons) protects from O<sub>2</sub> (ref. 45).

We conclude that the resistance of FeFe hydrogenases to O<sub>2</sub> is largely dependent on the availability of the electrons that are required

for completely reducing the attacking O<sub>2</sub> to water, as recently suggested by Reiher and co-authors<sup>23</sup>. This reaction—which may be physiological, considering the observation that FeFe hydrogenase can be upregulated in response to oxidative stress<sup>46</sup>—also allows certain NiFe hydrogenases to resist O<sub>2</sub> (refs 2–4,42,47,48). O<sub>2</sub> reduction by NiFe hydrogenases uses electrons produced upon H<sub>2</sub> oxidation and requires the presence of a peculiar FeS cluster that is near the NiFe active site. Considering FeFe hydrogenases, the four electrons required cannot be produced at the H-cluster after O<sub>2</sub> binding and must originate externally. When the enzyme is adsorbed onto an electrode, as occurs in our experiments and in many situations where one seeks to use hydrogenases as a supported catalyst, the electrode functions as an electron reservoir. However, ‘electron-poor’ conditions have been used in X-ray absorption spectroscopy (XAS) and X-ray crystallography investigations of the structure of the degradation products<sup>18,25</sup>, with the enzyme in the oxidized state and no H<sub>2</sub> or any electron donor (although we note that X-rays can sometimes reduce inorganic active sites<sup>49</sup>). If the O<sub>2</sub> reduction cycle that we described cannot proceed due to a lack of electrons, the O<sub>2</sub> adduct **2** may oxidize either the amino acids around the active site, or the H-cluster of other proteins in solution (in an intermolecular reaction). Differences in proton/electron availability may account for some of the variability as to the nature of the degradation products described in the literature<sup>18,25</sup>, when FeFe hydrogenases are exposed to O<sub>2</sub>.

We have shown that side-chain fluctuations, the availability of electrons and protons, and the presence of ionizable protein residues in the active site pocket all contribute to defining the O<sub>2</sub> sensitivity of FeFe hydrogenase. We have identified the two electron–two proton reduced state as a critical branching point for the formation of water versus ROS and have revealed key residues that are likely to control the access of O<sub>2</sub> to the H cluster. We have observed that substitutions of these residues affect the diffusion rates and the kinetics of anaerobic inactivation, similarly to the valine that gates the substrate access channel in NiFe hydrogenase<sup>5,27</sup>.

Two lines of investigation are worth pursuing in future work. The first is the screening of the effects of all possible substitutions at positions 290 and 296 (*Cr* numbering) using both electrochemistry and MD simulation, with the aim to restrict O<sub>2</sub> access to the active site and slow the formation of the dead-end species. The second is the systematic search for mutations that accelerate the third ET/PT step (transformation **4**→**6** in Fig. 5a) using electrochemistry and quantum chemical calculations, to eliminate likely bottlenecks for O<sub>2</sub> reduction. The reason the enzyme from *Ca* forms the dead-end species much more slowly than the enzyme from *Cr* (ref. 16) should also be investigated; this may be related to the presence of a chain of auxiliary FeS clusters that may help deliver electrons to the active site of the clostridial enzyme.

## Methods

**Biochemistry and molecular biology.** The methods for the purification of the two WT enzymes and *Cr* F290Y hydrogenase have all been fully described previously<sup>22</sup> (but residue F290 was mistakenly numbered 234 in ref. 32). The production and electrochemical characterization of the C169D, F290W and V296F mutants are described in the Supplementary Information.

**Electrochemistry.** All potentials are quoted with respect to the standard hydrogen electrode (SHE). The method for measuring  $k_1$ ,  $k_2$  and  $k_3$  is fully described in ref. 16. In short, the method consists in performing anaerobic experiments (voltammetry and chronoamperometry) to determine all the parameters that define the anaerobic inhibition of the enzyme under oxidizing conditions<sup>32</sup>, then recording the response of the enzyme to repeated exposure to O<sub>2</sub> while monitoring the O<sub>2</sub> concentration and fitting a model based on equation (1) to these data, adjusting only the values of  $k_1$ ,  $k_2$  and  $k_3$ , all other parameters being fixed to their independently determined values. To determine the isotope effects, the pD was measured with a glass electrode using the correction  $\text{pD} = 0.4 + \text{pH meter reading}$ <sup>50</sup>. With hydrogenase on the electrode, the open-circuit potential in experiments carried out at pH 7 under 1 atm. H<sub>2</sub> was within 10 mV of the value at pD 7 under 1 atm. of D<sub>2</sub>. The electrochemical data were analysed using the new home-made, portable, open source program QSoas ([www.qsoas.org](http://www.qsoas.org)) (ref. 51).

**Molecular dynamics.** The Gromacs software package<sup>52</sup> was used to run atomistic MD simulations of *Cp* hydrogenase (PDB 3C8Y<sup>29</sup>) in explicit water. Simulations were run using an optimized force field for both protein (ref. 53) and water (ref. 54), a published set of parameters for the inorganic clusters (ref. 55), and in the presence of 50 O<sub>2</sub> molecules (for further details see Supplementary Section 2). We analysed the simulation trajectories to construct an MSM, using the same methodology as described before<sup>30</sup>. Using this approach the dynamics of the gas molecules as they diffuse within the protein is described by a rate matrix  $K$ , containing rate coefficients  $k_{ji}$  corresponding to transitions between pairs of microstates  $i$  and  $j$ . These microstates are defined from pockets within the protein frequently populated by the O<sub>2</sub> molecules. In our extensive equilibrium MD runs, the gas molecules did not sufficiently sample transitions corresponding to the binding to the geminate site (G). We therefore combined the equilibrium rate matrix with rate constants for the  $i$ →G process obtained from pulling simulations from multiple initial states. The rate coefficients  $k_{Gi}$  at zero force were derived from a kinetic theory for force-induced transitions (ref. 56). The combination of the MSM and fitted rates at zero force has been validated in our previous work<sup>29</sup>. From the rate matrix we obtain the binding ( $k_{+1}$ ) and dissociation ( $k_{-1}$ ) rate constants as described before<sup>29</sup>. We use the Berezhkovskii–Hummer–Szabo method (ref. 57) to estimate fluxes from the solvent to the geminate site and obtain the two pathways from which the H-cluster can be accessed.

**Quantum chemical calculations.** Calculations were performed with the model system (Supplementary Fig. 9) extracted from the crystal structure of the *Cp* protein (H<sub>ox</sub> state). It consists of a small diiron subsite Fe<sub>2</sub><sup>II</sup>Fe<sub>2</sub><sup>I</sup> linked to the iron–sulfur cubane [Fe<sub>4</sub>S<sub>4</sub>]. Anchoring cysteine residues as well as the proximal cysteine, important in the reaction studied here, were replaced with methanethiols, and their carbon atom coordinates were fixed to the crystal positions. To compensate for a high negative charge of the active site (–3) we included three protonated CH<sub>3</sub>NH<sub>3</sub><sup>+</sup> molecules at the positions occupied by the lysine residues in the crystal structure. All molecules considered in this study have the lowest possible spin state (singlet or doublet) except dioxygen and OOH<sup>•</sup>, which have a triplet ground state. Single-point energy calculations were performed with the B3LYP+D3 functional and the COSMO solvation model to obtain more accurate energy changes and to account for the charge screening by the protein matrix, respectively. For the latter we used a typical dielectric constant of 4, while  $\epsilon = 78$  was used for water. The def2-TZVP basis set was used throughout the study. We note that the selected methodology (moderate amount of the Hartree–Fock exchange in the density functional, large basis set on the sulfur and oxygen atoms as well as a pairwise correction for the dispersion interactions) also gives an accurate description of the isomerization reactions involving sulfoxxygenated species<sup>58</sup>. Further details of the calculations, validation of the density functional against high-level *ab initio* calculations and references relevant to this section can be found in Supplementary Section 4. The XYZ coordinates of all molecular structures discussed are given in Supplementary Section 6.

Received 2 December 2015; accepted 8 July 2016;  
published online 22 August 2016

## References

- Lubitz, W., Ogata, H., Rüdiger, O. & Reijerse, E. Hydrogenases. *Chem. Rev.* **114**, 4081–4148 (2014).
- Flanagan, L. A. & Parkin, A. Electrochemical insights into the mechanism of NiFe membrane-bound hydrogenases. *Biochem. Soc. Trans.* **44**, 315–328 (2016).
- Fritsch, J. *et al.* The crystal structure of an oxygen-tolerant hydrogenase uncovers a novel iron–sulphur centre. *Nature* **479**, 249–252 (2011).
- Volbeda, A. *et al.* Crystal structure of the O<sub>2</sub>-tolerant membrane-bound hydrogenase 1 from *Escherichia coli* in complex with its cognate cytochrome *b*. *Structure* **21**, 184–190 (2013).
- Hamdan, A. A. *et al.* Relation between anaerobic inactivation and oxygen tolerance in a large series of NiFe hydrogenase mutants. *Proc. Natl Acad. Sci. USA* **109**, 19916–19921 (2012).
- Plumeré, N. *et al.* A redox hydrogel protects hydrogenase from high-potential deactivation and oxygen damage. *Nature Chem.* **6**, 822–827 (2014).
- Fourmond, V. *et al.* Mechanism of protection of catalysts supported in redox hydrogel films. *J. Am. Chem. Soc.* **137**, 5494–5505 (2015).
- Fourmond, V. *et al.* The mechanism of inhibition by H<sub>2</sub> of H<sub>2</sub>-evolution by hydrogenases. *Chem. Commun.* **49**, 6840–6842 (2013).
- Pandey, A. S., Harris, T. V., Giles, L. J., Peters, J. W. & Szilagy, R. K. Dithiomethylether as a ligand in the hydrogenase H-cluster. *J. Am. Chem. Soc.* **130**, 4533–4540 (2008).
- Berggren, G. *et al.* Biomimetic assembly and activation of [FeFe]-hydrogenases. *Nature* **499**, 66–69 (2013).
- Silakov, A., Wenk, B., Reijerse, E. & Lubitz, W. <sup>14</sup>N HYSCORE investigation of the H-cluster of [FeFe] hydrogenase: evidence for a nitrogen in the dithiol bridge. *Phys. Chem. Chem. Phys.* **11**, 6592–6599 (2009).
- Esselborn, J. *et al.* A structural view of synthetic cofactor integration into [FeFe]-hydrogenases. *Chem. Sci.* **7**, 959–968 (2016).
- Mulder, D. W. *et al.* Stepwise [FeFe]-hydrogenase H-cluster assembly revealed in the structure of HydA<sup>ΔEPG</sup>. *Nature* **465**, 248–251 (2010).

14. Ghirardi, M. L. Implementation of photobiological H<sub>2</sub> production: the O<sub>2</sub> sensitivity of hydrogenases. *Photosynth. Res.* **125**, 383–393 (2015).
15. Cohen, J., Kim, K., King, P., Seibert, M. & Schulten, K. Finding gas diffusion pathways in proteins: application to O<sub>2</sub> and H<sub>2</sub> transport in Cpl [FeFe]-hydrogenase and the role of packing defects. *Structure* **13**, 1321–1329 (2015).
16. Orain, C. *et al.* Electrochemical measurements of the kinetics of inhibition of two FeFe hydrogenases by O<sub>2</sub> demonstrate that the reaction is partly reversible. *J. Am. Chem. Soc.* **137**, 12580–12587 (2015).
17. Baffert, C. *et al.* Hydrogen-activating enzymes: activity does not correlate with oxygen sensitivity. *Angew. Chem. Int. Ed.* **47**, 2052–2055 (2008).
18. Stripp, S. T. *et al.* How oxygen attacks [FeFe] hydrogenases from photosynthetic organisms. *Proc. Natl Acad. Sci. USA* **106**, 17331–17336 (2009).
19. Stiebritz, M. T. & Reiher, M. Theoretical study of dioxygen induced inhibition of [FeFe]-hydrogenase. *Inorg. Chem.* **48**, 7127–7140 (2009).
20. Kubas, A., Sancho, D. D., Best, R. B. & Blumberger, J. Aerobic damage of [FeFe] hydrogenases activation barriers for O<sub>2</sub> chemical attachment. *Angew. Chem. Int. Ed.* **53**, 4081–4084 (2014).
21. Lambertz, C. *et al.* O<sub>2</sub> reactions at the six-iron active site (H-cluster) in [FeFe]-hydrogenase. *J. Biol. Chem.* **286**, 40614–40623 (2011).
22. Bruska, M. K., Stiebritz, M. T. & Reiher, M. Regioselectivity of H cluster oxidation. *J. Am. Chem. Soc.* **133**, 20588–20603 (2011).
23. Finkelmann, A. R., Stiebritz, M. T. & Reiher, M. Activation barriers of oxygen transformation at the active site of [FeFe] hydrogenases. *Inorg. Chem.* **53**, 11890–11902 (2014).
24. Hong, G. & Pachter, R. Inhibition of biocatalysis in [Fe–Fe] hydrogenase by oxygen: molecular dynamics and density functional theory calculations. *ACS Chem. Biol.* **7**, 1268–1275 (2012).
25. Swanson, K. D. *et al.* [FeFe]-hydrogenase oxygen inactivation is initiated at the H cluster 2Fe subcluster. *J. Am. Chem. Soc.* **137**, 1809–1816 (2015).
26. Greco, C. *et al.* Combining experimental and theoretical methods to learn about the reactivity of gas-processing metalloenzymes. *Energy Environ. Sci.* **7**, 3543–3573 (2014).
27. Liebgott, P.-P. *et al.* Relating diffusion along the substrate tunnel and oxygen sensitivity in hydrogenase. *Nature Chem. Biol.* **6**, 63–70 (2010).
28. Wang, P.-H. & Blumberger, J. Mechanistic insight into the blocking of CO diffusion in [NiFe]-hydrogenase mutants through multiscale simulation. *Proc. Natl Acad. Sci. USA* **109**, 6399–6404 (2012).
29. Wang, P.-h., Best, R. B. & Blumberger, J. Multiscale simulation reveals multiple pathways for H<sub>2</sub> and O<sub>2</sub> transport in a [NiFe]-hydrogenase. *J. Am. Chem. Soc.* **133**, 3548–3556 (2011).
30. De Sancho, D., Kubas, A., Wang, P.-h., Blumberger, J. & Best, R. B. Identification of mutational hot spots for substrate diffusion: application to myoglobin. *J. Chem. Theory Comput.* **11**, 1919–1927 (2015).
31. Baffert, C. *et al.* CO disrupts the reduced H-cluster of FeFe hydrogenase. A combined DFT and protein film voltammetry study. *J. Am. Chem. Soc.* **133**, 2096–2099 (2011).
32. Fourmond, V. *et al.* The oxidative inactivation of FeFe hydrogenase reveals the flexibility of the H-cluster. *Nature Chem.* **6**, 336–342 (2014).
33. Léger, C., Dementin, S., Bertrand, P., Rousset, M. & Guigliarelli, B. Inhibition and aerobic inactivation kinetics of *Desulfovibrio fructosovorans* NiFe hydrogenase studied by protein film voltammetry. *J. Am. Chem. Soc.* **126**, 12162–12172 (2004).
34. Cornish, A. J., Gärtner, K., Yang, H., Peters, J. W. & Hegg, E. L. Mechanism of proton transfer in [FeFe]-hydrogenase from *Clostridium pasteurianum*. *J. Biol. Chem.* **286**, 38341–38347 (2011).
35. Knörzer, P. *et al.* Importance of the protein framework for catalytic activity of [FeFe]-hydrogenases. *J. Biol. Chem.* **287**, 1489–1499 (2012).
36. Hong, G., Cornish, A. J., Hegg, E. L. & Pachter, R. On understanding proton transfer to the biocatalytic [Fe–Fe] H sub-cluster in [Fe–Fe] H<sub>2</sub>ases: QM/MM MD simulations. *Biochim. Biophys. Acta* **1807**, 510–517 (2011).
37. Long, H., King, P. W. & Chang, C. H. Proton transport in *Clostridium pasteurianum* [FeFe] hydrogenase I: a computational study. *J. Phys. Chem. B* **118**, 890–900 (2014).
38. Morra, S. *et al.* Site saturation mutagenesis demonstrates a central role for cysteine 298 as proton donor to the catalytic site in CaHydA [FeFe]-hydrogenase. *PLoS ONE* **7**, e48400 (2012).
39. Morra, S. *et al.* The effect of a C298D mutation in CaHydA [FeFe]-hydrogenase: insights into the protein–metal cluster interaction by EPR and FTIR spectroscopic investigation. *Biochim. Biophys. Acta* **1857**, 98–106 (2016).
40. Goldet, G. *et al.* Electrochemical kinetic investigations of the reactions of [FeFe]-hydrogenases with carbon monoxide and oxygen: comparing the importance of gas tunnels and active-site electronic/redox effects. *J. Am. Chem. Soc.* **131**, 14979–14989 (2009).
41. Dey, S. *et al.* Electrocatalytic O<sub>2</sub> reduction by [Fe–Fe]-hydrogenase active site models. *J. Am. Chem. Soc.* **136**, 8847–8850 (2014).
42. Wulff, P., Day, C., Sargent, F. & Armstrong, F. A. H. How oxygen reacts with oxygen-tolerant respiratory [NiFe]-hydrogenases. *Proc. Natl Acad. Sci. USA* **111**, 6606–6611 (2014).
43. Mulder, D. W. *et al.* Investigations on the role of proton-coupled electron transfer in hydrogen activation by [FeFe]-hydrogenase. *J. Am. Chem. Soc.* **136**, 15394–15402 (2014).
44. Ginovska-Pangovska, B. *et al.* Molecular dynamics study of the proposed proton transport pathways in [FeFe]-hydrogenase. *Biochim. Biophys. Acta* **1837**, 131–138 (2014).
45. Noth, J. *et al.* Lyophilization protects [FeFe]-hydrogenases against O<sub>2</sub>-induced H-cluster degradation. *Sci. Rep.* **5**, 1–10 (2015).
46. Fournier, M., Dermoun, Z., Durand, M.-C. & Dolla, A. A new function of the *Desulfovibrio vulgaris* Hildenborough [Fe] hydrogenase in the protection against oxidative stress. *J. Biol. Chem.* **279**, 1787–1793 (2004).
47. Pandelia, M.-E. E. *et al.* Electronic structure of the unique [4Fe–3S] cluster in O<sub>2</sub>-tolerant hydrogenases characterized by <sup>57</sup>Fe Mössbauer and EPR spectroscopy. *Proc. Natl Acad. Sci. USA* **110**, 483–488 (2013).
48. Stiebritz, M. T. & Reiher, M. Hydrogenases and oxygen. *Chem. Sci.* **3**, 1739–1751 (2012).
49. Yano, J. *et al.* X-ray damage to the Mn<sub>4</sub>Ca complex in single crystals of photosystem II: a case study for metalloprotein crystallography. *Proc. Natl Acad. Sci. USA* **102**, 12047–12052 (2005).
50. Glasoe, P. K. & Long, F. A. Use of glass electrodes to measure acidities in deuterium oxide. *J. Phys. Chem.* **64**, 188–190 (1960).
51. Fourmond, V. QSoas: a versatile software for data analysis. *Anal. Chem.* **88**, 5050–5052 (2016).
52. Pronk, S. *et al.* GROMACS 4.5: a high-throughput and highly parallel open source molecular simulation toolkit. *Bioinformatics* **29**, 845–854 (2013).
53. Best, R. B. & Mittal, J. Protein simulations with an optimized water model: cooperative helix formation and temperature-induced unfolded state collapse. *J. Phys. Chem. B* **114**, 14916–14923 (2010).
54. Abascal, J. L. F. & Vega, C. A general purpose model for the condensed phases of water: TIP4P/2005. *J. Chem. Phys.* **123**, 234505–234512 (2005).
55. Chang, C. H. & Kim, K. Density functional theory calculation of bonding and charge parameters for molecular dynamics studies on [FeFe] hydrogenases. *J. Chem. Theory Comput.* **5**, 1137–1145 (2009).
56. Dudko, O. K., Hummer, G. & Szabo, A. Intrinsic rates and activation free energies from single-molecule pulling experiments. *Phys. Rev. Lett.* **96**, 108101–108104 (2006).
57. Berezhkovskii, A., Hummer, G. & Szabo, A. Reactive flux and folding pathways in network models of coarse-grained protein dynamics. *J. Chem. Phys.* **130**, 205102–205105 (2009).
58. Liu, C., Liu, T. & Hall, M. B. Influence of the density functional and basis set on the relative stabilities of oxygenated isomers of diiron models for the active site of [FeFe]-hydrogenase. *J. Chem. Theory Comput.* **11**, 205–214 (2015).

## Acknowledgements

The French teams were supported by CNRS, INSA, CEA, Agence Nationale de la Recherche (ANR-12-BS08-0014, ANR-14-CE05-0010) and the A\*MIDEX project (n° ANR-11-IDEX-0001-02) funded by the «Investissements d’Avenir» French Government program, managed by the French National Research Agency (ANR). The authors thank R. van Lis for constructing the V296F and F290W mutants. D.D.S. acknowledges support from EPSRC grant no. EP/J016764/1 and an Ikerbasque Research Fellowship. A.K. was supported by EPSRC grant no. EP/J015571/1. R.B.B. was supported by the Intramural Research Program of the National Institute of Diabetes and Digestive and Kidney Diseases of the National Institutes of Health. J.B. thanks the Royal Society for a University Research Fellowship. This work was carried out on the HECToR and Archer computing facilities (Edinburgh), access to which was granted through the Materials Chemistry Consortium (EPSRC grants nos EP/F067496 and EP/L000202). The authors acknowledge the use of the UCL Legion High Performance Computing Facility (Legion@UCL) and associated support services in the completion of this work as well as the computational resources of the NIH HPC Biowulf cluster (<http://hpc.nih.gov>). D.D.S. acknowledges PRACE for awarding access to the FERMI resource based in Italy at CINECA. D.D.S. thanks A. Szabo and E. Rosta for discussions.

## Author contributions

A.K., C.O. and D.D.S. contributed equally to this work. All authors discussed the results and commented on the manuscript. A.K., D.D.S., R.B.B. and J.B. performed the calculations and analysed the data. C.O., M.S., C.B., V.F. and C.L. performed the electrochemical measurements and analysed the data. L.S., C.G., I.M.-S., P.S. and H.B. prepared the enzyme samples. A.K., D.D.S., R.B.B., C.B., V.F., J.B. and C.L. co-wrote the manuscript.

## Additional information

Supplementary information is available in the [online version of the paper](#). Reprints and permissions information is available online at [www.nature.com/reprints](http://www.nature.com/reprints). Correspondence and requests for materials should be addressed to J.B. and C.L.

## Competing financial interests

The authors declare no competing financial interests.





## Chapter 4

# Effect of light on FeFe hydrogenases inhibited by CO

## 4.1 Summary

FTIR, EPR<sup>48,63</sup> and direct electrochemistry<sup>87</sup> studies have shown that DdHydAB is sensitive to visible light. This could hinder the use of this enzyme in dyad systems for the photo-production of hydrogen.

To study this issue, we developed a new approach that combines direct photo-electrochemistry measurements and TDDFT calculations. To test this methodological approach, we first used it to study the effect of light on the inhibition of FeFe-hydrogenases by CO. This process is easier to study than the photo-sensitivity, because the inhibition of FeFe-hydrogenases by CO has been extensively studied before<sup>95,105–107</sup> and it is a simple reaction. Indeed, carbon monoxide is a competitive, reversible inhibitor of FeFe-hydrogenases and binds to Fe<sub>D</sub> in the apical position when the H-cluster is oxidized, forming the H<sub>ox</sub>CO state.<sup>17</sup> The photo-sensitivity of metal-carbonyl bonds is well known. FTIR studies showed that the irradiation of the enzyme with white light dissociates one of the COs bound to Fe<sub>D</sub> when the active site is in the H<sub>ox</sub>CO state.<sup>47,48,63,120</sup> PFV showed qualitatively that the irradiation of DdHydAB by white light increases the rate of reactivation of the enzyme inhibited by CO.<sup>95</sup>

Our work is the first study of the kinetics and of the action spectrum of the photodissociation of CO from FeFe-hydrogenases. In direct photo-electrochemistry experiments, we irradiated the FeFe-hydrogenases from *Me*, *Ca* and *Cr* with monochromatic lasers, changing the wavelength and the power of light and exposing the enzymes to CO. The values of the rate constants for CO binding and release in the dark and under irradiation indicated that blue-violet light increases the rate of CO release and this effect is power dependent. From kinetic data, we determined the action spectra of CO photodissociation, and we calculated for the first time the molecular absorption cross-section relative to the photodissociation of CO. Most of the absorbed blue-violet light leads to the dissociation of CO, as shown by the comparison of the cross-section values obtained in this work with those of H-cluster biomimetic complexes. We described for the first time the photodissociation of CO from the H-cluster using DFT and TDDFT, to obtain an electronic and mechanistic

description of the process. The calculated spectra showed that only excitations at lower wavelengths in the visible light range are active toward CO dissociation, in agreement with the experimental results. The CO bound in apical position to  $\text{Fe}_D$  has to overcome a lower energy barrier than the other COs to dissociate from the H-cluster in the ground state. The exploration of the potential energy surfaces of the excited states, as a function of the Fe-CO bond length, clearly showed that there are energy pathways that end up with the release of the CO in the apical position. Using TDDFT optimizations we also simulated one of these possible excited states energy pathways for the dissociation of the apical CO.

In conclusion, we obtained a full description of the photodissociation of the inhibitor CO from FeFe hydrogenases from photochemical, kinetic and theoretical point of view. The methodological approach that we developed in this study allowed us to study the photo-sensitivity of FeFe-hydrogenases (chapter 6), which is our main concern.

## 4.2 Résumé

Des études de spectroscopie IR, RPE<sup>48,63</sup> et d'électrochimie directe<sup>87</sup> ont montré que DdHydAB est sensible à la lumière visible. Cela pourrait entraver l'utilisation de cette enzyme dans les systèmes dyadiques pour la photo-production d'hydrogène.

Afin d'étudier ce problème, nous avons développé une nouvelle approche qui combine des mesures de photo-électrochimie directe et des calculs TDDFT. Pour tester cette approche méthodologique, nous l'avons utilisé pour étudier l'effet de la lumière sur l'inhibition des hydrogénases-FeFe par le CO. Ce processus est plus facile à étudier que la photo-sensibilité, car l'inhibition des hydrogénases-FeFe par le CO a été largement étudié<sup>95,105-107</sup> et c'est une réaction simple. En effet, le monoxyde de carbone est un inhibiteur compétitif et réversible des hydrogénases-FeFe et se lie au Fe<sub>D</sub> en position apicale lorsque le cluster-H est oxydé, en formant l'état H<sub>ox</sub>CO.<sup>17</sup> La photo-sensibilité des liaisons métal-carbonyle est bien connue. Les études FTIR ont montré que l'irradiation de l'enzyme avec la lumière blanche dissocie l'un des CO liés au Fe<sub>D</sub> lorsque le site actif est dans l'état H<sub>ox</sub>CO.<sup>47,48,63,120</sup> PFV a montré qualitativement que l'irradiation de DdHydAB par la lumière blanche augmente la vitesse de réactivation de l'enzyme inhibée par CO.<sup>95</sup>

Nous décrivons dans ce chapitre la première étude de la cinétique et du spectre d'action de la photodissociation du CO des hydrogénases-FeFe. Dans les expériences de photo-électrochimie directe, nous avons irradié les hydrogénases-FeFe de *Me*, *Ca* et *Cr* avec les lasers monochromatiques, en changeant la longueur d'onde et la puissance de la lumière et en exposant les enzymes au CO. Les valeurs des constantes de vitesse pour la liaison et la libération du CO dans l'obscurité et sous irradiation ont montré que la lumière bleu-violette augmente la vitesse de libération du CO et cet effet dépend de la puissance. A partir de ces données cinétiques, nous avons déterminé les spectres d'action de la photodissociation de CO, et Nous avons calculé pour la première fois la section efficace d'absorption moléculaire par rapport à la photodissociation de CO. La plupart de la lumière bleu-violette absorbée conduit à la dissociation du CO, comme le montre la comparaison des valeurs des sections efficaces obtenues dans ce travail avec celles des complexes biomimétiques

du cluster-H. Nous avons également décrit pour la première fois la photodissociation du CO du cluster-H en utilisant des calculs DFT et TDDFT, pour obtenir une description électronique et mécanistique du processus. Les spectres calculés ont montré que seules les excitations à des longueurs d'onde faibles dans la gamme de lumière visible sont actives pour la dissociation du CO, en accord avec les résultats expérimentaux. Le CO lié en position apicale sur le Fe<sub>D</sub> doit surmonter une barrière d'énergie inférieure à celle des autres CO pour se dissocier du cluster-H à l'état fondamental. L'exploration des surfaces d'énergie potentielles des états excités, en fonction de la longueur de liaison Fe-CO, a clairement montré qu'il existe des voies de désexcitation conduisant à la libération du CO en position apicale. En utilisant les optimisations TDDFT, nous avons également simulé une de ces possibles voies de désexcitation entraînant la dissociation du CO apical.

En conclusion, nous avons obtenu une description complète de la photodissociation du l'inhibiteur CO des hydrogénases-FeFe du point de vue photochimique, cinétique et théorique. L'approche méthodologique que nous avons développée dans cette étude nous a permis d'étudier la photo-sensibilité des FeFe-hydrogénases (chapitre 6), qui est notre question principale.

# Reactivity of the Excited States of the H-Cluster of FeFe Hydrogenases

Matteo Sensi,<sup>†,∇</sup> Carole Baffert,<sup>†</sup> Claudio Greco,<sup>‡</sup> Giorgio Caserta,<sup>§</sup> Charles Gauquelin,<sup>||</sup> Laure Saujet,<sup>⊥</sup> Marc Fontecave,<sup>§</sup> Souvik Roy,<sup>#</sup> Vincent Artero,<sup>#</sup> Philippe Soucaille,<sup>||</sup> Isabelle Meynial-Salles,<sup>||</sup> Hervé Bottin,<sup>⊥</sup> Luca de Gioia,<sup>∇</sup> Vincent Fourmond,<sup>†</sup> Christophe Léger,<sup>\*,†</sup> and Luca Bertini<sup>\*,∇</sup>

<sup>†</sup>Aix Marseille Univ., CNRS, BIP UMR 7281, Marseille, France

<sup>‡</sup>Department of Earth and Environmental Sciences, Milano-Bicocca University, Piazza della Scienza 1, 20126 Milan, Italy

<sup>§</sup>Laboratoire de Chimie des Processus Biologiques, UMR 8229 CNRS, Collège de France, Université Paris 6, 11 Place Marcelin Berthelot, Paris 75231 Cedex 05, France

<sup>||</sup>Université de Toulouse, INSA, UPS, INP, LISBP, INRA:UMR792,135 CNRS:UMR 5504, avenue de Rangueil, 31077 Toulouse, France

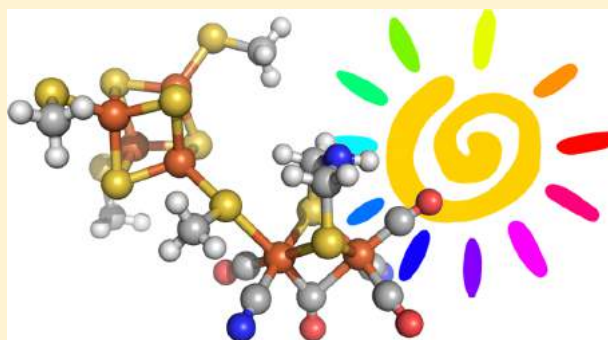
<sup>⊥</sup>Institut de Biologie et de Technologies de Saclay IBITECS, SB2SM/Institut de Biologie Intégrative de la Cellule I2BC, UMR 9198, CEA, CNRS, Université Paris Sud, F-91191 Gif sur Yvette, France

<sup>#</sup>Laboratoire de Chimie et Biologie des Métaux, Université Grenoble Alpes, CNRS, CEA, 17 rue des Martyrs, 38054 Grenoble, France

<sup>∇</sup>Department of Biotechnologies and Biosciences, University of Milano-Bicocca, Piazza della Scienza 2, 20126 Milan, Italy

## Supporting Information

**ABSTRACT:** FeFe hydrogenases catalyze H<sub>2</sub> oxidation and formation at an inorganic active site (the “H-cluster”), which consists of a [Fe<sub>2</sub>(CO)<sub>3</sub>(CN)<sub>2</sub>(dithiomethylamine)] subcluster covalently attached to a Fe<sub>4</sub>S<sub>4</sub> subcluster. This active site is photosensitive: visible light has been shown to induce the release of exogenous CO (a reversible inhibitor of the enzyme), shuffle the intrinsic CO ligands, and even destroy the H-cluster. These reactions must be understood because they may negatively impact the use of hydrogenase for the photoproduction of H<sub>2</sub>. Here, we explore in great detail the reactivity of the excited states of the H-cluster under catalytic conditions by examining, both experimentally and using TDDFT calculations, the simplest photochemical reaction: the binding and release of exogenous CO. A simple dyad model can be used to predict which excitations are active. This strategy could be used for probing other aspects of the photoreactivity of the H-cluster.



## INTRODUCTION

Hydrogenases are metalloenzymes that oxidize and produce dihydrogen.<sup>1–3</sup> They are involved in the bioenergetic metabolism of most microorganisms. The observation that light reverses the inhibition by CO of certain hydrogenases was made soon after these enzymes were first identified in the 1930s; the photosensitivity of the CO-bound complex and the competitive character of the inhibition were used to demonstrate that both exogenous CO and substrate H<sub>2</sub> bind to an active site iron atom.<sup>4</sup> Now we know that there are two types of hydrogenase active sites, and that the photorelease of CO under catalytic conditions was only observed with the so-called “FeFe hydrogenases” (see however ref 5 for a report of CO photorelease from NiFe hydrogenase under cryogenic conditions).

The active site of FeFe hydrogenase is a [Fe<sub>2</sub>(CO)<sub>3</sub>(CN)<sub>2</sub>-(dithiomethylamine)] subcluster covalently attached to a Fe<sub>4</sub>S<sub>4</sub>

subcluster, as depicted in Figure 1A.<sup>6–9</sup> The 2Fe subcluster bears terminal and bridging intrinsic CO and CN<sup>−</sup> ligands. The

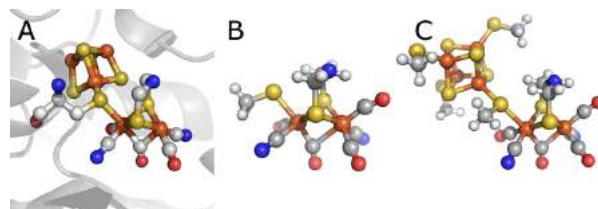


**Figure 1.** H-cluster of hydrogenase. (A) Structures of the active site of *C. acetobutylicum* FeFe hydrogenase, adapted from pdb 3C8Y.<sup>23</sup> (B and C) Two models of H<sub>ox</sub>-CO used in our TDDFT calculations.

Received: June 30, 2016

Published: September 20, 2016

binding of exogenous CO to the “distal” Fe (outermost, Fe<sub>d</sub>) of the active site in the H<sub>ox</sub> redox state (Fe<sup>I</sup>Fe<sup>II</sup>) yields the inhibited H<sub>ox</sub>-CO form of the enzyme.<sup>10</sup> Exogenous CO dissociates to give back the active form of the H-cluster upon irradiation with white light either at room temperature<sup>4,11</sup> or at cryogenic temperature below 20 K, but other photoproducts are formed upon irradiation at cryogenic temperature in the range 20–80 K.<sup>12–15</sup> Albracht, Stripp, and co-workers have also shown that the CO ligands that are bridging and terminally bound on Fe<sub>d</sub> can be exchanged with extrinsic CO upon illumination;<sup>14–16</sup> this shuffling of the coordination sphere of Fe<sub>d</sub> is relevant to the reversible inactivation of the enzyme that occurs in the dark under oxidizing conditions.<sup>17</sup> The photosensitivity of the iron–carbonyl bonds can also lead to photoinduced damage when the enzyme is illuminated in the absence of exogenous CO; indeed, according to a study of the hydrogenase from *D. desulfuricans*,<sup>14,15</sup> long exposure to “normal laboratory light” at room temperature destroys the H-cluster. Such photodamage adds biotechnological barriers that will limit the effectiveness of H<sub>2</sub>-photoproduction processes, whether they consist of using FeFe hydrogenases attached to photosensitizers<sup>18,19</sup> or microorganisms that couple photosynthesis to hydrogen production.<sup>20</sup> NiFe hydrogenases, in contrast, are apparently not damaged by light.<sup>21,22</sup>

The photolability of CO is a typical aspect of the reactivity of all transition metal carbonyl complexes, which has been investigated in dinuclear models of the H-cluster.<sup>24</sup> UV irradiation triggers CO photolysis in model compounds such as  $\mu$ -propanedithiolate-Fe<sub>2</sub>(CO)<sub>6</sub> and its derivatives; this has been studied using ultrafast transient IR spectroscopy,<sup>25,26</sup> and is supported by Density Functional Theory (DFT) calculations.<sup>27</sup> This reactivity is very solvent and ligand-dependent, and more complex than in the enzyme, probably because the protein that surrounds the active site prevents certain transformations. Time-dependent DFT (TDDFT) simulations shed light on the early stages of the photodynamics, showing that CO is loosely bound on the low energy excited-state surfaces, and that the photoreactivity strongly depends on the coordination sphere of the iron atoms.<sup>28</sup>

Here, we examine in great detail, both experimentally and theoretically, the effect of visible irradiation on the simplest reaction of the H-cluster: binding and release of the extrinsic inhibitor CO. We compare the results obtained with three different FeFe hydrogenases, and we examine for the first time how wavelength and light power affect the kinetics of inhibition under turnover conditions. The results are explained by TDDFT calculations of the electronic spectra and excited-state PES topologies of two different H<sub>ox</sub>-CO models, which show how the photodynamics of the system depends on the nature and excitation energy of the electronic transitions considered. A very simple description of the system in terms of a donor–acceptor molecular dyad system proves useful for identifying which excitations contribute to CO photolysis, although we conclude that intramolecular charge transfer is not the main photochemical process resulting in CO release.

## RESULTS/ELECTROCHEMISTRY

We have previously described a method for measuring the rates of CO binding and release to/from hydrogenases.<sup>29,30</sup> Briefly, a tiny amount of purified enzyme is either adsorbed or covalently attached<sup>31</sup> to a rotating disc electrode and inserted into the H<sub>2</sub>-saturated solution of an electrochemical cell. Catalytic H<sub>2</sub> oxidation results in a positive current whose magnitude is

proportional to turnover rate. The enzyme is repeatedly exposed to CO by injecting a small amount of CO-saturated buffer in the electrochemical cell; the concentration of inhibitor instantly increases and then decays because CO is constantly flushed away from the cell by the flow of H<sub>2</sub>; the decay is exponential,<sup>32,33</sup> as indicated in Figure 2A, with time constant  $\tau$ .

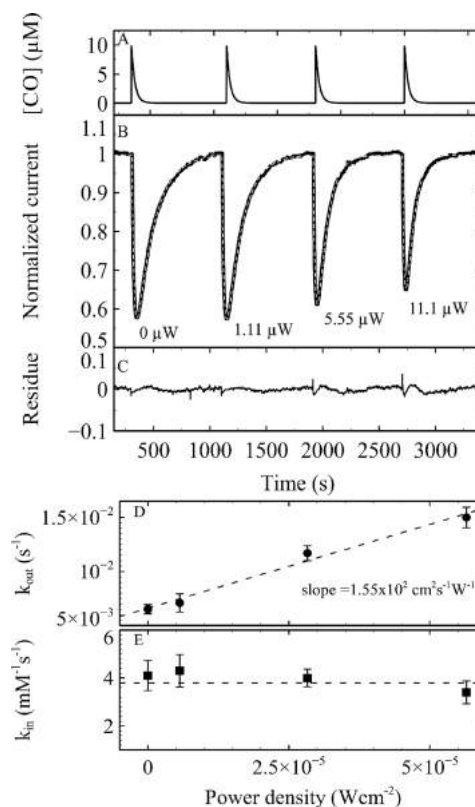


**Figure 2.** Electrochemical experiment showing the effect of 450 nm irradiation on the inhibition by CO of the FeFe hydrogenase from *M. elsdenii*. Data obtained with the FeFe hydrogenases from *C. acetobutylicum* and *C. reinhardtii* are shown in Supporting Information section 3.1, Supplementary Figures 18 and 19. Panel A shows the change in CO concentration against time, and panel B shows the resulting change in turnover rate and the fit of the kinetic model (dotted line), adjusting four values of  $k_{in}$ , four values of  $k_{out}$ , and a single value of  $\tau$ . Panel C shows the residue of the fit. The fit returned the values of the rate constants shown in panels D and E. The Y-errors show the standard deviations observed in two independent experiments (the error on  $k_{in}$  includes the error in the value of  $[CO]_0$ ).  $p(H_2) = 1$  atm,  $[CO]_0 = 10 \mu M$ ,  $\tau = 18$  s, pH = 7,  $T = 30$  °C. Electrode rotation rate = 3000 rpm.

The resulting change in catalytic current (turnover rate) is illustrated in Figure 2B. The current decreases after each injection at a rate that depends on the second-order constant of CO binding to the enzyme ( $k_{in}$ ), and returns to its initial value after the CO concentration goes back to zero, at a rate that depends on the first-order rate constant of CO release ( $k_{out}$ ) and on the value of  $\tau$ . The change in current can be analyzed to measure  $k_{in}$ ,  $k_{out}$ , and  $\tau$  (when experiments such as that in Figure 2 are analyzed, the value of  $\tau$  is forced to be the same in the fitting procedure for all four injections).

Here, we describe how the irradiation of the enzyme changes the kinetics of binding and release of CO under turnover conditions. The experimental setup that we used in this

investigation is such that the parallel beam of a monochromatic laser diode ( $\lambda = 405, 450, 532, \text{ or } 635 \text{ nm}$ ) is directed upward, toward the electrode surface, across a quartz window at the bottom of the thermostated electrochemical cell. The experiment in Figure 2 was performed by adding the same amount of CO four times in a row, the first time in the dark (actually, with the low intensity of the light of the lab), and then after increasing stepwise the power output of the diode,  $P$ , as indicated.

Figure 2B shows that all things being equal, the more powerful is the 450 nm light, the less pronounced is the inhibition. The effect is small, but it is revealed by the fit of the model (dotted line), which allows the values of  $k_{\text{in}}$  and  $k_{\text{out}}$  to be precisely measured. Figure 2D shows that illumination with violet/blue light (405 or 450 nm) has a significant effect on  $k_{\text{out}}$  (up to 3-fold at maximal power) and none on  $k_{\text{in}}$ . Green or red light (532 or 635 nm) has an effect neither on CO binding nor on CO release. We show in Figure 3 the slope of the linear

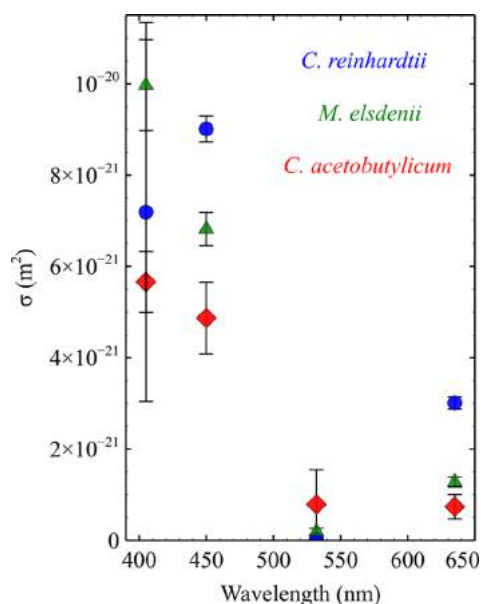


**Figure 3.** Dependence on wavelength of the effective cross section for the photodissociation of CO (calculated from the slope of the line in Figure 2D multiplied by  $h\nu$ ) on the rate of CO release from the active site of the FeFe hydrogenases from *C. reinhardtii* (blue), *C. acetobutylicum* (red), and *M. elsdenii* (green).

change in  $k_{\text{out}}$  as a function of wavelength (expressed as a cross section) against power density, for experiments carried out with three distinct FeFe hydrogenases: those from *C. reinhardtii*,<sup>34</sup> *M. elsdenii*,<sup>35</sup> and *C. acetobutylicum*.<sup>23</sup> The enzyme from *C. reinhardtii* has no other cofactor than the H-cluster, whereas the other two bear additional electron-transferring FeS clusters.<sup>1,23,34,35</sup> In all cases, only violet/blue light ( $\lambda < 500 \text{ nm}$ ) has a detectable effect on  $k_{\text{out}}$ . The effect is about the same for all three enzymes (although its magnitude decreases in the order *M. elsdenii* > *C. reinhardtii* > *C. acetobutylicum*, for reasons that cannot be elucidated at that point). Therefore, our experiments reveal an intrinsic property of the conserved H-cluster.

The change in kinetics of inhibition is not an artifact from heating. Indeed, in control experiments, we observed a current variation of less than 5 nA (<0.5% of the value of the current)

when the laser diode (any wavelength) was suddenly switched on at maximal power, whereas the catalytic current increases 2-fold upon increasing the temperature from 10 to 35 °C, showing that the light-induced temperature variation is lower than 0.1 °C. For *Clostridium acetobutylicum*, we measured an activation energy for CO release in the dark of 74 kJ/mol (in the range 16–32 °C, Supplementary Figure 20); therefore, a temperature variation of 0.1 °C increases the rate of CO release no more than 1%. Incidentally, we note that this value of the activation energy is very close to the value that we calculate in Supporting Information section 2.3 (Supplementary Table 7) and Figure 4A with the small model of the active site.

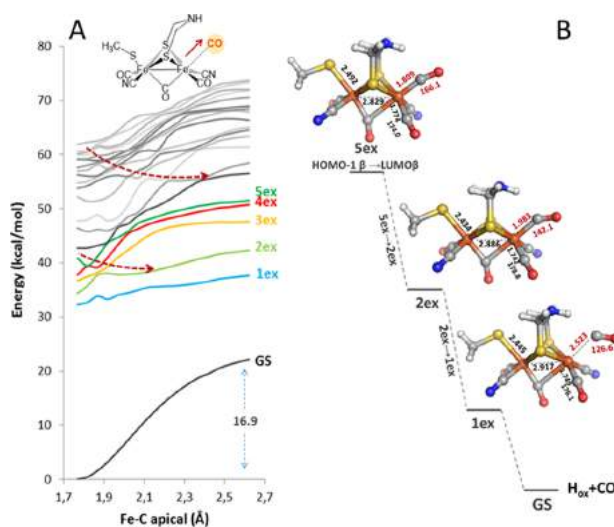


**Figure 4.** (A) Potential energy surfaces of the ground state and the first 20 excited doublet states of  $\text{Fe}_2\text{S}_2 \text{H}_{\text{ox}}\text{-CO}$  model along the apical Fe–C stretching coordinate. Energy differences in kcal/mol, computed with respect to the minimum ground-state energy. The value of the free energy dissociation barrier is also reported, and compares well with the experimental value determined in experiments shown in Supplementary Figure 20. Red arrows guide the eye to follow the dissociation pathway through the surface crossings. (B) Geometry-optimized structures for the  $\text{Fe}_2\text{S}_2$  fifth (5ex) excited state, along the CO dissociation pathway. Distances in angstroms, angles in degrees.

## TDDFT MODELING

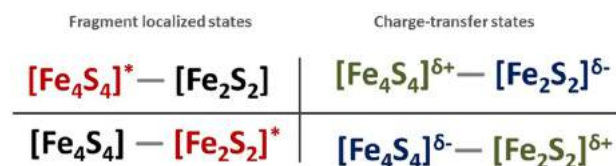
We use previously described methods<sup>36–38</sup> to characterize the electronic structure of the CO-inhibited H-cluster on the basis of the composition and energy diagram of their molecular orbital (MO) (Supplementary Figure 3a,b). Each MO can be labeled according to its localization on the  $\text{Fe}_4\text{S}_4$  or  $\text{Fe}_2\text{S}_2$  fragment. This classification will help the discussion of the electronic transitions of the H-cluster, which we shall consider as a dyad system, consisting of a  $\text{Fe}_4\text{S}_4$  cubane covalently linked to the  $\text{Fe}_2\text{S}_2$  subcluster.

Scheme 1 depicts the four possible types of electronic transitions in the H-cluster. The fragment localized excitations are those in which the mono-electronic transitions involve MO localized on a single fragment ( $\text{Fe}_4\text{S}_4$  or  $\text{Fe}_2\text{S}_2$ ), while charge-transfer (CT) excitations involve MO localized on different fragments, yielding  $\text{Fe}_4\text{S}_4 \rightarrow \text{Fe}_2\text{S}_2$  or  $\text{Fe}_2\text{S}_2 \rightarrow \text{Fe}_4\text{S}_4$  CT states, which might decay toward their corresponding CT species.

We shall use Scheme 1 to discuss the excitations of the CO inhibited H-cluster based on their propensity to induce CO



## Scheme 1. H-Cluster Electronic Excitation Resulting from Frontier MO Composition



<sup>a</sup>From left: fragment localized (in red) states (on  $\text{Fe}_4\text{S}_4$  or  $\text{Fe}_2\text{S}_2$ ), and  $\text{Fe}_4\text{S}_4 \rightarrow \text{Fe}_2\text{S}_2/\text{Fe}_2\text{S}_2 \rightarrow \text{Fe}_4\text{S}_4$  charge-transfer states.

release, which should increase in the order  $\text{Fe}_4\text{S}_4$ -localized <  $\text{Fe}_2\text{S}_2 \rightarrow \text{Fe}_4\text{S}_4$  CT states <  $\text{Fe}_4\text{S}_4 \rightarrow \text{Fe}_2\text{S}_2$  CT states <  $\text{Fe}_2\text{S}_2$  localized. Indeed, the  $\text{Fe}_4\text{S}_4$  localized states are inactive with respect to CO photolysis because the MOs involved do not show any Fe–CO orbital contributions (Supporting Information section 2.1). The  $\text{Fe}_2\text{S}_2 \rightarrow \text{Fe}_4\text{S}_4$  CT states can decay via transient  $\text{Fe}_4\text{S}_4^- - \text{Fe}_2\text{S}_2^+$  species, which should bind CO even more strongly than the  $\text{H}_{\text{ox}}-\text{CO}$  ground state because the Fe(II)Fe(II)CO fragment is undersaturated. In contrast, the decay of the  $\text{Fe}_4\text{S}_4 \rightarrow \text{Fe}_2\text{S}_2$  CT states toward  $\text{Fe}_4\text{S}_4^+ - \text{Fe}_2\text{S}_2^-$  species should result in the formation of a transient Fe(I)Fe(I)CO fragment, characterized by lower affinity for CO and lower dissociation barriers.<sup>27,36</sup> In the case of the CT states, the Fe–C bonding MO remains singly occupied, and the corresponding potential energy surface (PES) cannot be fully dissociative. The  $\text{Fe}_2\text{S}_2$  localized states should be the most active toward CO photolysis because an Fe–C antibonding/nonbonding MO is populated to the detriment of a Fe–C bonding MO, as observed previously in studies of biomimetic models of the H-cluster.<sup>27,39,40</sup>

To confirm the above model, we computed the electronic spectrum of the full  $\text{Fe}_6\text{S}_6$   $\text{H}_{\text{ox}}-\text{CO}$  system (Figure 1C) and a structural model of the CO-bound  $\text{Fe}_2\text{S}_2$  fragment (Figure 1B), the latter either including or excluding the side chains or the residues that form the H-bond network around the dtma and cyanide ligands (Supporting Figure 11). The relationship between computed excitation energies and experimental wavelength irradiation is proposed in Supporting Information section 2.5, on the basis of the comparison of TDDFT spectra computed for different models (adopting pure GGA BP86 and the hybrid PBE0 functionals) and the UV–vis spectrum of the noninhibited enzyme.<sup>41</sup> We must emphasize that the computed excitation energies for the  $\text{Fe}_6\text{S}_6$  model are not reliable enough for quantitative comparison with the experimental spectrum due to the highly negative total charge of the model, but the nature of the excitations and main mono electronic transitions can be compared to those calculated with the smaller model, for example, to identify the  $\text{Fe}_2\text{S}_2$  localized excitations. Indeed, the comparison between BP86 and PBE0 shows the well-known blue shift of the excitation energy, but not significant change in the nature of the excited states (Supporting Figure 12a).

Considering the  $\text{Fe}_6\text{S}_6$  model, we computed the first BP86 600 excitations, and we observed that most of them are of the  $\text{Fe}_4\text{S}_4$  localized type (they involve a large number of  $\text{Fe}_4\text{S}_4$  localized MOs, and the excitations are described as  $\text{Fe} \rightarrow \text{S}$  or  $\text{S} \rightarrow \text{Fe}$  intracubane CT states) (Supporting Table 2). In the low energy part of the spectrum, several weak  $\text{Fe}_4\text{S}_4 \rightarrow \text{Fe}_2\text{S}_2$  CT excitations involve the  $\text{Fe}_2\text{S}_2$  localized LUMO $\beta$ , while the intense band at higher energy results from the superposition of a large number of excitations including  $\text{Fe}_2\text{S}_2$  localized transitions. In the middle of the spectrum, we identify three

moderately intense excitations (two  $\text{Fe}_4\text{S}_4$  localized and one  $\text{Fe}_4\text{S}_4 \rightarrow \text{Fe}_2\text{S}_2$  CT) that should correspond to the shoulder at 415 nm in the experimental spectrum.<sup>41</sup> We conclude that higher energy irradiation is more effective with respect to CO photolysis because it populates  $\text{Fe}_2\text{S}_2$  localized states, whereas lower energy irradiation populates  $\text{Fe}_4\text{S}_4 \rightarrow \text{Fe}_2\text{S}_2$  CT states that are not fully dissociative.

This investigation of the  $\text{Fe}_6\text{S}_6$  model fully supports the “pencil and paper” donor–acceptor model, by confirming the fragment localized and CT nature of the excitations as proposed in Scheme 1. To reach more definite conclusions, we had to explore the excited-state surfaces of the  $\text{Fe}_2\text{S}_2$  model, as described below (unfortunately, we could not investigate the excited PES topology of the relevant states for the large model).

The computed electronic spectrum of the small model (Figure 1B) is dominated by ligand to metal and metal to ligand charge-transfer (LMCT and MLCT) excitations (Supporting Tables 5 and 6). To identify the Fe–CO loosely bound excited states, a first approach is to explore the excited PES along the CO dissociation pathways on the ground-state PES. Considering the first 20 doublet excitations (hereafter referred to as “ $n\text{ex}$ ”, with  $n = 1-20$ ), we observed a different topology of the excited PES along the reaction coordinates of apical or equatorial CO dissociation. Figure 4A reports the scans for the apical CO ligand release. As compared to the ground state,<sup>28</sup> the lower energy surfaces are loosely bound along the CO dissociation coordinate. Two series of surface crossings are observed (red arrows), the most evident starting from  $5\text{ex}$ , and indicate putative dissociation pathways. The result of the calculation regarding the release of the equatorial CO ligand is shown in Supporting Figure 13. The energy barrier for the CO dissociation (estimated from the difference between the excitation energies computed at the beginning and at the end of the PES scan, and averaged over the first 20 excited states) is twice as large for equatorial CO than for apical CO. Moreover, as described below, the dissociation of the apical CO along the pathway starting from  $5\text{ex}$  appears almost barrierless.

We investigated the decay of the MLLCT  $5\text{ex}$  state by optimizing its structure, taking the ground-state geometry as starting point, and then examining the geometry changes that result from each surface crossing (Figure 4B). The apical Fe–C bond is 0.04 Å longer in optimized  $5\text{ex}$  than in the structure of the ground state, and the Fe–C–O angle bends 4.7°, which supports the dissociative nature of this excitation. This conclusion was further confirmed by TDDFT geometry optimization of the corresponding MLLCT state (12ex) of the  $\text{Fe}_2\text{S}_2$  model in which side chain residues have been included (Supporting Information section 2.7). After optimization,  $5\text{ex}$  can be considered a  $5\text{ex}-4\text{ex}$  conical intersection, being only 0.06 kcal/mol higher than  $4\text{ex}$ . Following the pathway depicted as an arrow in Figure 4A, we mimic the vibrational relaxation by a small stretch (+0.086 Å) of the apical Fe–C to force the crossing, reaching directly the  $2\text{ex}$  state. After optimization, the  $2\text{ex}$  structure is characterized by a significant lengthening and bending of the apical Fe–CO bond (+0.183 Å, 25.6°) as compared to the ground state. In a similar manner, we observed the decay of  $2\text{ex}$  to  $1\text{ex}$ , where, after optimization, the apical Fe–CO is partially dissociated. The  $1\text{ex}$  surface crosses the ground state at  $d(\text{Fe}-\text{C}) = 2.523$  Å (Supporting Information section 2.7). At this point, a small amount of vibrational energy should be sufficient to fully dissociate the Fe–C bond.

The results of the TDDFT investigation of the large  $\text{Fe}_6\text{S}_6$  model (Figure 1C) show that the  $5\text{ex}$  in the  $\text{Fe}_2\text{S}_2$  model investigated above corresponds to a high energy excited state (242ex) in the large model (Supplementary Table 8 and Supplementary Figure 12a), consistent with the low energy excitations of the H-cluster being ineffective for CO release. We could not use the large  $\text{Fe}_6\text{S}_6$  model (Figure 1C) to investigate the  $\text{Fe}_4\text{S}_4 \rightarrow \text{Fe}_2\text{S}_2$  CT states because most of our attempts to use the spin-flip approach to optimize the geometry of the broken-symmetry  $\text{Fe}_4\text{S}_4^+ - \text{Fe}_2\text{S}_2^-$  species failed. However, we were able to optimize the structure of the  $1\text{ex}$   $\text{Fe}_6\text{S}_6$  excited state, converging to a final structure in which the Fe–S bond that connects the cubane to the  $\text{Fe}_2\text{S}_2$  subcluster is 0.13 Å longer than in the ground state, while all other distances are the same. This is consistent with the above qualitative argument according to which the CT states are not involved in CO dissociation.

## DISCUSSION

We have defined the kinetics of the reaction with CO of the oxidized H-cluster of three distinct FeFe hydrogenases as a function of wavelength in the visible range and light power. The effects are about the same for the three enzymes that we studied despite differences in cofactor compositions: the enzyme from *Chlamydomonas reinhardtii* bears only the H-cluster, whereas the other two have additional electron transferring clusters.<sup>1,23,34,35</sup> Therefore, our experiments reveal an intrinsic property of the conserved H-cluster. From the point of view of the modeling, this implies that one only needs to investigate the photochemical properties of the H-cluster.

We have characterized before the “dark” kinetics of CO binding to and release from FeFe hydrogenases.<sup>29,30,42</sup> We have shown that the reaction can be described in terms of intramolecular diffusion of CO (leading to the reversible formation a “geminate state” with rate constants  $k_1$  and  $k_{-1}$ ), and reversible  $\text{Fe}_d\text{--CO}$  bond formation (rate constants  $k_2$  and  $k_{-2}$ ). We used the results of MD and DFT calculations to calculate all four individual rate constants, which we could combine to calculate the value of the rate of inhibition, which compares well with the experimental value.<sup>42</sup> Regarding the effect of light, the usual method for studying the photo-dissociation of CO from inorganic active sites consists of triggering CO release by a short laser pulse, and following the dissociation and rebinding using time-resolved spectroscopic techniques. Such investigation has only recently been carried out with a FeFe hydrogenase.<sup>43</sup> In the experiments presented in this Article, in contrast, we measure the steady-state effect of constant monochromatic illumination; the total concentration of enzyme–CO complex is not constant, but continuous irradiation nonetheless leads to a steady-state ratio of  $[\text{E}^*\text{--CO}]$  over  $[\text{E--CO}]$  (Figure 5), which is determined by the competition between excitation, dissociative ( $k_{-2}^{h\nu}$ ), and nondissociative ( $k^{-h\nu}$ ) decay. Measuring the global rate of CO release informs on the nature and reactivity of the excited state that is formed upon illumination at a certain wavelength.

The simple binding/release kinetic model that we have used to analyze experiments carried out in the dark<sup>29,30,42</sup> can be fitted to the data recorded with the light on, showing that  $\text{E}^*\text{CO}$  is in a quasi-steady state. We show in Supporting Information section 4 that the measured values of  $k_{\text{in}}$  and  $k_{\text{out}}$  are therefore related to the rate constants in Figure 5 by the following relations:

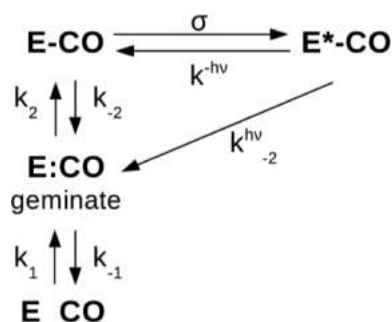


**Figure 5.** Kinetic scheme depicting the various steps that contribute to CO binding and (photo)release. Step “1” is the formation of a geminate state, from which the Fe–CO bond can be reversibly formed. The excited states decay either dissociatively or non-dissociatively.

$$k_{\text{in}} = k_1 k_2 / (k_{-1} + k_2)$$

$$k_{\text{out}} = k_{-1} (k_{-2} + k_{-2}^{h\nu} \Lambda) / ((1 + \Lambda)(k_{-1} + k_2))$$

where  $\Lambda$  is  $\sigma I / (k^{-h\nu} + k_{-2}^{h\nu})$ , with  $I$  the incident flux of photons,  $\sigma$  the cross section for light absorption,  $k^{-h\nu}$  the rate at which the excited states decay without CO dissociation, and  $k_{-2}^{h\nu}$  the rate at which the excited state dissociates CO. Our observation that the plot of  $k_{\text{out}}$  against  $P$  is a line (Figure 2D) shows that  $\Lambda \ll 1$ , consistent with the low absorption of the H-cluster. We conclude that at the low illumination power that we used, the excited states are populated more slowly than they decay either dissociatively or nondissociatively.

The absorption coefficient of  $\text{H}_{\text{ox}}\text{--CO}$  has not been published, but using the spectra of FeFe biomimetic complexes, we estimate  $\epsilon \approx 1 \text{ mM}^{-1} \text{ cm}^{-1}$  in the 400 nm region.<sup>9,44,45</sup> Using  $\sigma = \epsilon \times \ln(10) / N_a$ , the value of  $\epsilon$  translates into a molecular absorption cross-section of  $4.10^{-22} \text{ m}^2$  (for all transitions, dissociative and nondissociative). This value is very close to the cross section for the dissociative absorption of photons,  $9.10^{-21} \text{ m}^2$  in Figure 2, suggesting that, at low wavelengths, most of the absorbed photons lead to photo-dissociation of the apical CO (thus  $k^{-h\nu} \ll k_{-2}^{h\nu}$ ).

Thinking of the H-cluster in terms of a  $\text{Fe}_4\text{S}_4\text{--Fe}_2\text{S}_2$  dyad system, a very common model in photochemistry, allowed us to predict which excitations are actually effective for CO release and to identify the relevant excitations in each photochemical process. This description emerges from the analysis of the H-cluster molecular orbitals in a natural manner and will probably prove useful in further investigations of its photochemical reactivity.

The most relevant point in this TDDFT investigation is the reliable correlation between the wavelengths that prove effective in the experiments and the computed excitation energies. We cannot expect TDDFT calculations to quantitatively predict the experimental excitation energies for such a negatively charged large system, but this level of theory is able to reproduce the features of the experimental absorption spectra available in the literature.<sup>41</sup>

Our calculations clearly show that only the excitations that involve the dinuclear subcluster are active with respect to CO photodissociation, and these are found at higher energy than the CT states. This conclusion qualitatively agrees with the experimental observation of ours that only irradiation in the high energy part of the visible spectrum increases the rate of CO dissociation.

Our PES analysis clearly indicates that dissociation of the apical CO is easier than that of the equatorial or bridging CO. This is not the consequence of the constraints provided by the protein. In the case of the first Fe<sub>2</sub>S<sub>2</sub> localized state (Sex in the binuclear model), we could characterize in detail the pathway to the ground state, which is the barrierless release of the apical CO. In support of this result, we observed that if we include first-shell residue side chains in the calculation, the excited state that is equivalent to Sex also shows barrierless apical CO dissociation (SI section 2.7 and Supplementary Figure 17). These theoretical results are fully consistent with our experimental observation that most violet/blue absorbed photons induce CO release (Figure 3).

It has been observed that visible irradiation at very low temperature (<8 K) also dissociates the apical CO from H<sub>ox</sub>-CO, but distinct photoproducts (the structures of which were not fully clarified) are formed under certain cryogenic conditions, such as temperature in the range 15–30 K.<sup>12–15</sup> A possible explanation is that in this intermediate range of *T*, the greater vibrational energy of the system overcomes the barrier for the formation of a second photoproduct, which is not stable at room temperature and isomerizes to the most stable form.

Albracht and co-workers<sup>14,15</sup> have shown that white light damages the enzyme from *D. desulfuricans*, and suggested that this could be a result of the photolysis of one or more intrinsic CO ligands. We have observed no effect of light (in the wavelength and power ranges described here) on the turnover rate, which suggests that photodamage might be induced by higher energy and/or longer irradiation. We are now investigating, both theoretically and experimentally, the hypothesis that the UV irradiation might irreversibly inactivate the enzyme by inducing the release of intrinsic CO ligands or breaking of other Fe–ligand bonds.

TDDFT calculations being particularly challenging, it will be essential that further results be supported by experimental data. For example, one may oppose to the calculations presented here that TDDFT cannot describe excited states of double-excitation character, but our experiments actually rule out the relevance of double absorption. Indeed, we observe a linear dependence of the rate of dissociation on light power. Moreover, the absorption of the H-cluster is very weak (light absorption limits the rate of photorelease), making double-excitation very unlikely.

A limitation of our work is the low quality of the excitation energies that are calculated using pure GGA functionals such as BP86 and/or small models of the H-cluster, but our aim was not to reproduce the experimental spectrum; instead, it was to shed light on the first instants of the photodynamics of CO-inhibited H-cluster upon irradiation. Here, it is more important to describe the nature of the excitations than to accurately calculate their energies.

We believe that in the future, the elucidation of the photochemical processes will also help in understanding the reactivity of the active site in the dark, because the main electronic transitions involved in the excited states may occur as transient ground states either in the catalytic cycle or upon formation of inactive states under oxidative or reductive conditions.<sup>17,46</sup>

## METHODS

**Enzymes.** We produced the FeFe hydrogenases from *C. acetobutylicum* and *C. reinhardtii* FeFe hydrogenases as described in

ref 17. The enzyme from *M. elsdenii* was heterologously expressed in *E. coli* and activated as described in ref 47.

**Electrochemistry.** We covalently attached the enzymes onto pyrolytic edge graphite rotating electrodes (diameter 1 mm) using the method described in ref 31. We analyzed the electrochemical data using the model in ref 28 and the open source program available at [www.qsoas.org](http://www.qsoas.org).<sup>48</sup> We used laser components Flexpoint dot lasers,  $\lambda = 405$  nm, 9.5  $\mu$ W;  $\lambda = 450$  nm, 11.1  $\mu$ W;  $\lambda = 532$  nm, 11.3  $\mu$ W; or  $\lambda = 635$  nm, 8.1  $\mu$ W. The diameter of the parallel beam was 5 mm. The power output could be tuned between 0 and 100% and measured with a Newton optical power meter 1916-C.

**Computational Details.** The quantum mechanics calculations performed have been carried out with the TURBOMOLE 7 suite of programs.<sup>49</sup> In particular, DFT and TDDFT calculations were carried out using the BP86 functional and an all-electron valence triple- $\zeta$  (def-TZVP) basis set with polarization functions on all atoms, in conjunction with the resolution-of-the-identity (RI) technique (Supporting Information section 1). Such computational approach proved appropriate for the correct representation of the electronic properties of the H-cluster, both considering binuclear Fe<sub>2</sub>S<sub>2</sub> and complete Fe<sub>6</sub>S<sub>6</sub> models, as reported in previous works.<sup>3,28,38,50,51</sup> The broken symmetry approach was implemented to reproduce the proper spin state of the full H-cluster model.<sup>36,38,52</sup>

## ASSOCIATED CONTENT

### Supporting Information

The Supporting Information is available free of charge on the ACS Publications website at DOI: 10.1021/jacs.6b06603.

DFT and TDDFT computational details and models; electronic structures of the models, CO-dissociation computed free energy barriers, TDDFT spectra of Fe<sub>2</sub>S<sub>2</sub>, Fe<sub>2</sub>S<sub>2</sub> with residues, and Fe<sub>6</sub>S<sub>6</sub> models (BP86 and/or PBE0), PES scans for the apical and equatorial CO dissociation, and explanation of the method used to study the CO dissociation pathway from Sex; experimental PFV data for the CO-photodissociation for the FeFe hydrogenase of *C. reinhardtii* and *C. acetobutylicum*; experimental determination of the CO-release activation energy; and kinetic scheme and derivation of the rate constants used in the main text (PDF)

## AUTHOR INFORMATION

### Corresponding Authors

\*leger@imm.cnrs.fr

\*luca.bertini@unimib.it

### Notes

The authors declare no competing financial interest.

## ACKNOWLEDGMENTS

The French teams were supported by CNRS, Aix Marseille Université, INSA, CEA, Agence Nationale de la Recherche (ANR-12-BS08-0014, ANR-14-CE05-0010, LABEX program ARCANE ANR-11-LABX-0003-01), and the A\*MIDEX grant (ANR-11-IDEX-0001-02) funded by the French Government “Investissements d’Avenir” program.

## REFERENCES

- (1) Fontecilla-camps, J. C.; Volbeda, A.; Cavazza, C.; Nicolet, Y. *Chem. Rev.* **2007**, *107*, 4273–4303.
- (2) Lubitz, W.; Ogata, H.; Ru, O.; Reijerse, E. *Chem. Rev.* **2014**, *114*, 4081–4148.
- (3) Greco, C.; Fourmond, V.; Baffert, C.; Wang, P.; Dementin, S.; Bertrand, P.; Bruschi, M.; Blumberger, J.; De Gioia, L.; Léger, C. *Energy Environ. Sci.* **2014**, *7* (11), 3543–3573.

- (4) Thauer, R. K.; Käufer, B.; Zähringer, M.; Jungermann, K. *Eur. J. Biochem.* **1974**, *42* (2), 447–452.
- (5) Pandelia, M. E.; Ogata, H.; Currell, L. J.; Flores, M.; Lubitz, W. *Biochim. Biophys. Acta, Bioenerg.* **2010**, *1797* (2), 304–313.
- (6) Nicolet, Y.; Lacey, A. L.; De Vernede, X.; Fernandez, V. M.; Hatchikian, E. C.; Fontecilla-camps, J. C. *J. Am. Chem. Soc.* **2001**, *123*, 1596–1601.
- (7) Fan, H.; Hall, M. B. *J. Am. Chem. Soc.* **2001**, *123*, 3828–3829.
- (8) Silakov, A.; Wenk, B.; Reijerse, E.; Lubitz, W. *Phys. Chem. Chem. Phys.* **2009**, *11*, 6592–6599.
- (9) Berggren, G.; Adamska, A.; Lambert, C.; Simmons, T. R.; Esselborn, J.; Atta, M.; Gambarelli, S.; Mouesca, J.-M.; Reijerse, E. J.; Lubitz, W.; Happe, T.; Artero, V.; Fontecave, M. *Nature* **2013**, *499* (7456), 66–69.
- (10) Lemon, B. J.; Peters, J. W. *J. Am. Chem. Soc.* **2000**, *122* (15), 3793–3794.
- (11) Parkin, A.; Cavazza, C.; Fontecilla-Camps, J. C.; Armstrong, F. A. *J. Am. Chem. Soc.* **2006**, *128* (4), 16808–16815.
- (12) Chen, Z.; Lemon, B. J.; Huang, S.; Swartz, D. J.; Peters, J. W.; Bagley, K. A. *Biochemistry* **2002**, *41*, 2036–2043.
- (13) Silakov, A.; Reijerse, E. J.; Lubitz, W. *Eur. J. Inorg. Chem.* **2011**, *2011* (7), 1056–1066.
- (14) Albracht, S. P. J.; Roseboom, W.; Hatchikian, E. C. *JBIC, J. Biol. Inorg. Chem.* **2006**, *11* (1), 88–101.
- (15) Roseboom, W.; De Lacey, A. L.; Fernandez, V. M.; Hatchikian, E. C.; Albracht, S. P. J. *JBIC, J. Biol. Inorg. Chem.* **2006**, *11* (1), 102–118.
- (16) Senger, M.; Mebs, S.; Duan, J.; Wittkamp, F.; Apfel, U.-P.; Heberle, J.; Haumann, M.; Stripp, S. T. *Proc. Natl. Acad. Sci. U. S. A.* **2016**, *113* (30), 8454–8459.
- (17) Fourmond, V.; Greco, C.; Sybirna, K.; Baffert, C.; Wang, P.; Ezanno, P.; Montefiori, M.; Bruschi, M.; Meynial-Salles, I.; Soucaille, P.; Blumberger, J.; Bottin, H.; De Gioia, L.; Léger, C. *Nat. Chem.* **2014**, *6* (4), 336–342.
- (18) Gust, D.; Moore, T. A.; Moore, A. L. *Acc. Chem. Res.* **2009**, *42* (12), 1890–1898.
- (19) Lubner, C. E.; Applegate, A. M.; Knörzer, P.; Ganago, A.; Bryant, D. A.; Happe, T.; Golbeck, J. H. *Proc. Natl. Acad. Sci. U. S. A.* **2011**, *108* (52), 20988–20991.
- (20) Ghirardi, M. L. *Photosynth. Res.* **2015**, *125* (3), 383–393.
- (21) Lee, C.; Park, H. S.; Fontecilla-camps, J. C.; Reiser, E. *Angew. Chem., Int. Ed.* **2016**, *55*, 5971–5974.
- (22) Ciaccafava, A.; Hamon, C.; Infossi, P.; Marchi, V.; Giudici-Orticoni, M.-T.; Lojou, E. *Phys. Chem. Chem. Phys.* **2013**, *15* (39), 16463–16467.
- (23) Peters, J. W.; Lanzilotta, W. N.; Lemon, B. J.; Seefeldt, L. C. *Science* **1998**, *282* (5395), 1853–1858.
- (24) Li, Y.; Rauchfuss, T. B. *Chem. Rev.* **2016**, *116* (12), 7043–7077.
- (25) Kania, R.; Frederix, P. W. J. M.; Wright, J. a; Ulijn, R. V.; Pickett, C. J.; Hunt, N. T. *J. Chem. Phys.* **2012**, *136* (4), 44521.
- (26) Caplins, B. W.; Lomont, J. P.; Nguyen, S. C.; Harris, C. B. *J. Phys. Chem. A* **2014**, *118* (49), 11529–11540.
- (27) Bertini, L.; Greco, C.; Fantucci, P.; De Gioia, L. *Int. J. Quantum Chem.* **2014**, *114* (13), 851–861.
- (28) Bertini, L.; Fantucci, P.; De Gioia, L.; Zampella, G. *Inorg. Chem.* **2013**, *52*, 9826–9841.
- (29) Liebgott, P.; Leroux, F.; Burlat, B.; Dementin, S.; Baffert, C.; Lautier, T.; Fourmond, V.; Ceccaldi, P.; Cavazza, C.; Meynial-Salles, I.; Soucaille, P.; Fontecilla-Camps, J. C.; Guigliarelli, B.; Bertrand, P.; Rousset, M.; Léger, C. *Nat. Chem. Biol.* **2010**, *6* (1), 63–70.
- (30) Baffert, C.; Bertini, L.; Lautier, T.; Greco, C.; Sybirna, K.; Ezanno, P.; Etienne, E.; Soucaille, P.; Bertrand, P.; Meynial-salles, I.; De Gioia, L.; Léger, C. *J. Am. Chem. Soc.* **2011**, *133*, 2096–2099.
- (31) Baffert, C.; Sybirna, K.; Ezanno, P.; Lautier, T.; Hajj, V.; Meynial-Salles, I.; Soucaille, P.; Bottin, H.; Léger, C. *Anal. Chem.* **2012**, *84* (18), 7999–8005.
- (32) Léger, C.; Dementin, S.; Bertrand, P.; Rousset, M.; Guigliarelli, B. *J. Am. Chem. Soc.* **2004**, *126* (38), 12162–12172.
- (33) Orain, C.; Saujet, L.; Gauquelin, C.; Soucaille, P.; Meynial-Salles, I.; Baffert, C.; Fourmond, V.; Bottin, H.; Léger, C. *J. Am. Chem. Soc.* **2015**, *137* (9), 12580–12587.
- (34) Mulder, D. W.; Boyd, E. S.; Sarma, R.; Lange, R. K.; Endrizzi, J. a; Broderick, J. B.; Peters, J. W. *Nature* **2010**, *465* (7295), 248–251.
- (35) Nicolet, Y.; Piras, C.; Legrand, P.; Hatchikian, C. E.; Fontecilla-Camps, J. C. *Structure* **1999**, *7* (1), 13–23.
- (36) Fiedler, A. T.; Brunold, T. C. *Inorg. Chem.* **2005**, *44* (25), 9322–9334.
- (37) Siegbahn, P. E. M.; Tye, J. W.; Hall, M. B. *Chem. Rev.* **2007**, *107*, 4414–4435.
- (38) Bruschi, M.; Greco, C.; Bertini, L.; Fantucci, P.; Ryde, U.; De Gioia, L. *J. Am. Chem. Soc.* **2010**, *132*, 4992–4993.
- (39) Bertini, L.; Greco, C.; Bruschi, M.; Fantucci, P.; De Gioia, L. *Organometallics* **2010**, *29* (9), 2013–2025.
- (40) Hunt, N. T.; Wright, J. A.; Pickett, C. *Inorg. Chem.* **2016**, *55* (2), 399–410.
- (41) Swanson, K. D.; Ratzloff, M. W.; Mulder, D. W.; Artz, J. H.; Ghose, S.; Hoffman, A.; White, S.; Zadovnyy, O. A.; Broderick, J. B.; Bothner, B.; King, P. W.; Peters, J. W. *J. Am. Chem. Soc.* **2015**, *137* (5), 1809–1816.
- (42) Kubas, A.; Orain, C.; De Sancho, D.; Saujet, L.; Sensi, M.; Gauquelin, C.; Meynial-Salles, I.; Soucaille, P.; Bottin, H.; Baffert, C.; Fourmond, V.; Best, R.; Blumberger, J.; Léger, C. *Nat. Chem.* **2016**, DOI: 10.1038/nchem.2592.
- (43) Mirmohades, M.; Adamska-Venkatesh, A.; Sommer, C.; Reijerse, E.; Lomoth, R.; Lubitz, W.; Hammarström, L. *J. Phys. Chem. Lett.* **2016**, *7* (16), 3290–3293.
- (44) Roy, S.; Jones, A. K. *Nat. Chem. Biol.* **2013**, *9* (10), 603–605.
- (45) Thornley, W. A.; Bitterwolf, T. E. *Chem. - Eur. J.* **2015**, *21*, 18218–18229.
- (46) Hajj, V.; Baffert, C.; Sybirna, K.; Meynial-Salles, I.; Soucaille, P.; Bottin, H.; Fourmond, V.; Léger, C. *Energy Environ. Sci.* **2014**, *7* (2), 715.
- (47) Caserta, G.; Adamska-Venkatesh, A.; Pecqueur, L.; Atta, M.; Artero, V.; Souvik, R.; Reijerse, E.; Lubitz, W.; Fontecave, M. *Biochim. Biophys. Acta, Bioenerg.* **2016**, *1857* (11), 1734–1740.
- (48) Fourmond, V. *Anal. Chem.* **2016**, *88*, 5050–5052.
- (49) Ahlrichs, R.; Bär, M.; Häser, M.; Horn, H.; Kölmel, C. *Chem. Phys. Lett.* **1989**, *162* (3), 165–169.
- (50) Stiebritz, M. T.; Reiher, M. *Inorg. Chem.* **2009**, *48* (15), 7127–7140.
- (51) Liu, C.; Liu, T.; Hall, M. B. *J. Chem. Theory Comput.* **2015**, *11* (1), 205–214.
- (52) Bruschi, M.; Greco, C.; Fantucci, P.; De Gioia, L. *Inorg. Chem.* **2008**, *47* (13), 6056–6071.

# Reactivity of the excited states of the H-cluster of FeFe hydrogenases

Matteo Sensi, Carole Baffert, Claudio Greco, Giorgio Caserta, Charles Gauquelin, Laure Saujet, Marc Fontecave, Souvik Roy, Vincent Artero, Philippe Soucaille, Isabelle Meynial-Salles, Hervé Bottin, Luca de Gioia, Vincent Fourmond, Christophe Léger, Luca Bertini.

## Supporting information

1 – DFT and TDDFT - Supplementary Methods.....	S2
1.1 - Computational details.....	S2
1.2 - The H <sub>ox</sub> -CO models.....	S2
2 - DFT and TDDFT - Supplementary Results .....	S4
2.1 - The electronic structure of the Fe <sub>6</sub> S <sub>6</sub> H <sub>ox</sub> -CO model.....	S4
2.2 - The electronic structure of the Fe <sub>2</sub> S <sub>2</sub> H <sub>ox</sub> -CO model.....	S11
2.3 - CO dissociation free energy barriers for Fe <sub>2</sub> S <sub>2</sub> and Fe <sub>6</sub> S <sub>6</sub> H <sub>ox</sub> -CO models .....	S18
2.4 - TDDFT computed spectrum of the Fe <sub>2</sub> S <sub>2</sub> H <sub>ox</sub> -CO model .....	S20
2.5 - Comparison of the Fe <sub>2</sub> S <sub>2</sub> and Fe <sub>6</sub> S <sub>6</sub> H <sub>ox</sub> -CO model TDDFT spectra for band assignment .....	S21
2.6 – Fe <sub>2</sub> S <sub>2</sub> -CO PES scan for apical and equatorial CO .....	S26
2.7 – Characterization of the apical CO dissociation in 5ex of Fe <sub>2</sub> S <sub>2</sub> -CO.....	S27
3 – PFV – Supplementary Results .....	S30
3.1 - CO inhibition as function of the power of illumination .....	S30
3.2 – Activation energy for CO release .....	S32
4 – Kinetic scheme and derivation of the rate constants .....	S33
References .....	S34

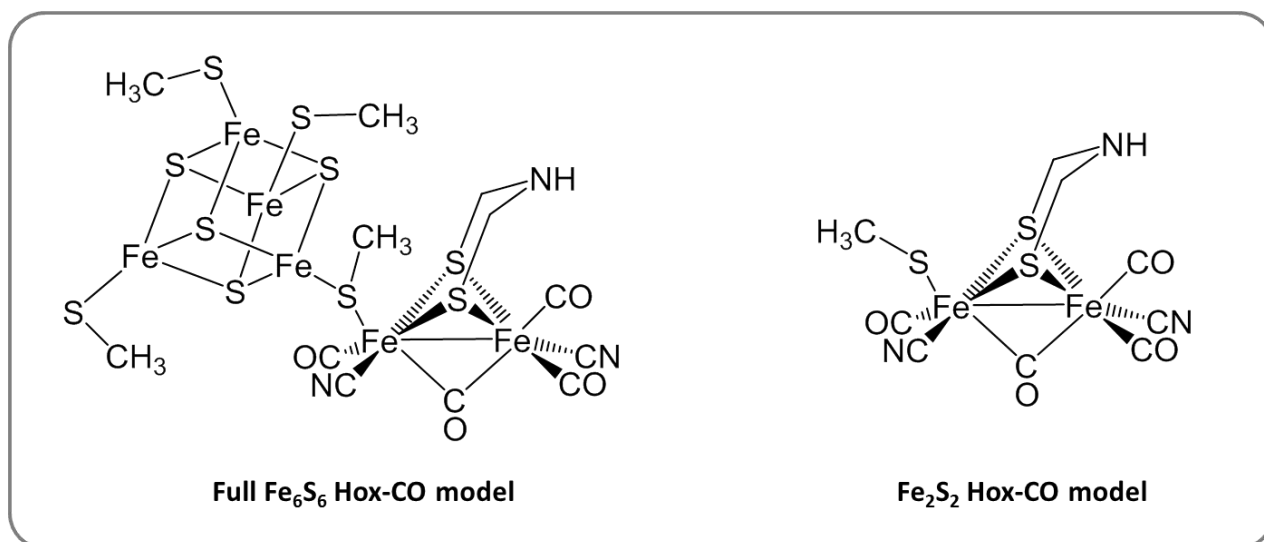
## 1 – DFT and TDDFT - Supplementary Methods

### 1.1 - Computational details

Computations were performed using pure Gradient Generalized Approximation BP86,<sup>iii</sup> and hybrid PBE0<sup>iii</sup> functionals. The Resolution of Identity (RI) technique was adopted for pure functionals in order to save CPU time.<sup>iv</sup> Basis sets of triple- $\zeta$  plus polarization split valence quality<sup>v</sup> were adopted for all atoms in the complex. All the computations presented have been carried out using TURBOMOLE<sup>vi</sup> suite of programs. DFT grid-size was set to standard m3 value. The optimization of transition state (TS) structures on the ground state PES was carried out according to a procedure based on a pseudo-Newton-Raphson method. Analytic excited state energy gradients were recently implemented<sup>vii</sup> within TURBOMOLE suite of programs in combination with the RI technique.<sup>viii</sup> Ground state and excited state geometry optimizations were carried out with convergence criteria fixed to  $10^{-6}$  hartree for the energy and  $0.001$  hartree·bohr<sup>-1</sup> for the gradient norm vector. The explorations of the excited state PES were carried out using the following approach. Starting from the ground state structure, a given bond was elongated from its equilibrium distance in a number of steps with constant increment ( $0.05\text{\AA}$ ). For each step, first the geometry parameters were optimized on the ground state PES imposing the constraint on the elongated distance and then the TDDFT excitation energies were computed. This computational setting<sup>ix,x,xi,xii,xiii,xiv</sup> provides ground state geometry parameters in good agreement with experimental X-ray values, and a reasonable picture for excited state PES properties.

### 1.2 - The H<sub>ox</sub>-CO models

The TDDFT modelling of the photochemical properties of H<sub>ox</sub>-CO has been carried out on two different models of the H-cluster. The larger model  $[\text{Fe}_4\text{S}_4(\text{SCH}_3)_4\text{Fe}_2(\mu\text{-adt})(\mu\text{CO})(\text{CO})_3(\text{CN})_2]^{2-}$  comprises the whole Fe<sub>6</sub>S<sub>6</sub> cluster. The iron atoms of the Fe<sub>4</sub>S<sub>4</sub> cubane are linked with four cysteine residues considered as <sup>-</sup>SCH<sub>3</sub> groups. One of the SCH<sub>3</sub><sup>-</sup> group binds the Fe<sub>2</sub>S<sub>2</sub> subcluster in the Fe<sup>I</sup>Fe<sup>II</sup> redox state. To account for anti-ferromagnetic spin-coupling we used the broken-symmetry approach. The Fe<sub>2</sub>S<sub>2</sub> subcluster model is a  $[\text{Fe}_2(\mu\text{-adt})(\mu\text{CO})(\text{CO})_3(\text{CN})_2]^{2-}$  complex, in which the Fe<sub>4</sub>S<sub>4</sub> cubane has been deleted, leaving a coordinated methylthiolate group coordinated to the proximal Fe atom.



**Supplementary Figure 1.** The two models considered in the TDDFT computation and characterization of the electronic spectrum of H<sub>ox</sub>-CO. The full Fe<sub>6</sub>S<sub>6</sub> model has been considered in its broken-symmetry ground state with total charge equal to -3; the model of the Fe<sub>2</sub>S<sub>2</sub> portion has total charge equal to -2. In both cases the electronic spectra have been computed at the DFT optimized geometry. We also considered the Fe<sub>2</sub>S<sub>2</sub> model with an extra Br<sup>-</sup> atom placed far from the 2Fe core to compute the electronic spectrum on a system with the same total charge as the full Fe<sub>6</sub>S<sub>6</sub> model.

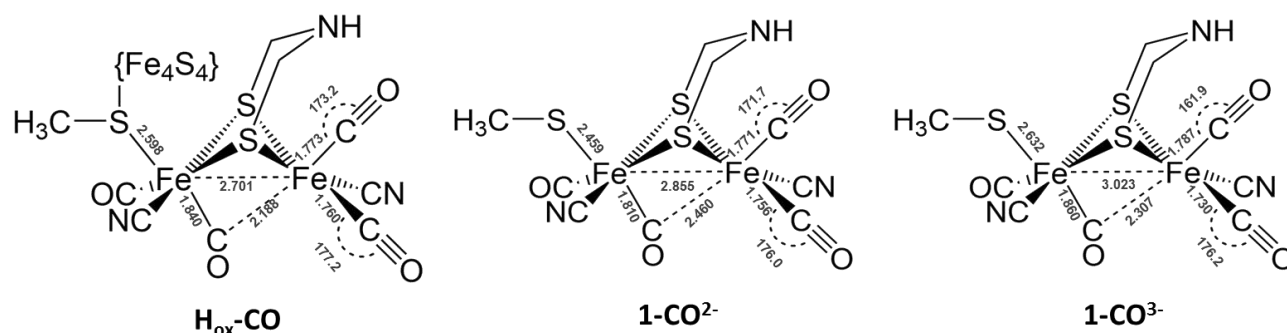
Regarding the two binuclear models studied in this paper, in principle a model with the HSCH<sub>3</sub> ligand instead SCH<sub>3</sub><sup>-</sup> would be a better choice because it holds only a single negative charge but, unfortunately, the HSCH<sub>3</sub> ligand tends to dissociate when the molecular structure is perturbed during TDDFT geometry optimizations.

The ground state structure of the **H<sub>ox</sub>** and **H<sub>ox</sub>-CO** model clusters have been investigated in this paper at the same level of theory adopted in a recent paper<sup>xv</sup> in which are reported the results of an extensive DFT investigation of the energetics, structure and bonding properties of a series Fe<sup>I</sup>Fe<sup>I</sup> and Fe<sup>I</sup>Fe<sup>II</sup> CO models characterized by a ligand coordination gradually more similar to the full *H-cluster*. The calculated  $\Delta G_f$  of the **H<sub>ox</sub>-CO** model, equal to -11.4 kcal·mol<sup>-1</sup>, is in reasonable agreement with the experimental value of -7.7 kcal·mol<sup>-1</sup> measured by Thauer<sup>xvi</sup> et al. and the value of -9 kcal·mol<sup>-1</sup> in our previous experimental study<sup>xvii</sup>. The Fe<sub>2</sub>S<sub>2</sub> sub-unit in **H<sub>ox</sub>** models is essentially a 35-electron unsaturated complex and therefore the new Fe-C bond in **H<sub>ox</sub>-CO** is formed to the detriment of the Fe-Fe bond which becomes 0.175Å longer. In Supplementary Figure 2 (left), we report the main **H<sub>ox</sub>-CO** optimized geometry parameters. It is important to underline that i) the  $\mu$ CO is not fully bridging, it is more closely bound to the proximal Fe atom than to the distal Fe; ii) the terminal apical CO ligand on Fe<sub>d</sub> is slightly less bound than the equatorial CO according to the comparison of the Fe-C distances and Fe-C-O angles.

In the following sections we report the optimized geometry computed at the level of theory adopted (Supplementary Fig. 2), the MO diagram and selected MO isosurface plots (Supplementary Fig. 3a/b), Mulliken MO populations (Supplementary Table 1), TDDFT electronic spectrum (Supplementary Table 2), and differential Mulliken MO populations computed according to the main one-electron transitions (Supplementary Table 3).

The analysis of the Frontier MOs (FMOs) involved in the main mono-electronic transitions (Supplementary Table 2) shows that the MOs around the Fermi level considered are Fe<sub>4</sub>S<sub>4</sub> localized except 231 $\beta$ . This implies that most of the lower energy excitations will be Fe<sub>4</sub>S<sub>4</sub> localized or Fe<sub>4</sub>S<sub>4</sub>→Fe<sub>2</sub>S<sub>2</sub> CT states. Occupied (respectively virtual) Fe<sub>2</sub>S<sub>2</sub> localized MOs are found at lower (respectively higher) energy, suggesting that Fe<sub>2</sub>S<sub>2</sub> localized states are higher in energy.

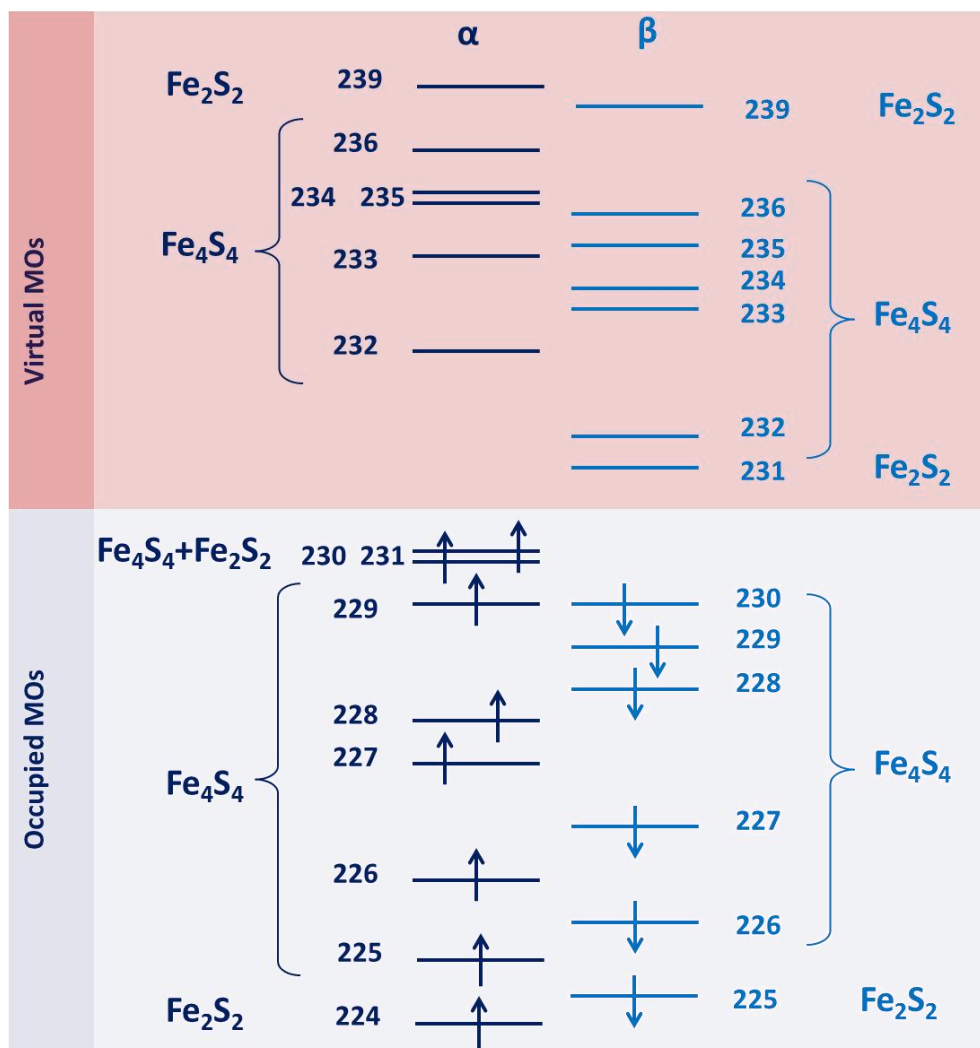
In Supplementary Table 2, we report the excitation energies for the most relevant transitions among the first 600 doublet excited states. Using the Mulliken population of the FMOs considered to compute the differential population for each excitation, we observed that the Fe<sub>4</sub>S<sub>4</sub>-Fe<sub>2</sub>S<sub>2</sub> dyad model can be properly applied to the H-cluster. Most of the excitations considered can be described in terms of localized Fe<sub>4</sub>S<sub>4</sub> or Fe<sub>2</sub>S<sub>2</sub> states or Fe<sub>4</sub>S<sub>4</sub>→Fe<sub>2</sub>S<sub>2</sub>/Fe<sub>2</sub>S<sub>2</sub>→Fe<sub>4</sub>S<sub>4</sub> charge transfer (CT) states. According to the differential Mulliken populations, most of the considered transitions have localized Fe<sub>4</sub>S<sub>4</sub> character, but at lower energy we found 8 Fe<sub>4</sub>S<sub>4</sub>→Fe<sub>2</sub>S<sub>2</sub> CT states. The Fe<sub>2</sub>S<sub>2</sub> localized states are found only at higher energy.



**Supplementary Figure 2.** Optimized geometries of the models considered in the TDDFT investigation. **1-CO<sup>2-</sup>** and **1-CO<sup>3-</sup>** are the Fe<sup>I</sup>Fe<sup>II</sup> H<sub>ox</sub>-CO and Fe<sup>I</sup>Fe<sup>I</sup> H<sub>red</sub>-CO models respectively Distances in Å, angles in degree.

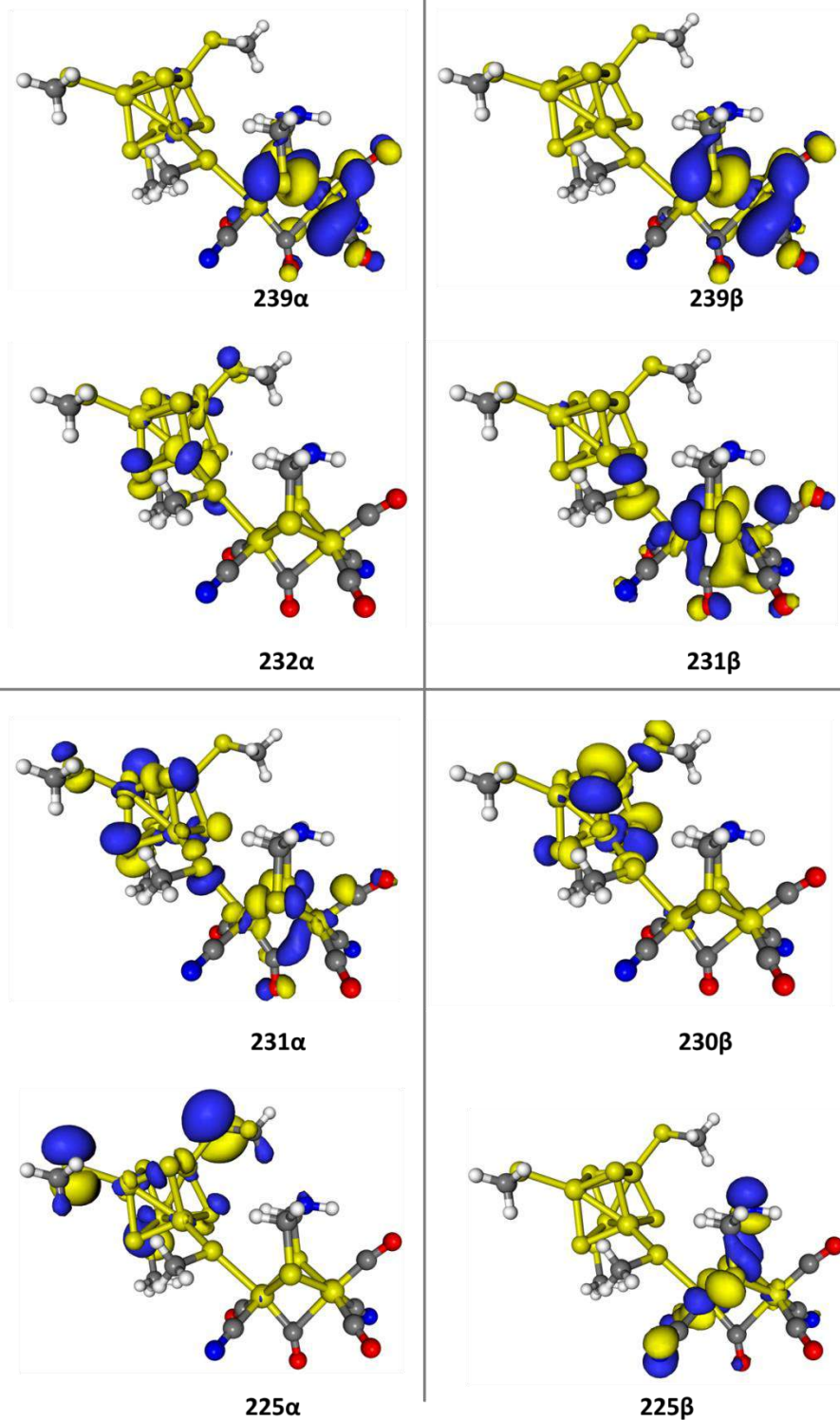
## 2 - DFT and TDDFT - Supplementary Results

### 2.1 - The electronic structure of the $\text{Fe}_6\text{S}_6 \text{H}_{\text{ox}}\text{-CO}$ model



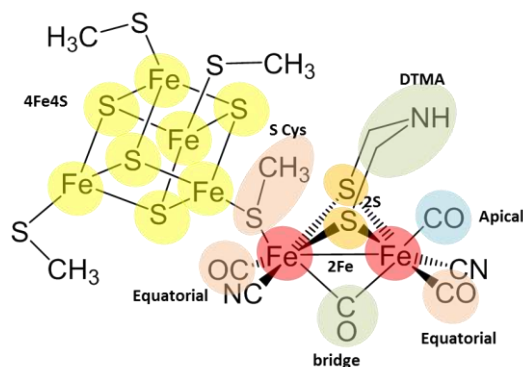
**Supplementary Figure 3a.** Molecular orbital (MO) diagram for the full  $\text{Fe}_6\text{S}_6 \text{H}_{\text{ox}}\text{-CO}$  model. The MOs considered here are those that are mainly involved in the computed electronic spectrum and are classified according to spin labels ( $\alpha$  on the right,  $\beta$  on the left) and localization (on the  $\text{Fe}_4\text{S}_4$  cubane or on the  $\text{Fe}_2\text{S}_2$  portion). We carried out this assignment according to the Mulliken MO populations reported in Supplementary Table 1.





**Supplementary Figure 3b.** MO Isosurfaces (0.05 a.u) for selected MO of the full Fe<sub>6</sub>S<sub>6</sub> H<sub>ox</sub>-CO model. For the discussion of the photochemical properties of H<sub>ox</sub>-CO is important to note the Fe<sub>2</sub>S<sub>2</sub> localized nature of the 231 $\beta$ , which is the first unoccupied  $\beta$  MO.

**Supplementary Table 1.** Mulliken MO populations of the Fe<sub>6</sub>S<sub>6</sub> frontier MO mainly involved in the TDDFT computed electronic spectrum. The population of all spin-orbit MO spin densities integrates to 1 electron. The values are collected as a function of a specific part of the systems (Fe<sub>4</sub>S<sub>4</sub> and Fe<sub>2</sub>S<sub>2</sub> collect the population of all the atoms that belong to the cubane or to the binuclear portions and their sum is equal to 1) or group of atoms (4FeS4 indicate the sum of the Fe and S atoms of the cubane; 2•Fe and 2•S the sum of the Fe and S atoms of the Fe<sub>2</sub>S<sub>2</sub> portion; CO apical, Co equatorial, CO bridge, DTMA and S cys correspond to the ligand of the Fe<sub>2</sub>S<sub>2</sub> portion). In the picture below, we summarize the atoms/group aggregations proposed in the table.



	212a	213a	214a	215a	216a	217a	218a	219a	220a	221a	222a	223a	224a	225a	226a
	H-19	H-18	H-17	H-16	H-15	H-14	H-13	H-12	H-11	H-10	H-9	H-8	H-7	H-6	H-5
<b>Fe<sub>4</sub>S<sub>4</sub></b>	0.17	1.00	0.96	0.07	0.92	0.91	0.03	0.66	0.27	0.56	0.35	0.88	0.08	0.97	1.00
<b>Fe<sub>2</sub>S<sub>2</sub></b>	0.83	0.00	0.04	0.93	0.08	0.09	0.97	0.34	0.73	0.44	0.65	0.12	0.92	0.03	0.00
<b>4Fe4S</b>	0.04	0.85	0.84	0.05	0.70	0.79	0.03	0.28	0.13	0.24	0.15	0.41	0.03	0.32	0.77
<b>2•Fe</b>	0.16	0.00	0.01	0.21	0.04	0.04	0.60	0.19	0.44	0.29	0.47	0.09	0.53	0.01	0.00
<b>2•S</b>	0.18	0.00	0.02	0.43	0.01	0.02	0.07	0.08	0.07	0.01	0.02	0.01	0.13	0.01	0.00
<b>CO apical</b>	0.00	0.00	0.00	0.03	0.00	0.00	0.05	0.01	0.02	0.01	0.00	0.00	0.00	0.00	0.00
<b>CO equatorial</b>	0.03	0.00	0.00	0.05	0.01	0.00	0.04	0.02	0.03	0.02	0.03	0.00	0.05	0.00	0.00
<b>μCO</b>	0.10	0.00	0.01	0.26	0.00	0.00	0.05	0.01	0.02	0.01	0.03	0.00	0.08	0.00	0.00
<b>DTMA</b>	0.27	0.00	0.00	0.04	0.01	0.01	0.02	0.01	0.03	0.01	0.01	0.00	0.13	0.01	0.00
<b>S cys</b>	0.11	0.00	0.00	0.01	0.02	0.05	0.00	0.22	0.01	0.05	0.05	0.07	0.02	0.01	0.00

	227a	228a	229a	230a	231a	232a	233a	234a	235a	236a	237a	248a	239a	240a
	H-4	H-3	H-2	H-1	HOMO	LUMO	L+1	L+2	L+3	L+4	L+5	L+6	L+7	L+8
<b>Fe<sub>4</sub>S<sub>4</sub></b>	0.99	0.98	0.94	0.63	0.62	0.94	0.99	0.98	0.90	0.98	0.98	0.96	0.08	0.55
<b>Fe<sub>2</sub>S<sub>2</sub></b>	0.01	0.02	0.06	0.37	0.38	0.06	0.01	0.02	0.10	0.02	0.02	0.04	0.92	0.45
<b>4Fe4S</b>	0.40	0.56	0.87	0.53	0.52	0.88	0.93	0.91	0.81	0.90	0.91	0.89	0.07	0.48
<b>2•Fe</b>	0.01	0.01	0.04	0.21	0.22	0.03	0.00	0.01	0.05	0.01	0.01	0.02	0.40	0.24
<b>2•S</b>	0.00	0.01	0.01	0.07	0.07	0.01	0.00	0.00	0.01	0.00	0.00	0.00	0.21	0.05
<b>CO apical</b>	0.00	0.00	0.00	0.02	0.03	0.01	0.00	0.00	0.01	0.00	0.00	0.00	0.09	0.05
<b>COequatorial</b>	0.00	0.00	0.00	0.01	0.01	0.00	0.00	0.00	0.01	0.00	0.00	0.00	0.10	0.04
<b>μCO</b>	0.00	0.00	0.00	0.04	0.04	0.00	0.00	0.00	0.01	0.00	0.00	0.00	0.13	0.00
<b>DTMA</b>	0.00	0.00	0.00	0.00	0.00	0.00	0.00	0.00	0.00	0.00	0.01	0.00	0.02	0.00
<b>S cys</b>	0.00	0.01	0.04	0.03	0.04	0.02	0.01	0.01	0.03	0.00	0.04	0.01	0.00	0.02

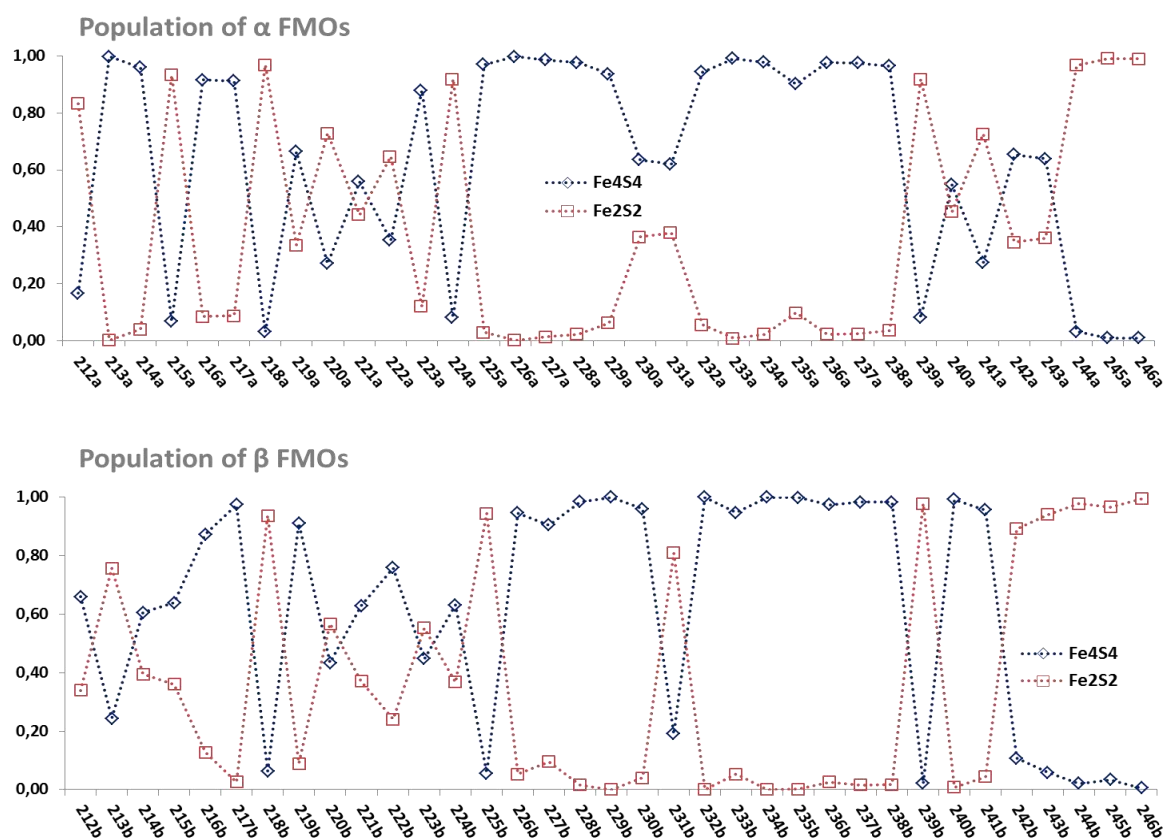
	<b>241<math>\alpha</math></b>	<b>242<math>\alpha</math></b>	<b>243<math>\alpha</math></b>	<b>244<math>\alpha</math></b>	<b>245<math>\alpha</math></b>	<b>246<math>\alpha</math></b>
	<b>L+9</b>	<b>L+10</b>	<b>L+11</b>	<b>L+12</b>	<b>L+13</b>	<b>L+14</b>
<b>Fe<sub>4</sub>S<sub>4</sub></b>	0.27	0.65	0.64	0.03	0.01	0.01
<b>Fe<sub>2</sub>S<sub>2</sub></b>	0.73	0.35	0.36	0.97	0.99	0.99
<b>4Fe4S</b>	0.24	0.59	0.57	0.02	0.00	0.00
<b>2·Fe</b>	0.34	0.17	0.17	0.27	0.22	0.16
<b>2·S</b>	0.15	0.06	0.04	0.01	0.01	0.01
<b>CO apical</b>	0.02	0.01	0.06	0.36	0.60	0.06
<b>COequatorial</b>	0.09	0.03	0.01	0.29	0.08	0.69
<b><math>\mu</math>CO</b>	0.08	0.05	0.03	0.01	0.00	0.01
<b>DTMA</b>	0.02	0.01	0.01	0.00	0.02	0.00
<b>S cys</b>	0.02	0.02	0.04	0.01	0.00	0.00

	<b>212<math>\beta</math></b>	<b>213<math>\beta</math></b>	<b>214<math>\beta</math></b>	<b>215<math>\beta</math></b>	<b>216<math>\beta</math></b>	<b>217<math>\beta</math></b>	<b>218<math>\beta</math></b>	<b>219<math>\beta</math></b>	<b>220<math>\beta</math></b>	<b>221<math>\beta</math></b>	<b>222<math>\beta</math></b>	<b>223<math>\beta</math></b>	<b>224<math>\beta</math></b>	<b>225<math>\beta</math></b>	<b>226<math>\beta</math></b>
	<b>H-18</b>	<b>H-17</b>	<b>H-16</b>	<b>H-15</b>	<b>H-14</b>	<b>H-13</b>	<b>H-12</b>	<b>H-11</b>	<b>H-10</b>	<b>H-9</b>	<b>H-8</b>	<b>H-7</b>	<b>H-6</b>	<b>H-5</b>	<b>H-4</b>
<b>Fe<sub>4</sub>S<sub>4</sub></b>	0.66	0.24	0.61	0.64	0.87	0.97	0.43	0.43	0.43	0.63	0.76	0.45	0.63	0.06	0.95
<b>Fe<sub>2</sub>S<sub>2</sub></b>	0.34	0.76	0.39	0.36	0.13	0.03	0.57	0.57	0.57	0.37	0.24	0.55	0.37	0.94	0.05
<b>4Fe4S</b>	0.43	0.22	0.54	0.60	0.65	0.79	0.20	0.20	0.20	0.25	0.22	0.26	0.43	0.03	0.40
<b>2·Fe</b>	0.21	0.21	0.13	0.19	0.06	0.01	0.33	0.33	0.33	0.23	0.15	0.40	0.25	0.59	0.04
<b>2·S</b>	0.02	0.29	0.15	0.07	0.01	0.00	0.10	0.10	0.10	0.03	0.01	0.02	0.01	0.11	0.00
<b>CO apical</b>	0.01	0.02	0.01	0.01	0.00	0.00	0.01	0.01	0.01	0.01	0.01	0.00	0.00	0.00	0.00
<b>COequatorial</b>	0.04	0.05	0.03	0.03	0.00	0.00	0.03	0.03	0.03	0.02	0.01	0.03	0.01	0.06	0.00
<b><math>\mu</math>CO</b>	0.02	0.20	0.08	0.03	0.00	0.00	0.02	0.02	0.02	0.01	0.00	0.02	0.01	0.07	0.00
<b>DTMA</b>	0.01	0.06	0.01	0.01	0.01	0.00	0.02	0.02	0.02	0.02	0.01	0.00	0.00	0.10	0.00
<b>S Cys</b>	0.13	0.00	0.03	0.01	0.08	0.01	0.05	0.05	0.05	0.01	0.11	0.02	0.02	0.00	0.00

	<b>227<math>\beta</math></b>	<b>228<math>\beta</math></b>	<b>229<math>\beta</math></b>	<b>230<math>\beta</math></b>	<b>231<math>\beta</math></b>	<b>232<math>\beta</math></b>	<b>233<math>\beta</math></b>	<b>234<math>\beta</math></b>	<b>235<math>\beta</math></b>	<b>236<math>\beta</math></b>	<b>237<math>\beta</math></b>	<b>258<math>\beta</math></b>	<b>239<math>\beta</math></b>	<b>240<math>\beta</math></b>
	<b>H-3</b>	<b>H-2</b>	<b>H-1</b>	<b>HOMO</b>	<b>LUMO</b>	<b>L+1</b>	<b>L+2</b>	<b>L+3</b>	<b>L+4</b>	<b>L+5</b>	<b>L+6</b>	<b>L+7</b>	<b>L+8</b>	<b>L+9</b>
<b>Fe<sub>4</sub>S<sub>4</sub></b>	0.90	0.98	1.00	0.96	0.19	1.00	0.95	1.00	1.00	0.97	0.98	0.98	0.02	0.99
<b>Fe<sub>2</sub>S<sub>2</sub></b>	0.10	0.02	0.00	0.04	0.81	0.00	0.05	0.00	0.00	0.03	0.02	0.02	0.98	0.01
<b>4Fe4S</b>	0.43	0.71	0.85	0.86	0.10	0.94	0.88	0.97	0.94	0.81	0.89	0.89	0.01	0.90
<b>2·Fe</b>	0.05	0.01	0.00	0.03	0.50	0.00	0.03	0.00	0.00	0.01	0.01	0.01	0.41	0.01
<b>2·S</b>	0.02	0.00	0.00	0.00	0.13	0.00	0.01	0.00	0.00	0.00	0.00	0.00	0.22	0.00
<b>CO apical</b>	0.00	0.00	0.00	0.00	0.06	0.00	0.01	0.00	0.00	0.00	0.00	0.00	0.11	0.00
<b>COequatorial</b>	0.00	0.00	0.00	0.00	0.02	0.00	0.00	0.00	0.00	0.00	0.00	0.00	0.10	0.00
<b><math>\mu</math>CO</b>	0.01	0.00	0.00	0.00	0.07	0.00	0.01	0.00	0.00	0.00	0.00	0.00	0.13	0.00
<b>DTMA</b>	0.01	0.00	0.00	0.00	0.01	0.00	0.00	0.00	0.00	0.00	0.00	0.00	0.02	0.00
<b>S Cys</b>	0.26	0.02	0.00	0.02	0.08	0.00	0.02	0.00	0.00	0.01	0.00	0.00	0.00	0.00

	<b>241<math>\beta</math></b>	<b>242<math>\beta</math></b>	<b>243<math>\beta</math></b>	<b>244<math>\beta</math></b>	<b>245<math>\beta</math></b>	<b>246<math>\beta</math></b>
	<b>L+10</b>	<b>L+11</b>	<b>L+12</b>	<b>L+13</b>	<b>L+14</b>	<b>L+15</b>
<b>Fe<sub>4</sub>S<sub>4</sub></b>	0.96	0.11	0.06	0.02	0.03	0.01
<b>Fe<sub>2</sub>S<sub>2</sub></b>	0.04	0.89	0.94	0.98	0.97	0.99
<b>4Fe4S</b>	0.89	0.06	0.03	0.01	0.00	0.00
<b>2·Fe</b>	0.02	0.43	0.46	0.30	0.21	0.17
<b>2·S</b>	0.00	0.12	0.16	0.01	0.00	0.01
<b>CO apical</b>	0.00	0.09	0.06	0.30	0.13	0.04
<b>COequatorial</b>	0.00	0.13	0.07	0.33	0.06	0.71
<b><math>\mu</math>CO</b>	0.00	0.05	0.12	0.01	0.00	0.01

<b>DTMA</b>	0.00	0.01	0.03	0.00	0.46	0.00
<b>S Cys</b>	0.00	0.04	0.02	0.01	0.00	0.00



**Supplementary Figure 4.**  $\text{Fe}_4\text{S}_4/\text{Fe}_2\text{S}_2$  Populations of  $\alpha$  and  $\beta$  FMOs. For each singly occupied MO the sum of the two values is equal to 1.

**Supplementary Table 2.** TDDFT electronic spectrum of the  $\text{Fe}_6\text{S}_6$   $\text{H}_{\text{ox}}\text{-CO}$  model. For each transition we reported the excitation energy (**nm**), the oscillation strength (**f**) and the main mono-electronic transition (**1e**) with the corresponding percentage composition. The band assignments are made on the basis of differential Mulliken population reported in the Supplementary Table 3 below.

	<b>nm</b>	<b>f</b>	<b>1e</b>		<b>Assignment</b>
1ex	1913	$4 \cdot 10^{-3}$	$230\beta \rightarrow 231\beta$	86.6	$\text{Fe}_4\text{S}_4 \rightarrow \text{Fe}_2\text{S}_2$
2ex	1868	$7 \cdot 10^{-5}$	$229\beta \rightarrow 232\beta$	88.6	$\text{Fe}_4\text{S}_4$ localized
3ex	1782	$2 \cdot 10^{-4}$	$230\beta \rightarrow 232\beta$	92.9	$\text{Fe}_4\text{S}_4$ localized ( $\text{Fe}_4\text{S} \rightarrow \text{Fe}$ )
4ex	1683	$1 \cdot 10^{-4}$	$229\beta \rightarrow 231\beta$	89.6	$\text{Fe}_4\text{S}_4 \rightarrow \text{Fe}_2\text{S}_2$
5ex	1617	$4 \cdot 10^{-3}$	$229\alpha \rightarrow 232\alpha$	58.2	$\text{Fe}_2\text{S}_2 \rightarrow \text{Fe}_4\text{S}_4$
			$230\alpha \rightarrow 232\alpha$	28.8	
			$229\beta \rightarrow 231\beta$	4.1	
6ex	1577	$2 \cdot 10^{-3}$	$231\alpha \rightarrow 232\alpha$	68.4	$\text{Fe}_4\text{S}_4 \rightarrow \text{Fe}_2\text{S}_2$
			$229\alpha \rightarrow 232\alpha$	11.1	
			$230\alpha \rightarrow 232\alpha$	10.9	
7ex	1493	$3 \cdot 10^{-3}$	$228\beta \rightarrow 231\beta$	52.7	$\text{Fe}_2\text{S}_2 \rightarrow \text{Fe}_4\text{S}_4$
			$230\alpha \rightarrow 232\alpha$	29.2	
			$229\alpha \rightarrow 232\alpha$	7.7	
8ex	1393	$2 \cdot 10^{-2}$	$228\beta \rightarrow 231\beta$	42.7	$\text{Fe}_4\text{S}_4 \rightarrow \text{Fe}_2\text{S}_2$

			230 $\alpha$ $\rightarrow$ 232 $\alpha$	18.1	
			231 $\alpha$ $\rightarrow$ 232 $\alpha$	12.7	
			229 $\alpha$ $\rightarrow$ 232 $\alpha$	9.7	
9ex	1351	$7 \cdot 10^{-5}$	228 $\beta$ $\rightarrow$ 232 $\beta$	94.8	Fe <sub>4</sub> S <sub>4</sub> localized
10ex	1290	$2 \cdot 10^{-4}$	231 $\alpha$ $\rightarrow$ 233 $\alpha$	74.2	Fe <sub>4</sub> S <sub>4</sub> $\rightarrow$ Fe <sub>2</sub> S <sub>2</sub>
			230 $\alpha$ $\rightarrow$ 233 $\alpha$	12	
11ex	1246	$2 \cdot 10^{-3}$	230 $\alpha$ $\rightarrow$ 233 $\alpha$	77.5	Fe <sub>2</sub> S <sub>2</sub> $\rightarrow$ Fe <sub>4</sub> S <sub>4</sub>
			231 $\alpha$ $\rightarrow$ 233 $\alpha$	12.5	
12ex	1201	$4 \cdot 10^{-3}$	229 $\alpha$ $\rightarrow$ 233 $\alpha$	18.1	Fe <sub>4</sub> S <sub>4</sub> localized
			229 $\alpha$ $\rightarrow$ 234 $\alpha$	12.4	
			230 $\alpha$ $\rightarrow$ 234 $\alpha$	12.1	
			229 $\beta$ $\rightarrow$ 234 $\beta$	10	
			230 $\beta$ $\rightarrow$ 234 $\beta$	8.3	
13ex	1174	$2 \cdot 10^{-4}$	230 $\beta$ $\rightarrow$ 233 $\beta$	64.1	Fe <sub>4</sub> S <sub>4</sub> localized
			231 $\alpha$ $\rightarrow$ 234 $\alpha$	10.3	
			229 $\alpha$ $\rightarrow$ 234 $\alpha$	7.6	
14ex	1143	$5 \cdot 10^{-4}$	229 $\beta$ $\rightarrow$ 234 $\beta$	29.2	Fe <sub>4</sub> S <sub>4</sub> localized
			229 $\beta$ $\rightarrow$ 233 $\beta$	24.1	
			230 $\beta$ $\rightarrow$ 233 $\beta$	11.3	
			231 $\alpha$ $\rightarrow$ 234 $\alpha$	8.2	
15ex	1136	$3 \cdot 10^{-3}$	229 $\alpha$ $\rightarrow$ 233 $\alpha$	24.4	Fe <sub>4</sub> S <sub>4</sub> localized
			229 $\beta$ $\rightarrow$ 234 $\beta$	17.4	
			229 $\beta$ $\rightarrow$ 235 $\beta$	9.5	
			231 $\alpha$ $\rightarrow$ 234 $\alpha$	8.4	
			229 $\beta$ $\rightarrow$ 233 $\beta$	8.2	
			230 $\beta$ $\rightarrow$ 233 $\beta$	7.2	
16ex	1127	$5 \cdot 10^{-4}$	229 $\beta$ $\rightarrow$ 233 $\beta$	39.9	Fe <sub>4</sub> S <sub>4</sub> localized
			231 $\alpha$ $\rightarrow$ 234 $\alpha$	20.8	
			230 $\beta$ $\rightarrow$ 234 $\beta$	9.5	
17ex	1114	$7 \cdot 10^{-4}$	230 $\beta$ $\rightarrow$ 234 $\beta$	41.7	Fe <sub>4</sub> S <sub>4</sub> localized
			231 $\alpha$ $\rightarrow$ 234 $\alpha$	20.2	
			229 $\alpha$ $\rightarrow$ 236 $\alpha$	6.4	
18ex	1107	$2 \cdot 10^{-3}$	229 $\alpha$ $\rightarrow$ 233 $\alpha$	34.4	Fe <sub>4</sub> S <sub>4</sub> localized
			230 $\alpha$ $\rightarrow$ 234 $\alpha$	14	
			231 $\alpha$ $\rightarrow$ 234 $\alpha$	10	
			229 $\alpha$ $\rightarrow$ 234 $\alpha$	8.3	
			230 $\alpha$ $\rightarrow$ 235 $\alpha$	6.1	
19ex	1097	$2 \cdot 10^{-3}$	231 $\alpha$ $\rightarrow$ 235 $\alpha$	38.4	Fe <sub>4</sub> S <sub>4</sub> $\rightarrow$ Fe <sub>2</sub> S <sub>2</sub>
			230 $\alpha$ $\rightarrow$ 234 $\alpha$	20.9	
			228 $\alpha$ $\rightarrow$ 232 $\alpha$	18.5	
			230 $\beta$ $\rightarrow$ 234 $\beta$	7.2	
20ex	1079	$3 \cdot 10^{-4}$	230 $\alpha$ $\rightarrow$ 235 $\alpha$	28.8	Fe <sub>4</sub> S <sub>4</sub> $\rightarrow$ Fe <sub>2</sub> S <sub>2</sub>
			230 $\alpha$ $\rightarrow$ 234 $\alpha$	16.9	
			229 $\alpha$ $\rightarrow$ 234 $\alpha$	15	
			231 $\alpha$ $\rightarrow$ 234 $\alpha$	10.9	
			229 $\alpha$ $\rightarrow$ 236 $\alpha$	6.4	
27ex	993	$3 \cdot 10^{-2}$	227 $\beta$ $\rightarrow$ 231 $\beta$	22.4	Fe <sub>4</sub> S <sub>4</sub> $\rightarrow$ Fe <sub>2</sub> S <sub>2</sub>
			228 $\beta$ $\rightarrow$ 23e $\beta$	18.6	
			227 $\alpha$ $\rightarrow$ 232 $\alpha$	16.9	
			231 $\alpha$ $\rightarrow$ 236 $\alpha$	13.9	
29ex	971	$1 \cdot 10^{-2}$	228 $\beta$ $\rightarrow$ 233 $\beta$	21.1	Fe <sub>2</sub> S <sub>2</sub> $\rightarrow$ Fe <sub>4</sub> S <sub>4</sub>
			230 $\alpha$ $\rightarrow$ 236 $\alpha$	19.7	
			229 $\alpha$ $\rightarrow$ 235 $\alpha$	12.8	

32ex	939	$1 \cdot 10^{-2}$	228 $\alpha$ $\rightarrow$ 234 $\alpha$	16.6	Fe <sub>4</sub> S <sub>4</sub> localized
			230 $\alpha$ $\rightarrow$ 236 $\alpha$	11.8	
			229 $\beta$ $\rightarrow$ 235 $\beta$	10.3	
33ex	935	$2 \cdot 10^{-2}$	227 $\beta$ $\rightarrow$ 232 $\beta$	21.3	Fe <sub>4</sub> S <sub>4</sub> localized
			229 $\alpha$ $\rightarrow$ 236 $\alpha$	11.4	
41ex	854	$3 \cdot 10^{-3}$	225 $\beta$ $\rightarrow$ 231 $\beta$	47.1	Fe <sub>4</sub> S <sub>4</sub> $\rightarrow$ Fe <sub>2</sub> S <sub>2</sub>
			226 $\beta$ $\rightarrow$ 231 $\beta$	26.3	
58ex	765	$5 \cdot 10^{-4}$	231 $\alpha$ $\rightarrow$ 239 $\alpha$	75.5	Fe <sub>4</sub> S <sub>4</sub> $\rightarrow$ Fe <sub>2</sub> S <sub>2</sub>
75ex	706	$6 \cdot 10^{-3}$	230 $\beta$ $\rightarrow$ 239 $\beta$	30.2	
			230 $\alpha$ $\rightarrow$ 240 $\alpha$	19.6	Fe <sub>4</sub> S <sub>4</sub> $\rightarrow$ Fe <sub>2</sub> S <sub>2</sub>
			229 $\alpha$ $\rightarrow$ 239 $\alpha$	13.5	
			220 $\beta$ $\rightarrow$ 231 $\beta$	10.3	
			216 $\beta$ $\rightarrow$ 231 $\beta$	62.2	
149ex	536	$4 \cdot 10^{-2}$	225 $\beta$ $\rightarrow$ 239 $\beta$	14.8	Fe <sub>2</sub> S <sub>2</sub> localized
242ex	480	$3 \cdot 10^{-3}$	212 $\beta$ $\rightarrow$ 239 $\beta$	13.4	
251ex	473	$1 \cdot 10^{-2}$	225 $\alpha$ $\rightarrow$ 239 $\alpha$	59.1	Fe <sub>4</sub> S <sub>4</sub> $\rightarrow$ Fe <sub>2</sub> S <sub>2</sub>
287ex	454	$1 \cdot 10^{-2}$	216 $\alpha$ $\rightarrow$ 234 $\alpha$	17.0	
			217 $\alpha$ $\rightarrow$ 234 $\alpha$	13.9	Fe <sub>4</sub> S <sub>4</sub> localized

**Supplementary Table 3.** Differential Mulliken MO populations computed according to the main one-electron transitions. For each excited state considered, the differential population is reported as a function of the fragment (Fe<sub>4</sub>S<sub>4</sub> and Fe<sub>2</sub>S<sub>2</sub> collect the differential population of all the atoms that belong to the cubane or to the binuclear portions and their sum is equal to 0) or group of atoms (4Fe4S indicate the sum of the Fe and S atoms of the cubane; 2•Fe and 2•S the sum of the Fe and S atoms of the Fe<sub>2</sub>S<sub>2</sub> portion; CO apical, CO equatorial, CO bridge, DTMA and S cys correspond to the ligand of the Fe<sub>2</sub>S<sub>2</sub> portion).

	1ex	2ex	3ex	4ex	5ex	6ex	7ex	8ex	9ex	10ex
<b>Fe<sub>4</sub>S<sub>4</sub></b>	-0.67	0.00	0.04	-0.73	0.09	0.25	-0.33	-0.24	0.04	0.32
<b>Fe<sub>2</sub>S<sub>2</sub></b>	0.67	0.00	-0.04	0.73	-0.09	-0.25	0.33	0.24	-0.04	-0.32
<b>4Fe4S</b>	-0.66	0.09	0.08	-0.67	0.11	0.28	-0.22	-0.15	0.08	0.35
<b>2•Fe</b>	0.41	0.00	-0.02	0.45	-0.06	-0.15	0.21	0.15	-0.03	-0.18
<b>2•S</b>	0.11	0.00	0.00	0.12	-0.02	-0.05	0.05	0.03	0.00	-0.06
<b>CO<sub>apical</sub></b>	0.05	0.00	0.00	0.06	0.00	-0.02	0.03	0.02	0.00	-0.02
<b>2•CO<sub>equ</sub></b>										
<b>at</b>	0.03	0.00	0.00	0.03	0.00	-0.01	0.02	0.01	0.00	-0.01
<b>CO<sub>bridge</sub></b>	0.06	0.00	0.00	0.06	-0.01	-0.03	0.03	0.02	0.00	-0.03
<b>DTMA</b>	0.00	0.00	0.00	0.01	0.00	0.00	0.00	0.00	0.00	0.00
<b>S Cys</b>	0.05	0.00	-0.02	0.07	-0.02	-0.02	0.03	0.02	-0.02	-0.02
	<b>11ex</b>	<b>12ex</b>	<b>13ex</b>	<b>14ex</b>	<b>15ex</b>	<b>16ex</b>	<b>17ex</b>	<b>18ex</b>	<b>19ex</b>	<b>20ex</b>
<b>Fe<sub>4</sub>S<sub>4</sub></b>	0.33	0.06	0.03	-0.01	-0.01	0.05	0.09	0.10	0.24	0.18
<b>Fe<sub>2</sub>S<sub>2</sub></b>	-0.33	-0.06	-0.03	0.01	0.01	-0.05	-0.09	-0.10	-0.24	-0.18
<b>4Fe4S</b>	0.37	0.08	0.05	0.04	0.03	0.09	0.12	0.12	0.26	0.20
<b>2•Fe</b>	-0.19	-0.03	-0.02	0.01	0.01	-0.03	-0.05	-0.06	-0.14	-0.10
<b>2•S</b>	-0.07	-0.01	0.00	0.00	0.00	-0.01	-0.02	-0.02	-0.05	-0.04
<b>CO<sub>apical</sub></b>	-0.02	0.00	0.00	0.00	0.00	0.00	-0.01	-0.01	-0.01	-0.01
<b>2•CO<sub>eq</sub></b>	-0.01	0.00	0.00	0.00	0.00	0.00	0.00	0.00	0.00	0.00
<b>μCO</b>	-0.03	-0.01	0.00	0.00	0.00	-0.01	-0.01	-0.01	-0.03	-0.02
<b>DTMA</b>	0.00	0.00	0.00	0.00	0.00	0.00	0.00	0.00	0.00	0.00
<b>S Cys</b>	-0.02	-0.01	-0.01	0.00	0.00	0.00	-0.02	-0.02	-0.01	-0.01
	<b>27ex</b>	<b>32ex</b>	<b>33ex</b>	<b>41ex</b>	<b>58ex</b>	<b>75ex</b>	<b>149ex</b>	<b>242ex</b>	<b>243ex</b>	<b>287ex</b>
<b>Fe<sub>4</sub>S<sub>4</sub></b>	-0.12	0.04	0.05	-0.14	-0.41	-0.45	-0.42	-0.03	-0.27	0.02

<b>Fe<sub>2</sub>S<sub>2</sub></b>	0.12	-0.04	-0.05	0.14	0.41	0.45	0.42	0.03	0.27	-0.02
<b>4Fe4S</b>	0.09	0.10	0.17	-0.05	-0.34	-0.39	-0.34	-0.02	-0.09	0.05
<b>2•Fe</b>	0.08	-0.02	-0.03	0.08	0.14	0.19	0.27	-0.18	0.09	-0.01
<b>2•S</b>	0.02	-0.01	-0.01	0.04	0.11	0.09	0.07	0.11	0.08	0.00
<b>CO<sub>apical</sub></b>	0.01	0.00	0.00	0.04	0.05	0.05	0.04	0.10	0.04	0.00
<b>2•CO<sub>eq</sub></b>	0.01	0.00	0.00	0.00	0.07	0.05	0.02	0.04	0.04	0.00
<b>μCO</b>	0.01	0.00	0.00	0.02	0.07	0.05	0.04	0.06	0.04	0.00
<b>DTMA</b>	0.00	0.00	0.00	-0.04	0.01	0.01	0.00	-0.08	0.00	0.00
<b>S Cys</b>	-0.04	-0.01	-0.06	0.06	-0.03	-0.01	0.00	0.00	-0.01	-0.01

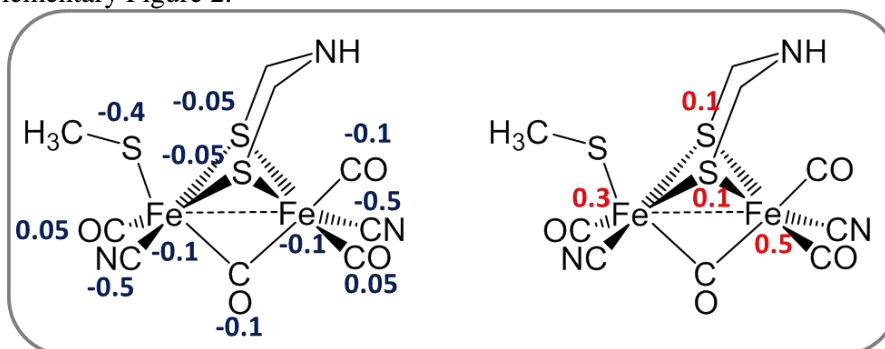
The differential MO populations for each excited state (*ex*), computed according to the following definition:

$$\Delta q_{ex} = \sum_n (q_{i,n} - q_{a,n}) c_n$$

where  $q_{i,n}$  and  $q_{a,n}$  are the atomic populations for the  $i$  virtual and  $a$  occupied MO involved in the  $a \rightarrow i$  mono-electronic transition with weight equal to  $c_n$ ;

## 2.2 - The electronic structure of the Fe<sub>2</sub>S<sub>2</sub> H<sub>ox</sub>-CO model

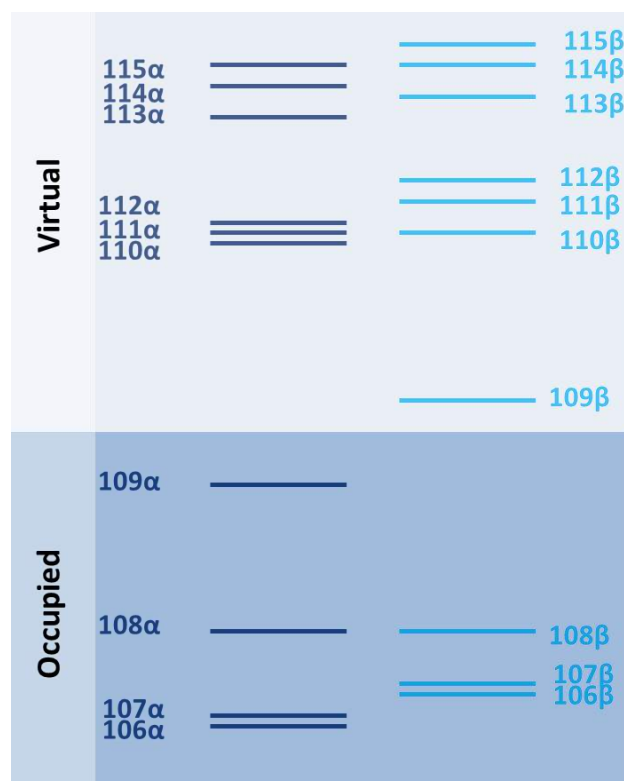
This model has a doublet ground state with a total charge of -2. The optimized geometry parameters are reported in Supplementary Figure 2.



**Supplementary Figure 5.** Atoms/ligand NBO charges and spin charges of Fe<sub>2</sub>S<sub>2</sub> H<sub>ox</sub>-CO model

The total charge is essentially localized on the cyanide and SCH<sub>3</sub> ligands; -1.4 out of -2 total charge is localized on these three ligands and the remaining charge is distributed on the other ligands and the two Fe atoms. The spin charge distribution is localized in a non-equal manner on the two Fe atoms suggesting a Fe<sub>p</sub>(I)Fe<sub>d</sub>(II) redox state.

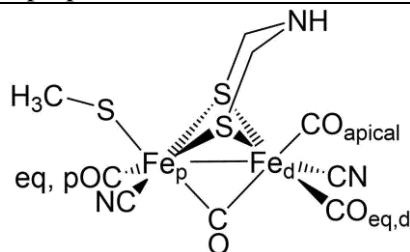
The Mulliken population (reported in Supplementary Table 3) of the FMOs involved in the electronic spectrum (Supplementary Fig. 6) is crucial to evaluate how the electronic structure of the Fe<sub>2</sub>S<sub>2</sub> model differs from that of the full Fe<sub>6</sub>S<sub>6</sub> cluster.



**Supplementary Figure 6.** MO energy diagram of the FMOs involved in the TDDFT spectrum of the Fe(I)Fe(II) Fe<sub>2</sub>S<sub>2</sub> H<sub>ox</sub>-CO model. The virtual 109β MO (see isosurface 0.05 a.u. plots below) is essentially similar to the 231β Fe<sub>2</sub>S<sub>2</sub> localized MO in the Fe<sub>6</sub>S<sub>6</sub> model (see Supplementary Figure 3b).

Non occupied MO from 110α,β to 115α,β have a non-bonding/antibonding  $\sigma^*$  Fe-Fe and Fe-CO characters, in particular the MO 113α and 115α. A second important aspects of the orbital composition of these FMOs is SCH<sub>3</sub><sup>-</sup> lone-pair contribution in 108α,β and 103β. When these MO are involved in an electronic excitation, the corresponding transition has a CT contribution from/to SCH<sub>3</sub><sup>-</sup>. It is important to observe (compare Supplementary Figure 3b and 7) that the first non-occupied MO 109β is essentially identical to the same MO in the Fe<sub>6</sub>S<sub>6</sub> model (231β).

**Supplementary Table 4.** Mulliken MO populations of the Fe<sub>2</sub>S<sub>2</sub> model frontier MO mainly involved in the TDDFT computed electronic spectrum. The population of each spin-orbit MO integrates to 1 electron. The values are collected as a function of a specific part of the systems or group of atoms. In the picture below are resumed the atoms/group aggregations proposed in the table.

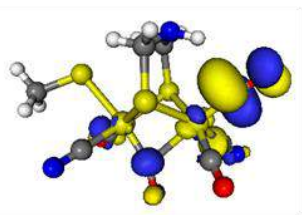


	106α	107α	108α	109α	110α	111α	112α	113α	114α	115α
Fe <sub>p</sub>	0.50	0.19	0.00	0.32	0.32	0.07	0.20	0.22	0.04	0.18
Fe <sub>d</sub>	0.08	0.43	0.18	0.18	0.11	0.40	0.28	0.07	0.14	0.03
2·S	0.12	0.11	0.03	0.17	0.18	0.16	0.17	0.02	0.02	0.02
NH	0.07	0.09	0.02	0.01	0.05	0.04	0.02	0.01	0.01	0.02
μCO	0.04	0.00	0.02	0.07	0.07	0.11	0.07	0.03	0.12	0.06

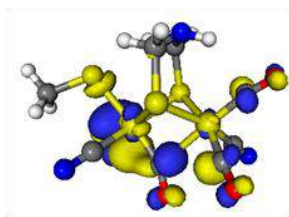
S12



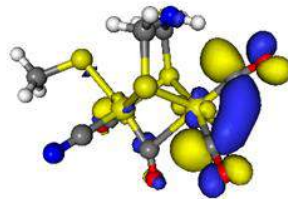
<b>CO<sub>Ap</sub></b>	0.04	0.02	0.00	0.09	0.08	0.03	0.05	0.37	0.06	0.58
<b>CO<sub>eq d</sub></b>	0.03	0.00	0.00	0.05	0.09	0.01	0.02	0.22	0.08	0.01
<b>CO<sub>eq p</sub></b>	0.01	0.05	0.00	0.00	0.02	0.09	0.02	0.04	0.49	0.04
<b>2·CN</b>	0.10	0.09	0.01	0.01	0.04	0.02	0.11	0.01	0.01	0.06
<b>SCH<sub>3</sub></b>	0.01	0.00	0.74	0.10	0.03	0.05	0.05	0.02	0.03	0.00
	<b>102β</b>	<b>103β</b>	<b>104β</b>	<b>105β</b>	<b>106β</b>	<b>107β</b>	<b>108β</b>	<b>109β</b>	<b>110β</b>	<b>111β</b>
<b>Fe<sub>p</sub></b>	0.30	0.10	0.47	0.10	0.28	0.49	0.00	0.30	0.19	0.19
<b>Fe<sub>d</sub></b>	0.08	0.23	0.22	0.52	0.27	0.19	0.20	0.21	0.24	0.29
<b>2·S</b>	0.31	0.06	0.05	0.04	0.14	0.07	0.03	0.14	0.17	0.22
<b>NH</b>	0.02	0.08	0.01	0.02	0.13	0.01	0.02	0.01	0.06	0.02
<b>μCO</b>	0.01	0.04	0.00	0.11	0.02	0.02	0.03	0.09	0.09	0.04
<b>CO<sub>Ap</sub></b>	0.07	0.03	0.06	0.00	0.00	0.06	0.00	0.08	0.07	0.05
<b>CO<sub>eq d</sub></b>	0.07	0.01	0.03	0.02	0.05	0.02	0.00	0.05	0.06	0.05
<b>CO<sub>eq p</sub></b>	0.01	0.01	0.03	0.00	0.03	0.03	0.00	0.00	0.06	0.07
<b>2·CN</b>	0.07	0.08	0.13	0.12	0.08	0.10	0.01	0.01	0.04	0.05
<b>SCH<sub>3</sub></b>	0.07	0.36	0.00	0.07	0.01	0.00	0.71	0.10	0.02	0.03



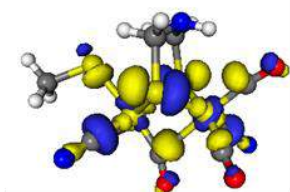
**115 $\alpha$**



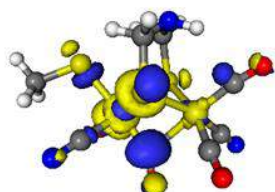
**114 $\alpha$**



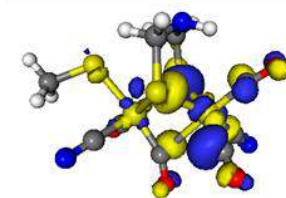
**113 $\alpha$**



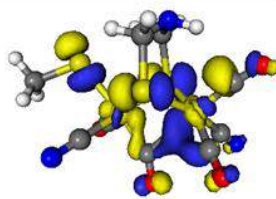
**112 $\alpha$**



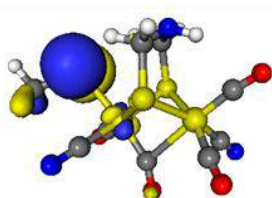
**111 $\alpha$**



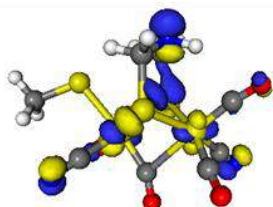
**110 $\alpha$**



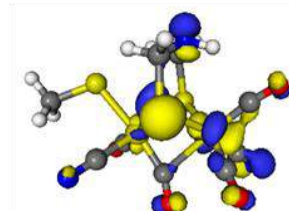
**109 $\alpha$**



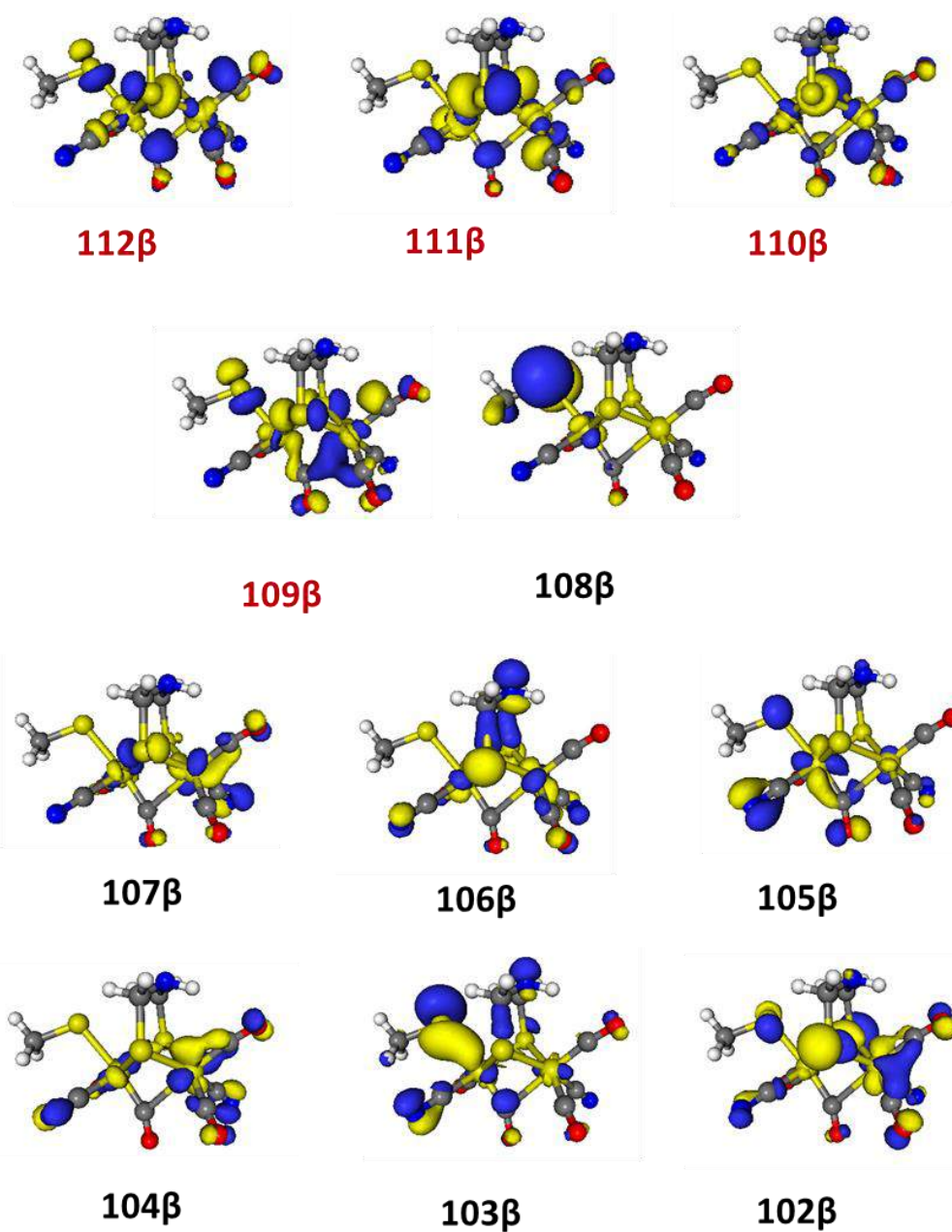
**108 $\alpha$**



**107 $\alpha$**



**106 $\alpha$**



**Supplementary Figure 7.** Fe<sub>2</sub>S<sub>2</sub> H<sub>ox</sub>-CO model MO diagram and isosurface plots (0.05 au) for the MO reported in Supplementary Table 4.

**Supplementary Table 5.** TDDFT electronic spectrum of the Fe<sub>2</sub>S<sub>2</sub> H<sub>ox</sub>-CO model. For the first 20 transitions, we report the excitation energy (**nm**), the oscillation strength (**f**) and the main monoenergetic transition (**1e**) with the corresponding percentage composition. The band assignments are made on the basis of differential Mulliken population reported in the Supplementary Table 4.

	<b>nm</b>	<b>f</b>	<b>1e</b>			<b>Band assignment</b>
1 ex	886.2	1·10 <sup>-4</sup>	108β→	109β	97.7	SCH <sub>3</sub> → Fe <sub>d</sub> LMCT
2 ex	832.1	1·10 <sup>-3</sup>	109α→	110α	91.2	Fe <sub>p</sub> , SCH <sub>3</sub> →ligands MLLCT
3 ex	778.1	9·10 <sup>-3</sup>	109α→	111α	84.2	Fe <sub>d</sub> → Fe <sub>p</sub> MMCT
4 ex	755.2	4·10 <sup>-3</sup>	109a→	112a	89.9	Fe <sub>d</sub> → Fe <sub>p</sub> MMCT
5 ex	699.4	3·10 <sup>-3</sup>	107b→	109b	93.1	Fe <sub>d</sub> ,CN→ ligands MLLCT
6 ex	669.5	6·10 <sup>-4</sup>	106b→	109b	94.8	MLLCT
7 ex	616.6	7·10 <sup>-4</sup>	104b→	109b	92.6	Fe <sub>d</sub> ,CN→ μCO MLCT
8 ex	599.4	1·10 <sup>-2</sup>	105b→	109b	75.3	Fe <sub>p</sub> → Fe <sub>d</sub> ,S,O MMLCT
9 ex	547.7	6·10 <sup>-3</sup>	109a→	113a	93.2	Fe,S→CO MLLCT
10 ex	531.7	3·10 <sup>-5</sup>	108a→	110a	28.9	SCH <sub>3</sub> →Fe,ligand LLMCT
			108b→	110b	28.1	
			108a→	111a	18.9	
11 ex	522.2	1·10 <sup>-3</sup>	108a→	111a	43.4	SCH <sub>3</sub> →Fe,ligand LLMCT
			108a→	110a	28.6	
			108b→	111b	9.8	
12 ex	508.5	9·10 <sup>-3</sup>	103b→	109b	54.8	SCH <sub>3</sub> →Fe,ligand LLMCT
			108b→	110b	13.3	
			108a→	110a	12.6	
13 ex	501.9	8·10 <sup>-4</sup>	102b→	109b	64.6	SCH <sub>3</sub> ,S→Fe,ligand LLMCT
			108a→	110a	11.4	
			108a→	112a	8.9	
14 ex	495.9	5·10 <sup>-3</sup>	108a→	112a	41.1	SCH <sub>3</sub> →Fe,ligand LLMCT
			102b→	109b	17.6	
			103b→	109b	17.0	
15 ex	484.2	3·10 <sup>-3</sup>	109a→	114a	69.3	Fe,S→CO MLLCT
16 ex	482.4	2·10 <sup>-3</sup>	108b→	110b	21.5	SCH <sub>3</sub> →Fe,ligand LLMCT
			107b→	111b	16.7	
			106a→	110a	13.1	SCH <sub>3</sub> →Fe,ligand LLMCT
17 ex	476.4	1·10 <sup>-3</sup>	107b→	110b	17.0	
			108b→	110b	13.2	
			108a→	112a	12.0	
18 ex	475.1	6·10 <sup>-4</sup>	106b→	110b	21.6	Fe <sub>d</sub> → ligand MLCT
			107a→	111a	10.4	
			108a→	112a	10.1	
19 ex	471.4	2·10 <sup>-3</sup>	109a→	115a	85.1	SCH <sub>3</sub> →Fe,ligand LLMCT
20 ex	461.9	1·10 <sup>-2</sup>	108b→	111b	44.4	SCH <sub>3</sub> →Fe,ligand LLMCT
			108a→	111a	26.3	
			108b→	110b	8.9	
21 ex	453.7	3·10 <sup>-4</sup>				
22 ex	452.2	2·10 <sup>-4</sup>				
23 ex	448.8	1·10 <sup>-3</sup>				
24 ex	446.8	3·10 <sup>-3</sup>				
25 ex	442.2	2·10 <sup>-3</sup>				
26 ex	437.5	4·10 <sup>-4</sup>				
27 ex	435.9	2·10 <sup>-3</sup>				
28 ex	432.4	1·10 <sup>-4</sup>				
29 ex	426.3	3·10 <sup>-4</sup>				
30 ex	423.1	4·10 <sup>-5</sup>				

31 ex	418.7	$5 \cdot 10^{-3}$
32 ex	416.7	$2 \cdot 10^{-3}$
33 ex	413.6	$1 \cdot 10^{-3}$
34 ex	409.7	$6 \cdot 10^{-4}$
35 ex	407.5	$8 \cdot 10^{-4}$
36 ex	405.0	$1 \cdot 10^{-4}$
37 ex	399.3	$4 \cdot 10^{-4}$
38 ex	396.5	$4 \cdot 10^{-4}$
39 ex	395.4	$2 \cdot 10^{-4}$
40 ex	393.2	$1 \cdot 10^{-3}$
41 ex	392.8	$3 \cdot 10^{-3}$
42 ex	391.7	$9 \cdot 10^{-4}$
43 ex	389.7	$5 \cdot 10^{-4}$
44 ex	389.0	$2 \cdot 10^{-3}$
45 ex	386.2	$7 \cdot 10^{-4}$
46 ex	382.3	$1 \cdot 10^{-3}$
47 ex	379.6	$5 \cdot 10^{-3}$
48 ex	379.3	$1 \cdot 10^{-3}$
49 ex	376.6	$5 \cdot 10^{-3}$
50 ex	373.5	$1 \cdot 10^{-3}$

**Supplementary Table 6.** Fe<sub>2</sub>S<sub>2</sub> model differential Mulliken MO populations computed according to the main one-electron transitions. For each excited state considered, the differential population is reported as a function of the fragment (see above).

	<b>1ex</b>	<b>2ex</b>	<b>3ex</b>	<b>4ex</b>	<b>5ex</b>	<b>6ex</b>	<b>7ex</b>	<b>8ex</b>	<b>9ex</b>	<b>10ex</b>
<b>Fe<sub>d</sub></b>	0.30	0.00	-0.21	-0.12	-0.18	0.02	-0.16	0.20	-0.10	0.16
<b>Fe<sub>p</sub></b>	0.02	-0.07	0.18	0.10	0.02	-0.05	-0.01	-0.30	-0.11	0.04
<b>2·S</b>	0.11	0.01	-0.01	0.00	0.07	0.00	0.09	0.10	-0.15	0.11
<b>NH</b>	-0.01	0.04	0.02	0.01	0.00	-0.12	-0.01	-0.02	0.00	0.02
<b>μCO</b>	0.06	0.00	0.04	0.00	0.07	0.07	0.09	-0.02	-0.04	0.05
<b>CO<sub>Ap</sub></b>	0.08	-0.01	-0.05	-0.04	0.03	0.08	0.02	0.08	0.28	0.05
<b>CO<sub>eq d</sub></b>	0.05	0.05	-0.03	-0.02	0.03	0.00	0.02	0.03	0.17	0.05
<b>CO<sub>eq p</sub></b>	0.01	0.02	0.08	0.02	-0.03	-0.03	-0.02	0.00	0.04	0.04
<b>2·CN</b>	0.00	0.03	0.01	0.09	-0.09	-0.07	-0.11	-0.11	-0.01	0.02
<b>SCH<sub>3</sub></b>	-0.61	-0.07	-0.04	-0.05	0.10	0.09	0.09	0.03	-0.08	-0.53
	<b>11ex</b>	<b>12ex</b>	<b>13ex</b>	<b>14ex</b>	<b>15ex</b>	<b>16ex</b>	<b>17ex</b>	<b>18ex</b>	<b>19ex</b>	<b>20ex</b>
<b>Fe<sub>d</sub></b>	0.14	0.18	0.06	0.15	-0.20	0.05	-0.02	-0.08	-0.12	0.12
<b>Fe<sub>p</sub></b>	0.09	-0.01	0.09	0.06	-0.02	0.03	0.03	0.00	-0.13	0.10
<b>2·S</b>	0.12	0.08	-0.08	0.06	-0.12	0.07	0.06	0.03	-0.13	0.13
<b>NH</b>	0.01	-0.03	-0.01	-0.01	0.00	0.01	0.02	-0.02	0.01	0.01
<b>μCO</b>	0.05	0.04	0.06	0.05	0.04	0.02	0.03	0.03	0.00	0.03
<b>CO<sub>Ap</sub></b>	0.04	0.05	0.02	0.04	-0.02	0.03	0.01	0.02	0.42	0.03
<b>CO<sub>eq d</sub></b>	0.04	0.04	0.00	0.02	0.02	0.03	0.02	0.01	-0.03	0.03
<b>CO<sub>eq p</sub></b>	0.06	0.01	0.00	0.01	0.34	0.03	0.02	0.01	0.04	0.06
<b>2·CN</b>	0.02	-0.03	-0.02	0.02	-0.01	0.01	0.00	-0.03	0.04	0.03
<b>SCH<sub>3</sub></b>	-0.57	-0.33	-0.13	-0.40	-0.05	-0.26	-0.17	0.01	-0.08	-0.54

The differential MO populations for each excited state (*ex*), computed according to the following definition:

$$\Delta q_{ex} = \sum_n (q_{i,n} - q_{a,n}) c_n$$

where  $q_{i,n}$  and  $q_{a,n}$  are the atomic populations for the  $i$  virtual and  $a$  occupied MO involved in the  $a \rightarrow i$  mono-electronic transition with weight equal to  $c_n$ .

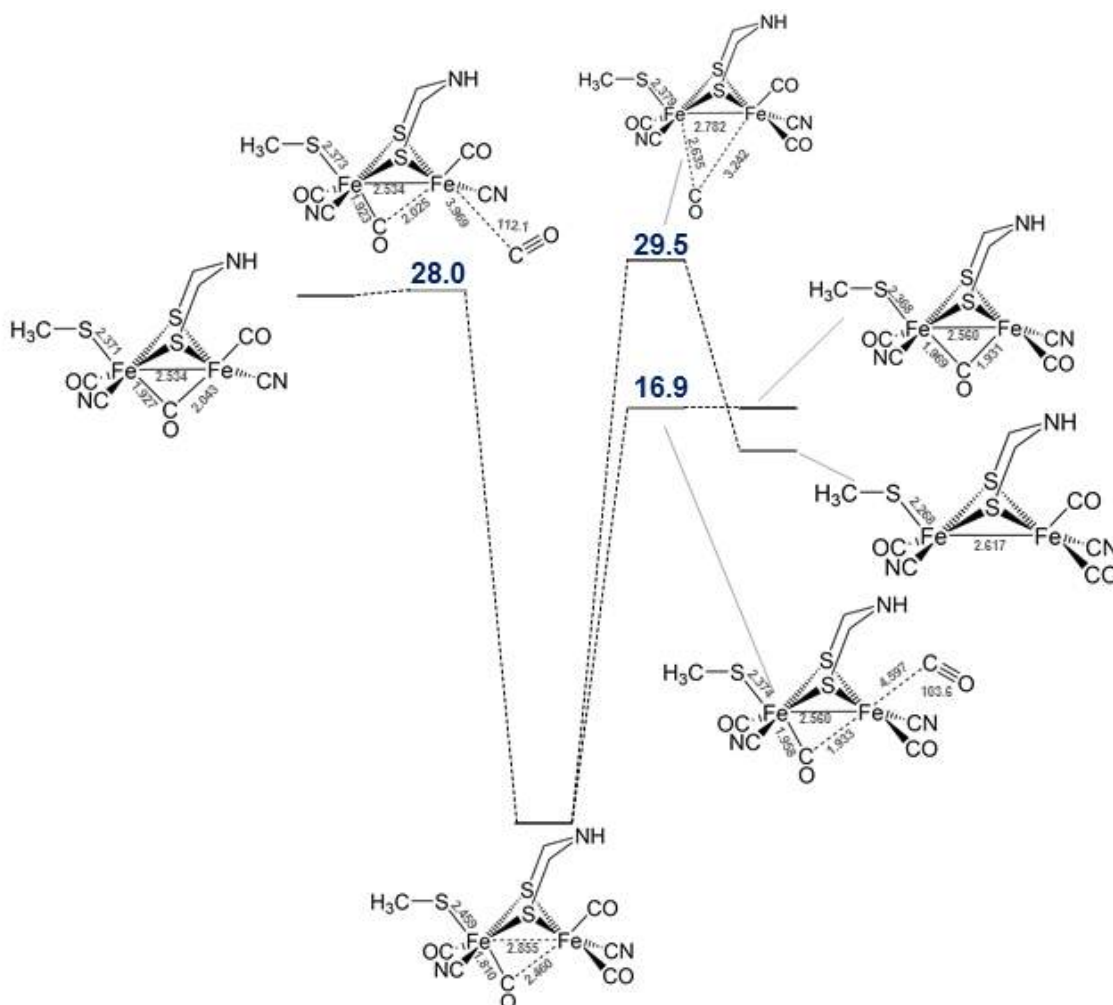
### 2.3 - CO dissociation free energy barriers for Fe<sub>2</sub>S<sub>2</sub> and Fe<sub>6</sub>S<sub>6</sub> H<sub>ox</sub>-CO models

The free energy dissociation barriers for Fe<sub>2</sub>S<sub>2</sub> Fe(I)Fe(II) and Fe<sub>6</sub>S<sub>6</sub> Fe(I)Fe(II) models have been computed by identifying the transition states (Supplementary Fig. 8 and 9) along the apical and equatorial CO ligand dissociation coordinates. For Fe<sub>2</sub>S<sub>2</sub> Fe(I)Fe(II) the bridging CO ligand dissociation TS has been also identified.

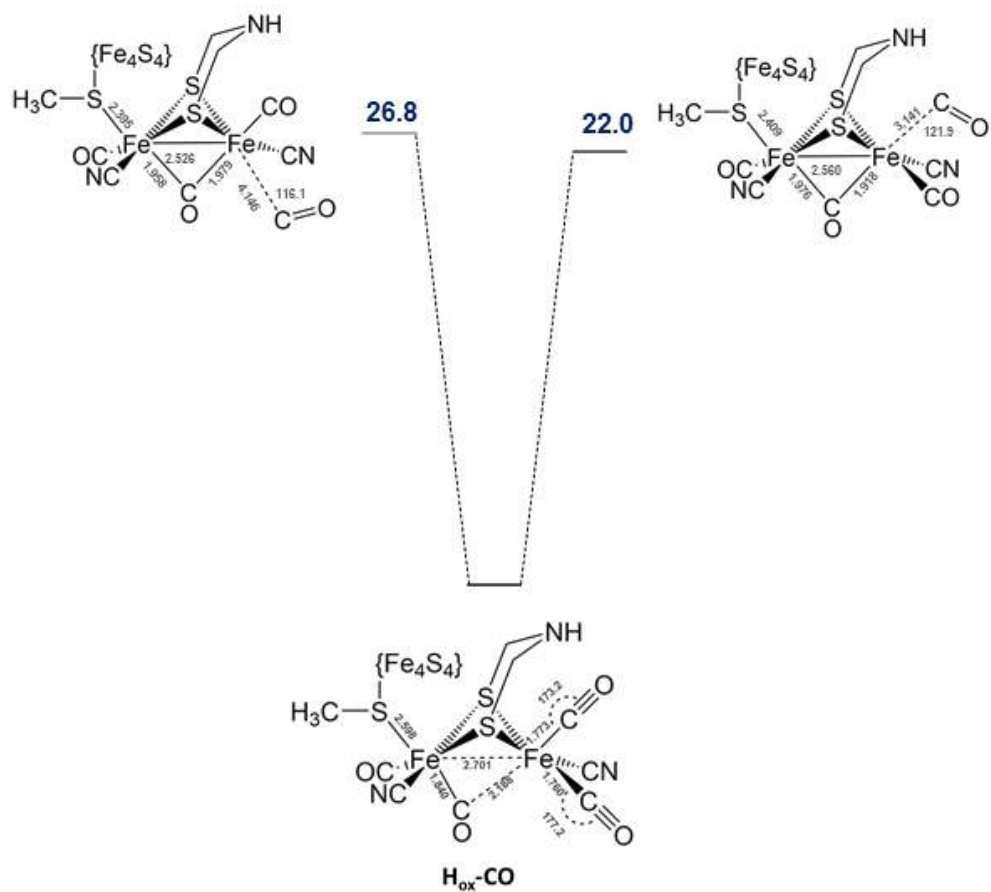
We show in Supplementary Table 7 the  $\Delta G^\ddagger$  CO dissociation barriers for the Fe<sub>2</sub>S<sub>2</sub> Fe(I)Fe(II) redox state which can be compared with the values obtained from the Fe(I)Fe(II) full H-cluster model. First, the comparison between the Fe<sub>2</sub>S<sub>2</sub> and Fe<sub>6</sub>S<sub>6</sub> Fe(I)Fe(II) barriers shows that the CO dissociation energetics of these two models are similar, in particular for the equatorial CO ligand (see Supplementary Table 7).

**Supplementary Table 7.** Calculated CO dissociation free energy barriers (in kcal·mol<sup>-1</sup>) for the Fe<sub>6</sub>S<sub>6</sub> H<sub>ox</sub>-CO model and the CO-bound Fe<sub>2</sub>S<sub>2</sub> fragment in their oxidized Fe(I)Fe(II) redox state.

	CO ligand	$\Delta G^\ddagger$ (kcal/mol)
Fe <sub>6</sub> S <sub>6</sub> H <sub>ox</sub> -CO	Apical CO	22.0
	Equatorial CO	26.8
Fe <sub>2</sub> S <sub>2</sub> H <sub>ox</sub> -CO	Apical CO	16.9
	Equatorial CO	28.0
	Bridging CO	29.5

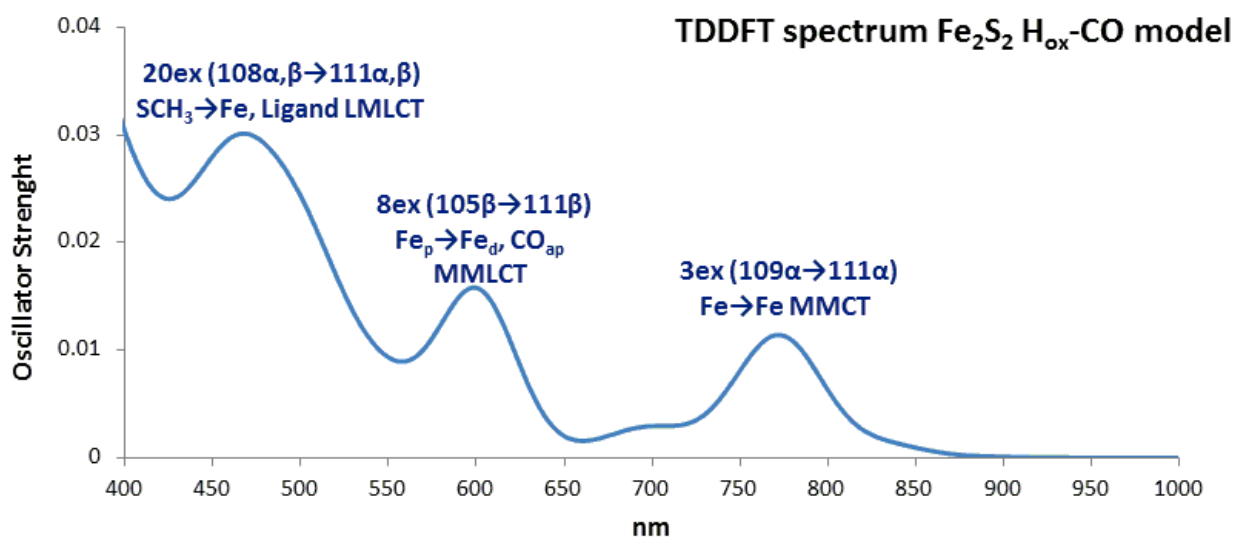


**Supplementary Figure 8.** Fe<sub>2</sub>S<sub>2</sub> H<sub>ox</sub>-CO Structures of transition states and products and free energy barriers (in kcal/mol) for the CO dissociation of the Fe<sub>2</sub>S<sub>2</sub> H<sub>ox</sub>-CO model. Distances in Å.



**Supplementary Figure 9.**  $\text{Fe}_6\text{S}_6$   $\text{H}_{\text{ox}}\text{-CO}$  Structures of transition states and products and free energy barriers (in kcal/mol) for the CO dissociation of the  $\text{Fe}_6\text{S}_6$   $\text{H}_{\text{ox}}\text{-CO}$  model. Distances in Å, angles in degree.

## 2.4 - TDDFT computed spectrum of the Fe<sub>2</sub>S<sub>2</sub> H<sub>ox</sub>-CO model



**Supplementary Figure 10.** TDDFT computed spectrum of the Fe<sub>2</sub>S<sub>2</sub> H<sub>ox</sub>-CO model. We assigned the bands on the basis of the differential Mulliken population reported in Supplementary Table 6.



## 2.5 - Comparison of the Fe<sub>2</sub>S<sub>2</sub> and Fe<sub>6</sub>S<sub>6</sub> H<sub>ox</sub>-CO model TDDFT spectra for band assignment

The correlation between TDDFT excitation energies and wavelengths used in our experiments is crucial. The band assignment is not trivial because no experimental spectrum of the specific model is available.

It is important to correlate the computed excitation energies for the various systems under investigation. We have to consider some issues before doing so:

- for the larger Fe<sub>6</sub>S<sub>6</sub> model, one must adopt BP86 DFT functional to compute excitation energies within the RI approach, in order to save a very significant portion of the CPU time needed for TDDFT computing of **600 excitations**. We also consider the first 70 PBE0 excitations to evaluate the BP86 red shift at least for the low energy part of the spectrum.
- We do not consider the role of the residues that interact directly with the H-cluster in the Fe<sub>2</sub>S<sub>2</sub> model, because in that case one needs to include a number of atom position constraints during the geometry optimization to avoid residues dissociation, making TDDFT geometry optimization useless.
- Either Fe<sub>2</sub>S<sub>2</sub> or Fe<sub>6</sub>S<sub>6</sub> models are highly charged (-3 for Fe<sub>6</sub>S<sub>6</sub>, -2 for Fe<sub>2</sub>S<sub>2</sub>); this tends to decrease in an anomalous way the computed excitation energy, in particular in the case of GGA BP86 functional.
- During TDDFT geometry optimization the HSCH<sub>3</sub> tends to dissociate; for this reason, we had to consider the SCH<sub>3</sub><sup>-</sup> ligand, which binds more tightly to the Fe<sub>2</sub>S<sub>2</sub> core.

In order to obtain a reasonable and semi-quantitative band assignment, we evaluated and compared the TDDFT spectra for the following systems

- Fe<sub>6</sub>S<sub>6</sub> H<sub>ox</sub>-CO at BP86 level
- Fe<sub>2</sub>S<sub>2</sub> H<sub>ox</sub>-CO at BP86 and PBE0 level considering i) the four residues that interact with the CN ligand and the bridging ligand ii) the HSCH<sub>3</sub> ligand instead of SCH<sub>3</sub><sup>-</sup>.
- Fe<sub>2</sub>S<sub>2</sub> H<sub>ox</sub>-CO at BP86 with the SCH<sub>3</sub><sup>-</sup> and without the residues;

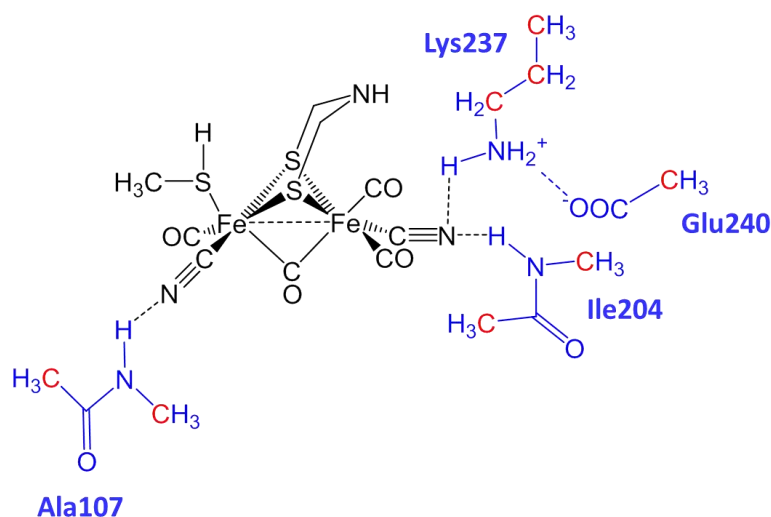
We made the band assignment for the Fe<sub>6</sub>S<sub>6</sub>/Fe<sub>2</sub>S<sub>2</sub> considering in particular the Fe<sub>2</sub>S<sub>2</sub> model at BP86 level

1. The first weak feature that comprises the first three excitations;
2. The HOMO-1β→LUMOβ 5ex state which has been investigated in great detail to identify the CO release channel;

The approach that we adopted is the following:

- We first considered the Fe<sub>2</sub>S<sub>2</sub> model with the four residues, computing its electronic spectrum at PBE0 and BP86 level;
- We considered the PBE0 spectrum of the model as the most accurate;
- We compared the Fe<sub>2</sub>S<sub>2</sub>/residues PBE0 and BP86 spectra, finding the correspondence between PBE0 and BP86 excitations according to the nature of the FMOs involved;
- We compared the BP86 spectra obtained with and without residues;
- We finally compared the BP86 spectra for Fe<sub>6</sub>S<sub>6</sub> and Fe<sub>2</sub>S<sub>2</sub>.

The model with the residues (Supplementary Fig. 11) was derived from the crystallographic structure of *D. desulfuricans* [FeFe] hydrogenase, following a previously published protocol<sup>xviii</sup>,



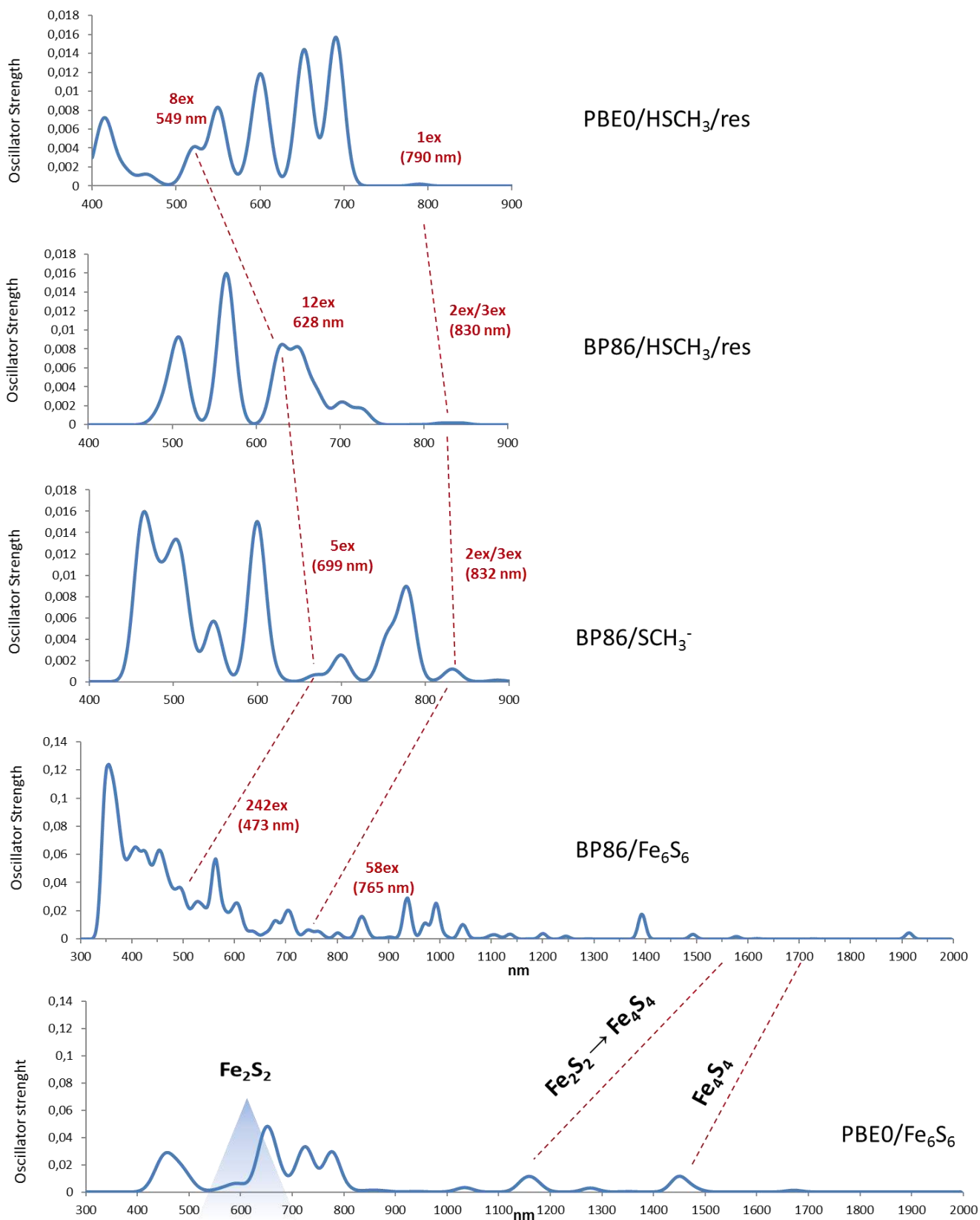
**Supplementary Figure 11.** HSCH<sub>3</sub>/residues model. In blue the four residues modeled as N-methyl acetamide for Ala107 and Ile204, as *n*-propylamine for Lys237 and acetic acid for Glu240. We show in red the carbon fixed at the crystallographic position during calculations to avoid unrealistic conformational rearrangements. The total charge of this model is -1.

**Supplementary Table 8a.** Data for low lying excitations using the four approaches mentioned above.

Functional/model	No.	nm	f	1e
PBE0/HSCH <sub>3</sub> /residues	1ex	789	5·10 <sup>-4</sup>	HOMO-1β→LUMOβ
BP86/HSCH <sub>3</sub> /residues	1ex	888	1·10 <sup>-5</sup>	HOMOβ→LUMOβ
	2ex	845	1·10 <sup>-4</sup>	HOMO-1β→LUMOβ
	3ex	821	2·10 <sup>-4</sup>	HOMO-2β→LUMOβ (56.1%) HOMO-1β→LUMOβ (31.0%)
BP86/SCH <sub>3</sub> <sup>-</sup>	1ex	886	2·10 <sup>-4</sup>	HOMOβ→LUMOβ
	2ex	832	1·10 <sup>-3</sup>	HOMOα→LUMOα
	3ex	778	9·10 <sup>-3</sup>	HOMOα→LUMO+1α
BP86/F <sub>6</sub> S <sub>6</sub>	58 ex	765	5·10 <sup>-4</sup>	231α→239α
PBE0/HSCH <sub>3</sub> /residues	8ex	549	1·10 <sup>-2</sup>	HOMO-7β→LUMOβ (18.9%)
				HOMO-8β→LUMOβ (11.7%)
BP86/HSCH <sub>3</sub> /residues	12ex	628	8·10 <sup>-3</sup>	HOMO-8β→LUMOβ (72.4%)
BP86/SCH <sub>3</sub> <sup>-</sup>	5ex	699	3·10 <sup>-3</sup>	HOMO-1β→LUMOβ
BP86/Fe <sub>6</sub> S <sub>6</sub>	242 ex	473	3·10 <sup>-4</sup>	225β→239β

To establish the correlation between the various spectra, we analyzed the MO involved in terms of similar shape and orbital contributions.

In the panel below, we show the computed spectra obtained by overlap of Gaussian functions centered at the computed excitation energy in nm. Each Gaussian function is built with an amplitude of 10 nm.



**Supplementary Figure 12a.** Comparison of the TDDFT spectra of Fe<sub>2</sub>S<sub>2</sub> and Fe<sub>6</sub>S<sub>6</sub> H<sub>ox</sub>-CO models. PBE0/HSCH<sub>3</sub>/res and BP86/HSCH<sub>3</sub>/res are those computed at PBE0 or BP86 level for the Fe<sub>2</sub>S<sub>2</sub> model with residues and the HSCH<sub>3</sub> ligand. The BP86/SCH<sub>3</sub><sup>-</sup> and BP86/Fe<sub>6</sub>S<sub>6</sub> are the models reported in Supplementary Figure 1. The band assignments sketched in with red dashed lines have been established on the basis of the similar nature of the MOs involved the TDDFT computed 1e transitions.

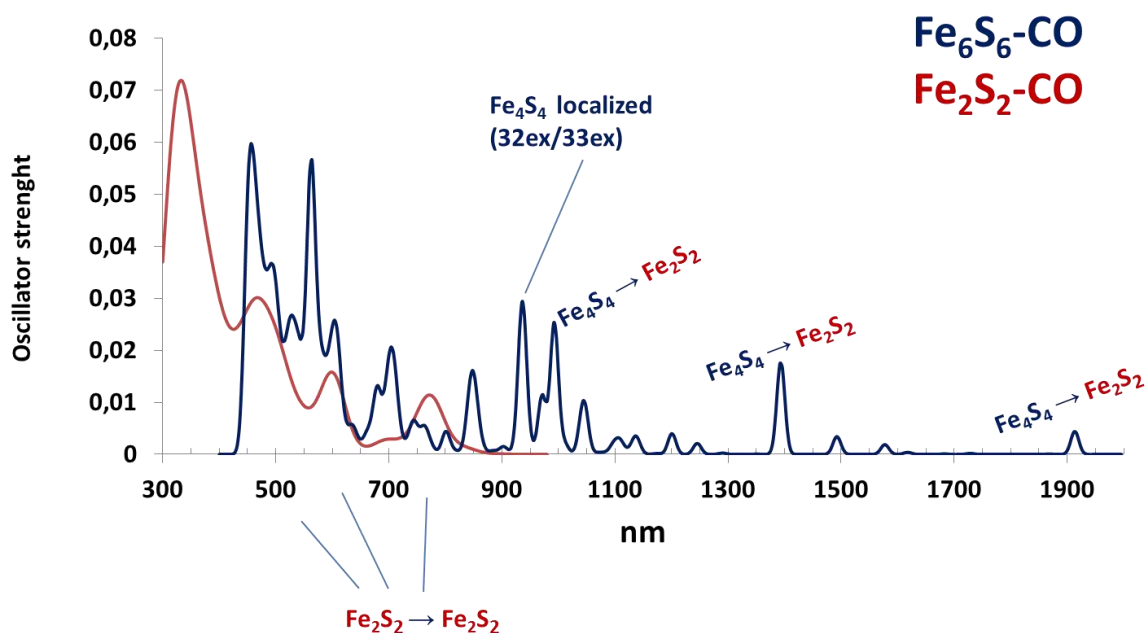
In the Figure 12a is also reported the Fe<sub>6</sub>S<sub>6</sub> PBE0 computed spectrum using the first 70 excitations. In the Supplementary table 8b are reported the Fe<sub>6</sub>S<sub>6</sub> PBE0 excitation data.

**Supplementary Table 8b.** Data for low lying excitations using the four approaches mentioned above.

Functional/model	No.	nm	f	1e	
PBE0/ Fe <sub>6</sub> S <sub>6</sub>	1ex	1672	1·10 <sup>-3</sup>	230α→235α (27.1%) 230α→239α (15.5%)	Fe <sub>2</sub> S <sub>2</sub> →Fe <sub>4</sub> S <sub>4</sub>
	2ex	1477	3·10 <sup>-3</sup>	230α→234α (33.6%) 230α→236α (10.6%)	Fe <sub>4</sub> S <sub>4</sub>
	7ex	1151	8·10 <sup>-3</sup>	230α→233α (18.0%) 230α→238α (16.6%) 230α→234α (11.1%)	Fe <sub>2</sub> S <sub>2</sub> →Fe <sub>4</sub> S <sub>4</sub>
	8ex	1034	3·10 <sup>-3</sup>	230α→232α (42.2%) 230α→233α (11.6%)	Fe <sub>4</sub> S <sub>4</sub> →Fe <sub>2</sub> S <sub>2</sub>
	16ex	777	3·10 <sup>-2</sup>	231α→241α (21.7%) 231α→241α (14.7%)	Fe <sub>4</sub> S <sub>4</sub> →Fe <sub>2</sub> S <sub>2</sub>
	24ex	637	4·10 <sup>-3</sup>	231α→240α (25.5%)	Fe <sub>2</sub> S <sub>2</sub>
	25ex	597	5·10 <sup>-3</sup>	231α→243α (16.3%)	Fe <sub>2</sub> S <sub>2</sub>
	27ex	570	4·10 <sup>-4</sup>	231α→240α (33.8%)	Fe <sub>2</sub> S <sub>2</sub>
	29ex	554	4·10 <sup>-4</sup>	231α→243α (16.1%)	Fe <sub>2</sub> S <sub>2</sub>
	49ex	454	9·10 <sup>-3</sup>	231α→242α (24.8%) 231α→234α (19.6%)	Fe <sub>4</sub> S <sub>4</sub> →Fe <sub>2</sub> S <sub>2</sub>

The Fe<sub>6</sub>S<sub>6</sub> PBE0 is essentially similar to that computed with BP86 except for the increased HOMO/LUMO gap (0.10578 hartree PBE0, 0.02226 hartree BP86). This fact implies a general blue shift of the whole computed PBE0 spectrum compared to BP86. However, the PBE0 1ex state lies at 1672 nm (1913 nm in BP86) as the effect of the -3 total charge of the Fe<sub>6</sub>S<sub>6</sub> model. Among the first 70 PBE0 excitations, the Fe<sub>4</sub>S<sub>4</sub>→Fe<sub>2</sub>S<sub>2</sub> 16ex one has the highest oscillator strength and lies at 777 nm, while the corresponding state at BP86 level (27ex) lies at 993 nm. We observe four very weak Fe<sub>2</sub>S<sub>2</sub> localized excitations between 637 and 554 nm, characterized by mono-electronic transitions of 231α→240α/243α type. However, since at BP86 level the first Fe<sub>2</sub>S<sub>2</sub> localized excitation is found much higher in energy (242 ex at 480 nm), we can reasonably suppose that further excitations of this type might be found at higher energy at PBE0 level.

The final step of this comparison is the band assignment of the UV-Vis experimental spectra found in literature using our TDDFT Fe<sub>6</sub>S<sub>6</sub> as a guess. In the Supplementary Figure 12b we overlaid the BP86 spectra of Fe<sub>2</sub>S<sub>2</sub> and Fe<sub>6</sub>S<sub>6</sub> H<sub>ox</sub>-CO model.



**Supplementary Figure 12b.** Superposition of the TDDFT spectra of  $\text{Fe}_2\text{S}_2$  (red, 50 excitations) and  $\text{Fe}_6\text{S}_6$  (blue, 600 excitations)  $\text{H}_{\text{ox}}\text{-CO}$  computed at BP86 level. It is evidenced the three transitions at around 835-993 nm which can be assigned to the weak shoulder at 415 nm experimentally observed by (Swanson et al.<sup>xi</sup>).

We consider as particularly relevant the two intense bands around 900/1000 nm, which can be assigned to the shoulder at 415-420 nm observed by Swanson et al.<sup>xi</sup>. In the experimental UV-vis spectra, this shoulder is assigned to the  $\text{Fe}_4\text{S}_4$  LMCT/MLCT bands<sup>xx</sup>. According to our computation, the transitions at 935 nm (32ex and 33ex) are  $\text{Fe}_4\text{S}_4$  localized state while the 993 nm transition is a  $\text{Fe}_4\text{S}_4 \rightarrow \text{Fe}_2\text{S}_2$  CT state.

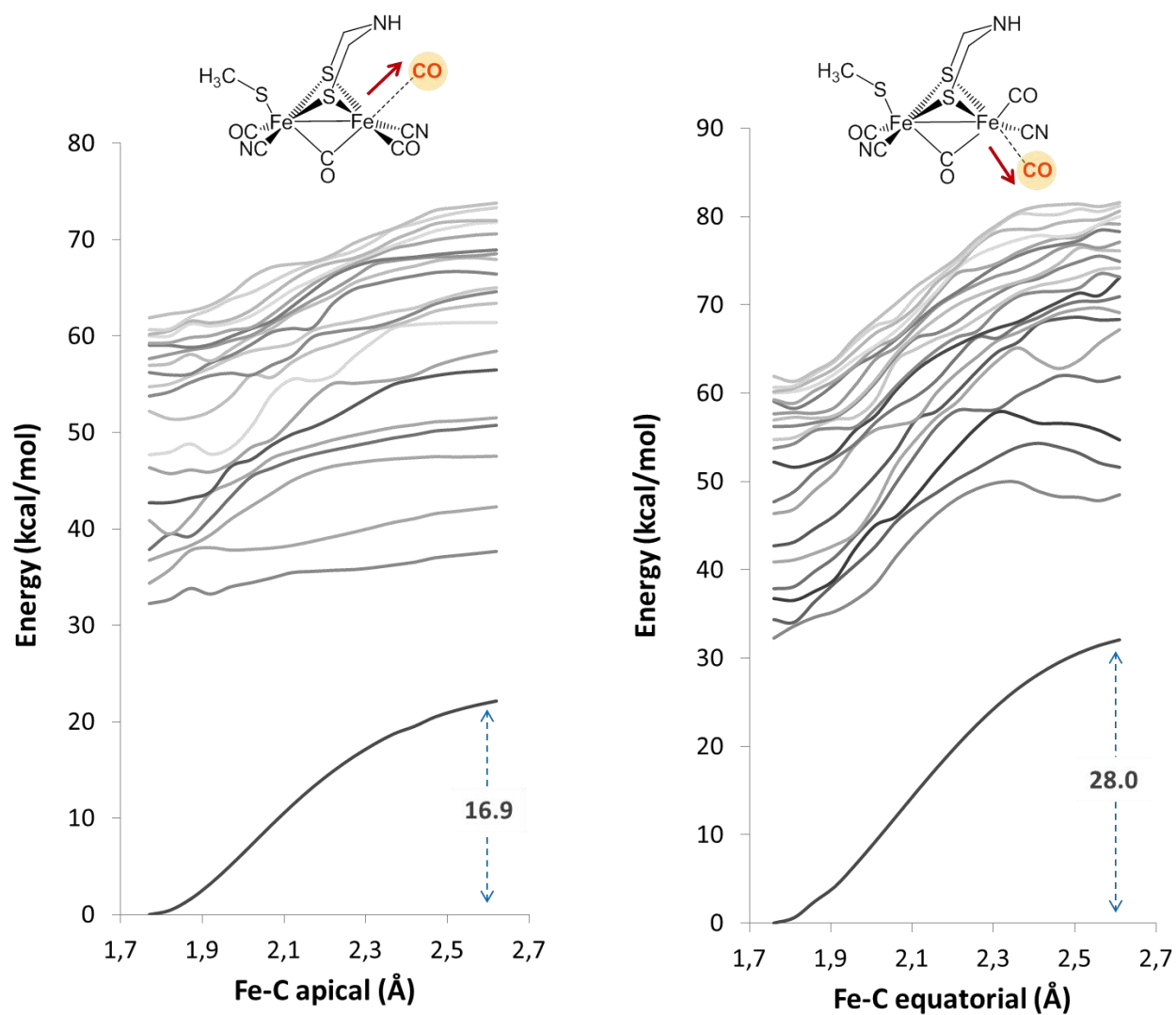
The results of this analysis can be summarized as follows.

- TDDFT, PBE0 predicts excitation wavelengths on average 50-70 nm shorter than BP86 for  $\text{Fe}_2\text{S}_2$  model;
- For the  $\text{Fe}_6\text{S}_6$  larger model, the discrepancy between BP86 and PBE0 excitation energies is much larger, the latter being higher in energy around 600-700 nm. In particular, the first  $\text{Fe}_4\text{S}_4 \rightarrow \text{Fe}_2\text{S}_2$  CT band at BP86 level at 1672 nm is found at 1034 nm at PBE0, as well as the first  $\text{Fe}_2\text{S}_2 \rightarrow \text{Fe}_4\text{S}_4$  CT band (1151 nm PBE0; 1913 nm BP86). The first  $\text{Fe}_4\text{S}_4$  localized state is found at 1477 nm. More interestingly, the first  $\text{Fe}_2\text{S}_2$  localized state band lies at 637-554 nm, although characterized by four very low oscillator strength excitations, meaning that it is almost not populated upon irradiation;
- When in the 2Fe model are introduced the residues, we observe a blue shift with respect to the “naked” 2Fe model;
- When the  $\text{Fe}_4\text{S}_4$  cubane is introduced, we observe a significant blue shift with respect to the 2Fe model at BP86 level.

Regarding the excitation energies of the  $\text{Fe}_2\text{S}_2$  localized states in the  $\text{Fe}_6\text{S}_6$  model, we observe that

- The first  $\text{Fe}_2\text{S}_2$  localized band occurs at 765 nm at BP86, which is 67 nm blue-shifted with respect to the  $\text{Fe}_2\text{S}_2$  model
- The CO dissociative 5ex state found for the  $\text{Fe}_2\text{S}_2$  model at BP86 level (699 nm) is 266 nm blue-shifted in the  $\text{Fe}_6\text{S}_6$  model.

## 2.6 – Fe<sub>2</sub>S<sub>2</sub>-CO PES scan for apical and equatorial CO



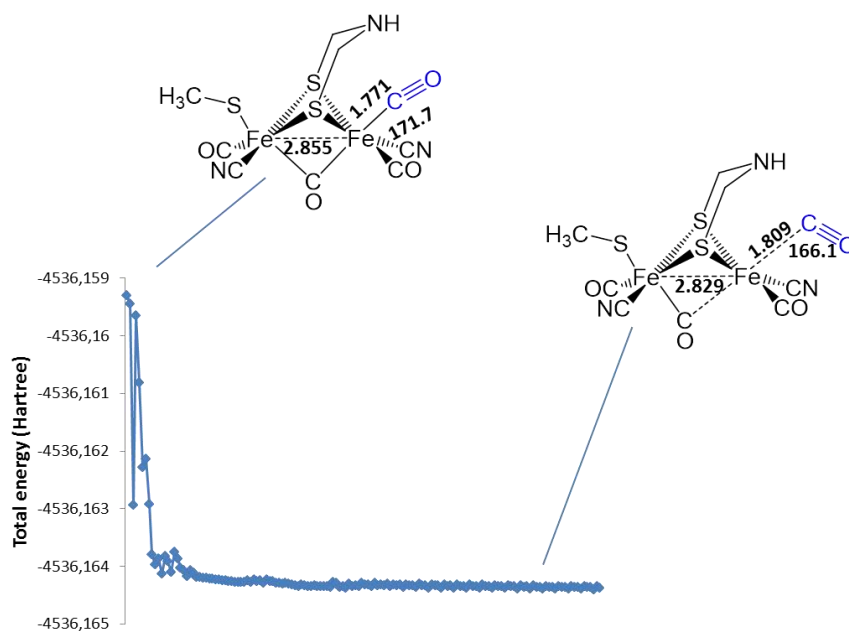
**Supplementary Figure 13.** Fe<sub>2</sub>S<sub>2</sub> H<sub>ox</sub>-CO PES scan. The plot shows the energies of the excited states as a function of the Fe-C<sub>apical</sub> and Fe-C<sub>equatorial</sub> distances. The values 16.9 kcal/mol and 28 kcal/mol are the free energy dissociation barriers (see Supplementary Fig. 8 and 9).

## 2.7 – Characterization of the apical CO dissociation in 5ex of Fe<sub>2</sub>S<sub>2</sub>-CO

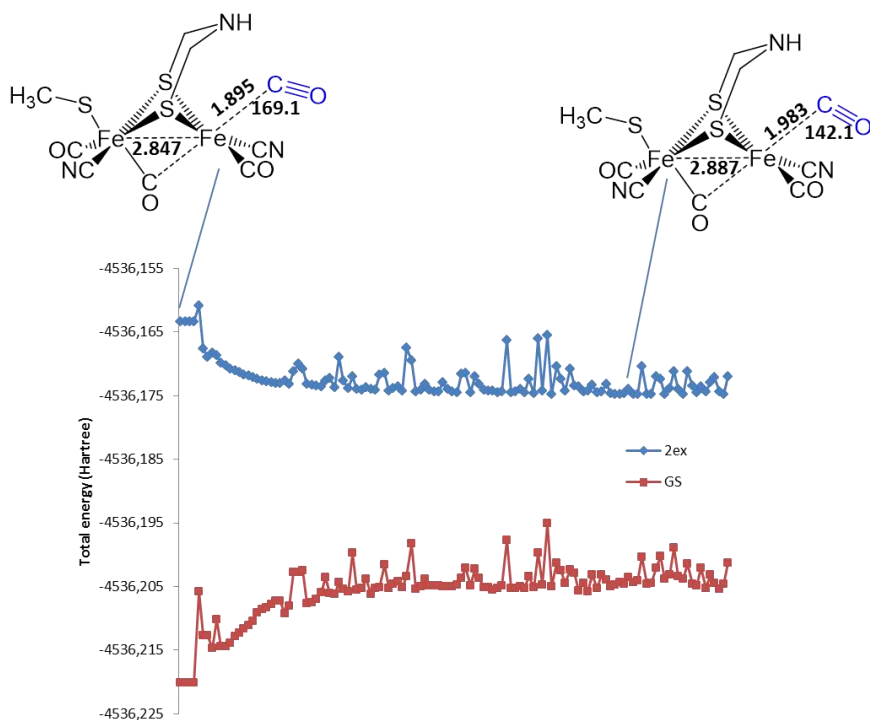
In the following figures we summarize the results of the TDDFT geometry optimizations of the Fe<sub>2</sub>S<sub>2</sub>-CO model that have allowed us to characterize the apical CO dissociation channel resulting from the population of the 5ex state. According to the band assignment proposed in section 2.6 above, the 5ex excitation can be reasonably assigned to the 242 Fe<sub>2</sub>S<sub>2</sub>-localized state in the full Fe<sub>6</sub>S<sub>6</sub>-CO model, which corresponds to the irradiation with the 405-450 purple-blue light in the experiments.

The MLLCT 5ex excitation involves the 107 $\beta$ →109 $\beta$  main mono-electronic transition, where the two singly occupied MOs have an apical Fe-C bonding and antibonding character, respectively. To characterize this channel, we performed:

- The TDDFT optimization of the structure of the model in its 5ex state (Supplementary Figure 14) starting from the ground state minimum geometry;
- Optimization of the 2ex state (Supplementary Figure 15) from the previous obtained 5ex optimized structure with the further elongation of the apical Fe-C (+0.086Å) to overcome the 5ex-2ex surface crossing points;
- Optimization of the 1ex structure (Supplementary Figure 16) using the previous obtained 2ex optimized structure as starting point reaching a reference state instability point in which 1ex becomes the ground state.

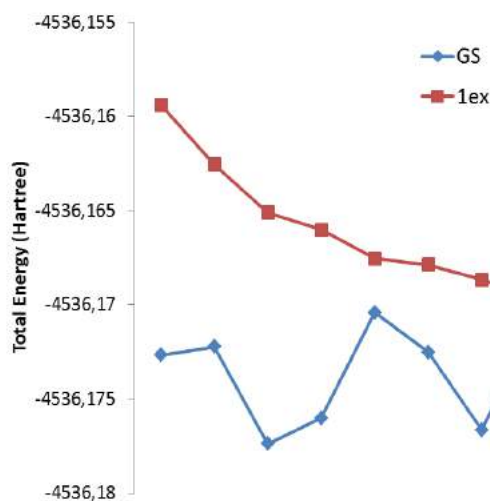


**Supplementary Figure 14.** Fe<sub>2</sub>S<sub>2</sub> H<sub>ox</sub>-CO TDDFT geometry optimization history of 5ex. We show here the 5ex excitation energies (in hartree). The starting point (on the left) is the ground state structure. This 150 cycles TDDFT optimization partially met the convergence criteria ( $\Delta E < 3 \cdot 10^{-5}$  hartree instead of  $10^{-6}$ ; gradient norm vector around 0.040 instead of 0.001 hartree/Å<sup>-1</sup>).



**Supplementary Figure 15.**  $\text{Fe}_2\text{S}_2$   $\text{H}_{\text{ox}}\text{-CO}$  TDDFT geometry optimization history of 2ex. We show here the 2ex excitation energies (in blue) and the corresponding GS (in red) energies (in hartree). The starting point structure (on the left) is the one obtained from 5ex geometry optimization (see above) with the dissociating apical  $\text{Fe}_d\text{-C}$  distance further elongated by  $0.086\text{\AA}$ . This 120 cycles TDDFT optimization does not meet the convergence criteria ( $\Delta E < 10^{-6}$  hartree; gradient norm vector less than  $0.001$  hartree/ $\text{\AA}^{-1}$ ) and the final form is the lowest energy structure obtained during the optimization.

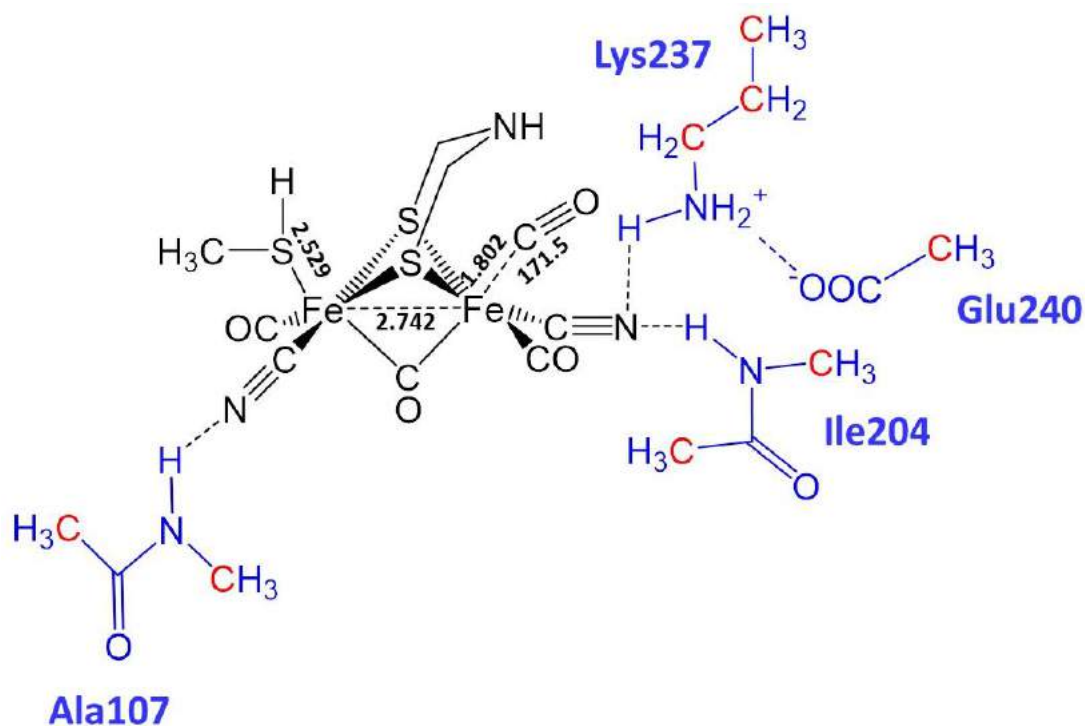
In Supplementary Figure 16, we show the history of the 1ex TDDFT geometry optimization to evidence the crossing between the 1ex PES with the ground state PES.



**Supplementary Figure 16.**  $\text{Fe}_2\text{S}_2$   $\text{H}_{\text{ox}}\text{-CO}$  1ex TDDFT geometry optimization history. We show the nine 1ex excitation energies (in red) and the corresponding GS (in blue) energies (in hartree) before the reference state instability of the TDDFT solution.



The dissociative nature of the 5ex state is confirmed also when the side chain residues are considered. According to section 2.5, we found that the 5ex state for the Fe<sub>2</sub>S<sub>2</sub> BP86/SCH<sub>3</sub><sup>-</sup> model corresponds to the 12ex state in the BP86/HSCH<sub>3</sub>/residues model. Starting from the minimum structure of the latter, we optimized the 12ex state geometry. After 446 optimization cycles (Supplementary Figure 17), we observed an apical Fe-C bond elongation of 0.023 Å and a bond angle bending of 4 degrees, in agreement with the 5ex state optimized form obtained for the smaller Fe<sub>2</sub>S<sub>2</sub> model.

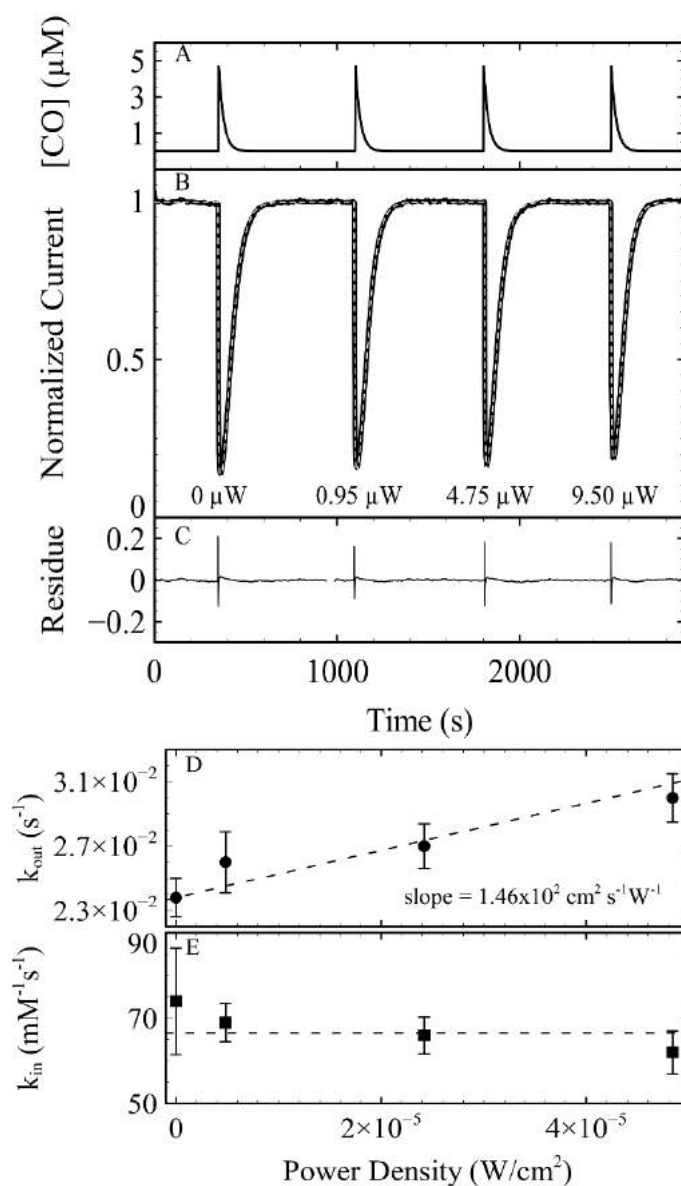


**Supplementary Figure 17.** Optimized structure of the 12ex of the BP86/HSCH<sub>3</sub>/residues model.

### 3 – PFV – Supplementary Results

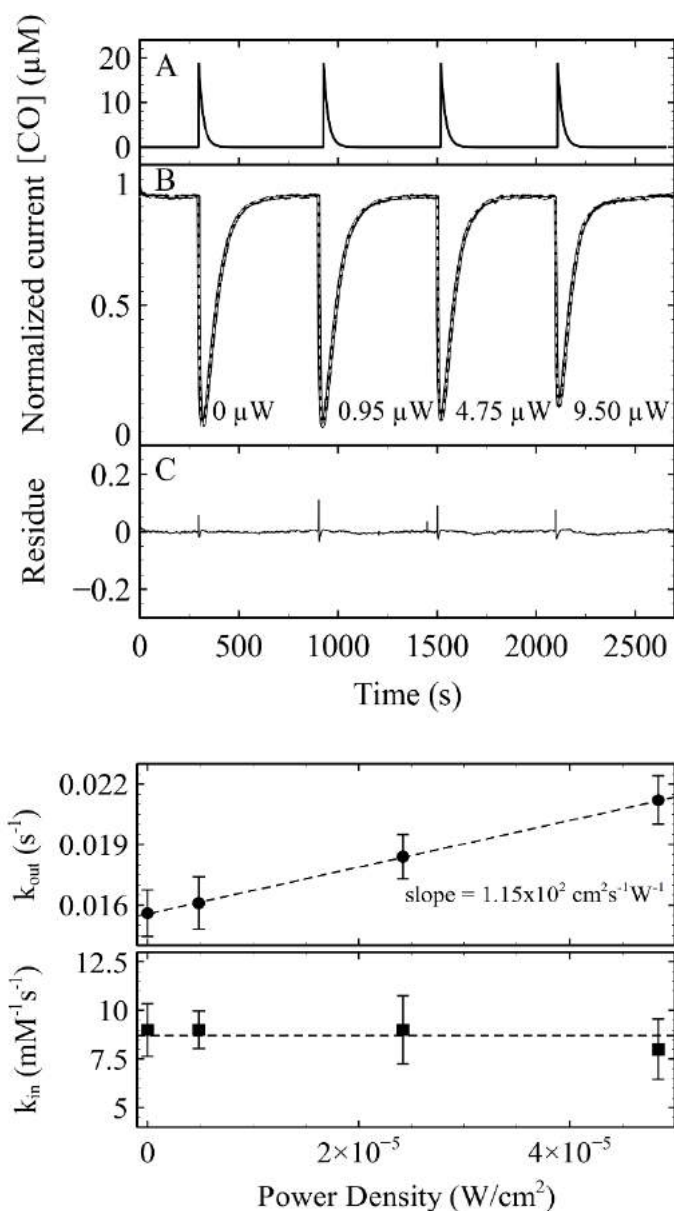
#### 3.1 - CO inhibition as function of the power of illumination

We report the same experiments as those shown in main text Figure 1, but for the enzymes from *C. reinhardtii* (Supplementary Fig.17) and *C. Acetobutylicum* (Supplementary Fig.18) under irradiation with the laser at 405 nm.



**Supplementary Figure 18.** Electrochemical experiment showing the effect of 405 nm irradiation on the inhibition by CO of the FeFe-hydrogenase from *C. reinhardtii*. Panel A shows the change in CO concentration against time, panel B shows the resulting change in turnover rate. Panel C shows the residue of the fit of the model. The fit returned the values of the rate constants shown in panels D and E. The Y-errors show the standard deviations observed in 2 independent experiments (the error on  $k_{in}$  includes the error in the value of  $[CO]_0$ ).

$p(H_2)=1 \text{ atm}$ ,  $[CO]_0= 5 \mu\text{M}$ ,  $\tau=19 \text{ s}$ ,  $pH= 7$ ,  $T= 30 \text{ }^\circ\text{C}$ . Electrode rotation rate = 3000 rpm.

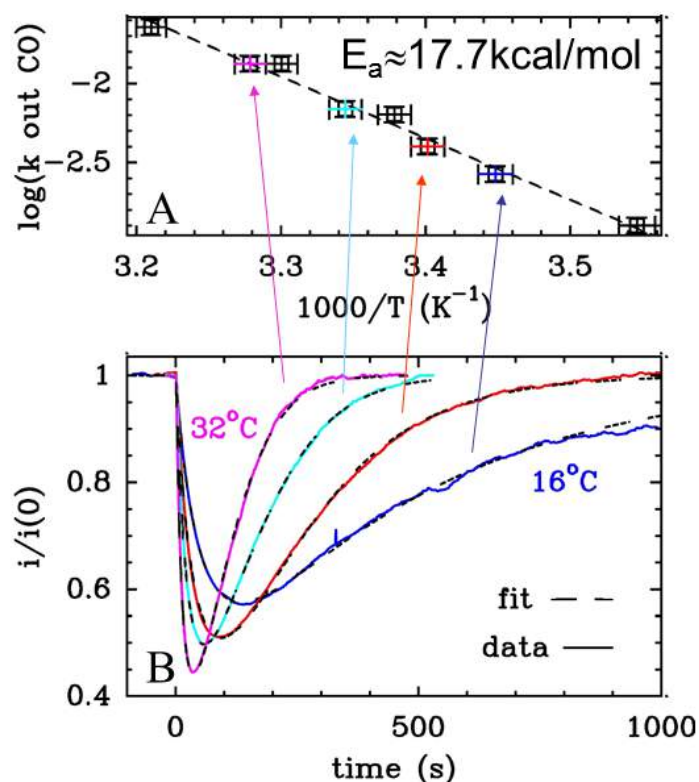


**Supplementary Figure 19.** Electrochemical experiment showing the effect of 405 nm irradiation on the inhibition by CO of the FeFe-hydrogenase from *C. acetobutylicum*. Panel A shows the change in CO concentration against time, panel B shows the resulting change in turnover rate. Panel C shows the residue of the fit of the model. The fit returned the values of the rate constants shown in panels D and E. The Y-errors show the standard deviations observed in 2 independent experiments (the error on  $k_{\text{in}}$  includes the error in the value of  $[\text{CO}]_0$ ).

$p(\text{H}_2)=1 \text{ atm}$ ,  $[\text{CO}]_0= 19.6 \mu\text{M}$ ,  $\tau=17 \text{ s}$ ,  $\text{pH}= 7$ ,  $T= 30 \text{ }^\circ\text{C}$ . Electrode rotation rate = 3000 rpm.

### 3.2 – Activation energy for CO release

We calculated the activation energy for CO release from the FeFe-hydrogenase of *C. acetobutylicum* by performing several experiments of inhibition of FeFe-hydrogenase by CO (same as those described in Supplementary Figure 1, only in the dark) with a fixed CO concentration but changing the temperature (16-32 °C) in each experiment. We fitted the kinetic model in ref. 15 to the data, to obtain the values of the rate constant for CO release ( $k_{out}$ ). Using the Arrhenius law, we calculated the activation energy ( $E_a$ ) from the slope of the plot of  $\log(k_{out})$  against  $1/T$ .



**Supplementary Figure 20.** Inhibition by CO of the FeFe- hydrogenase from *C. acetobutylicum* at different temperatures and activation energy for CO release. Panel A: Log of  $k_{out}$  (obtained from the experiments in Panel B) as function of the reciprocal of the temperature. Panel B: turnover rate as function of time, after injection of CO at  $t = 0$  s. Different colors indicate the different temperature at which the experiment was performed, the dashed line is the fit of the kinetic model.

$p(H_2) = 1 \text{ atm}$ ,  $[CO]_0 = 6 \mu\text{M}$ ,  $pH = 7$ ,  $T = 16\text{-}32 \text{ }^\circ\text{C}$ . Electrode rotation rate = 3000 rpm

#### 4 – Kinetic scheme and derivation of the rate constants

We apply the quasi-steady state approximation (QSSA) on E\*-CO of the kinetic model in fig.5 in the main text:

$$[E^* - CO] = \Lambda [E - CO] \quad \text{eq. 1}$$

We define  $\Lambda$  in eq. 1 as:

$$\Lambda = \frac{\sigma I}{(k^{-hv} + k_{-2}^{hv})}$$

We define  $[E-CO]^\#$  as the sum of the enzyme in the ground state and in the excited state inhibited by CO:

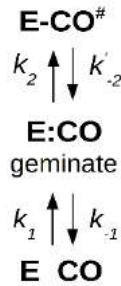
$$[E^\# - CO] = [E - CO] + [E^* - CO]$$

We can write:

$$[E^* - CO] = \frac{[E - CO]^\#}{1 + \Lambda} \quad \text{eq. 2}$$

$$[E - CO] = \frac{\Lambda [E - CO]^\#}{1 + \Lambda} \quad \text{eq. 3}$$

Under these assumptions, the mechanism of figure 5 in text can be simplified as:



The evolution of E-CO<sup>#</sup> as function of time is given by:

$$\frac{d[E - CO]^\#}{dt} = k_{+2} [E:CO] - k_{-2}^{hv} [E^* - CO] - k_{-2} [E - CO] = k_{+2} [E:CO] - k'_{-2} [E - CO]^\# \quad \text{eq. 4}$$

where we define:

$$k'_{-2} = \frac{(k_{-2} + k_{-2}^{hv}\Lambda)}{1 + \Lambda}$$

Substituting  $k_{-2}$  in the model that describes the CO inhibition (previously reported in ref. 28) with  $k'_{-2}$  gives the first order rate constant for CO release ( $k_{out}$ ) for the kinetic scheme in fig. 5:

$$k_{out} = \frac{k_{-1}k'_{-2}}{k_{-1} + k_2} = \frac{k_{-1}(k_{-2} + k_{-2}^{hv}\Lambda)}{(1 + \Lambda)(k_{-1} + k_2)} \quad \text{eq. 5}$$

## References

---

- i. Becke, A. D. *Phys. Rev. A*, **1988**, *38*, 3098-3100.
- ii. Perdew, J. P. *Phys. Rev. B.*, **1986**, *33*, 8822-8824
- iii. Adamo, C.; Scuseria, G.; Barone, V. *J. Chem. Phys.* **1999**, *111*, 2889-2899.
- iv. Eichkorn, K.; Weigend, F.; Treutler, O.; Ahlrichs, R. *Theor. Chem. Acc.* **1997**, *97*, 119-124.
- v. Schafer, A.; Huber, C.; Ahlrichs, R. *J. Chem. Phys.*, **1994**, *100*, 5829-5835.
- vi. Ahlrichs, R.; Bar, M.; Haser, M.; Horn, H.; Kolmel, C. *Chem. Phys. Lett.*, **1989**, *162*, 165-169.
- vii. Furche, F.; Ahlrichs, R. *J. Chem. Phys.*, **2002**, *117*, 7433-7447.
- viii. Rappoport, D.; Furche, F.; *J. Chem. Phys.*, **2005**, *122*, 064105
- ix. Bertini, L.; Greco, C.; De Gioia, L.; Fantucci, P. *J. Phys. Chem. A*, **2006**, *110*, 12900-12907.
- x. Bertini, L.; Greco, C.; De Gioia, L.; Fantucci, P. *J. Phys. Chem. A*, **2009**, *113*, 5657-5670.
- xi. Bertini, L.; Fantucci, P.; De Gioia, L. *Organometallics*, **2011**, *30*, 487-498.
- xii. Wang, W.; Rauchfuss, T. B.; Bertini, L.; Zampella, G. *J. Am. Chem. Soc.*, **2012**, *134*, 4525-4528.
- xiii. Bertini, L.; Fantucci, P.; De Gioia, L.; Zampella, G.; *Inorg. Chem.* **2013**, *52*, 9826–41
- xiv. Bertini, L.; Greco, C.; Fantucci, P.; De Gioia, L. *Int. J. Quantum Chem.*, **2014**, *114*, 851-861
- xv. Bertini, L.; Greco, C.; Bruschi, M.; Fantucci, P.; De Gioia, L. *Organometallics*, **2010**, *29*, 2013.
- xvi. Thauer, R. K.; Käufer, B.; Zähringer, M.; Jungermann, K. *Eur. J. Biochem.* **1974**, *42*, 447–452.
- xvii. Baffert, C.; Bertini, L.; Lautier, T.; Greco, C.; Sybirna, K.; Ezanno, P.; Etienne, E.; Soucaille, P.; Bertrand, P.; Bottin, H.; Meynial-Salles, I.; De Gioia, L.; Léger, C. *J. Am. Chem. Soc.* **2011**, *133*, 2096–2099.
- xviii. Bruschi, M.; Greco, C.; Kaukonen, M.; Fantucci, P.; Ryde, U.; De Gioia, L. *Angew. Chemie - Int. Ed.*, **2009**, *48*, 3503–3506.
- xix. Swanson, K.D., Ratzloff, M.W., Mulder, D. W., Artz, J. H., Ghose, S., Hoffman, A., White, S., Zadornyy, O. A., Broderick, J. B., Bothner, B., King, P. W. and Peters J. W. *J. Am. Chem. Soc.*, **2015**, *137*, 1809-1816
- xx. Mulder, D. W.; Ortillo, D. O.; Gardenghi, D. J.; Naumov, A. V.; Ruebush, S. S.; Szilagyi, R. K.; Huynh, B.; Broderick, J. B.; Peters, J. W. *Biochemistry*, **2009**, *48*, 6240–6248.

## Chapter 5

# Effect of light on the active forms of FeFe hydrogenases

## 5.1 Summary

We used the methodological approach developed in the previous chapter to study the photoinhibition of FeFe-hydrogenases. Although the photo-sensitivity could be a major obstacle to the use of FeFe-hydrogenases for H<sub>2</sub> photo-production, we could find only a couple of papers on this topic in the literature. Spectroscopic studies<sup>48,63</sup> showed that DdHydAB is destroyed by visible light. Direct electrochemistry<sup>87</sup> experiments showed that DdHydAB is inactivated upon irradiation with a Halogen lamp and the process is partially reversible. The authors of these papers did not report the action spectrum of this reaction, nor did they propose a mechanism of photodamage.

To investigate this photoinhibition, we performed direct photo-electrochemistry measurements with CrHydA1 and CaHydA. Under both H<sub>2</sub> oxidation and H<sup>+</sup> reduction conditions, the irradiation by a Xenon lamp induces an inactivation of these enzymes. The action spectra of photoinhibition, determined by using a Xenon lamp with glass filters and an Halogen lamp, showed that UVB is responsible for this process. To obtain a mechanistic description of the photoinhibition we performed TDDFT calculations. The calculated UV-visible spectrum of the active site in the H<sub>ox</sub> state is characterized by the presence of charge-transfer excited states, involving the intrinsic CO ligands, populated upon absorption of light in the UV domain. We explored the potential energy surfaces (PES) of the excited states as function of the length of the Fe-CO and Fe-S bonds in the active site. Only the PESs of the excited states as a function of the distance of the two COs bound in equatorial position to the irons, show energy pathways that end up with CO dissociation. We studied the possible consequences of apical or equatorial CO dissociation from both H<sub>ox</sub> and H<sub>red</sub>. The most stable photo-product has an all-terminal geometry without the bridging CO and with two equatorial COs, irrespective of the starting state. The reduced form of this photo-product could easily form a stable, inactive state with a bridging hydride.

In conclusion, we determined the action spectra of photoinhibition, and we proposed for the first time a mechanistic description of the process using DFT and



TDDFT. Comparing the results of this study with previous studies, we observed that the photo-sensitivity changes among FeFe-hydrogenases. Indeed, CrHydA1 and CaHydA are resistant to visible light whereas DdHydAB is not. The factors that determine the sensitivity or the resistance to visible light are still unknown.

We performed all the PFV experiments described above with a phosphate buffer. The reason of this is that incidentally we observed that the presence of  $\text{Cl}^-$  anions in the buffer changes the shape at high potential of cyclic voltammograms of CrHydA1, compared to cyclic voltammograms recorded in potassium phosphate buffer. The effect is present both in the dark and under irradiation. In the second part of this chapter we present our preliminary results on this topic. The dependence of the  $\text{Cl}^-$  effect on the experimental conditions in the dark and under irradiation is still unclear. DFT calculations and MD simulations could help to determine if  $\text{Cl}^-$  anions reach the active site or interact with charged residues on the surface of the enzyme.

## 5.2 Résumé

Nous avons utilisé l'approche méthodologique développée dans le chapitre précédent pour étudier la photoinhibition des hydrogénases-FeFe. Bien que la photo-sensibilité puisse constituer un obstacle majeur à l'utilisation des hydrogénases-FeFe pour la photo-production de  $H_2$ , il n'existe que quelques travaux sur ce sujet dans la littérature. Des études spectroscopiques<sup>48,63</sup> ont montré que DdHydAB est détruit par la lumière visible. Des expériences d'électrochimie directe<sup>87</sup> ont montré que DdHydAB est inactivé par irradiation avec une lampe halogène et que le processus est partiellement réversible. Les auteurs de ces articles n'ont pas étudié le spectre d'action de cette réaction et n'ont pas non plus proposé un mécanisme de photo-dommage.

Pour étudier cette photoinhibition, nous avons effectué des mesures de photo-électrochimie directe avec CrHydA1 et CaHydA. Dans les conditions de réduction de  $H_2$  et d'oxydation de  $H^+$ , l'irradiation par une lampe au xénon induit une inactivation de ces enzymes. Les spectres d'action de la photoinhibition, déterminés en utilisant une lampe au xénon avec des filtres en verre et une lampe halogène, ont montré que les UVB sont responsables de ce processus. Pour obtenir une description mécanique de la photoinhibition, nous avons effectué des calculs de type TDDFT. Le spectre UV-visible calculé du site actif dans l'état  $H_{ox}$  est caractérisé par la présence des bandes de transfert de charge, impliquant les ligands CO intrinsèques, peuplés lors de l'absorption de lumière dans le domaine UV. Nous avons exploré les surfaces énergétiques potentielles (PES) des états excités en fonction de la longueur des liaisons Fe-CO et Fe-S du site actif. Seul les PESs des états excités en fonction de la distance des deux CO liés en position équatoriale des ions Fe, montrent les voies de desexcitation qui conduisant à la dissociation du CO. Nous avons étudié les possibles conséquences de la dissociation des CO en position apicale ou équatoriale à partir de  $H_{ox}$  et  $H_{red}$ . Le photo-produit le plus stable a une géométrie dans laquelle tous les CO sont en position terminale équatoriale (pas de CO pontant), indépendamment de l'état de départ. La forme réduite du photo-produit pourrait facilement former un état stable et inactif avec un hydrure pontant.

En conclusion, nous avons déterminé le spectre d'action de la photoinhibition.

Nous avons également proposé pour la première fois une description mécanistique du processus en utilisant la DFT et la TDDFT. En comparant les résultats de cette étude avec des études antérieures, on peut constater que la photo-sensibilité varie beaucoup d'une hydrogénase-FeFe à l'autre. En effet, CrHydA1 et CaHydA sont résistantes à la lumière visible alors que DdHydAB ne l'est pas. Les facteurs qui déterminent la sensibilité ou la résistance à la lumière visible sont encore inconnus.

Nous avons effectué toutes les expériences de PFV décrites ci-dessus avec un tampon phosphate. La raison en est que, incidemment, nous avons observé que la présence d'anions  $\text{Cl}^-$  dans le tampon change la forme à un potentiel élevé des voltammogrammes cycliques de CrHydA1 à haut potentiel, par rapport aux voltammogrammes cycliques enregistrés dans le tampon phosphate. L'effet est présent à la fois dans l'obscurité et sous l'irradiation. Dans la deuxième partie de ce chapitre, nous présentons nos résultats préliminaires sur ce sujet. La dépendance de l'effet du  $\text{Cl}^-$  sur les conditions expérimentales dans l'obscurité et sous l'irradiation n'est toujours pas claire. Les calculs de DFT et les simulations de MD pourraient aider à déterminer si les anions  $\text{Cl}^-$  atteignent le site actif ou interagissent avec des résidus chargés à la surface de l'enzyme.

# Photoinhibition of FeFe hydrogenase

Matteo Sensi,<sup>†,∇</sup> Carole Baffert,<sup>†</sup> Laura Fradale,<sup>†</sup> Charles Gauquelin,<sup>//</sup> Philippe Soucaille,<sup>//</sup> Isabelle Meynial-Salles,<sup>//</sup> Hervé Bottin,<sup>⊥</sup> Luca de Gioia,<sup>∇</sup> Maurizio Bruschi,<sup>∇</sup> Vincent Fourmond,<sup>†</sup> Christophe Léger<sup>\*,†</sup> and Luca Bertini<sup>\*,∇</sup>

<sup>†</sup> Aix Marseille Univ., CNRS, BIP UMR 7281, Marseille, France

<sup>‡</sup> Department of Earth and Environmental Sciences, Milano-Bicocca University, Piazza della Scienza 1, 20126 Milan, Italy

<sup>//</sup> Université de Toulouse, INSA, UPS, INP, LISBP, INRA:UMR792,135 CNRS:UMR 5504, avenue de Rangueil, 31077 Toulouse, France

<sup>⊥</sup> Institut de Biologie Intégrative de la Cellule (I2BC), Institut Frédéric Joliot, CEA, CNRS, Univ Paris-Sud, Université Paris-Saclay, F-91198, Gif-Sur-Yvette cedex, France.

<sup>∇</sup> Department of Biotechnologies and Biosciences, University of Milano-Bicocca, Piazza della Scienza 2, 20126 Milan, Italy

## Abstract

In the enzyme FeFe hydrogenase, hydrogen oxidation and production occur at the H-cluster, a Fe<sub>6</sub>S<sub>6</sub> active site that bears intrinsic carbonyl and cyanide ligands. This enzyme has been coupled to photosensitizers to design H<sub>2</sub> photoproduction systems, and yet, according to earlier reports, the enzyme from *Desulfovibrio desulfuricans* is "easily destroyed" in "normal laboratory light". Here we report direct electrochemistry measurements of the effect of light on the activity of the enzymes from *Chlamydomonas reinhardtii* and *Clostridium acetobutylicum*, together with TDDFT and DFT calculations of the reactivity of the excited states of the H-cluster. We conclude that visible light does not inhibit these enzymes, but absorption of UV-B (280-315 nm) irreversibly damages the H-cluster by triggering the release of an intrinsic CO ligand; the resulting unsaturated species rearranges and protonates to form a stable, inactive dead-end. Answering the question of which particular hydrogenase can resist which particular wavelengths is important regarding solar H<sub>2</sub> production, and our results show that some but not all FeFe hydrogenases can actually be combined with photosensitizers that utilise the solar spectrum, provided a UV screen is used. We suggest that further investigations of the compatibility of hydrogenases or hydrogenase mimics with light-harvesting systems should also consider the possibility of irreversible photoinhibition.

## Introduction

FeFe hydrogenases are enzymes that catalyze the oxidation and evolution of molecular hydrogen at an organometallic active site called the H-cluster (figure 1). The H-cluster consists of a Fe<sub>4</sub>S<sub>4</sub> cluster bound by a cysteine to a 2Fe site. Each of the two iron atoms is coordinated by a carbonyl and a cyanide ligands and the two Fe are bridged by a third carbonyl and an azadithiolate (adt) group.<sup>1-4</sup> A particular FeFe hydrogenase may house zero (as in the enzyme from *Chlamydomonas reinhardtii*<sup>5</sup>), two (*Desulfovibrio desulfuricans*<sup>6</sup> and *Megasphaera elsdenii*<sup>7</sup>) or four (*Clostridium pasteurianum*<sup>8</sup> or *C. acetobutylicum*) accessory FeS clusters involved in electron transfer to/from the redox partner. (See ref <sup>9</sup> for a recent account on the diversity of FeFe hydrogenases). Spectroscopic investigations have helped to identify various states of the H-cluster, including some of the catalytic intermediates.<sup>10</sup> It is

1  
2  
3  
4  
5  
6  
7  
8  
9  
10  
11  
12  
13  
14  
15  
16  
17  
18  
19  
20  
21  
22  
23  
24  
25  
26  
27  
28  
29  
30  
31  
32  
33  
34  
35  
36  
37  
38  
39  
40  
41  
42  
43  
44  
45  
46  
47  
48  
49  
50  
51  
52  
53  
54  
55  
56  
57  
58  
59  
60

believed that H<sub>2</sub> binds in the catalytic cycle to the state referred to as "H<sub>ox</sub>" (Fe<sup>I</sup>Fe<sup>II</sup>) in which the iron atom that is distal from the Fe<sub>4</sub>S<sub>4</sub> cluster (Fe<sub>d</sub>) has a free coordination site in the apical position. The same binding site is the target of competitive inhibitors such as CO (refs 11,12) and O<sub>2</sub> (refs 13–15). Binding of extrinsic CO to H<sub>ox</sub> leads to an inactive state termed "H<sub>ox</sub>-CO" which is also detected after the active site has been destroyed in response to oxidative stress, be it oxic<sup>16</sup> or anoxic.<sup>17</sup> In the absence of extrinsic CO, the formation of H<sub>ox</sub>-CO occurs because damage of the H-cluster leads to the release of intrinsic carbonyls, some of which are grabbed by nearby intact H-clusters. The latter reaction has been called cannibalisation. Reductive conditions also inhibit the enzyme, in a complex manner.<sup>18,19</sup>

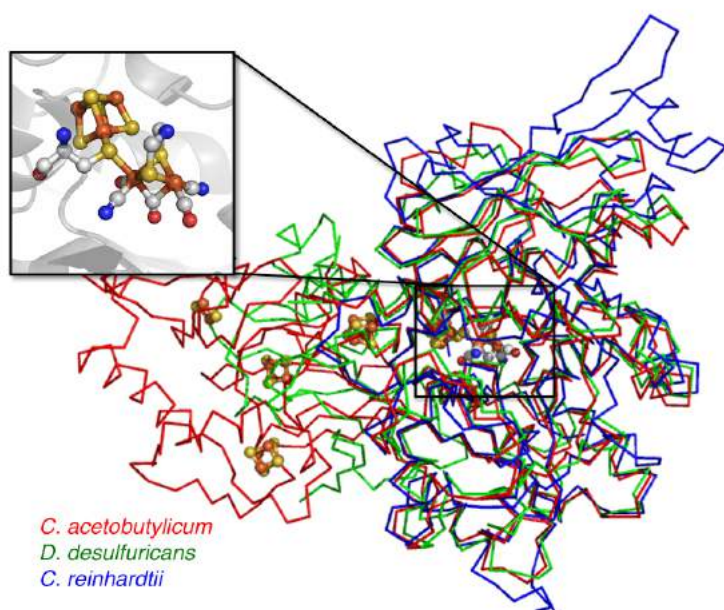


**Figure 1.** The backbones and active site ("H-cluster") of FeFe hydrogenases discussed in this work (from PDB 3LX4,<sup>5</sup> 1HFE,<sup>6</sup> and 3C8Y<sup>8</sup>).

Light affects the H-cluster. The most obvious reason the enzyme is sensitive to UV-vis irradiation is the presence in the active site of photolabile iron carbonyl bonds. That exogenous CO binds less tightly to the H-cluster under the white light of a halogen lamp than in the dark was discovered more than 40 years ago.<sup>20</sup> Now we understand the molecular reasons for this: light has no effect on the CO binding rate, but the absorption of purple or blue light produces an excited state that spontaneously dissociates the exogenous ligand. This results in an increase in the rate of dissociation compared to the kinetics observed in the dark. This effect is small and proportional to the power of the incident light because the H-cluster is a very weak chromophore.<sup>21</sup> Irradiation in the UVA range (355 nm) also photo-dissociates exogenous CO,<sup>22</sup> as was observed in time-resolved infrared spectroscopy experiments designed to monitor the subsequent rebinding of the carbonyl. Illumination with red light (632.8 nm) results in partial dissociation of exogenous CO when the enzyme is in the solid state.<sup>23</sup>

1  
2  
3  
4  
5  
6  
7  
8  
9  
10  
11  
12  
13  
14  
15  
16  
17  
18  
19  
20  
21  
22  
23  
24  
25  
26  
27  
28  
29  
30  
31  
32  
33  
34  
35  
36  
37  
38  
39  
40  
41  
42  
43  
44  
45  
46  
47  
48  
49  
50  
51  
52  
53  
54  
55  
56  
57  
58  
59  
60

Illumination also has other, more complex effects, not all of which could be rationalized at that point. Under certain cryogenic conditions, the photodissociation of CO from  $H_{ox}$ -CO leads to various photoproducts.<sup>24</sup> With the enzyme in fluid solution (2 °C to room T), illumination in the presence of exogenous  $^{13}CO$  exchanges the extrinsic and intrinsic CO ligands.<sup>25,26</sup> Even more notable, Albracht and coworkers reported in an EPR investigation that the H-cluster of the enzyme from *D. desulfuricans* (*Dd*) is "easily destroyed by light (...) under normal laboratory conditions, i.e. daylight plus the light from fluorescent lamps on the ceiling".<sup>27</sup> The conversion of the  $H_{ox}$  form of the *D. desulfuricans* enzyme into the  $H_{ox}$ -CO state upon illumination with *visible* light has been detected by FTIR,<sup>25,28</sup> this was taken as evidence of light-induced H-cluster destruction.

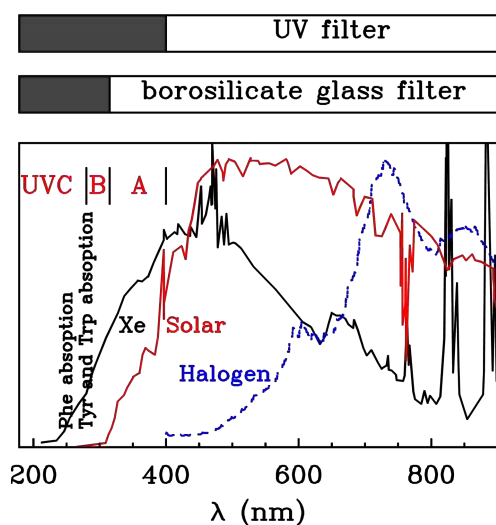


**Figure 2.** The typical emission spectra of Xe and Halogen lamps (black and dashed blue lines, respectively), and the spectrum of solar irradiation at sea level (red line, from [www.newport.com/](http://www.newport.com/)). On top we show the cut-off of the glass and UV filters used in this work (see their absorption spectra in fig. S11). Vertical text indicates the positions of the UV absorption bands of Ph, Tyr and Trp residues.<sup>29</sup>

The conclusion that irradiation destroys the enzyme from *Dd* has not been supported yet by the results of solution assays or by any other experiments with an FeFe hydrogenase from a different organism. Moreover, photoelectrochemical experiments reported so far, where the activity of various FeFe hydrogenases adsorbed onto an electrode is monitored following illumination,<sup>30</sup> are not consistent with the above-described dramatic effects of visible light. In the experiments of Ruediger et al, the effect of white light on the turnover rate of the enzyme from *Dd* is either mostly reversible (under oxidizing conditions, at -159 mV vs SHE in pH 5, fig. 2A in ref<sup>28</sup>) or absent (under reductive conditions, at -560 mV or -460 mV vs SHE, pH 5, *ibid.*). Armstrong *et al* report no effect of white light on the activity of *Chlamydomonas reinhardtii* (*Cr*) and *Clostridium acetobutylicum* (*Ca*) hydrogenases, except the photo-induced release of exogenous CO.<sup>31</sup> In the experiments described in refs<sup>28</sup> and<sup>31</sup>, all-glass electrochemical cells and halogen lamps were used, suggesting that there was no exposure to UV. In our previous investigation,<sup>21</sup> we could not detect any *irreversible* effect of irradiation with monochromatic purple/blue/green or red light on the activity of the FeFe

1  
2  
3 hydrogenases from *Cr*, *Ca* and *Megasphaera elsdenii*. This prompted us to examine the  
4 effect of UV irradiation, which we report in this work.  
5  
6

7 Fig. 2 shows the emission spectrum of the so-called white lamps mentioned in earlier studies  
8 of hydrogenases and used in this work, together with the solar spectrum that is relevant to  
9 the discussion of any device that would aim at using either hydrogenase or hydrogenase  
10 mimics and the energy from sunlight to produce hydrogen from water. The obvious  
11 difference between tungsten halogen incandescent lamps and Xenon arc lamps is that the  
12 latter generate substantial ultraviolet A and B radiation. In this work we used a Xe arc lamp,  
13 and optional filters that cut the high energy part of the emission (figure S11). We  
14 demonstrate that UVB are responsible for irreversible photo-damage to FeFe hydrogenase;  
15 we propose a mechanism based on the results of TDDFT calculations of the photoreactivity  
16 of a small model of the H-cluster, and we use a larger model to run DFT calculations of the  
17 structure of the end-product.  
18  
19  
20  
21

## 22 Results

### 23 Electrochemical assays

24  
25 Fig. 3A and 3B show the change in turnover rates of H<sub>2</sub> oxidation and production measured  
26 in direct electrochemistry experiments, as we expose the enzymes to light from various  
27 sources.<sup>30,32</sup> The enzyme from *Cr* was adsorbed onto a rotating disc electrode poised at  
28 -158 mV or -508 mV to drive H<sub>2</sub> oxidation or production, which is observed as a positive or  
29 negative current, respectively. The light beam of a Xe lamp (150 W electrical power  
30 according to manufacturer's specifications) was directed by an optical fiber (transmittance  
31 range 280-2200 nm) towards the surface of the electrode, across a quartz window fused with  
32 the bottom of the electrochemical cell (fig. S15).  
33  
34  
35  
36  
37

38 The signals in panels A and B show that irradiation makes the current decrease faster (the  
39 slow background decrease in the dark results from the desorption of the enzyme film). Upon  
40 switching on and off the Xe lamp, we saw no *instant* increase in current which would have  
41 resulted from a light induced change in turnover rate (that is, an effect on the catalytic cycle  
42 and/or an effect of heating). The effect of irradiation with the Xe lamp is only to *slowly*  
43 transform the active enzyme into a form that cannot oxidize or produce H<sub>2</sub>. We could  
44 measure the time constant of the inactivation from the "light minus dark" difference between  
45 the 1st order rate constants of decay.  
46  
47  
48

49 This photoinactivation is apparently irreversible: no recovery of activity is observed after the  
50 light is turned off. All our attempts to reactivate the enzyme were unsuccessful (we tried to  
51 step the potential down or to expose the inactivated enzyme to 150 μM exogenous CO, data  
52 not shown).  
53  
54

55 The kinetics of photodamage appears to be independent of the redox state of the H-cluster.  
56 Indeed, in our electrochemical experiments, photoinhibition was observed under conditions  
57 of oxidative and reductive turnover, although the photoinactivation may be slightly faster  
58 when the enzyme is oxidizing H<sub>2</sub> than when it is producing H<sub>2</sub>. Indeed, the decay time  
59 constant equates  $\tau = 24 \pm 5$  min (n=6 independent determinations) in the range -258 mV to  
60

0 mV, versus  $38 \pm 1$  min  $n=2$  at  $-508$  mV, at  $30$  °C, pH 6.8, 1 bar  $H_2$ , (Fig. S13); we did not see an effect of varying the electrode potential above the open circuit potential).

Figure S13 also shows that the kinetics of inactivation of the enzyme from *Cr* is the same under 1 and 0.1 bar  $H_2$  (the Michaelis constant of FeFe hydrogenase is close to 1 bar,<sup>33</sup> so the saturation with  $H_2$  changes from 50% to 10% upon decreasing ten-fold the  $H_2$  concentration).

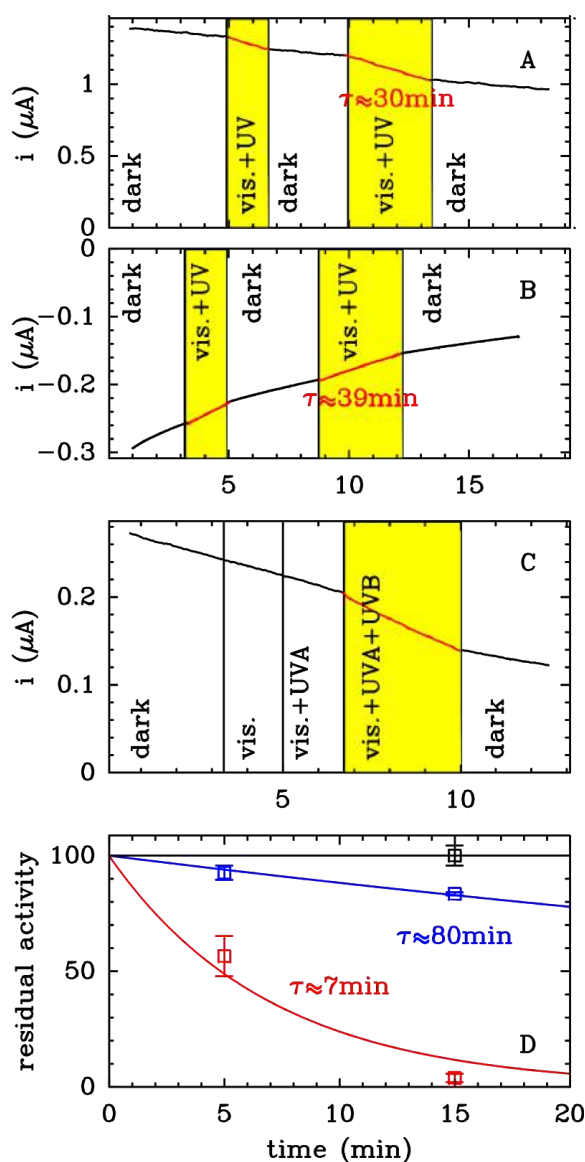


**Figure 3.** Effect of irradiation on the activity ( $H_2$  oxidation in panels A, C and D;  $H_2$  production in panel B) of *Chlamydomonas reinhardtii* hydrogenase, measured either electrochemically with the enzyme undergoing direct electron transfer to a rotating electrode (panels A, B and C), or in a solution assay (panel D). The yellow surfaces indicate simultaneous exposure to visible light, UVA and UVB.

In experiments such as those shown in Panels A, B and C, the time constant of inactivation ( $\tau$ ) was calculated as the reciprocal of the difference between the 1st order rate constants of current decrease measured in the dark and upon irradiation; this corrects from the current decay that is due to film loss. **Panel A:** hydrogen oxidation at  $E=-158$  mV vs SHE, pH=6.8, alternating dark and exposure to the "white light" of a Xe lamp. **Panel B:** hydrogen production at  $E=-508$  mV vs SHE (30



1  
2  
3  
4 °C, pH=6.8), alternating dark and exposure to the "white light" of a Xe lamp. **Panel C:** hydrogen  
5 oxidation at  $E=-158$  mV vs SHE, pH=6.8, in the dark, upon exposure to the Xe light behind the UV  
6 filter, the borosilicate glass filter, or no filter, then in the dark again. **Panel D:** a stock solution of  
7 enzyme (pH = 8, TRIS/NaCl buffer) was kept in a quartz cell at around  $T=30$  °C, in equilibrium with  
8 the atmosphere of the glove box that contained substantial amounts of  $H_2$ , either in the dark (black  
9 point), or subjected to the light of a Xe lamp with (blue data points) or without (red data points) the  
10 UV filter, and the  $H_2$  oxidation activity was assayed after 5 or 15 minutes (at 30 °C, pH 7, using  
11 20 mM methyl viologen as electron acceptor). The error bars represent the difference between the  
12 results of two independent experiments.  
13

14  
15 We repeated the same experiments with the FeFe hydrogenase from Ca and obtained  
16 similar results: the time constant of inactivation upon irradiation with the Xe lamp is  $36\pm 3$  min  
17  $n=5$  in the range -258 mV to -58 mV, and  $34\pm 4$  min  $n=3$  at -508 mV (all at 30 °C, pH 6.8,  
18 1 bar  $H_2$ , figure S13).  
19

20  
21 We designed the experiment in fig. 3C to determine which part of the emission spectrum of  
22 the Xe lamp induces the inactivation under oxidative conditions. We used two filters, whose  
23 absorption spectra are schematized on top of fig. 2 and plotted in fig. S11: a microscope  
24 glass slide and a UV filter, which block the wavelengths shorter than 300 nm and 340 nm,  
25 respectively. The current shown in the inset was recorded (1) first in the dark, (2) then the  
26 light was switched on and the two longpass filters interposed between the source and the  
27 electrochemical cell, (3) then the UV filter was removed, (4) then the glass filter was also  
28 removed, and (5) finally the light was switched off. The observation that either of the two  
29 filter prevents photodamage and the fact that the Xe source does not emit in the UVC range  
30 (fig. 2), shows that UVB (280-315 nm) is responsible for inactivating the enzyme. We  
31 reached the same conclusion when we repeated the experiments with the enzyme from Ca  
32 (fig. S14).  
33  
34  
35  
36  
37

38 Similar experiments carried out with Cr and Ca hydrogenases under reductive conditions  
39 (-508 mV, pH 6.8, 1 bar  $H_2$ ) also showed that UV-B is responsible for the photoinhibition  
40 (except that both enzymes show a very small sensitivity to UV-A under reductive conditions,  
41 fig. S14).  
42  
43

44 To test whether aromatic residues near the H-cluster may contribute to light absorption, we  
45 examined the properties of the F290Y mutant of Cr FeFe hydrogenase where a  
46 phenylalanine that is close to the active site is replaced with a tyrosine.<sup>34</sup> At  $E = -158$  mV,  
47 pH 6.8, 30 °C, we measured  $\tau = 22\pm 4$  min ( $n=2$ ) with this mutant, similar to the WT  
48 ( $25\pm 5$  min  $n=3$ , under the same conditions), suggesting that the absorption of UV that  
49 causes the damage is from the H-cluster, not aromatic side-chains.  
50  
51  
52

### 53 Solution assays

54 Figure 3D shows how exposure of Cr FeFe hydrogenase to Xe light affects its  $H_2$ -oxidation  
55 activity assayed in solution, with oxidized MV as electron acceptor (see methods). The stock  
56 solution of enzyme (approximately 20 nM) was kept in a quartz cuvette, thermostated at  
57 30 °C, either in the dark or exposed to the full Xe beam (power = 150 W), or the same beam  
58 but filtered by a UV filter (which absorbs light below 400 nm). Exposed to the full Xe  
59 spectrum, the enzyme loses activity with a time constant of about 7 min (red data in fig. 3D),  
60

the red curve shows an ideal first-order decay). Using the UV filter protects the sample (blue data in fig. 3D), confirming the above conclusion that the damage results from UV light. The control sample kept in the dark shows no change in activity over this time period.

### TDDFT and DFT modelling.

To investigate the mechanism of UVB-dependent irreversible degradation of the H-cluster, we examine the first instant of the photodynamics of the active form of the H-cluster by using TDDFT potential energy surface (PES) explorations on a small  $\text{Fe}_2\text{S}_2$  model of the H-cluster<sup>21</sup> (see SI section 1). In a second step, we elucidate the fate of the photoproducts at the DFT level using a much larger  $\text{Fe}_2\text{S}_2$  model in which we include surrounding residues.

For the TDDFT characterization, we assume that the H-cluster is in the  $\text{H}_{\text{ox}}$  redox state and therefore the total charge of the  $\text{Fe}_2\text{S}_2$  model is -2. Fig. 4 shows the computed spectrum obtained from the first 100 doublet excitations. The requirement for calculating that many excited states comes from the complexity of the structure of the dinuclear cluster and our goal to understand the effect of high-energy irradiation. We keep in mind that the TDDFT spectrum of a negatively charged model of a metal-containing active site can give the natures and relative energies of the different excitations, but is not accurate enough to give the absolute excitation energies.

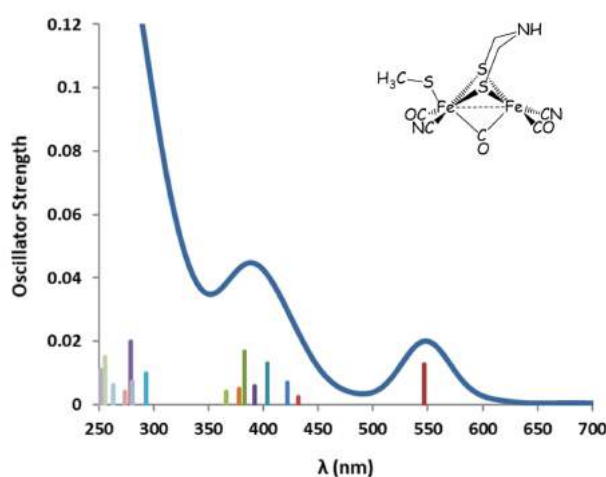


**Figure 4.**

The computed electronic spectrum of  $\text{Fe}_2\text{S}_2 \text{H}_{\text{ox}}$ . We show as sticks the most intense absorptions, and the resulting spectrum (solid line) calculated as a sum of Gaussian functions centered on the excitation energies and weighted by the computed oscillator strengths.

Three main features are observed in fig. 4. The weak absorption at 550 nm is due to a single Fe-S charge-transfer (CT) excitation. In the experimental spectrum of the FeFe hydrogenase from *C. reinhardtii*,<sup>15</sup> the weak shoulder observed at 420 nm was assigned to the Fe-S CT band states of the  $\text{Fe}_4\text{S}_4$  subcluster and it is reasonable to assume that the CT excitations localized on the di-iron subcluster occur in the same energy range. Therefore, we match the computed 550 nm weak band to the experimental feature at 420 nm. This provides an

estimate of the red shift of the TDDFT excitation energies compared to the experimental values.

In fig. 4, we also observe two more intense absorption bands around 380 and 300 nm, which all have a CT character (SI Table 2). Based on the above analysis of the weak feature at 420 nm, we conclude that these bands correspond to absorption in the UV range. From the analysis of the molecular orbital (MO) populations (table S3, Fig. 4), we conclude that occupied frontier MOs are characterized by lower CO ligand contributions and higher adt sulfur contributions, while the opposite is observed for non-occupied frontier MOs. This implies that all excitations that involve these frontier MOs have a S to CO CT contribution. Moreover, the first four virtual MOs show Fe-C  $\pi^*$  antibonding orbital combinations, favouring the Fe-C bond breaking and therefore CO dissociation.<sup>35,36</sup>

Regarding the  $\text{Fe}_2\text{S}_2$  portion of the H-cluster, the possible photochemical processes are CO release, adt Fe-S bond breaking/weakening, and Fe-S bond breaking/weakening followed by the detachment of the  $\text{Fe}_4\text{S}_4$  and  $\text{Fe}_2$  subclusters. To determine which of these reactions occurs, we examined the potential energy surfaces (PES) of the first 20 excited states, calculated by increasing the distal and proximal Fe-C stretching coordinates (fig. 5, panels A and B, respectively), the distal and proximal Fe-S stretching coordinates (panels C and D), and the Fe-SCH<sub>3</sub> stretching coordinate (panel E).

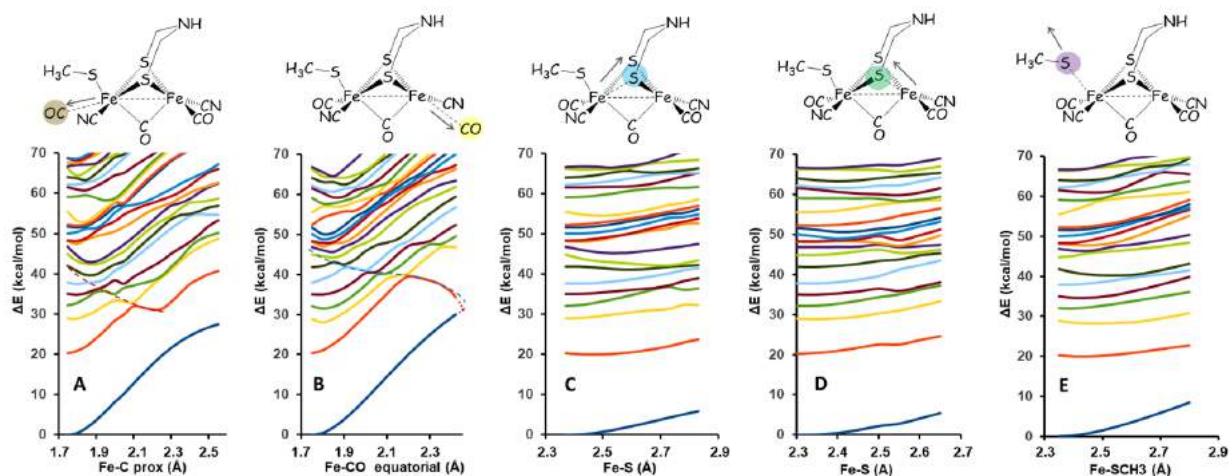


**Figure 5.** Potential energy surfaces of the ground state and the first 20 excited states of  $\text{Fe}_2\text{S}_2 \text{H}_{\text{ox}}$  model along the stretching coordinates (in Å) indicated by arrows: the distance between the proximal Fe ( $\text{Fe}_p$ ) and the proximal CO (panel A), between the distal Fe ( $\text{Fe}_d$ ) and the distal CO (Panel B), between  $\text{Fe}_p$  and a bridging S (Panel C), between  $\text{Fe}_d$  and a bridging S (Panel D), and between  $\text{Fe}_p$  and the S atom that bridges the cubane and the dinuclear cluster (Panel D). Energy differences in  $\text{kcal}\cdot\text{mol}^{-1}$  computed with respect to the minimum ground state energy. Dotted lines (in panels A and B) show the CO dissociation pathways. In panel B the 1ex/ground state crossing along distal stretching coordinate seems to occur just above  $d(\text{Fe}-\text{C}) = 2.41 \text{ \AA}$ .

We first focus on the dissociation of the proximal and distal intrinsic CO ligands. Regarding the ground states, figures 5 A & B show the energy required to release a CO is lower for  $\text{Fe}_p$  than  $\text{Fe}_d$  (22.7  $\text{kcal/mol}$  versus 30.3  $\text{kcal/mol}$ , see SI section 1.4 for details). This is easily explained in terms of individual redox states of the two Fe ions. According to DFT

1  
2  
3 calculations, the oxidation states of the iron atoms in  $H_{ox}$  are  $Fe^{II}$  for the proximal and  $Fe^I$  for  
4 the distal. (This assignment agrees with some IR<sup>24,25</sup>, EPR<sup>3738</sup> and DFT<sup>39,40</sup> investigations, but  
5 contrasts with the conclusions from other investigations using Hyscore<sup>41</sup>, and FTIR<sup>42</sup>.) In the  
6 ground state, it is more difficult to break a  $Fe^I$ -CO bond than a  $Fe^{II}$ -CO because  $\pi$   
7 back-donation of the metal-CO bond decreases as the redox state of the Fe increases.<sup>43</sup>  
8  
9

10  
11 Regarding the excited states, Figs 5A and B show that the lower energy surfaces are loosely  
12 bound along either CO dissociation coordinates. Indeed, two series of surface crossings  
13 (indicated by dotted lines) indicate putative dissociative pathways for the proximal (panel A)  
14 and distal (panel B) CO ligands, starting from 8ex and 9ex, respectively. Higher energy  
15 states are very closely spaced, so that the state crossing that one is tempted to observe at  
16 high energy cannot not be safely interpreted as a CO dissociation channel. Along the distal  
17 dissociation coordinate, 1ex undergoes state crossing with the ground state at about  $d(Fe-C)$   
18 = 2.42 Å (panel B).  
19  
20  
21

22  
23 Figs 5 C, D and E show the PES calculated by increasing the distances of two Fe-S bonds  
24 that belong to the  $Fe_2S_2$  core (one distal and one proximal with respect to the  $SCH_3^-$  ligand)  
25 and the elongation of the Fe- $SCH_3^-$  bond. They do not show any clear dissociative character.  
26 In all three cases, the energy of the excited states shows little dependence on bond length.  
27 This suggests that either Fe-S bond weakening/breaking is not an active photochemical  
28 pathway, or that a transient Fe-S weakening process is followed by fast recombination to the  
29 initial structure. The latter possibility is supported by the TDDFT geometry optimizations of  
30 the 1ex and 2ex states, starting from the structure of the ground state (see Figure S8): in  
31 both cases, the calculation evidences a state crossing with the ground state, in which at  
32 least one Fe-S bond and the Fe- $SCH_3^-$  bond are elongated, but these elongations are too  
33 small to suggest bond breaking.  
34  
35  
36  
37

38 We conclude that the most likely photochemical process after irradiation in the UV range of  
39 the enzyme is the photolysis of one of the two intrinsic CO ligands, resulting in the formation  
40 of a catalytically inactive 33-electron unsaturated photoproduct ( $H_{ox}^{uns}$  hereafter).  
41  
42

43 We now examine the fate of these putative initial photoproducts, aiming at explaining the  
44 irreversibility of the photodamage. Irrespective of whether the proximal or distal CO  
45 dissociates, the photoproduct is a reactive unsaturated species. From simple electron  
46 counting, considering  $H_{ox}$  as the starting point, the dissociation of the proximal CO should  
47 yield a more stable and less reactive 16e+17e species than the dissociation of the distal CO,  
48 which gives a 18e+15e species.  
49  
50  
51  
52  
53  
54  
55  
56  
57  
58  
59  
60

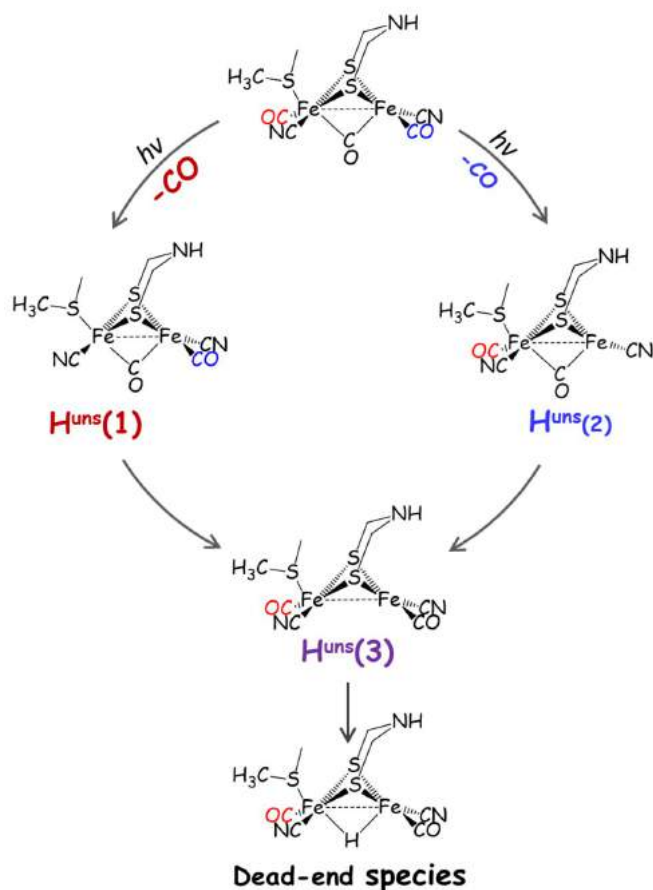


**Figure 6.** The possible intermediates formed upon photodissociation of an intrinsic CO. Irrespective of the initial  $35e H_{ox}$  or  $36e H_{red}$  state, the first photoproduct could be  $H^{uns}$  ( $= H_{ox}^{uns}$  or  $H_{red}^{uns}$ ) in which the proximal **1** or the distal **2** CO is photodissociated without further isomerization. Structure **3** is the most stable state and derives from the isomerization of **1** or **2** by moving the bridging CO in equatorial position. The protonation of the reduced form of **3** produces the  $\mu H^+$  dead-end species.

Figure 6 depicts some of the species that may be produced upon CO photodissociation. **1** and **2** are obtained by removing the distal and the proximal CO ligand respectively without any ligand rearrangement. We also consider the isomerization products **3** and **4**, where the bridging CO replaces the photolyzed distal or proximal CO or occupies the apical position, respectively.

To calculate at the DFT level the structures of these unsaturated forms, we considered a large model in which we embedded the  $Fe_2S_2$  fragment used for TDDFT modelling in a 45 residues double-shell, based on the structure of the enzyme from *Dd* (PDB code 1HFE<sup>6</sup>). SI Table 5 lists the relative energies of the four species shown in fig. 6, and some of their structural and electronic properties. Structure **3** can be easily obtained after photodissociation of either CO ligand by a simple movement of the bridging CO toward a terminal position, with a little or no movement of the other ligands. This mechanism is consistent with current knowledge. The DFT calculations of Reiher *et al.*,<sup>44</sup> and Greco *et al.*,<sup>45,46</sup> have shown that a conserved and essential lysine forms a salt bridge with the distal  $CN^-$ . This strong interaction, stabilized by a further salt bridge between the lysine and a

1  
2  
3 glutamate, should prevent the movement of the equatorial cyanide. Molecular dynamics  
4 simulations have shown that the side chain of the conserved phenylalanine that is near the  
5 equatorial CO on Fe<sub>d</sub> is flexible enough to allow the movement of the ligand to the apical  
6 position.<sup>34</sup> Shuffling of the ligands of the H-cluster has been evidenced by FTIR,<sup>25,26</sup> and a  
7 mechanism in which the bridging CO moves to an apical position was proposed to occur  
8 even at cryogenic temperature.<sup>24</sup>  
9  
10

11  
12 The following two observations are true irrespective of the initial redox state of the H-cluster  
13 (H<sub>ox</sub> or H<sub>red</sub>). First, the structure in which all ligands occupy terminal positions (**3**) is the most  
14 stable of the four species that we considered, and it is characterized by a shorter Fe-Fe  
15 bond compared to the saturated form (-0.102 Å in the reduced form, -0.048 Å in the oxidized  
16 form). This implies an increase of the Fe-Fe bond order which results in the stabilization of  
17 the unsaturated form, similarly to what it is observed in Fe<sub>2</sub>(CO)<sub>8</sub> with IR spectroscopy<sup>47</sup> and  
18 DFT<sup>48</sup>. Second, the loss of a strong field ligand such as CO upon irradiation implies a  
19 decrease of the HOMO/LUMO gap and in particular a decrease of the LUMO energy. This  
20 suggests that both H<sub>ox</sub><sup>uns</sup> and H<sub>red</sub><sup>uns</sup> may be more easily reduced than the corresponding  
21 saturated species, and that reduction follows up the formation of initial photoproduct.  
22 Reduction of H<sub>red</sub><sup>uns</sup> gives the state that we call H<sub>sred</sub><sup>uns</sup>.  
23  
24  
25  
26  
27

28 Finally we investigated the stability of the H<sub>red</sub><sup>uns</sup> protonated forms. Large model calculations  
29 described in SI section 1.6 suggest that irrespective of the starting point (H<sub>red</sub> or H<sub>ox</sub>) the final  
30 unsaturated photoproduct is H<sub>red</sub><sup>uns</sup> (**3**), which is more basic than H<sub>red</sub>. Geometry optimization  
31 of the two possible protonated species predicts that the μH<sup>+</sup> form is more stable than the  
32 apical H<sup>+</sup> form by 8.7 kcal/mol. We suggest that the μH<sup>+</sup> form is the dead-end, stable,  
33 inactive state formed upon UVB irradiation.  
34  
35

## 36 Discussion

37  
38 There is a very large body of recent work regarding the use of either purified hydrogenases,  
39 or photosynthetic organisms that contain hydrogenases or synthetic mimics of the H-cluster  
40 for the photoproduction of H<sub>2</sub>.<sup>49–52</sup> In all cases, the catalyst is somehow connected to a  
41 photosensitizer and exposed to light. Answering the question of which hydrogenase can  
42 resist to which wavelengths is therefore crucial. Photodamage of FeFe hydrogenase has  
43 been reported in a handful of investigations of the enzyme from *D. desulfuricans* (*Dd*).<sup>25,27,28</sup>  
44 The action spectrum and molecular mechanism of the corresponding reaction has not been  
45 described, despite the potential relevance of hydrogenase photoinhibition in the context of  
46 hydrogen biological photoproduction. The comparison herein between the data now  
47 available from *Ca*, *Cr* and *Dd* hydrogenases (this work and refs <sup>25,27,28,31</sup>) shows that their  
48 photoreactivities vary.  
49  
50  
51  
52

53 We have previously combined direct photoelectrochemistry and TD-DFT calculations to  
54 examine the simplest photochemical reaction of the H-cluster (the photo-induced release of  
55 exogenous CO from the so-called H<sub>ox</sub>-CO form), and found good semi-quantitative  
56 agreement.<sup>21,53</sup> We stress again that TD-DFT calculations on inorganic clusters can predict  
57 the nature of the excitations, their relative energies and the mechanisms of decay, but not  
58 the exact values of the excitation energies (the latter are very dependent on the total charge  
59 of the model used in the calculation). Here we use this combined approach to investigate the  
60

1  
2  
3 effect of light on the active form of the H-cluster of FeFe hydrogenases; in contrast to our  
4 earlier study on the reactivation of H<sub>ox</sub>-CO, our goal here was to search for the mechanism of  
5 the reaction and to identify the structure(s) of the photoproduct(s).  
6  
7

8  
9 We ran experiments where the enzyme is irradiated and its activity is measured either  
10 electrochemically (during irradiation, with the enzyme undergoing direct electron transfer  
11 to/from a rotating graphite electrode)<sup>32</sup> or using solution assays (after irradiation, with the  
12 artificial redox acceptor methyl viologen). We detected this photodamage with the two  
13 hydrogenases that we tested, those from *C. reinhardtii* (*Cr*) and *C. acetobutylicum* (*Ca*).  
14 They house the same, conserved H-cluster, but differ by their size and the number of  
15 accessory FeS clusters (four and zero, respectively).  
16  
17

18  
19 Our experiments show that photoinhibition is irreversible (it is not reversed by going back to  
20 dark conditions and we could not reactivate the enzyme by stepping the electrode potential  
21 down or by exposing it to exogenous CO). We observed in fig. 3 that the activity of the  
22 enzyme irradiated by a 150W Xe lamp decays with 1st order kinetics, with a time constant in  
23 the range of 10-30 min (the process is slightly faster with the enzyme in solution than when it  
24 is wired to an electrode, which somehow "protects" the enzyme against photodamage).  
25  
26

27  
28 We used filters to examine which range of wavelength is responsible for the photodamage of  
29 *Cr* and *Ca* hydrogenases (figures 3C and D) and we concluded that the effect is induced by  
30 UVB irradiation. This is consistent with our earlier report that monochromatic light in the  
31 visible range has no effect (neither activation nor inactivation) on the active enzymes.<sup>21</sup> We  
32 observed that activity of the enzymes changes continuously when the Xe lamp is switched  
33 on or off (there is no instant light-induced (in)activation, only a slow decrease). Armstrong  
34 and coworkers reported that irradiation with a halogen lamp (which emits no UV) does not  
35 inactivate the enzymes from *Ca* and *Cr*, but induces a small, reversible, instant change in  
36 catalytic current (SI of ref <sup>31</sup>); we saw the same effect, which we tentatively attribute to  
37 heating, when we also used a halogen lamp (fig. S12). The data presented herein are  
38 therefore consistent with previously published results obtained with the same enzymes.  
39  
40  
41  
42

43  
44 We considered the possibility that absorption in the UVB range is due to aromatic residues.  
45 The acid side chains tyrosine (Y) and tryptophan (W) residues absorb in the range  
46 270-290 nm ( $\epsilon_{280}$  = 1000 and 5000 M<sup>-1</sup>cm<sup>-1</sup>, respectively).<sup>29</sup> All Y and W residues in FeFe  
47 hydrogenases are remote from the H-cluster. There are 9 Y and 4 W (3 of which are surface  
48 exposed) in *Cr* FeFe hydrogenase, 15 Y and 1 buried W in *Ca* FeFe hydrogenase, 15 Y and  
49 6 W (3 of which are surface exposed) in *Dd* hydrogenase. It is not practical to replace all of  
50 these residues, but we could compare the rates of photo-induced inactivation in the native  
51 enzyme and a site-directed mutant where we replaced the phenylalanine that is in Van der  
52 Waals contact with the H-cluster with a tyrosine. We observed no effect of the mutation on  
53 the rate of photoinhibition; this suggests that there is no energy transfer between excited Y  
54 and W and the H-cluster and that the latter is actually the photoreceptor of the  
55 photoinhibition. UV irradiation also inactivates other inorganic enzyme active sites. The case  
56 of the oxygen evolving cluster (OEC) of Photosystem II is particularly documented,<sup>54,55</sup> and  
57 the idea that it is damaged *in vitro* by direct absorption of UV has been supported by  
58  
59  
60

1  
2  
3 experiments with other manganese enzymes<sup>56</sup> and synthetic manganese complexes.<sup>57</sup> The  
4 OEC is also affected by visible or IR irradiation.<sup>58</sup>  
5  
6

7 We performed TD-DFT calculations to examine which excited states can be produced and  
8 how they decay to the ground state. The Fe<sub>4</sub>S<sub>4</sub> cubane was not included in the H<sub>ox</sub> model for  
9 reasons that we have discussed in our study of H<sub>ox</sub>-CO photochemistry.<sup>21</sup> Briefly, considering  
10 the H-cluster as a Fe<sub>4</sub>S<sub>4</sub>-Fe<sub>2</sub>S<sub>2</sub> dyad system, the electronic transitions can be of Fe<sub>2</sub>S<sub>2</sub> or  
11 Fe<sub>4</sub>S<sub>4</sub> localized type or Fe<sub>4</sub>S<sub>4</sub>/Fe<sub>2</sub>S<sub>2</sub> CT type, depending on the MO involved in the  
12 mono-electronic transitions. Of these excitations, only the former are relevant to Fe-ligand  
13 photochemistry (CO photolysis and Fe-S bond photodissociation). This is because in a Fe<sub>2</sub>S<sub>2</sub>  
14 localized excitation, an Fe-C/Fe-S antibonding or nonbonding MO is populated to the  
15 detriment of a Fe-C/Fe-S bonding MO, as observed previously in studies of biomimetic  
16 models of the H-cluster.<sup>35</sup>  
17  
18  
19  
20

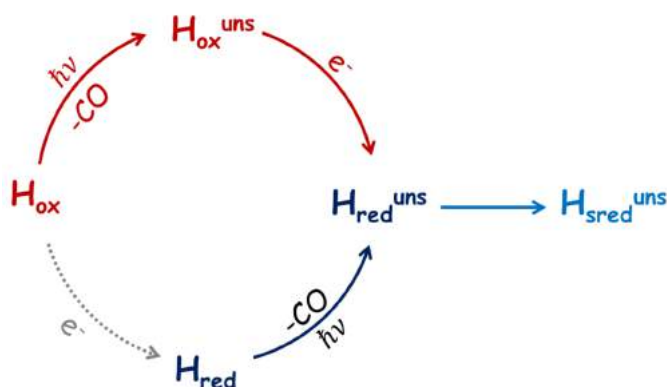
21 The low energy feature in the calculated spectrum (fig. 4) corresponds to the absorption of  
22 the 2Fe subcluster, which, in experiments, occurs around 420 nm. This band is weak and  
23 results from a single Fe to S charge transfer. The corresponding low energy excited state  
24 cannot decay to a dead-end species, suggesting that this weak absorption band is not  
25 responsible for the observed photodamage. This is consistent with our observation that  
26 irradiation in the visible range causes no damage. In contrast, the more intense features at  
27 higher energy, which probably correspond to absorption in the UV range, correspond to CT  
28 from metal ions and the sulfur ligands to CO ligands (SI table 3). Together with the  
29 observation that photodamage only occurs at high energy (UVB), this points to the first step  
30 of the photoinactivation being the ejection of an intrinsic CO ligand. Indeed, the potential  
31 energy surfaces in fig. 5 rule out photoinduced breaking of the FeS bonds of the H-cluster  
32 and evidence the sequence of internal conversions that lead to the dissociation of an  
33 intrinsic CO. The picture that emerges of this calculation is therefore that in the first instants  
34 of the photodynamics, the absorption of light populates an H-cluster excited state localized  
35 on the Fe<sub>2</sub>S<sub>2</sub> core, and the subsequent decay of the high energy excited state goes through  
36 a proximal or distal Fe-C bond dissociative channel, inducing CO photolysis and inactivation  
37 of the enzyme. This kind of photoreactivity is very common for diiron carbonyl  
38 complexes<sup>35,59-63</sup> but we note that *not all* Fe-carbonyl bonds in organometallic cofactors are  
39 photolabile. For example, the [NiFe(CN)<sub>2</sub>CO] binuclear active of NiFe hydrogenases is not  
40 susceptible to photodamage: violet irradiation actually *activates* the O<sub>2</sub>-tolerant NiFe enzyme  
41 from *A. aeolicus*,<sup>64</sup> and unpublished experiments of ours show that the under same  
42 conditions as those used in this paper, irradiation by a Xe lamp only activates the standard  
43 NiFe hydrogenase from *D. fructosovorans* (we could not detect any photoinhibition of this  
44 NiFe hydrogenase).  
45  
46  
47  
48  
49  
50  
51  
52

53 In the experiments described herein, the CO ligand that is released from the H-cluster  
54 cannot contribute to inhibition by the so-called cannibalization effect, whereby the CO ligand  
55 is grabbed by a nearby, intact H-cluster, to form the inhibited H<sub>ox</sub>-CO state. Indeed, in PFV  
56 experiments, the amount of enzyme adsorbed on the electrode is tiny (in the sub picomolar  
57 range), the total amount of CO molecules released from the H-cluster is even lower, and the  
58 free CO ligands are quickly removed from the rotating electrode surface by convection. In  
59 our solution assays, the concentration of enzyme in the stock solution (20 nM) is lower than  
60



the inhibition constant (13  $\mu\text{M}$ ) and the stock solution of hydrogenase is diluted before the assay, so no significant cannibalization can occur.<sup>12</sup> The situation is different when a highly concentrated sample is used in a FTIR or EPR investigation.

The TD-DFT calculations described here cannot define which of the two intrinsic CO ligands actually dissociates from the H-cluster in response to UV irradiation, because the protein environment is not taken into account. On the basis of the structure and the proximity of the substrate channel<sup>14</sup> from  $\text{Fe}_d$ , we speculate that the dissociation of the distal CO dissociation is easier than that of the proximal CO, but this has no consequence on what we believe happens next. The photodissociation of an intrinsic CO ligands has to be followed by rearrangement. Using DFT computations of a very large model (fig. S2), we concluded that **3**, where all ligands are in terminal positions, is the most stable unsaturated form irrespective of the initial redox state ( $\text{H}_{\text{ox}}$  or  $\text{H}_{\text{red}}$ ). Also in favor of **3** compared to **4** is our observation that the F290Y mutation has no effect on the kinetics of inhibition (whereas we have concluded before that it slows the isomerization of the distal CO from the equatorial to the apical position).<sup>34</sup> The unsaturated species are more easily reduced than the initial forms, suggesting that the photodamage involves the series of event sketched in scheme 1. Starting from e.g.  $\text{H}_{\text{ox}}$ , the  $\text{H}_{\text{ox}}^{\text{uns}}$  photoproduct could undergo reduction directly to the most stable  $\text{H}_{\text{red}}^{\text{uns}}$ , the same species can be produced directly from  $\text{H}_{\text{red}}$ . Further reduction may give a hyper reduced  $\text{H}_{\text{sred}}^{\text{uns}}$  form with about the same reactivity.



**Scheme 1.** The series of steps occurring during the photodamage of  $\text{H}_{\text{ox}}$  or  $\text{H}_{\text{red}}$ . In both cases the H-cluster reaches an unsaturated reduced state ( $\text{H}_{\text{red}}^{\text{uns}}$ ) which could be further reduced to a super reduced state ( $\text{H}_{\text{sred}}^{\text{uns}}$ ).

Both  $\text{H}_{\text{red}}^{\text{uns}}$  and  $\text{H}_{\text{sred}}^{\text{uns}}$  have two open coordination sites, one bridging the Fe ions and the other apical on  $\text{Fe}_d$ , and they may react with nearby ligands, such as the photolyzed intrinsic carbonyl,  $\text{H}_2\text{O}$ ,  $\text{H}_2$  or  $\text{H}^+$ . The recombination with CO would restore the initial  $\text{H}_{\text{red}}/\text{H}_{\text{ox}}$  form, so this recombination process, which probably occurs, merely decreases the apparent rate of inactivation. Binding of a water molecule would be possible, but in all available crystal structures, the environment of the H-cluster is rather dry. We also consider the binding of dihydrogen as unlikely, first because we have observed no effect of hydrogen pressure on the kinetics of inactivation, second because we expect that binding of  $\text{H}_2$  to a reduced or hyper-reduced unsaturated system should be endergonic. Last, we note that both  $\text{H}_{\text{red}}^{\text{uns}}$  or

1  
2  
3  
4  
5  
6  
7  
8  
9  
10  
11  
12  
13  
14  
15  
16  
17  
18  
19  
20  
21  
22  
23  
24  
25  
26  
27  
28  
29  
30  
31  
32  
33  
34  
35  
36  
37  
38  
39  
40  
41  
42  
43  
44  
45  
46  
47  
48  
49  
50  
51  
52  
53  
54  
55  
56  
57  
58  
59  
60

$H_{\text{sred}}^{\text{uns}}$  should be much more basic than  $H_{\text{red}}$ . A first protonation will surely occur at the bridging position, as indicated by the geometry optimization of the  $H_{\text{red}}^{\text{uns}}$  protonated forms (the  $\mu\text{H}^+$  is lower in energy than apical terminal  $\text{H}^+$  by 8.7 kcal/mol). This  $\mu\text{H}^+$  form is very stable<sup>65</sup> and its further protonation should not lead to the formation of the  $\sigma\text{-H}_2$  complex and the release of molecular hydrogen. We propose that it is the final, dead-end product of the photoinactivation reaction. Let us note that Haumann *et al.* have recently proposed that a hydride bridges the two Fe ions of the *saturated* dinuclear subcluster in reduced, inactive forms of the H-cluster.<sup>66</sup>

Our conclusion that UVB is responsible for the photoinhibition of *Ca* and *Cr* hydrogenases contrasts with the earlier observation that the enzyme from *Dd* is destroyed upon illumination *in the visible range*.<sup>25,27,28</sup> Indeed, in ref <sup>25</sup>, Albracht and coworkers emphasized that they used a halogen or a Xe arc lamp, and a glass light guide that "eliminated most of the UV contribution from the light used," and in ref <sup>28</sup>, Ruediger *et al* observed the effects of light with a halogen lamp and a glass electrochemical cell. At this point, we can only speculate that the photoinhibition mechanism that we described is also operational in *Dd* hydrogenase, but for a reason that is unclear, absorption in the visible range, rather than UV, triggers the reaction. We can hypothesize that the protein environment shifts the CT excitations that are active in photodamage to the high energy range of the halogen lamp spectrum. Whether UV or visible light is responsible for photodamage does not depend on just the number of accessory FeS clusters (two in *Dd* hydrogenase, compared to zero and four in *Ca* and *Cr* hydrogenases). We note that the enzyme from *Dd* is only sensitive to photoinhibition under oxidizing conditions (according to the results in fig 2 of ref <sup>28</sup>), unlike the enzymes from *Ca* and *Cr* (fig 3 B & C herein). For unknown reasons, the enzyme from *Dd* appears to have a number of peculiar properties (the formation of the so-called  $\text{H}_{\text{ox}}$ -inact state, for example, has only been observed with *Dd* and *Clostridium beijerinckii* FeFe hydrogenases<sup>67</sup>), and it is also particularly sensitive to aerobic<sup>14</sup> and anaerobic<sup>34</sup> oxidative inactivation.<sup>31,68</sup>

We end this paper by commenting on the consequences of hydrogenase photoinhibition in the context of  $\text{H}_2$  photoproduction. There are attempts to "domesticate" photosynthetic microorganisms such as green algae to make them produce dihydrogen using the energy from sunlight.<sup>69-72</sup> Algae are notoriously sensitive to UV,<sup>73,74</sup> but we are not aware of any previous investigation of the photodamage of hydrogenase *in vivo*. Regarding the development of " $\text{H}_2$  farms," hydrogenase photoinhibition should not be an issue since the bioreactor used for biological  $\text{H}_2$  photoproduction should screen the UV. Photoinhibition may be more of an issue in artificial photocatalytic dyads where either an enzyme or a bacterium receives electrons from a sunlight-harvesting organic dye, a photosynthetic enzyme or a semiconductor.<sup>49,52,75-79</sup> Happe and coworkers have indeed observed that UV light contributes to light-dependent ET between 5-carboxyeosin ( $\lambda_{\text{max}} = 516$  nm) and *Cr* FeFe hydrogenase,<sup>72</sup> and in the light of our results, exposure to UV may actually negatively contribute to the efficiency of this device.

## Methods

### Experiments.

The enzyme from *Cr* was expressed in *Shewanella oneidensis*. The enzyme from *Ca* was produced homologously. The samples were prepared as described previously.<sup>80,81</sup>

The light sources used in this work were a Newport 150 W Xenon arc lamp (Oriel Apex Monochromator illuminator 70612), directed to the sample by a Newport Oriel 77578 optical fiber (1 cm diameter, transmittance range 280-2200 nm according to the manufacturer's specifications), or a Fiberoptic-Heim LQ 1600 Halogen lamp. The diameter of the beam was around 1.5 cm at the level of the electrode. Our setup does not allow the power of the Xe light source to be varied. We used two longpass filters, whose absorption spectra are shown in figure S11: a borosilicate filter which blocks UVB, and a UV filter which blocks UV-A and UV-B.

In electrochemical experiments, we irradiated the enzyme adsorbed on the surface of a graphite working RDE (typical electrode rotation rate 3 krpm), through quartz window at the bottom of the glass electrochemical cell (see the photograph in fig. S15); this prevented light diffraction and UV absorption. The electrochemical experiments were performed in a 0.1 M potassium phosphate buffer pH 6.8. Regarding the experiments shown in figs 3 A, B & C, the time constant of inactivation ( $\tau$ , in the equation  $i = cst \times \exp(-t/\tau)$ ) (where "cst" is a constant) was deduced by fitting  $y = cst \times (1-t/\tau)$  to the linear current trace, using the free software QSoas.<sup>82</sup>

Solution assays (fig. 3D) were performed at 30 °C, pH = 7, 1 atm H<sub>2</sub>, in a mixed buffer consisting of MES, CHES, HEPES, TAPS, acetate, EDTA (5 mM each), 0.1 M NaCl, under 1 bar H<sub>2</sub>, and with 20 mM oxidized methyl viologen (MV) as electron acceptor. The enzyme sample was illuminated for 5 or 15 min with the Xenon lamp in a quartz cell (1 mm light path, Precision Cells). In a glass cell containing 1.8 ml of mixed buffer saturated with H<sub>2</sub>, we put 200  $\mu$ l of MV (0.2 M stock solution) and we recorded the absorbance at 604 nm to obtain the baseline. The reaction was started by adding 5  $\mu$ l of enzyme solution (previously exposed to white light or kept in the dark) and the increase in absorbance induced by the reduction of MV was measured at 604 nm. The concentration of the enzyme stock solution was unknown, which prevented us from determining absolute turnover rates.

### Computations.

The level of theory adopted is different for TDDFT and DFT computations. For the former it is crucial to better describe the charge-transfer character of the excitations and for this reason a hybrid functional is needed. For the latter, however, due to the size of the model considered, it is important to use Resolution-of-identity (RI) technique to speed up computations and in this case only a pure functional can be used.

The TDDFT computation were performed using the hybrid Generalized Gradient Approximation (GGA) PBE0<sup>83</sup> DFT functional as implemented in the TURBOMOLE suite of programs<sup>84</sup>. Basis sets of triple- $\zeta$  plus polarization split valence quality<sup>85</sup> were adopted for all

atoms. The choice of this functional has been made on the basis of the  $H_{ox} Fe_2S_2$  optimized geometry compared to the XRD structure. Indeed PBE0 gives the best agreement among the hybrid functional considered (further information on the calculations is available in the SI section 1). In section 1.3 are also reported the effect of the DFT functionals and of the total charge of the model on the computed spectra. Excited PESs have been scanned along selected Fe-Ligand (Fe-L) bond stretching coordinates as follows. For each step, the ground state structure was first optimized by keeping the elongated Fe-L distance fixed. The sampling of the excited PES has been carried out with a step of 0.05Å. For each distance the vertical excitation energies have been computed and the resulting profile for each excited state approximates the effect of stretching the bond on the excited surface.<sup>86</sup>

The DFT computation on the large  $Fe_2S_2$  model were performed using the pure GGA BP86<sup>87,88</sup> DFT functional and RI technique<sup>89</sup> as implemented in TURBOMOLE. Basis sets of double- $\zeta$  plus polarization split valence quality<sup>85</sup> were adopted for all atoms.

## Associated content

### Author Information

Corresponding authors

\* [christophe.leger@imm.cnrs.fr](mailto:christophe.leger@imm.cnrs.fr)

\* [luca.bertini@unimib.it](mailto:luca.bertini@unimib.it)

### Author contributions

The manuscript was written through contributions of all authors.

### Supporting Information

The Supporting Information is available free of charge on the ACS Publications website. Models and computational details of DFT and TDDFT calculations. Absorption spectra of the filters. Photography of the electrochemical cell. Experimental data with Halogen Lamp and UV photoinhibition by Xenon lamp on FeFe hydrogenases from *Cr* (100% and 10%  $H_2$ ) and *Ca*.

### Acknowledgements

The French teams were supported by CNRS, Aix Marseille Université, INSA, CEA, Agence Nationale de la Recherche (ANR-12-BS08-0014, ANR-14-CE05-0010) and the Excellence Initiative of Aix-Marseille University - A\*MIDEX, a French "Investissements d'Avenir" programme (ANR-11-IDEX-0001-02). The French authors are part of the French bioinorganic chemistry network ([www.frenchbic.cnrs.fr](http://www.frenchbic.cnrs.fr)).

## Bibliography

- (1) Nicolet, Y.; de Lacey, A. L.; Vernède, X.; Fernandez, V. M.; Hatchikian, E. C.; Fontecilla-Camps, J. C. *J. Am. Chem. Soc.* **2001**, *123*, 1596–1601.
- (2) Silakov, A.; Wenk, B.; Reijerse, E.; Lubitz, W. *Phys. Chem. Chem. Phys.* **2009**, *11*, 6592–6599.
- (3) Berggren, G.; Adamska, A.; Lambert, C.; Simmons, T. R.; Esselborn, J.; Atta, M.; Gambarelli, S.; Muesca, J. M.; Reijerse, E.; Lubitz, W.; Happe, T.; Artero, V.; Fontecave, M. *Nature* **2013**, *499*, 66–69.
- (4) Fontecilla-Camps, J. C.; Volbeda, A.; Cavazza, C.; Nicolet, Y. *Chem. Rev.* **2007**, *107*, 4273–4303.
- (5) Mulder, D. W.; Boyd, E. S.; Sarma, R.; Lange, R. K.; Endrizzi, J. A.; Broderick, J. B.; Peters, J. W. *Nature* **2010**, *465*, 248–251.
- (6) Nicolet, Y.; Piras, C.; Legrand, P.; Hatchikian, C. E.; Fontecilla-Camps, J. C. *Structure* **1999**, *7*, 13–23.
- (7) Caserta, G.; Adamska-Venkatesh, A.; Pecqueur, L.; Atta, M.; Artero, V.; Roy, S.; Reijerse, E.; Lubitz, W.; Fontecave, M. *Biochim. Biophys. Acta* **2016**, *1857*, 1734–1740.
- (8) Peters, J. W.; Lanzilotta, W. N.; Lemon, B. J.; Seefeldt, L. C. *Science* **1998**, *282*, 1853–1858.
- (9) Poudel, S.; Tokmina-Lukaszewska, M.; Colman, D. R.; Refai, M.; Schut, G. J.; King, P. W.; Maness, P. C.; Adams, M. W. W.; Peters, J. W.; Bothner, B.; Boyd, E. S. *Biochim. Biophys. Acta* **2016**, *1860*, 1910–1921.
- (10) Lubitz, W.; Ogata, H.; Rüdiger, O.; Reijerse, E. *Chem. Rev.* **2014**, *114*, 4081–4148.
- (11) Bennett, B.; Lemon, B. J.; Peters, J. W. *Biochemistry* **2000**, *39*, 7455–7460.
- (12) Baffert, C.; Bertini, L.; Lautier, T.; Greco, C.; Sybirna, K.; Ezanno, P.; Etienne, E.; Soucaille, P.; Bertrand, P.; Bottin, H.; Meynial-Salles, I.; De Gioia, L.; Léger, C. *J. Am. Chem. Soc.* **2011**, *133*, 2096–2099.
- (13) Orain, C.; Saujet, L.; Gauquelin, C.; Soucaille, P.; Meynial-Salles, I.; Baffert, C.; Fourmond, V.; Bottin, H.; Léger, C. *J. Am. Chem. Soc.* **2015**, *137*, 12580–12587.
- (14) Kubas, A.; Orain, C.; De Sancho, D.; Saujet, L.; Sensi, M.; Gauquelin, C.; Meynial-Salles, I.; Soucaille, P.; Bottin, H.; Baffert, C.; Fourmond, V.; Best, R. B.; Blumberger, J.; Léger, C. *Nat. Chem.* **2017**, *9*, 88–95.
- (15) Swanson, K. D.; Ratzloff, M. W.; Mulder, D. W.; Artz, J. H.; Ghose, S.; Hoffman, A.; White, S.; Zadovnyy, O. A.; Broderick, J. B.; Bothner, B.; King, P. W.; Peters, J. W. *J. Am. Chem. Soc.* **2015**, *137*, 1809–1816.
- (16) Kowal, A. T.; Adams, M. W.; Johnson, M. K. *J. Biol. Chem.* **1989**, *264*, 4342–4348.
- (17) Silakov, A.; Kamp, C.; Reijerse, E.; Happe, T.; Lubitz, W. *Biochemistry* **2009**, *48*, 7780–7786.
- (18) Hajj, V.; Baffert, C.; Sybirna, K.; Meynial-Salles, I.; Soucaille, P.; Bottin, H.; Fourmond, V.; Léger, C. *Energy Environ. Sci.* **2014**, *7*, 715–719.
- (19) Megarity, C. F.; Esselborn, J.; Hexter, S. V.; Wittkamp, F.; Apfel, U. P.; Happe, T.; Armstrong, F. A. J. *Am. Chem. Soc.* **2016**, *138*, 15227–15233.
- (20) Thauer, R. K.; Käufer, B.; Zähringer, M.; Jungermann, K. *Eur. J. Biochem.* **1974**, *42*, 447–452.
- (21) Sensi, M.; Baffert, C.; Greco, C.; Caserta, G.; Gauquelin, C.; Saujet, L.; Fontecave, M.; Roy, S.; Artero, V.; Soucaille, P.; Meynial-Salles, I.; Bottin, H.; de Gioia, L.; Fourmond, V.; Léger, C.; Bertini, L. *J. Am. Chem. Soc.* **2016**, *138*, 13162–13168.
- (22) Mirmohades, M.; Adamska-Venkatesh, A.; Sommer, C.; Reijerse, E.; Lomoth, R.; Lubitz, W.; Hammarström, L. *J. Phys. Chem. Lett.* **2016**, *7*, 3290–3293.
- (23) Lemon, B. J.; Peters, J. W. *J. Am. Chem. Soc.* **2000**, *122*, 3793–3794.
- (24) Chen, Z.; Lemon, B. J.; Huang, S.; Swartz, D. J.; Peters, J. W.; Bagley, K. A. *Biochemistry* **2002**, *41*, 2036–2043.
- (25) Roseboom, W.; De Lacey, A. L.; Fernandez, V. M.; Hatchikian, E. C.; Albracht, S. P. J. *J. Biol. Inorg. Chem.* **2006**, *11*, 102–118.
- (26) Senger, M.; Mebs, S.; Duan, J.; Wittkamp, F.; Apfel, U. P.; Heberle, J.; Haumann, M.; Stripp, S. T. *Proc. Natl. Acad. Sci. U. S. A.* **2016**, *113*, 8454–8459.
- (27) Albracht, S. P. J.; Roseboom, W.; Hatchikian, E. C. *J. Biol. Inorg. Chem.* **2006**, *11*, 88–101.
- (28) Rodríguez-Maciá, P.; Birrell, J. A.; Lubitz, W.; Rüdiger, O. *ChemPlusChem* **2016**, *82*, 540–545.
- (29) Wetlaufer, D. B. *Adv. Protein Chem.* **1962**, *17*, 333–390.
- (30) Sensi, M.; del Barrio, M.; Baffert, C.; Fourmond, V.; Léger, C. *Current Opinion in Electrochemistry* **2017**, doi: 10.1016/j.coelec.2017.08.005.
- (31) Goldet, G.; Brandmayr, C.; Stripp, S. T.; Happe, T.; Cavazza, C.; Fontecilla-Camps, J. C.; Armstrong, F. A. J. *J. Am. Chem. Soc.* **2009**, *131*, 14979–14989.
- (32) Fourmond, V.; Léger, C. *Current Opinion in Electrochemistry* **2017**, *1*, 110–120.
- (33) Fourmond, V.; Baffert, C.; Sybirna, K.; Dementin, S.; Abou-Hamdan, A.; Meynial-Salles, I.; Soucaille, P.; Bottin, H.; Léger, C. *Chem. Commun.* **2013**, *49*, 6840–6842.
- (34) Fourmond, V.; Greco, C.; Sybirna, K.; Baffert, C.; Wang, P. H.; Ezanno, P.; Montefiori, M.; Bruschi, M.; Meynial-Salles, I.; Soucaille, P.; Blumberger, J.; Bottin, H.; De Gioia, L.; Léger, C. *Nat. Chem.* **2014**, *6*, 336–342.
- (35) Bertini, L.; Greco, C.; Fantucci, P.; De Gioia, L. *Int. J. Quantum Chem.* **2014**, *114*, 851–861.
- (36) Bertini, L.; Fantucci, P.; De Gioia, L.; Zampella, G. *Inorg. Chem.* **2013**, *52*, 9826–9841.
- (37) Mulder, D. W.; Ratzloff, M. W.; Shepard, E. M.; Byer, A. S.; Noone, S. M.; Peters, J. W.; Broderick, J. B.; King, P. W. *J. Am. Chem. Soc.* **2013**, *135*, 6921–6929.
- (38) Myers, W. K.; Stich, T. A.; Suess, D. L. M.; Kuchenreuther, J. M.; Swartz, J. R.; Britt, R. D. *J. Am. Chem.*

- Soc. **2014**, *136*, 12237–12240.
- (39) Fiedler, A. T.; Brunold, T. C. *Inorg. Chem.* **2005**, *44*, 9322–9334.
- (40) Bruschi, M.; Greco, C.; Fantucci, P.; De Gioia, L. *Inorg. Chem.* **2008**, *47*, 6056–6071.
- (41) Silakov, A.; Reijerse, E. J.; Albracht, S. P. J.; Hatchikian, E. C.; Lubitz, W. *J. Am. Chem. Soc.* **2007**, *129*, 11447–11458.
- (42) Adamska, A.; Silakov, A.; Lambertz, C.; Rüdiger, O.; Happe, T.; Reijerse, E.; Lubitz, W. *Angew. Chem. Int. Ed Engl.* **2012**, *51*, 11458–11462.
- (43) Willner, H.; Aubke, F. *Organometallics* **2003**, *22*, 3612–3633.
- (44) Finkelmann, A. R.; Stiebritz, M. T.; Reiher, M. *Chem. Sci.* **2014**, *5*, 215–221.
- (45) Greco, C.; Bruschi, M.; Heimdal, J.; Fantucci, P.; De Gioia, L.; Ryde, U. *Inorg. Chem.* **2007**, *46*, 7256–7258.
- (46) Greco, C.; Bruschi, M.; Fantucci, P.; Ryde, U.; De Gioia, L. *Chemistry* **2011**, *17*, 1954–1965.
- (47) Fletcher, S. C.; Poliakoff, M.; Turner, J. J. *Inorg. Chem.* **1986**, *25*, 3597–3604.
- (48) Bertini, L.; Bruschi, M.; De Gioia, L.; Fantucci, P. *J. Phys. Chem. A* **2007**, *111*, 12152–12162.
- (49) Mersch, D.; Lee, C. Y.; Zhang, J. Z.; Brinkert, K.; Fontecilla-Camps, J. C.; Rutherford, A. W.; Reisner, E. *J. Am. Chem. Soc.* **2015**, *137*, 8541–8549.
- (50) Brown, K. A.; Wilker, M. B.; Boehm, M.; Dukovic, G.; King, P. W. *J. Am. Chem. Soc.* **2012**, *134*, 5627–5636.
- (51) Reisner, E.; Powell, D. J.; Cavazza, C.; Fontecilla-Camps, J. C.; Armstrong, F. A. *J. Am. Chem. Soc.* **2009**, *131*, 18457–18466.
- (52) Lubner, C. E.; Applegate, A. M.; Knörzer, P.; Ganago, A.; Bryant, D. A.; Happe, T.; Golbeck, J. H. *Proc. Natl. Acad. Sci. U. S. A.* **2011**, *108*, 20988–20991.
- (53) Greco, C.; Fourmond, V.; Baffert, C.; Wang, P. H.; Dementin, S.; Bertrand, P.; Bruschi, M.; Blumberger, J.; de Gioia, L.; Léger, C. *Energy Environ. Sci.* **2014**, *7*, 3543–3573.
- (54) Keren, N.; Krieger-Liszkay, A. *Physiol. Plant.* **2011**, *142*, 1–5.
- (55) Vass, I. *Biochim. Biophys. Acta* **2012**, *1817*, 209–217.
- (56) Hakala, M.; Rantamäki, S.; Puputti, E. M.; Tyystjärvi, T.; Tyystjärvi, E. *J. Exp. Bot.* **2006**, *57*, 1809–1816.
- (57) Antal, T. K.; Lo, W.; Armstrong, W. H.; Tyystjärvi, E. *Photochem. Photobiol.* **2009**, 663–668.
- (58) Boussac, A.; Sugiura, M.; Lai, T. L.; Rutherford, A. W. *Philos. Trans. R. Soc. Lond. B Biol. Sci.* **2008**, *363*, 1203–1210.
- (59) Johnson, M.; Thuman, J.; Letterman, R. G.; Stromberg, C. J.; Webster, C. E.; Heilweil, E. J. *J. Phys. Chem. B* **2013**, *117*, 15792–15803.
- (60) Ridley, A. R.; Stewart, A. I.; Adamczyk, K.; Ghosh, H. N.; Kerkeni, B.; Guo, Z. X.; Nibbering, E. T. J.; Pickett, C. J.; Hunt, N. T. *Inorg. Chem.* **2008**, *47*, 7453–7455.
- (61) Bingaman, J. L.; Kohnhorst, C. L.; Van Meter, G. A.; McElroy, B. A.; Rakowski, E. A.; Caplins, B. W.; Gutowski, T. A.; Stromberg, C. J.; Webster, C. E.; Heilweil, E. J. *J. Phys. Chem. A* **2012**, *116*, 7261–7271.
- (62) Kania, R.; Frederix, P. W. J. M.; Wright, J. A.; Ulijn, R. V.; Pickett, C. J.; Hunt, N. T. *J. Chem. Phys.* **2012**, *136*, 044521.
- (63) Goy, R.; Bertini, L.; Rudolph, T.; Lin, S.; Schulz, M.; Zampella, G.; Dietzek, B.; Schacher, F. H.; De Gioia, L.; Sakai, K.; Weigand, W. *Chem. - Eur. J.* **2016**, *23*, 334–345.
- (64) Ciaccafava, A.; Hamon, C.; Infossi, P.; Marchi, V.; Giudici-Ortoniconi, M. T.; Lojou, E. *Phys. Chem. Chem. Phys.* **2013**, *15*, 16463.
- (65) Barton, B. E.; Zampella, G.; Justice, A. K.; De Gioia, L.; Rauchfuss, T. B.; Wilson, S. R. *Dalton Trans.* **2010**, *39*, 3011–3019.
- (66) Mebs, S.; Senger, M.; Duan, J.; Wittkamp, F.; Apfel, U. P.; Happe, T.; Winkler, M.; Stripp, S. T.; Haumann, M. *J. Am. Chem. Soc.* **2017**, doi 10.1021/jacs.7b07548.
- (67) Morra, S.; Arizzi, M.; Valetti, F.; Gilardi, G. *Biochemistry* **2016**, *55*, 5897–5900.
- (68) Liebgott, P. P.; Leroux, F.; Burlat, B.; Dementin, S.; Baffert, C.; Lautier, T.; Fourmond, V.; Ceccaldi, P.; Cavazza, C.; Meynial-Salles, I.; Soucaille, P.; Fontecilla-Camps, J. C.; Guigliarelli, B.; Bertrand, P.; Rousset, M.; Léger, C. *Nat. Chem. Biol.* **2010**, *6*, 63–70.
- (69) Hemschemeier, A.; Melis, A.; Happe, T. *Photosynth. Res.* **2009**, *102*, 523–540.
- (70) Ghirardi, M. L. *Photosynth. Res.* **2015**, *125*, 383–393.
- (71) Noone, S.; Ratcliff, K.; Davis, R.; Subramanian, V.; Meuser, J.; Posewitz, M. C.; King, P. W.; Ghirardi, M. L. *Algal Research* **2017**, *22*, 116–121.
- (72) Adam, D.; Bösch, L.; Castañeda-Losada, L.; Winkler, M.; Apfel, U. P.; Happe, T. *ChemSusChem* **2017**, *10*, 894–902.
- (73) Holzinger, A.; Lütz, C. *Micron* **2006**, *37*, 190–207.
- (74) Pescheck, F.; Lohbeck, K. T.; Roleda, M. Y.; Bilger, W. *J. Photochem. Photobiol. B* **2014**, *132*, 85–93.
- (75) Ladomenou, K.; Natali, M.; Iengo, E.; Charalampidis, G.; Scandola, F.; Coutsolelos, A. G. *Coord. Chem. Rev.* **2015**, *304-305*, 38–54.
- (76) Wang, F.; Wang, W. G.; Wang, H. Y.; Si, G.; Tung, C. H.; Wu, L. Z. *ACS Catal.* **2012**, *2*, 407–416.
- (77) Honda, Y.; Hagiwara, H.; Ida, S.; Ishihara, T. *Angew. Chem. Int. Ed Engl.* **2016**, *55*, 8045–8048.
- (78) Hambourger, M.; Gervaldo, M.; Svedruzic, D.; King, P. W.; Gust, D.; Ghirardi, M.; Moore, A. L.; Moore, T. A. *J. Am. Chem. Soc.* **2008**, *130*, 2015–2022.
- (79) Lomoth, R.; Ott, S. *Dalton Trans.* **2009**, *0*, 9952–9959.
- (80) Gauquelin, C.; Baffert, C.; Richaud, P.; Kamionka, E.; Etienne, E.; Guieysse, D.; Girbal, L.; Fourmond,

- 1  
2  
3 V.; André, I.; Guigliarelli, B.; Léger, C.; Soucaille, P.; Meynial-Salles, I. *Biochim. Biophys. Acta* **2017**, doi:  
4 [10.1016/j.bbabo.2017.08.010](https://doi.org/10.1016/j.bbabo.2017.08.010) .
- 5 (81) Sybirna, K.; Antoine, T.; Lindberg, P.; Fourmond, V.; Rousset, M.; Méjean, V.; Bottin, H. *BMC*  
6 *Biotechnol.* **2008**, *8*, 73.
- 7 (82) Fourmond, V. *Anal. Chem.* **2016**, *88*, 5050–5052.
- 8 (83) Adamo, C.; Scuseria, G. E.; Barone, V. *J. Chem. Phys.* **1999**, *111*, 2889–2899.
- 9 (84) Ahlrichs, R.; Bär, M.; Häser, M.; Horn, H.; Kölmel, C. *Chem. Phys. Lett.* **1989**, *162*, 165–169.
- 10 (85) Schäfer, A.; Huber, C.; Ahlrichs, R. *J. Chem. Phys.* **1994**, *100*, 5829–5835.
- 11 (86) Dunietz, B. D.; Dreuw, A.; Head-Gordon, M. *J. Phys. Chem. B* **2003**, *107*, 5623–5629.
- 12 (87) Becke, A. D. *Phys. Rev. A Gen. Phys.* **1988**, *38*, 3098–3100.
- 13 (88) Perdew, J. P. *Phys. Rev. B Condens. Matter* **1986**, *33*, 8822–8824.
- 14 (89) Eichkorn, K.; Weigend, F.; Treutler, O.; Ahlrichs, R. *Theor. Chem. Acc.* **1997**, *97*, 119–124.
- 15  
16  
17  
18  
19  
20  
21  
22  
23  
24  
25  
26  
27  
28  
29  
30  
31  
32  
33  
34  
35  
36  
37  
38  
39  
40  
41  
42  
43  
44  
45  
46  
47  
48  
49  
50  
51  
52  
53  
54  
55  
56  
57  
58  
59  
60

# Supporting Information - Photoinhibition of FeFe hydrogenase

Matteo Sensi,<sup>†,∇</sup> Carole Baffert,<sup>†</sup> Laura Fradale,<sup>†</sup> Charles Gauquelin,<sup>||</sup> Philippe Soucaille,<sup>||</sup>  
Isabelle Meynial-Salles,<sup>||</sup> Hervé Bottin,<sup>‡</sup> Luca de Gioia,<sup>∇</sup> Maurizio Bruschi,<sup>∇</sup> Vincent  
Fourmond,<sup>†</sup> Christophe Léger,<sup>\*,†</sup> and Luca Bertini<sup>\*,∇</sup>

<sup>†</sup> Aix Marseille Univ., CNRS, BIP UMR 7281, Marseille, France

<sup>‡</sup> Department of Earth and Environmental Sciences, Milano-Bicocca University, Piazza della Scienza 1, 20126 Milan, Italy

<sup>||</sup> Université de Toulouse, INSA, UPS, INP, LISBP, INRA:UMR792,135 CNRS:UMR 5504, avenue de Rangueil, 31077 Toulouse, France

<sup>⊥</sup>Institut de Biologie Intégrative de la Cellule (I2BC), Institut Frédéric Joliot, CEA, CNRS, Univ Paris-Sud, Université Paris-Saclay, F-91198, Gif-Sur-Yvette cedex, France.

<sup>∇</sup> Department of Biotechnologies and Biosciences, University of Milano-Bicocca, Piazza della Scienza 2, 20126 Milan, Italy

\* [christophe.leger@imm.cnrs.fr](mailto:christophe.leger@imm.cnrs.fr)

\* [luca.bertini@unimib.it](mailto:luca.bertini@unimib.it)



## Table of contents

<b>1 - DFT and TDDFT</b>	<b>3</b>
1.1 - Fe <sub>2</sub> S <sub>2</sub> models and DFT level of theory	3
1.2 - Fe <sub>2</sub> S <sub>2</sub> Small model MO populations	6
1.3 - Fe <sub>2</sub> S <sub>2</sub> Small model electronic spectra.	11
1.3 - Small model TDDFT geometry optimizations of 1ex and 2ex	16
1.4 - CO dissociation energy barriers	17
1.5 - Large Fe <sub>2</sub> S <sub>2</sub> model structures	18
1.6 - H <sub>red</sub> <sup>uns</sup> protonated	19
1.7 - Optimized coordinates PBE0	20
<b>2 - Absorption spectra of the filters</b>	<b>24</b>
<b>3 - Experiments carried out with a halogen lamp</b>	<b>24</b>
<b>4 - Photoinhibition time constant values for <i>C. reinhardtii</i> and <i>C. acetobutylicum</i> FeFe hydrogenases</b>	<b>25</b>
<b>5 - <i>C. acetobutylicum</i> FeFe hydrogenases inactivation by xenon lamp with or without UV</b>	<b>26</b>
<b>6 - Photo-electrochemical cell</b>	<b>27</b>
<b>Bibliography</b>	<b>27</b>

# 1 - DFT and TDDFT

## 1.1 - Fe<sub>2</sub>S<sub>2</sub> models and DFT level of theory

**Models.** In this paper we used two different Fe<sub>2</sub>S<sub>2</sub> models. To identify the main photochemical pathways along the excited surfaces we investigated the H<sub>ox</sub> [Fe<sub>2</sub>(μ-adt)(SCH<sub>3</sub>)(CO)<sub>3</sub>(CN)<sub>2</sub>]<sup>2-</sup> model complex (adt = azadithiolate), while we investigated the relative stability of the possible photoproducts with a large model in which the same Fe<sub>2</sub>S<sub>2</sub> model cluster was embedded in a 45-residues shell.

**Small Fe<sub>2</sub>S<sub>2</sub> model.** This model was obtained from the full Fe<sub>6</sub>S<sub>6</sub> H-cluster model in which the Fe<sub>4</sub>S<sub>4</sub> cubane has been deleted, leaving a coordinated methylthiolate group coordinated to the proximal Fe atom. We consider the SCH<sub>3</sub><sup>-</sup> instead of the HSCH<sub>3</sub> in order to avoid the unrealistic dissociation of this ligand during the geometry optimization along the distal or proximal CO dissociation coordinates.

In the figure below we report the main bond distances computed at the PBE0/TZVP level, which is the best hybrid DFT level, on the basis of the benchmark reported in the following section.

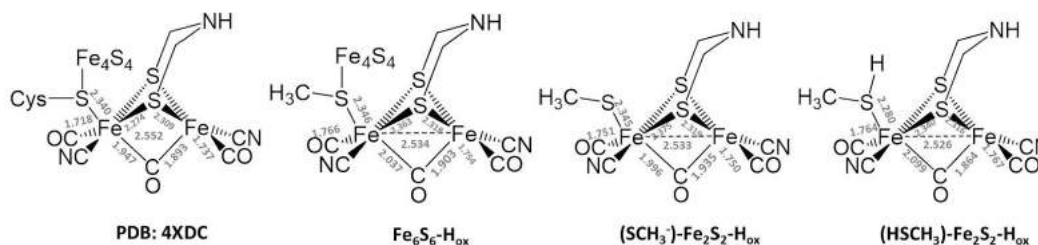


**Figure S1** - Comparison between the crystallographic structure of the diiron site (PDB: 4XDC) and the structures of the PBE0 optimized models.

We compared the 4XDC PDB crystallographic structure with the Fe<sub>6</sub>S<sub>6</sub>-H<sub>ox</sub> model and the SCH<sub>3</sub><sup>-</sup> and HSCH<sub>3</sub> Fe<sub>2</sub>S<sub>2</sub>-H<sub>ox</sub> models as described above. All the three optimized model structures are in good agreement with the crystallographic structures. More importantly for the computations presented in this paper, replacing SCH<sub>3</sub><sup>-</sup> with HSCH<sub>3</sub> has no effect on the other structural parameters and, in particular, the SCH<sub>3</sub><sup>-</sup> better reproduces the Fe-S bond length in the Fe<sub>6</sub>S<sub>6</sub> model.

**Large Fe<sub>2</sub>S<sub>2</sub> model.** The large model consists of 487 atoms and was obtained by embedding the small model in a 45-residues shell built from the structure of the FeFe hydrogenase from *D. desulfuricans* (pdb 1HFE<sup>1</sup>).

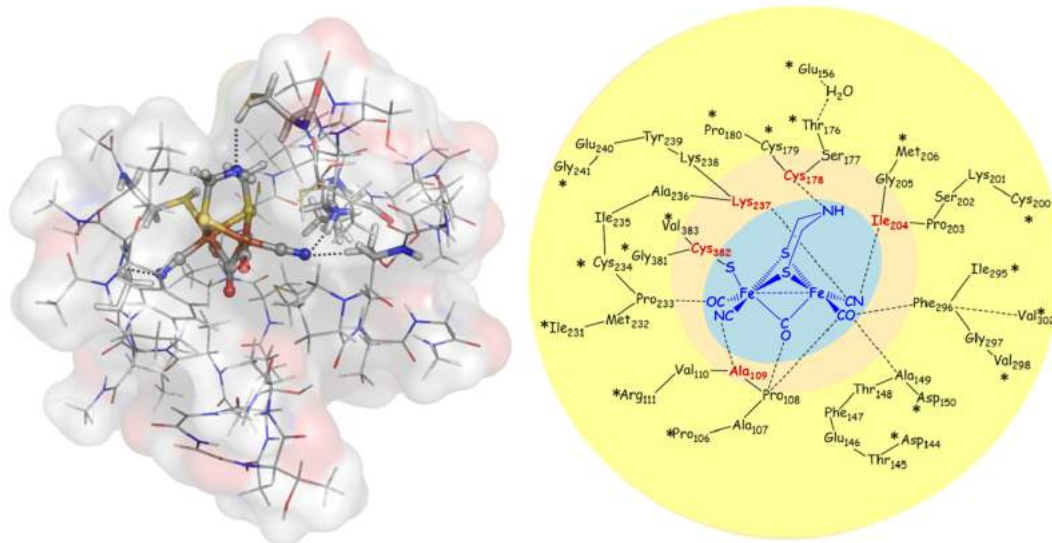


**Figure S2** - The large model for DFT computations on the unsaturated  $H_{ox}$  and  $H_{red}$  forms. (On the left) Structure of the large model, the  $Fe_2S_2$  small model is shown as spheres and sticks, the five residues of the inner shell that form H-bonds with the active site as sticks (Ile 204, Ala 109, Cys 382, Cys 178 and Lys 237, *D. desulfuricans* numbering), the other residues included in the model are shown as lines. (On the right) In blue the  $Fe_2S_2$  core; in red the first-shell residues directly interacting with the  $Fe_2S_2$  cluster through H-bonds or Fe-S bond (Cys 382); in the light yellow band the second 44 residues shell. This second shell is made of 9 clusters (Asp144-Asp150, Pro106-Arg111, Ile231-Gly241, Gly381-Val383, Glu156, Trp156-Pro180, Cys200-Met206, Ile295-Val298, Val302,). The Ca of the terminal residues of each cluster (indicated with an asterisk) have been constrained to their X-ray positions. Glu156 and Trp156 interact with a water molecule which is present in the pdb file.

The shell is divided into two parts. The inner shell includes the five residues (Ile204, Ala109, Cys382, Cys178 and Lys237) that form an H-bond network with the CN<sup>-</sup> and the ADT of the  $Fe_2S_2$  subcluster. In turn, the  $Fe_2S_2$  subcluster and its first shell residues are encapsulated in a 40 residues sphere which maintains the first shell residues in their crystallographic position, avoiding unrealistic conformational rigidity imposed by constraints during the geometry optimizations. This last point allow us to predict the structure of the CO dissociation photoproduct. Indeed we need to leave the first-shell residues free to rearrange after CO dissociation to estimate the relative stability of the unsaturated  $Fe_2S_2$  subcluster structures. The second shell also contains a water molecule H-bonded to Cys169 and Glu141, which is conserved in the crystallographic structures, and is part of the proton transfer chain<sup>2,3</sup>.

The optimized geometry of the  $Fe_2S_2$  core in the model of  $H_{ox}$  reproduces well the crystallographic data as the RMSD calculated with respect to the X-ray structure of the binuclear cluster in the semisynthetic enzyme from Cpl (PDB code 4XDC)<sup>4</sup>, assigned to the  $H_{ox}$  redox state, is equal to 0.19 Å. Regarding the outer shell residues, the RMSD calculated including all of the (non-hydrogen) atoms is equal to 0.86 Å and 0.95 Å for the  $H_{red}$  and  $H_{ox}$  models, respectively, which is acceptable considering the very small number of atoms

constrained to the crystallographic positions in the geometry optimizations. The most relevant conformational change observed in the geometry optimized models of both  $H_{ox}$  and  $H_{red}$  is a significant displacement of the side chain of Phe 296 (equivalent to Cr F290) compared to the crystallographic position: in the optimized geometries the side chain of this residue moves about 3 Å away from the  $Fe_2S_2$  core. The displacement of Phe 296 increases the size of a pocket close to  $Fe_q$ , which may accommodate the CO ligand after the photo-dissociation. It is worth noting that Phe 296 is embedded in our large model, and outer residues, such as Val 302 and Cys 200, should prevent any unrealistic movement of its side chain. In the  $H_{ox}$  and  $H_{red}$  models we also observed a rotation of the Cys 179 side chain that increases the distance between the  $Fe_2S_2$  and the thiol group by more than 1.0 Å with respect to the X-ray value, probably due to a different pattern in the H-bond network.

**Level of theory.** We carried out the computations using two different levels of theory depending on the model system to be investigated. The DFT and TDDFT computations were carried out on the small model to explore its excited state PES along selected bond elongation coordinates. In this case, we performed the computation using the hybrid Generalized Gradient Approximation (GGA) PBE0<sup>5</sup> DFT functional as implemented in the TURBOMOLE suite of programs<sup>6</sup>. Basis sets of triple- $\zeta$  plus polarization split valence quality<sup>7</sup> were adopted for all atoms in the model.

Excited PESs have been scanned along selected Fe-Ligand (Fe-L) bond stretching coordinates as follows. For each step, the ground state structure was first optimized by keeping the elongated Fe-L distance fixed. The sampling of the excited PES has been carried out with a step of 0.05 Å, until complete ligand dissociation. For each point the vertical excitation energies have been computed and the resulting profile for each excited state is the approximation of the stretching coordinate on the excited surface using the structures computed on the ground state surface.

DFT calculations on the large model have been carried out using the BP86<sup>8,9</sup> functional combined with the Resolution of Identity (RI) technique in order to save CPU time.<sup>10</sup>

The DFT functional for the TDDFT computations was chosen on the basis of the comparison between the X-ray structure of the  $Fe_2S_2$  subcluster and the binuclear  $H_{ox}$  model optimised at DFT level, using a set of functionals usually adopted in the computational investigation of FeFe hydrogenase models.<sup>11–13</sup>

We compare the *in vacuo* geometries and energies optimized with these DFT functionals, namely the pure GGA BP86<sup>8,9</sup>, pure Perdew–Burke–Ernzerhof PBE functional and the corresponding 25% Hartree-Fock exchange ( $E_x^{HF}$ ) hybrid PBE0<sup>5</sup>, the hybrid B3LYP<sup>9,14</sup> functional, the meta-hybrid GGA M06 and M06-2X<sup>15</sup> functionals with 27% and 54%  $E_x^H$  respectively, and TPSS and the corresponding hybrid TPSSh<sup>16,17</sup> with 10%  $E_x^H$ . All computation were carried out using the def-TZVP basis set<sup>18</sup>.

In this comparison our goal is to identify the best hybrid functional for the exploration of the excited state properties of the system. Indeed, it is known that pure functionals better reproduce experimental geometries of the H-cluster and of the corresponding models. In particular in this work it was crucial to find the hybrid functional that stabilizes the full-rotated form (see figure S3, left), which is the inverted square pyramids edge-shared Fe coordination in the  $Fe_2S_2$  core of the H-cluster, with respect to the semi-rotated form. These

two coordinations can be described by the S-Fe-Fe-CN dihedral angle which measures the rotation of the SCH<sub>3</sub><sup>-</sup> ligand respect to the cyanide around the Fe-Fe bond axes.

The comparison among the various optimized forms has been made on the basis of the absolute values of the differences between the H<sub>ox</sub> X-ray structure (PDB code: 4XDC<sup>4</sup>) and computed Fe-Fe, Fe-S and Fe-C bond distances for the Fe<sub>2</sub>S<sub>2</sub> model. All the results are reported in Table 1. First, we observe that all the hybrid functionals predict the stabilization of the full-rotated form with the exception of M06-2X, for which the calculated geometry is in very poor agreement with the crystallographic data. Starting from the full-rotated form, using pure functionals, the optimization converges to the semi rotated form except for TPSS. Among the complete set of functionals, TPSS gives the best agreement with X-ray data, while among hybrid functionals PBE0 is the best choice, while B3LYP and the two meta GGA M06 and M06-2X give the worst results. For these reason, TDDFT calculations were carried out using the PBE0 functional.

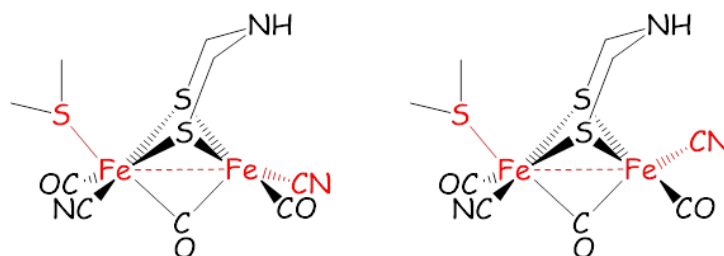
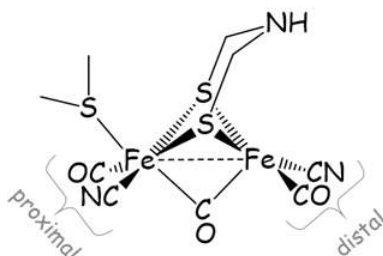


**Figure S3** - The full rotated and the semi-rotated forms described by the S-Fe-Fe-CN dihedral angle (around 100 degree for the full rotated and 40 degree for the semi-rotated).



## 1.2 - Fe<sub>2</sub>S<sub>2</sub> Small model MO populations

In the following panel, we report for each alpha and beta FMOs involved in the electronic spectrum (95 $\alpha$ -111 $\alpha$ ; 94 $\beta$ -108 $\beta$ ) the atomic/ligand (2Fe, distal and proximal CO, distal and proximal CN<sup>-</sup>, the 2S that belong to the ADT ligand, the SCH<sub>3</sub><sup>-</sup>) mulliken orbital populations. From these values we can observe:

- 1) on average occupied FMOs 2Fe populations are always higher than those of the virtual FMOs.

- 2) on average occupied FMOs distal and proximal CO populations are always lower than those of the virtual FMOs.
- 3) on average the 2S and SCH<sub>3</sub><sup>-</sup> contributions are slightly lower for virtual FMOs
- 4) for all the FMOs considered, the CN<sup>-</sup> contributions are low.

The 102 $\alpha$  and 101 $\beta$  orbitals are mainly composed by the lone-pairs strongly localized on the S atom that belong to the SCH<sub>3</sub><sup>-</sup> ligand. This fact could be considered as an artifact since in the H-cluster the bonding network of the atom is saturated by the Fe<sub>4</sub>S<sub>4</sub> cluster.

On the basis of these MO population, we can conclude that the excitations that involve these FMOs will be characterized by

- 1) charge transfer (CT) from Fe to both CO ligands;
- 2) CT from sulfur ligands to CO ligands

**Table S1** - *In vacuo* geometries energies optimized with the following DFT functionals: PBE0, BP86, B3LYP, TPSSh, TPSS, M06 and M06-2X.

	XRD	PBE0	$\delta$	PBE	$\delta$	BP86	$\delta$	B3LYP	$\delta$	TPSSh	$\delta$	TPSS	$\delta$	M06	$\delta$	M06-2X	$\delta$	
<b>Fe-Fe</b>	2.552	2.533	0.019	2.520	0.032	2.530	0.022	2.599	0.047	2.541	0.011	2.551	0.002	2.550	0.002	2.881	0.329	
<b>Fe-S</b>	<b>prox front</b>	2.321	2.374	0.053	2.379	0.058	2.345	0.024	2.424	0.103	2.378	0.057	2.385	0.064	2.380	0.060	2.511	0.190
	<b>prox back</b>	2.274	2.357	0.084	2.338	0.065	2.390	0.117	2.408	0.134	2.355	0.082	2.354	0.081	2.382	0.067	2.500	0.226
	<b>dist front</b>	2.289	2.319	0.030	2.323	0.034	2.314	0.024	2.361	0.072	2.317	0.028	2.315	0.026	2.340	0.065	2.473	0.184
	<b>dist back</b>	2.309	2.333	0.024	2.308	0.001	2.330	0.021	2.373	0.064	2.334	0.025	2.335	0.025	2.355	0.060	2.362	0.053
<b>Fe-SCH<sub>3</sub></b>		2.340	2.345	0.005	2.362	0.022	2.370	0.030	2.397	0.057	2.356	0.016	2.363	0.023	2.369	0.029	2.497	0.157
<b>Fe-C</b>	<b>dist</b>	1.737	1.750	0.013	1.744	0.007	1.746	0.009	1.769	0.032	1.755	0.018	1.751	0.014	1.770	0.033	1.889	0.152
<b>Fe-C</b>	<b>prox</b>	1.718	1.751	0.033	1.742	0.024	1.744	0.026	1.768	0.050	1.755	0.037	1.753	0.035	1.772	0.054	1.930	0.212
<b><math>\mu</math>-CO</b>		1.947	1.996	0.049	1.976	0.029	1.979	0.032	2.043	0.096	1.999	0.052	1.989	0.042	2.040	0.092	2.117	0.170
		1.893	1.935	0.042	1.923	0.030	1.926	0.033	1.954	0.061	1.936	0.043	1.931	0.038	1.942	0.049	2.171	0.278
<b>Fe-CN</b>	<b>dist</b>	1.911	1.923	0.012	1.916	0.005	1.912	0.001	1.949	0.038	1.928	0.017	1.922	0.011	1.950	0.039	2.070	0.159
<b>Fe-CN</b>	<b>prox</b>	1.841	1.936	0.095	1.909	0.068	1.918	0.077	1.965	0.124	1.939	0.098	1.935	0.094	1.940	0.099	2.100	0.259
	<b>Sum</b>			0.457		0.375		0.415		0.877		0.483		0.455		0.650		2.368
<b>S-Fe-Fe-CN</b>		110.2		40.02		41.2		107.6		108.5		106.6		108.6		35.5		

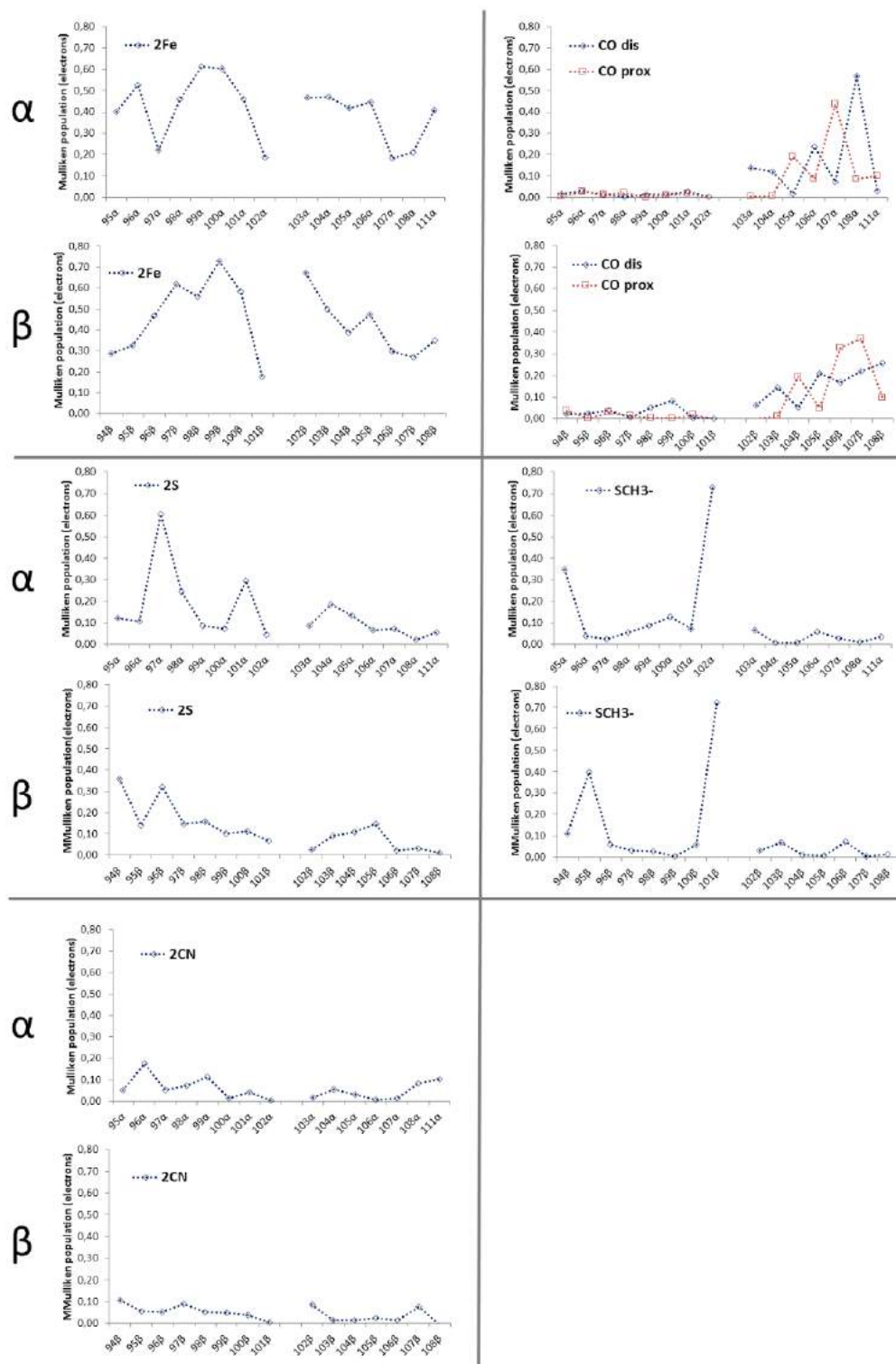


**Figure S4** - Atomic/ligand (2Fe, distal and proximal CO, distal and proximal CN; the 2S that belong to the ADT ligand, the SCH3) mulliken orbital populations of alpha and beta FMOs involved in the electronic spectrum (95 $\alpha$ -111 $\alpha$ ; 94 $\beta$ -108 $\beta$ ).



In figure S5 we report the isosurfaces of the 3 highest occupied and the 3 lowest unoccupied MOs. The virtual MOs are characterized by antibonding-non bonding combinations between Fe and S of ADT atomic orbitals and non-bonding/antibonding combinations between Fe and distal or proximal CO orbitals.

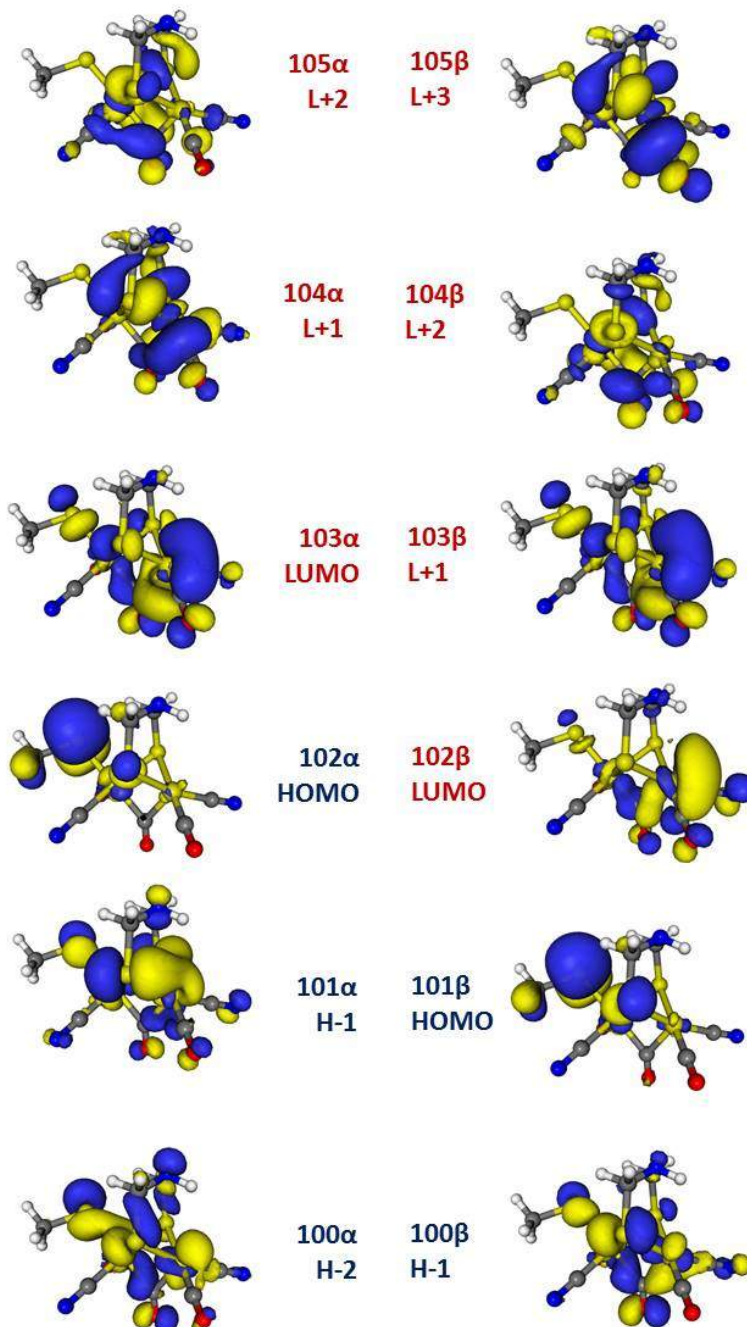


**Figure S5** - Isosurfaces of the first 6 FMOs around the HOMO/LUMO gap.

### 1.3 - Fe<sub>2</sub>S<sub>2</sub> Small model electronic spectra.

**Table S2** - SCH<sub>3</sub><sup>-</sup> Fe<sub>2</sub>S<sub>2</sub> model TDDFT electronic spectrum. For each transition we list the excitation energy  $\lambda$  (nm), the oscillator strength (f) and the main mono-electronic excitations (1e) with the corresponding percentage composition, band assignment and localization of the Charge Transfer (CT)

n. ex	$\lambda$ (nm)	f	1e	Assignment
1	1413	$1 \cdot 10^{-2}$	100 $\beta$ $\rightarrow$ 102 $\beta$ (50.1%) 99 $\beta$ $\rightarrow$ 102 $\beta$ (21.1%)	LLMCT
2	988	$1 \cdot 10^{-3}$	99 $\beta$ $\rightarrow$ 102 $\beta$ (21.6%) 99 $\beta$ $\rightarrow$ 103 $\beta$ (12.2%)	LLCT
3	890	$1 \cdot 10^{-4}$	98 $\beta$ $\rightarrow$ 102 $\beta$ (45.8%) 97 $\beta$ $\rightarrow$ 102 $\beta$ (16.7%)	LLMCT
13	547	$1 \cdot 10^{-2}$	102 $\alpha$ $\rightarrow$ 103 $\alpha$ (18.7%) 101 $\alpha$ $\rightarrow$ 103 $\alpha$ (14.0%)	LLMCT
19	432	$2 \cdot 10^{-3}$	97 $\beta$ $\rightarrow$ 104 $\beta$ (11.0%)	MLCT
21	422	$1 \cdot 10^{-2}$	100 $\beta$ $\rightarrow$ 105 $\beta$ (11.0%)	MLLCT
24	404	$1 \cdot 10^{-2}$	100 $\alpha$ $\rightarrow$ 103 $\alpha$ (13.0%)	MLLCT
25	392	$1 \cdot 10^{-2}$	98 $\alpha$ $\rightarrow$ 103 $\alpha$ (10.4%)	LLMCT
27	383	$2 \cdot 10^{-2}$	100 $\beta$ $\rightarrow$ 103 $\beta$ (13.4%)	MLCT
28	378	$1 \cdot 10^{-2}$	100 $\alpha$ $\rightarrow$ 103 $\alpha$ (6.8%) 99 $\alpha$ $\rightarrow$ 103 $\alpha$ (6.7%)	MLLCT
29	366	$1 \cdot 10^{-2}$	95 $\beta$ $\rightarrow$ 102 $\beta$ (31.5%) 101 $\beta$ $\rightarrow$ 103 $\beta$ (10.4%)	LMCT
66	279	$2 \cdot 10^{-2}$	101 $\alpha$ $\rightarrow$ 106 $\alpha$ (4.4%)	LLCT
70	274	$3 \cdot 10^{-3}$	100 $\alpha$ $\rightarrow$ 106 $\alpha$ (5.7%)	MLCT
88	256	$2 \cdot 10^{-2}$	101 $\beta$ $\rightarrow$ 111 $\beta$ (6.3%) 98 $\alpha$ $\rightarrow$ 107 $\alpha$ (5.0%)	LLMCT MLLCT
95	251	$1 \cdot 10^{-2}$	97 $\alpha$ $\rightarrow$ 104 $\alpha$ (5.7%)	LMCT

**Table S3** - MO differential populations computed according to the TDDFT main one-electron excitations of the  $\text{Fe}_2\text{S}_2$  small model for selected excited states.

	1ex	2ex	3ex	13ex	19ex	21ex	24ex	25ex	27ex	28ex	29ex	66ex
2·Fe	0,05	0,00	0,07	0,10	-0,07	-0,03	-0,03	0,04	0,02	0,03	0,16	0.00
2·S	-0,06	-0,03	-0,09	-0,05	0,00	0,00	-0,03	-0,01	0,00	0,00	-0,06	-0.05
$\text{SCH}_3^-$	-0,03	-0,05	0,00	-0,18	-0,02	-0,04	-0,02	-0,16	-0,15	-0,11	-0,22	-0.06
CO dist	0,03	0,02	0,02	0,05	0,02	0,06	0,07	0,04	0,05	0,05	0,06	0.04
CO prox	-0,01	0,00	-0,01	0,00	0,07	0,01	0,00	0,04	0,03	0,01	0,00	0.05
$\mu\text{CO}$	-0,01	0,05	0,05	0,08	0,04	0,01	0,07	0,06	0,05	0,05	0,07	0.03
$2\text{CN}^-$	0,03	0,01	0,02	0,01	-0,03	-0,01	-0,02	0,00	-0,01	-0,01	0,00	0.00
$\text{CH}_2\text{NH-CH}_2$	0,00	0,00	-0,06	-0,01	-0,01	-0,01	-0,03	-0,01	-0,01	-0,01	-0,01	-0.05

Figure S6 shows i) the computed electronic spectra of the  $\text{SCH}_3^-$  and  $\text{HSCH}_3$   $\text{Fe}_2\text{S}_2$  small models at PBE0 level ii) the computed electronic spectra of the  $\text{SCH}_3^-$  computed at PBE0 and TPSSh levels. The aim of the first comparison is to underline the small effect of the ligand choice in modelling the Fe-S-Cys bond network to the  $\text{Fe}_4\text{S}_4$  cluster, while the second comparison is useful to figure out the variability of the computed excitation energies as a function of the DFT functional adopted. In particular in the latter we consider the comparison between two hybrid functionals (PBE0 and TPSSh) which has been shown to better reproduce the H-cluster geometry in the  $\text{H}_{\text{ox}}$  state.

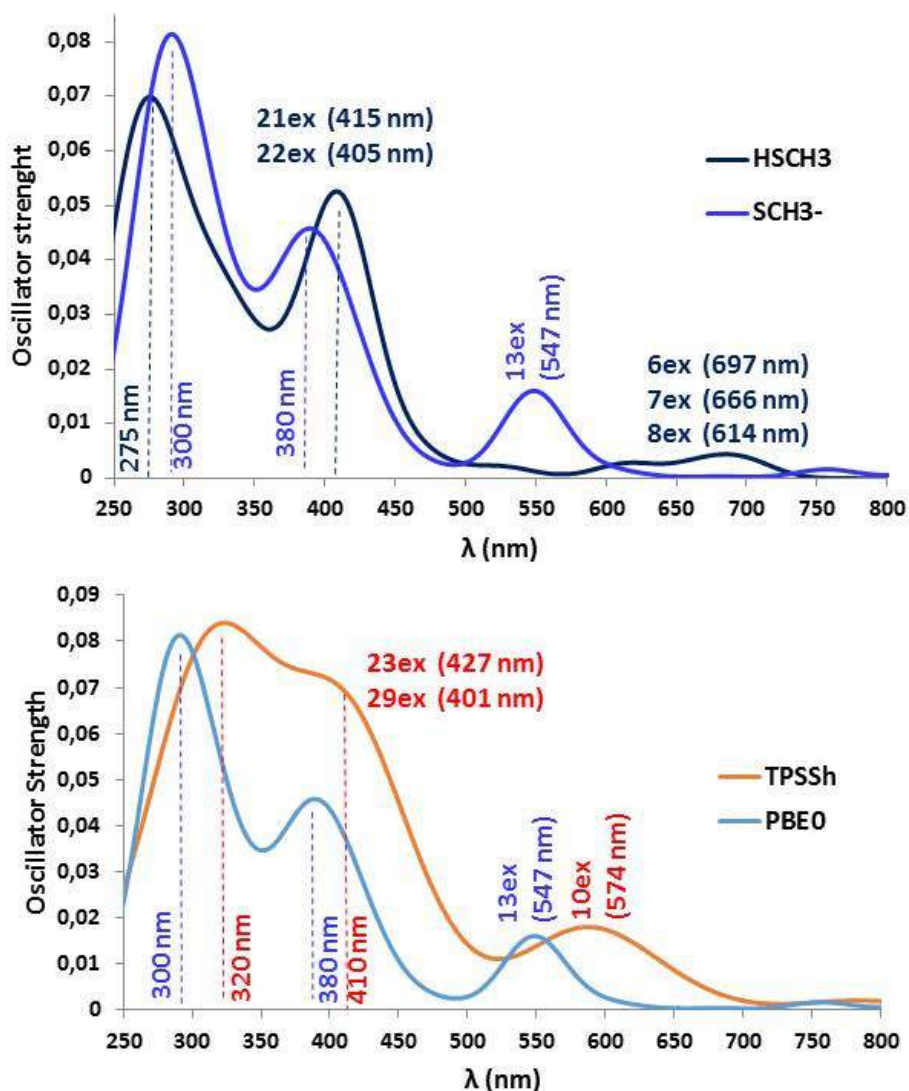


**Figure S6** - Hox Computed Spectra Superimpositions. On top the comparison between the computed spectra (PBE0) of the HSCH<sub>3</sub> and SCH<sub>3</sub><sup>-</sup> Fe<sub>2</sub>S<sub>2</sub> models to evaluate the effect of the two ligands; on bottom the comparison between SCH<sub>3</sub><sup>-</sup> Fe<sub>2</sub>S<sub>2</sub> model PBE0 and TPSSh spectra computed with the corresponding minimum geometries.

From the comparison with the SCH<sub>3</sub><sup>-</sup> spectrum emerges that the HSCH<sub>3</sub><sup>-</sup> spectrum presents:

- 1) a bathochromic shift of the first intense feature of around 23 nm;
- 2) an hypsochromic shift of the second intense feature of around 17 nm;

The weak feature computed for the HSCH<sub>3</sub> model is characterized by a three excitations of similar intensity and therefore this band results broad compared to the SCH<sub>3</sub><sup>-</sup> model. We estimate a bathochromic shift in a range between 100 to 150 nm. Regarding the nature of the MO involved in the spectrum, it is useful to compare MO population for SCH<sub>3</sub><sup>-</sup> and HSCH<sub>3</sub> models (figure S7).

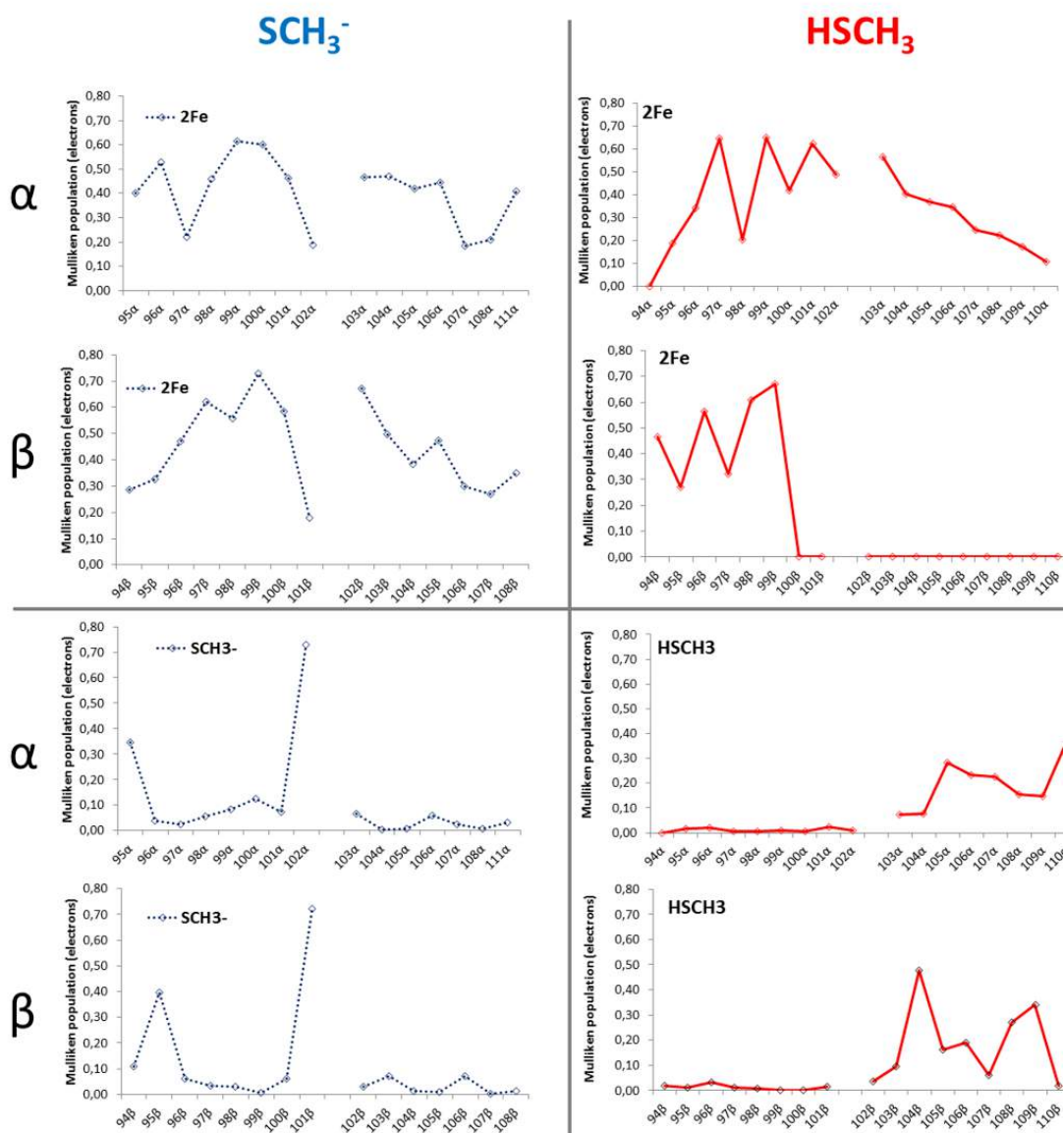


Figure S7 - MO populations for the iron atoms and the HSCH<sub>3</sub>/SCH<sub>3</sub><sup>-</sup> ligand.

It is important to note that the FMOs involved in the electronic spectrum of the two models are similar except for the SCH<sub>3</sub><sup>-</sup> population of the HOMO in the SCH<sub>3</sub><sup>-</sup> Fe<sub>2</sub>S<sub>2</sub> model, due to the negative charge on this ligand. This is probably the reason why the weak feature changes significantly between the two models.

**Table S4** - Differential populations for the excitation involved in the weak feature of the PBE0 computed electronic spectra for the HSCH<sub>3</sub> and SCH<sub>3</sub><sup>-</sup> Fe<sub>2</sub>S<sub>2</sub> model (13ex state for SCH<sub>3</sub><sup>-</sup> model; 6ex-8ex for HSCH<sub>3</sub> model).

	HSCH <sub>3</sub>			SCH <sub>3</sub> <sup>-</sup>
	6ex	7ex	8ex	13ex
<b>2Fe</b>	0.05	-0.01	0.02	0.1
<b>2S</b>	-0.09	-0.03	-0.09	-0.05
<b>HSCH3/ SCH<sub>3</sub><sup>-</sup></b>	0.02	0.04	0.03	-0.18
<b>CO dist</b>	0.03	0.06	0.03	0.05
<b>CO prox</b>	-0.01	0.00	0.00	0
<b>μCO</b>	0.03	0.00	0.06	0.08
<b>adt</b>	-0.02	-0.04	-0.01	-0.01
<b>2CN-</b>	-0.02	-0.02	-0.02	0.01

The comparison among differential populations (Table S4) of the 13ex state for the SCH<sub>3</sub><sup>-</sup> model and the 6ex-8ex for the HSCH<sub>3</sub> Fe<sub>2</sub>S<sub>2</sub> model indicates that the nature of these excitations is similar and can be assigned in both cases to a LLMCT band which involves the sulfur ligands.

We also computed the spectrum of the SCH<sub>3</sub><sup>-</sup> Fe<sub>2</sub>S<sub>2</sub> model with the TPSSh hybrid functional, starting from the minimum geometry obtained with the same functional (Figure S6). The TPSSh spectrum shows a broadening and an average ~20-30 nm bathochromic shift of the peaks compared to the PBE0 one.

Regarding the comparison of the spectra computed with different models and different functionals presented above we observed that

- the effect of the HSCH<sub>3</sub> ligand compared to SCH<sub>3</sub><sup>-</sup> ligand
  - is more significant for low energy states which involve CT from the sulfur atoms, mainly due to the negative charge localized on the SCH<sub>3</sub><sup>-</sup> ligand in the HOMO;
  - is less significant for higher energy states which involve the CO ligands;
- considering two hybrid functionals which better reproduce the X-ray H-cluster geometry in the Hox state, the effect is a general red shift of 20-30 nm, while the nature of the excitations are similar

### 1.3 - Small model TDDFT geometry optimizations of 1ex and 2ex

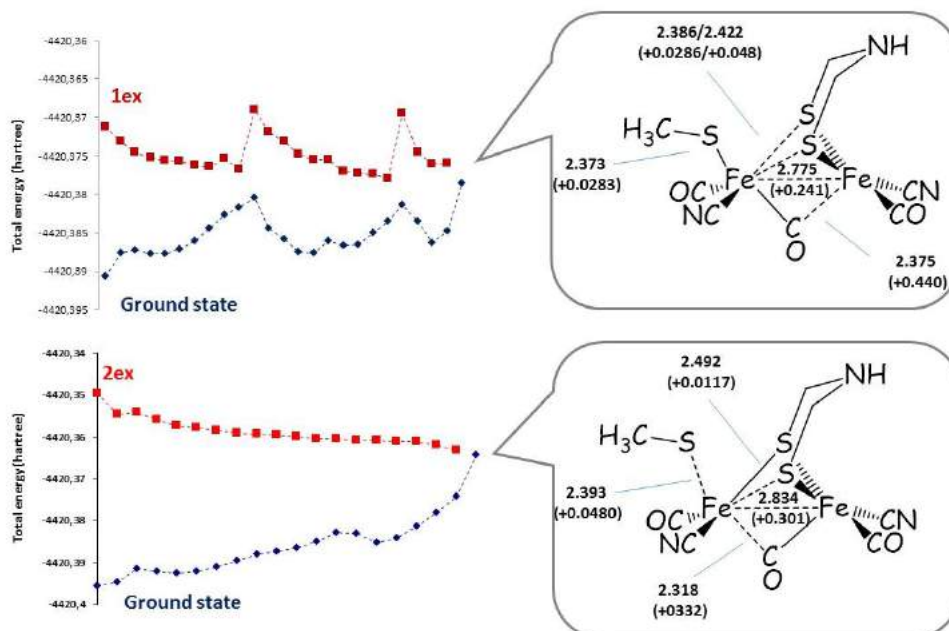


**Figure S8** - 1ex and 2ex TDDFT geometry optimizations of the SCH<sub>3</sub>-Fe<sub>2</sub>S<sub>2</sub> model and internal conversion between the excited states and the ground state. On the left are shown the geometries at the intersection point (distances in Å).

## 1.4 - CO dissociation energy barriers

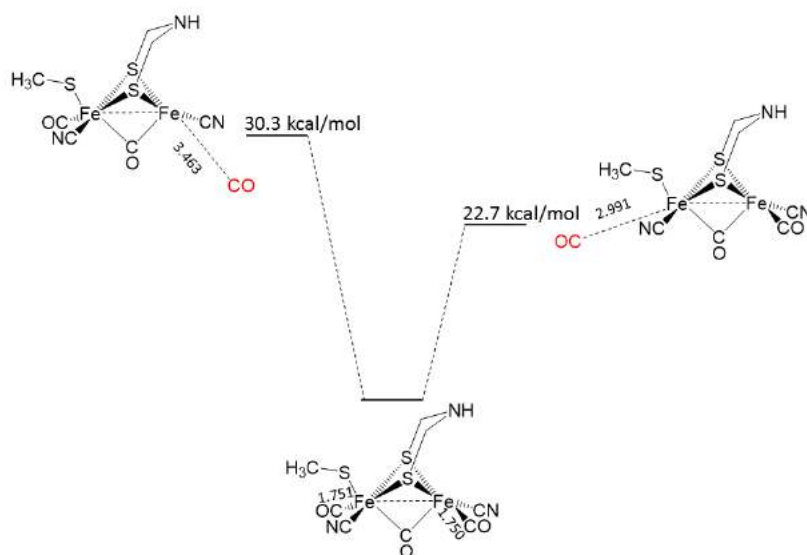


**Figure S9** - Small model  $\text{SHC3-Fe}_2\text{S}_2\text{-Hox}$  structures of transition states and free energy barriers (in kcal/mol) for the dissociation of CO in proximal or distal position. The imaginary frequencies of the normal modes that describes the dissociation are  $188.10\text{ cm}^{-1}$  for  $\text{CO}_{\text{distal}}$  and  $171.59\text{ cm}^{-1}$  for  $\text{CO}_{\text{prox}}$ . Distances in Å.



## 1.5 - Large Fe<sub>2</sub>S<sub>2</sub> model structures

Compared to the crystallographic structure, the large model in the H<sub>ox</sub> state shows a decrease of the d(Fe-Fe) of 0.03 Å and of the d(Fe-SCH<sub>3</sub><sup>-</sup>) of 0.20 Å (0.17 Å in H<sub>red</sub>). The distance between both the Fe atoms and the bridging CO is lower in the model in H<sub>ox</sub> state than in the one in H<sub>red</sub> state. In the latter structure the distances between the Fe atoms and the two terminal CO is lower (-0.03 Å). The relative stability of the H<sub>ox</sub><sup>uns</sup> and H<sub>red</sub><sup>uns</sup> forms correlates with the Fe-Fe bond distances.

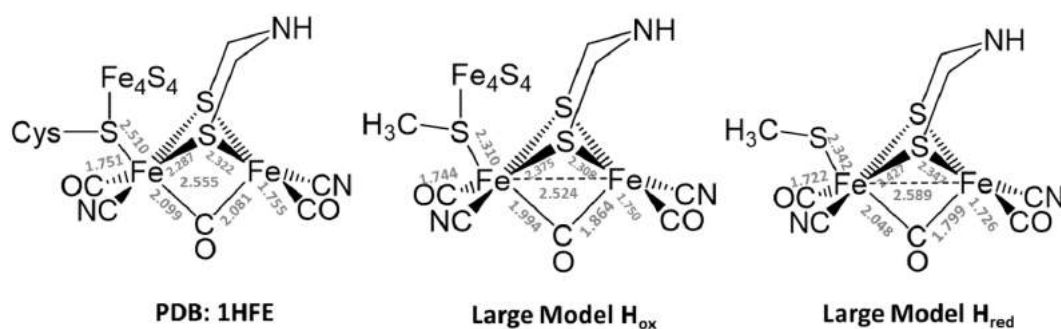


**Figure S10** - Comparison between the crystallographic structure of the diiron (PDB: 1HFE) and the structures of H<sub>ox</sub> and H<sub>red</sub> large models optimized with BP86. The bridging CO was added manually.

**Table S5** - Resume of the optimizations of H<sub>red</sub>, H<sub>red</sub><sup>uns</sup>, H<sub>ox</sub> and H<sub>ox</sub><sup>uns</sup> with the large model.

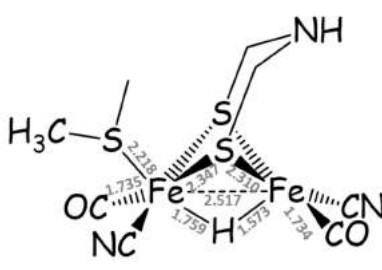
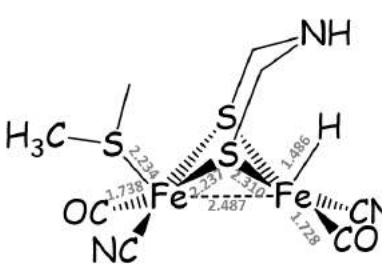
	ΔE (kcal/mol)	Fe-Fe (Å)	E(HOMO) eV	E(LUMO) eV
H <sub>red</sub>	-	2.589	-0.8763	-0.2948
H <sub>red</sub> <sup>uns</sup>				
1	1.5	2.491	-0.7522	-0.0109
2	5.4	2.542	-0.5661	-0.0314
3	0.0	2.487	-0.6246	-0.0773
4	5.5	2.616	-0.8431	-0.0403
H <sub>ox</sub>		2.524	-3.2200	-2.3390
H <sub>ox</sub> <sup>uns</sup>				
1	1.1	2.477	-2.9939	-2.4305
2	5.2	2.512	-3.0259	-2.3739
3	0.0	2.473	-3.0256	-2.5882
4	7.3	2.516	-3.2436	-2.3835

## 1.6 - $H_{\text{red}}^{\text{uns}}$ protonated

We added a proton in apical position on the  $\text{Fe}_d$  or in bridging position ( $\mu\text{H}^+$ ) between the two Fe atoms of  $H_{\text{red}}^{\text{uns}}$  form 3 (see main text fig. 6).

The optimized structures show that the binding of a proton in bridging position increases the  $d(\text{Fe}-\text{Fe})$  by 0.03 Å and decreases the  $d(\text{Fe}-\text{SCH}_3)$  by 0.11 Å.

**Table S6** - Relative energies and geometries of the optimized  $H_{\text{red}}^{\text{uns}}$  large model protonated in bridging or apical position.

	$\Delta E$ (kcal/mol)	Geometry
$H_{\text{red}}^{\text{uns}} + \mu\text{H}^+$	0.0	
$H_{\text{red}}^{\text{uns}} + \text{terminal H}^+$	8.7	

## 1.7 - Optimized coordinates PBE0

Model	Coordinates (atomic units)			
Fe <sub>6</sub> S <sub>6</sub> Hox	5.81080535014191	57.71989686707392	57.15329373990119	fe
	4.56923642638079	53.76857326697451	55.50449599980489	s
	4.09574087336189	49.75056306718419	61.69169390413702	s
	1.22675081023325	51.52425806414441	62.47653240855141	c
	0.05957048648522	50.37891642183153	63.73914444090592	h
	0.13852876167692	51.95269733797753	60.77839064051678	h
	1.69932025054731	53.29465150501215	63.42077582536746	h
	6.23254409710555	52.78497754335533	59.43363392216826	fe
	6.62274958572854	56.61301155777577	61.38350567012471	s
	3.31475779156671	61.24350983742652	56.66140784174710	s
	5.11690799766659	63.79853370306723	58.10231438207044	c
	3.80394091849611	65.25631296786922	58.73334779018125	h
	6.39862310644849	64.62644814666206	56.72223982409638	h
	6.17171580452207	63.02495732454117	59.69593080371398	h
	0.50900771683444	63.01602809310312	53.72229190704493	fe
	-4.19978684473726	63.86309387550450	53.50640002830279	fe
	-1.74424845309392	64.43447673102126	50.94267387678887	c
	-1.56314667773619	65.09584346105135	48.85622281948916	o
	2.54348025941173	66.00749115871449	53.28358857478921	c
	3.75800215885071	67.81581405096499	52.99201975772895	n
	2.16084281768218	61.48146058456630	51.26090361105130	c
	3.27436358700570	60.53651327544893	49.66997100055659	o
	-6.93734638116288	62.66136591715383	51.40328172477759	c
	-8.71725141685268	62.01983403549868	50.28243425987739	n
	-5.37826336014119	66.95043634531818	53.25988839316993	c
	-6.18568874059059	68.96406121524875	53.08864763528491	o
	-2.54893750388723	59.81880851117124	54.05213815477550	s
	-2.87173221635250	58.89329734324012	57.41025018069697	c
	-3.91408058605852	60.73030342603185	59.11489951384597	n
	-2.31492395388705	62.86830548483168	59.56652027827633	c
	-1.77534213333574	65.11652003883135	56.93191448610050	s
	-1.00259604415644	58.34274267937512	58.08582698216033	h
	-4.08679757798368	57.22654011765098	57.39087163789797	h
	-5.61116560583823	61.32595816032543	58.44668097298277	h
	-3.12359421566040	64.01195742344419	61.08420686673453	h
	-0.45838059062679	62.18186717297962	60.15389069210528	h
	10.61171214850794	55.95599956902353	59.52802788194847	fe
	10.23645542182041	51.65031868271000	58.27742266937483	s
	10.61549203367422	53.39594103716555	51.22157558567349	s
	11.13802353453915	56.44722608869662	49.69618905785286	c
11.86496663632045	56.10359660186386	47.79255932189610	h	
12.50015012448194	57.57102434119471	50.75696994210393	h	
9.37943809340065	57.51103973978702	49.56061114019386	h	
8.77639275916412	53.93351825835913	54.96839088038901	fe	
9.86458440762793	57.95530088241556	55.77206113890549	s	
14.36203058884170	56.96374224126133	61.29573280848008	s	
14.28459661333639	60.41959110895603	61.46950426013920	c	
14.12494266828041	61.23470731006492	59.58090331227831	h	
12.68101786787739	61.07102017683486	62.59302710565727	h	
16.02618934521948	61.11195593527371	62.34435841142183	h	

Fe <sub>2</sub> S <sub>2</sub> HSCH <sub>3</sub> Hox	-41.89483001187321	24.27246369648162	-6.59968171955257	h	
	-42.23124559492533	24.12206420046604	-8.62519453892029	c	
	-45.19763204959049	25.67650830423168	-9.41526752559436	s	
	-46.01790372829429	25.31497882403544	-13.63038674788717	fe	
	-49.07107035899867	27.19518728782347	-16.78034428790611	fe	
	-48.10615547945212	29.13299525046998	-19.32279542501628	c	
	-47.49168472055619	30.37686844152859	-20.97930148182353	o	
	-46.72030261477788	29.66230859773901	-14.03457069682950	s	
	-48.86928362146091	30.74814975443858	-11.48502813550091	c	
	-51.40481877533840	29.81030092866806	-11.44312273429892	n	
	-51.65171637492350	27.17313077631185	-10.91241488105048	c	
	-50.39001432074159	24.88642366741519	-13.25745316070968	s	
	-45.54309019925829	22.01594175719755	-13.61858455593900	c	
	-45.17723440838752	19.88590856071344	-13.53971873714446	o	
	-42.49457988000159	25.88348061428108	-14.30479958876543	c	
	-40.32706303490400	26.17531990591256	-14.50048180054212	n	
	-46.58195752655830	24.81678372177757	-17.52436196945557	c	
	-45.70423423138875	23.54298352496140	-19.07329574677895	o	
	-51.76114250099297	25.85350802902154	-18.81668907910437	c	
	-53.47441820345225	25.19888298967419	-20.02272426123754	n	
	-40.78063215095271	25.11566283516829	-9.69454241549364	h	
	-42.25778703486431	22.15622269906594	-9.23052352249227	h	
	-48.91378742133644	32.80033297750255	-11.67820169630326	h	
	-47.96792822338090	30.29893319738160	-9.68020316408842	h	
	-50.76991251663671	26.78817444933226	-9.08199922334755	h	
	-53.65386471847027	26.70462783618898	-10.76082053530716	h	
	-52.30442665222658	30.23933927948188	-13.08052881839019	h	
	-46.73218660859112	23.95965048506881	-8.30194319770306	h	
	Fe <sub>2</sub> S <sub>2</sub> SCH <sub>3</sub> <sup>-</sup> Hox	-42.14014888682988	24.81903368870568	-6.55843948338223	h
		-42.34115600628162	24.79551816714691	-8.61787864323274	c
-45.69833764354120		24.98211600379869	-9.36519186882416	s	
-46.17063215416918		25.12131808054645	-13.76874475696289	fe	
-49.11106309127288		27.28433914788062	-16.86613091548642	fe	
-47.97994571056324		29.19462524968080	-19.31686496339990	c	
-47.26366762897812		30.45915079058738	-20.94085459287275	o	
-46.67658975100058		29.57208772962775	-14.02947174318164	s	
-48.61831820921913		30.54232075440514	-11.29768969313551	c	
-51.22689573794887		29.77838298459196	-11.24999725392745	n	
-51.58718632585597		27.11249886994311	-10.86927969593362	c	
-50.60990880725217		24.95141216181075	-13.43855806063867	s	
-45.81916348560075		21.83998957665667	-13.52634496968008	c	
-45.52601512294183		19.69815621915812	-13.32422924581436	o	
-42.61763456609077		25.52824246486512	-14.41090506223367	c	
-40.45901968096822		25.72312239090870	-14.78537884986434	n	
-46.62841568797175		24.67263037615874	-17.48574267238756	c	
-45.90299316666369		23.41646003926634	-19.13746462299648	o	
-51.73701747218900		25.98352338599589	-19.05483948241723	c	
-53.39973752312307		25.38836995502340	-20.36637403655083	n	
-41.30339718075328		26.37631423496332	-9.43576821564560	h	
-41.50374571571272		23.05639683971169	-9.34875687844957	h	
-48.52210915675666		32.60583645080366	-11.24940297540919	h	
-47.67749265501912		29.76963575946598	-9.62616554138771	h	
-50.56590271803820		26.54819422135249	-9.16537857758022	h	
-53.60126464877966		26.74514975948060	-10.59522111809206	h	
-52.05864689692346		30.28691391139561	-12.90472290580486	h	

Fe <sub>2</sub> S <sub>2</sub> SCH3 <sup>-</sup> Hox, CO <sub>dist</sub> TS	-41.19300046591601	25.43257113408177	-6.97113356380049	h
	-41.65156518877431	25.08252015495216	-8.95836578569076	c
	-44.99919424619376	25.74610504541949	-9.43219004707211	s
	-45.91929056193898	25.34379180035880	-13.72351809963653	fe
	-49.32972655711102	26.87179789524427	-16.63130773044846	fe
	-46.85159639822878	30.61103867863389	-21.39630319712519	c
	-46.17022729512486	32.30263836484327	-22.50456710282637	o
	-46.83478161509836	29.75725852207002	-14.40196757586513	s
	-48.69262617839609	30.80571637511763	-11.64075644227662	c
	-51.19157167063207	29.77731985469673	-11.30590264070768	n
	-51.28219348733460	27.16078804356808	-10.57265299635153	c
	-50.26828927662681	24.73238413814658	-12.88784340915184	s
	-45.23423271342367	22.14841986719208	-13.33671383694843	c
	-44.70900223204944	20.06053705201204	-13.02319882287204	o
	-42.51932553926925	26.01814812978358	-14.81504281125261	c
	-40.44450451111973	26.39752198931716	-15.44268133122018	n
	-46.83491389592766	24.58445070728590	-17.53820241942934	c
	-45.99889338556066	23.32325126565028	-19.14120229589837	o
	-52.12269075891042	26.41842802952528	-19.14171063222812	c
	-53.79806903599511	26.29921654615832	-20.56274122045707	n
-40.48140708304273	26.27592189211824	-10.16376350434840	h	
-41.20855669144192	23.11029235855700	-9.39204470510509	h	
-48.83182340534444	32.86311412832195	-11.77665042794469	h	
-47.55312698944445	30.31681398892199	-9.98631822047043	h	
-50.10620557648307	26.90524793752248	-8.89458374925361	h	
-53.23415964013297	26.68359440049179	-10.09220713460055	h	
-52.19824767888158	30.01561998923201	-12.92253311177322	h	
Fe <sub>2</sub> S <sub>2</sub> SCH3 <sup>-</sup> Hox, CO <sub>prox</sub> TS	-42.76502962079319	24.59151639329675	-6.26324971332606	h
	-42.85932128564578	25.22282476141439	-8.23105555057027	c
	-45.92967838649145	24.33296595352147	-9.53717567211071	s
	-46.17280299184399	25.34741440535554	-13.72037359535141	fe
	-49.05157398815932	27.14022593351615	-17.02444068595558	fe
	-47.91519284732694	29.16257115668157	-19.37153156560514	c
	-47.18486282984609	30.50294823355896	-20.93132852322415	o
	-47.14526172900534	29.70608662811761	-13.97128576209757	s
	-49.34870129721133	30.25219669353410	-11.30704214556581	c
	-51.83494216065592	29.16556259314993	-11.46223968368131	n
	-51.90374141997589	26.46599621574228	-11.17056990370108	c
	-50.56472683564031	24.53231505300571	-13.76218567576764	s
	-45.50298011541201	19.74147191228337	-13.49368204845045	c
	-45.07396504009365	17.94913470538211	-12.40678905558607	o
	-42.53010831658350	25.66965995416587	-14.06840445724496	c
	-40.33974187376482	25.79282852405509	-14.23989332435207	n
	-46.21102459260774	24.76137064729892	-17.37259249032164	c
	-45.27893985427549	23.52560880913808	-18.93105341156469	o
	-51.28831808973129	25.57419098993249	-19.45084904058075	c
	-52.73769268022738	24.80138181871050	-20.91500695861441	n
-42.60832408122364	27.27080222984628	-8.29221464713498	h	
-41.32115980252218	24.37822111495182	-9.31034239574978	h	
-49.53367902945497	32.30488902866753	-11.14627369481057	h	
-48.42906040546413	29.51834611626769	-9.61073515155941	h	
-50.88120116084080	25.96338008700028	-9.44767257327884	h	
-53.87344076280525	25.86860276253154	-10.99404491644983	h	
-52.62410691155802	29.63788263252950	-13.14783382024038	h	
Fe <sub>2</sub> S <sub>2</sub> SCH3 <sup>-</sup> Hox 1ex TDDFT opt	-42.23291577281307	24.64426102724795	-6.51737154425936	h
	-42.42276149801403	24.81775066668009	-8.57002922183962	c
	-45.77116056084986	24.98747578118977	-9.35544122745171	s
	-46.14462983178593	25.03858640842434	-13.82402415295839	fe
	-49.44781585728042	27.59541045502963	-16.98962426192003	fe
	-48.34099857738305	29.34013185984404	-19.54152264413848	c
	-47.64789809922925	30.51953618357089	-21.25876659082965	o
	-46.66491853655718	29.57251077991268	-14.16756730105891	s
-48.48520862643780	30.48566690779161	-11.32116060271327	c	

	-51.10162431511112	29.74059945440388	-11.17442662195609	n
	-51.49138817032071	27.06790040212913	-10.87580229601208	c
	-50.64713972391104	25.00526728499498	-13.58117345467749	s
	-45.80334835763745	21.76670959281920	-13.27221230449575	c
	-45.48438932050368	19.64490834132551	-12.97121886251824	o
	-42.55766384541911	25.41209741448089	-14.29282274461653	c
	-40.40346183628009	25.55524237427704	-14.70449580735343	n
	-46.17176091182996	24.53601021411533	-17.21199999513187	c
	-45.76165569991974	23.71574721242236	-19.16520386715170	o
	-51.93879812027477	26.13863567682524	-19.20877680814624	c
	-53.42043871441080	25.31153023388904	-20.62754862730374	n
	-41.42443599830314	26.50030964838855	-9.21424107168262	h
	-41.54176472914567	23.18049703677352	-9.46058380991491	h
	-48.37788963509716	32.54657744775455	-11.19226661133277	h
	-47.48418240187135	29.64593708437899	-9.72199962311221	h
	-50.44942608802315	26.42217497920943	-9.21640588981364	h
	-53.50185639984418	26.72676960520038	-10.55045072534256	h
	-52.02687400147013	30.33349514044842	-12.74866015735657	h
Fe <sub>2</sub> S <sub>2</sub> SCH <sub>3</sub> <sup>-</sup> Hox 2ex TDDFT opt	-41.83531862905672	25.25497685670801	-6.39749214575473	h
	-42.29219599273127	24.75619464724957	-8.35696775328443	c
	-45.68383799919233	25.00798017438881	-8.91985180507533	s
	-46.01878658298919	25.06326476803541	-13.42910402951751	fe
	-49.23333678170825	27.44833201131398	-16.98812834151780	fe
	-47.94782000282129	29.24623927453920	-19.46388679778606	c
	-46.98336844663030	30.37520171879623	-21.08506081713042	o
	-46.66871566063519	29.66791267658789	-14.16899303251621	s
	-48.71911611119194	30.54837950507040	-11.45163437733478	c
	-51.28096991593460	29.65324874468129	-11.38125259185610	n
	-51.53287592770111	26.98228998337542	-10.95701024996854	c
	-50.49927283080810	24.84470877186597	-13.53164395062344	s
	-45.61832669824216	21.66548393326494	-13.57286549540757	c
	-45.18455673400410	19.55533970013837	-13.38948050866110	o
	-42.46231036749609	25.53533965821009	-14.26689192815017	c
	-40.37277365679314	25.82956374444990	-14.83461247734295	n
	-46.76344836569168	24.64230329110054	-17.72543727686801	c
	-46.11850214373743	23.31328726199412	-19.16198336214505	o
	-52.08368680075848	26.46053061112891	-18.98995116423571	c
	-53.91252359999846	25.96122712480640	-20.19237493513775	n
	-41.25738203931380	26.01215059914950	-9.63175119062951	h
	-41.63995918187405	22.81736924071702	-8.72259327262073	h
	-48.73120770120239	32.62104546846452	-11.42108980993395	h
	-47.73844584647877	29.82912991044687	-9.78063950927310	h
	-50.44760524968160	26.48203092598218	-9.27252505674842	h
	-53.53400493092188	26.55239104257138	-10.63250886033385	h
	-52.18605743951505	30.12581757263559	-13.01006608732005	h

## 2 - Absorption spectra of the filters

We recorded the absorption spectra of the two filters that we used with a PerkinElmer UV/vis lambda 25 spectrophotometer.

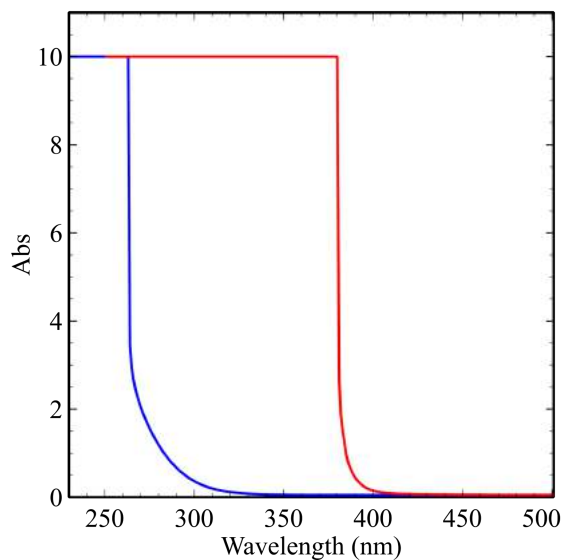


**Figure S11** - Absorption spectra of the borosilicate filter (blue) and of the UV filter (red).

## 3 - Experiments carried out with a halogen lamp

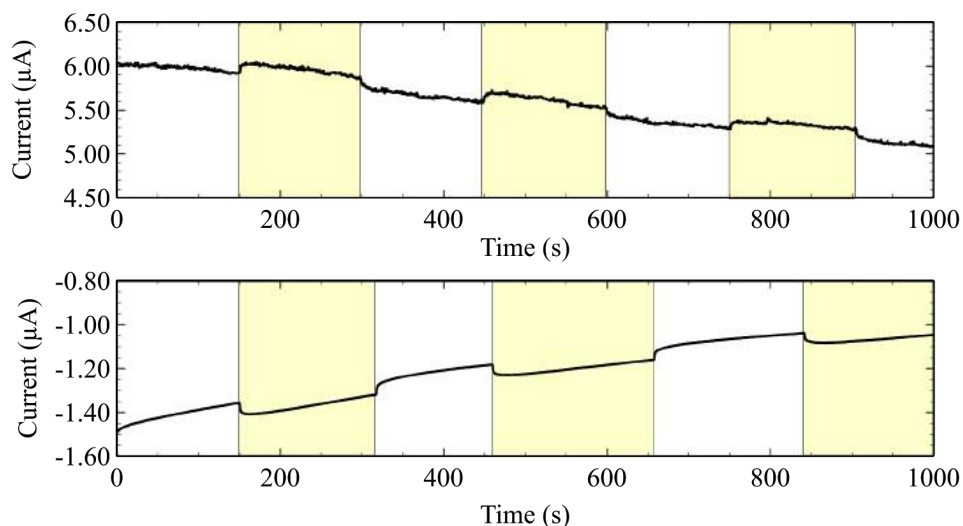


**Figure S12** - Chronoamperogram recorded at 30°C, 1 bar  $\text{H}_2$ , pH 7, 3 krpm, with *C. reinhardtii* HydA1 adsorbed on PGE.

We tested on *C. reinhardtii* the effect of illumination with a halogen lamp. Figure S10 shows that both at -0.158 mV (top panel) and -0.508 mV potential (bottom panel), the current slightly increases when the illumination starts and then it stabilizes (same decay as in the dark, resulting from film loss). When the irradiation is switched off the current decreases and stabilizes. (This is the same observation as the SI of ref<sup>19</sup>).

#### 4 - Photoinhibition time constant values for *C. reinhardtii* and *C. acetobutylicum* FeFe hydrogenases

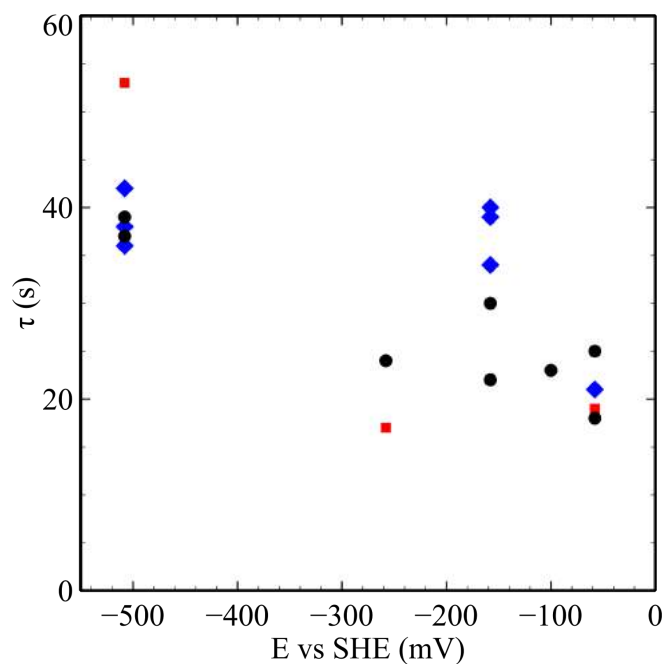


**Figure S13** - Photoinhibition values of  $\tau$  for *C. reinhardtii* (blue rhombus) and *C. acetobutylicum* (black circles) FeFe hydrogenases exposed to 100%  $H_2$  and *C. reinhardtii* in 10%  $H_2$  (red squares). Conditions:  $T= 30^\circ C$ , 3000 rpm, pH 6.8 phosphate buffer.



## 5 - *C. acetobutylicum* FeFe hydrogenases inactivation by xenon lamp with or without UV

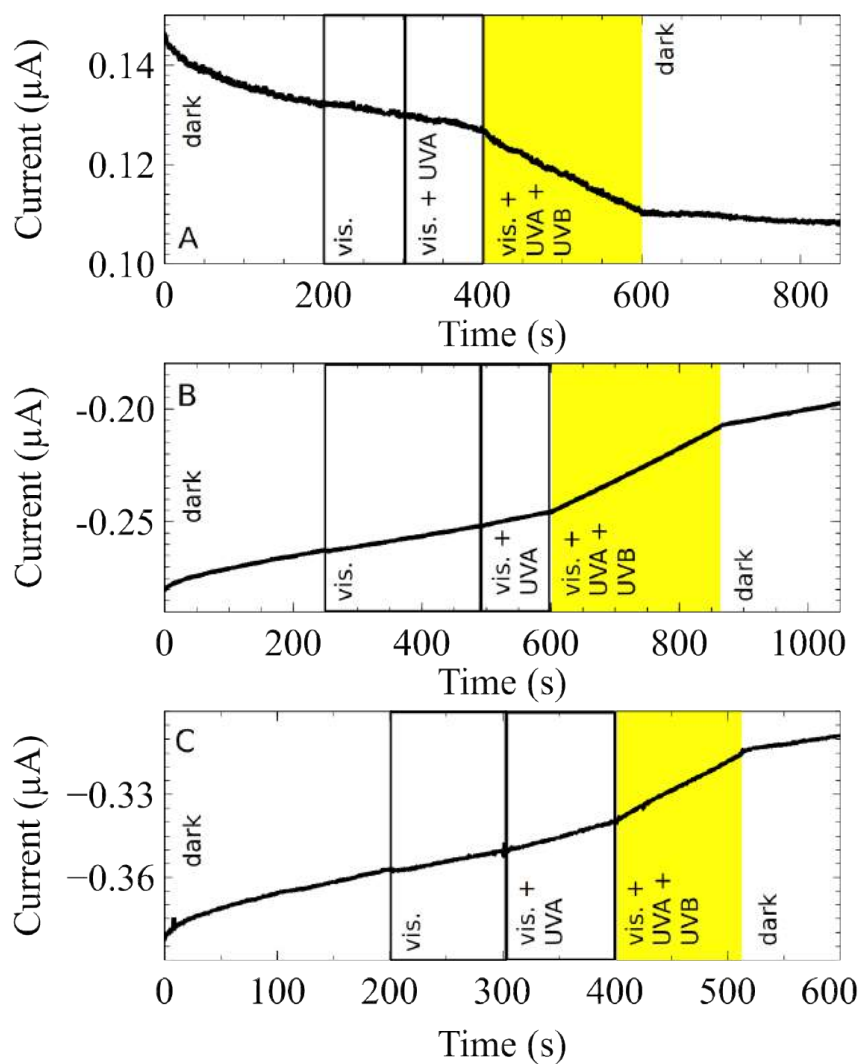


**Figure S14** - Effect of irradiation with a xenon lamp with/without filters. (A) FeFe hydrogenase from *C. acetobutylicum* at  $E = -0.158\text{ V}$  and (B)  $E = -0.508\text{ V}$  vs SHE. (C) FeFe hydrogenase from *C. reinhardtii*  $E = -0.508\text{ V}$  vs SHE. Conditions:  $T = 30^\circ\text{C}$ , 1 bar  $\text{H}_2$ , pH 6.8, 3 krpm.

## 6 - Photo-electrochemical cell

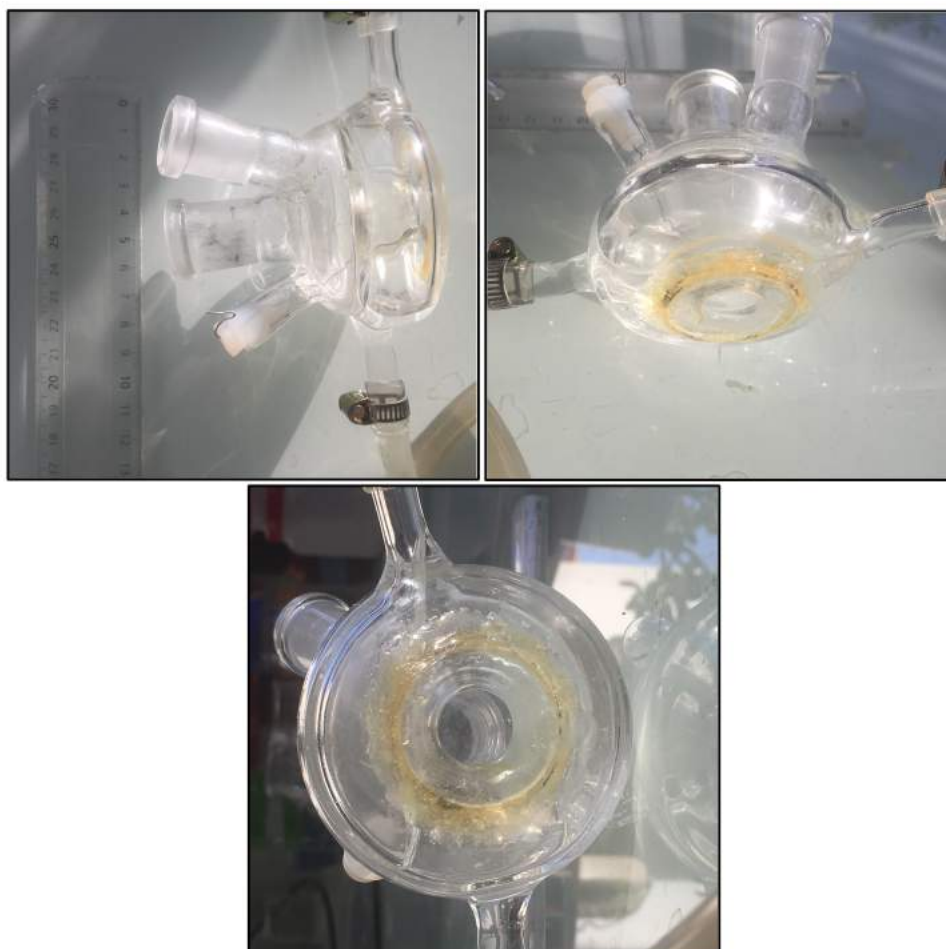


**Figure S15** - Photographs of the photo-electrochemical cell used for the experiments. At the bottom of the cell there is a quartz window. The photographs were taken by the authors.

## References

- (1) Nicolet, Y.; Piras, C.; Legrand, P.; Hatchikian, C. E.; Fontecilla-Camps, J. C. *Structure* **1999**, *7*, 13–23.
- (2) Cornish, A. J.; Gärtner, K.; Yang, H.; Peters, J. W.; Hegg, E. L. *J. Biol. Chem.* **2011**, *286*, 38341–38347.
- (3) Mulder, D. W.; Ratzloff, M. W.; Bruschi, M.; Greco, C.; Koonce, E.; Peters, J. W.; King, P. W. *J. Am. Chem. Soc.* **2014**, *136*, 15394–15402.

- (4) Esselborn, J.; Muraki, N.; Klein, K.; Engelbrecht, V.; Metzler-Nolte, N.; Apfel, U.-P.; Hofmann, E.; Kurisu, G.; Happe, T. *Chem. Sci.* **2016**, *7*, 959–968.
- (5) Adamo, C.; Scuseria, G. E.; Barone, V. *J. Chem. Phys.* **1999**, *111*, 2889–2899.
- (6) Ahlrichs, R.; Bär, M.; Häser, M.; Horn, H.; Kölmel, C. *Chem. Phys. Lett.* **1989**, *162*, 165–169.
- (7) Schäfer, A.; Huber, C.; Ahlrichs, R. *J. Chem. Phys.* **1994**, *100*, 5829–5835.
- (8) Becke, A. D. *Phys. Rev. A* **1988**, *38*, 3098–3100.
- (9) Perdew, J. P. *Phys. Rev. B: Condens. Matter Mater. Phys.* **1986**, *33*, 8822–8824.
- (10) Eichkorn, K.; Weigend, F.; Treutler, O.; Ahlrichs, R. *Theor. Chem. Acc.* **1997**, *97*, 119–124.
- (11) Siegbahn, P. E. M.; Tye, J. W.; Hall, M. B. *Chem. Rev.* **2007**, *107*, 4414–4435.
- (12) Bruschi, M.; Greco, C.; Fantucci, P.; De Gioia, L. *Inorg. Chem.* **2008**, *47*, 6056–6071.
- (13) Bertini, L.; Bruschi, M.; de Gioia, L.; Fantucci, P.; Greco, C.; Zampella, G. In *Atomistic Approaches in Modern Biology*; Topics in Current Chemistry; Springer Berlin Heidelberg, 2006; Vol. 268, pp 1–46.
- (14) Lee, C.; Yang, W.; Parr, R. G. *Phys. Rev. B: Condens. Matter Mater. Phys.* **1988**, *37*, 785–789.
- (15) Zhao, Y.; Truhlar, D. G. *Theor. Chem. Acc.* **2008**, *119*, 525–525.
- (16) Tao, J.; Perdew, J. P.; Staroverov, V. N.; Scuseria, G. E. *Phys. Rev. Lett.* **2003**, *91*, 146401.
- (17) Staroverov, V. N.; Scuseria, G. E.; Tao, J.; Perdew, J. P. *J. Chem. Phys.* **2003**, *119*, 12129–12137.
- (18) Weigend, F.; Ahlrichs, R. *Phys. Chem. Chem. Phys.* **2005**, *7*, 3297–3305.
- (19) Goldet, G.; Brandmayr, C.; Stripp, S. T.; Happe, T.; Cavazza, C.; Fontecilla-Camps, J. C.; Armstrong, F. A. J. *Am. Chem. Soc.* **2009**, *131*, 14979–14989.

## 5.5 Effect of $\text{Cl}^-$ on photoinhibition

We observed for the first time that at high potential the shape of CVs of CrHydA1 recorded in potassium phosphate buffer is different from that obtained in mixed buffer. We demonstrated that this difference is due to the presence of chloride anions in the buffer. The investigation of the effect of  $\text{Cl}^-$  is important because it has a role in the formation of inactive states at high potential. We decided to investigate also how this could affect the photoinhibition process. In the following subsections we shall qualitatively describe the effect of chloride on the CVs in the dark and under irradiation.

### 5.5.1 The effect of $\text{Cl}^-$ on the shape of the CV of CrHydA1

Performing PFV experiments with potassium phosphate buffer, we observed that in cyclic voltammograms of CrHydA1 there is no hysteresis at high potential, in contrast with the CV recorded in the same conditions but using a mixed buffer (MES, CHES, HEPES, TAPS, sodium acetate each 5 mM, 1 mM EDTA and 0.1 M NaCl). The team is still investigating this effect. We know that the hysteresis is present only when chloride is present in the buffer, whereas it is absent when we use buffers with other anions, like bromide. We are actually working on the hypothesis that the role of  $\text{Cl}^-$  is to influence the formation of the inactive species reversibly formed at high potential by interacting with charged residues. We also observed that in the crystals of the apo-form of CrHydA1 (3LX4, 4R0V) there are  $\text{Cl}^-$  anions near the active site. There is no experimental evidence that  $\text{Cl}^-$  can reach the  $[\text{2Fe}]_{\text{H}}$ , but if we consider this possibility we have also to take into account that chloride anions could interact directly with the active site at high potential. The only free binding site for chloride in the active site is  $\text{Fe}_{\text{D}}$ . We assume that the distal iron in the  $\text{H}_{\text{ox}}$  state is a  $\text{Fe}^{\text{I}}$  ion while the proximal iron is an  $\text{Fe}^{\text{II}}$  ion. The  $\text{H}_{\text{overox}}$  states formed reversibly at high potential proposed by Fourmond et al.<sup>96</sup> are characterized by  $\text{Fe}_{\text{D}}^{\text{II}}$  ion and by an hydride bound terminally to the distal iron or in bridging position between  $\text{Fe}_{\text{P}}$  and  $\text{Fe}_{\text{D}}$  (see subsection 1.8). Based on DFT calculations, the authors proposed that the first step of the formation of the hydride-bound over-oxidized species is the binding

of an hydrogen molecule in an unusual position on an isomerized form of  $\text{H}_{\text{ox}}$  (see fig. 1.13). This mechanism explains the  $\text{H}_2$  dependence of the rate of formation of the reversibly formed inactive species observed by PFV. We can hypothesize that  $\text{Cl}^-$  inactivates the enzyme by binding to the distal iron only when it is an  $\text{Fe}^{\text{II}}$  ion at high potential. The reduction to  $\text{H}_{\text{ox}}$  at lower potential would generate a  $\text{Fe}^{\text{I}}$  ion and cause the dissociation of the chloride anion, leaving free the binding site for  $\text{H}_2$ . This could explain the reversible character of the inactivation. In contrast, this hypothesis does not agree with the experimental evidence that the rate of formation of inactive species at high potential depends on hydrogen concentration. Both  $\text{Cl}^-$  binding and  $\text{Cl}^-$  interaction with residues hypothesis need further investigations by direct electrochemistry, DFT calculation and spectroscopy.

### 5.5.2 The effect of irradiation on the CV of CrHydA1 recorded in potassium phosphate or mixed buffer

Figure 5.1 shows three cycles of a CV of CrHydA1 in potassium phosphate buffer: the black line is the first cycle in the dark, the red line is the second cycle where the film was irradiated with a Xenon lamp and the dashed black line is the last cycle recorded in the dark. In these CVs the hysteresis commonly observed at high potential (see section 1.8) is absent. Light seems to have no effect on the CV, except an overall decrease of activity between the first cycle (black line) and the second cycle (exposed to light, red line).

Figure 5.2 shows four chronoamperograms of CrHydA1 in mixed buffer with NaCl (0.1 M) recorded at  $T = 10^\circ\text{C}$  and each with a different scan rate (2, 5, 10, 20 mV/s). In each experiment we recorded 3 cycles like in figure 5.1, the first cycle in the dark (black solid line), the second cycle under irradiation with a Xenon lamp (red line) and the last cycle in the dark (black dashed line). In all the CVs the black trace is characterized by an hysteresis at high potential, as expected. The red trace obtained from the enzyme under irradiation is characterized by an overall decrease in current and the shape of the signal in the high potential region changes. Indeed, the reactivation on the reverse scan (from high to low potential) shows a

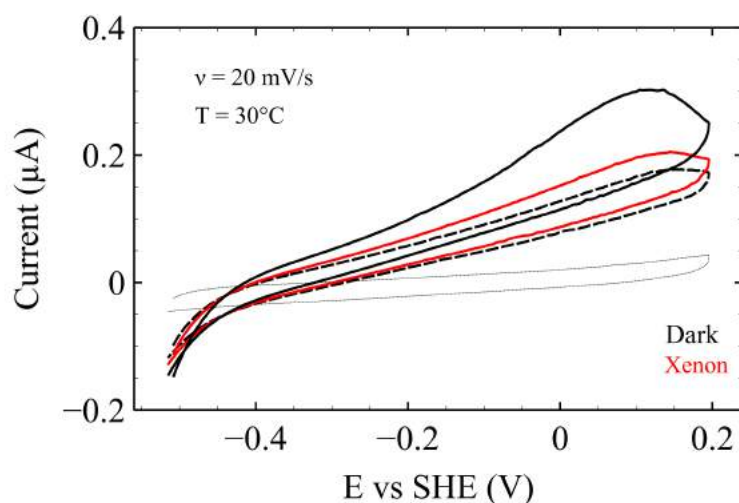


Figure 5.1: Cyclic voltammograms of CrHydA1 exposed to Xenon light in potassium phosphate buffer at  $30^\circ\text{C}$ . The black solid line is the first cycle without irradiation; the red line is the second cycle under irradiation of a Xenon lamp and the black dashed line is the third cycle without irradiation. The dotted line represent the background current recorded without the enzyme. Conditions: potassium phosphate buffer pH = 6.8,  $\nu = 20 \text{ mV/s}$ ,  $\omega = 3000 \text{ rpm}$ , 1 bar  $\text{H}_2$ ,  $T = 30^\circ\text{C}$ .

local minimum of current between -0.2 and 0 mV vs SHE. As shown in the CVs in fig. 5.2, the local minimum is absent in the subsequent cycle in the dark (dashed black). The lower the scan rate, the more apparent this feature.

As reviewed in subsection 1.8, Fourmond et al.<sup>96</sup> proposed that the hysteresis at high potential is determined by the formation of three inactive species, two reversibly formed and one irreversibly formed. The irradiation seems to affect the kinetics of reactivation of the inactive species but as yet we cannot propose a mechanism for this process.

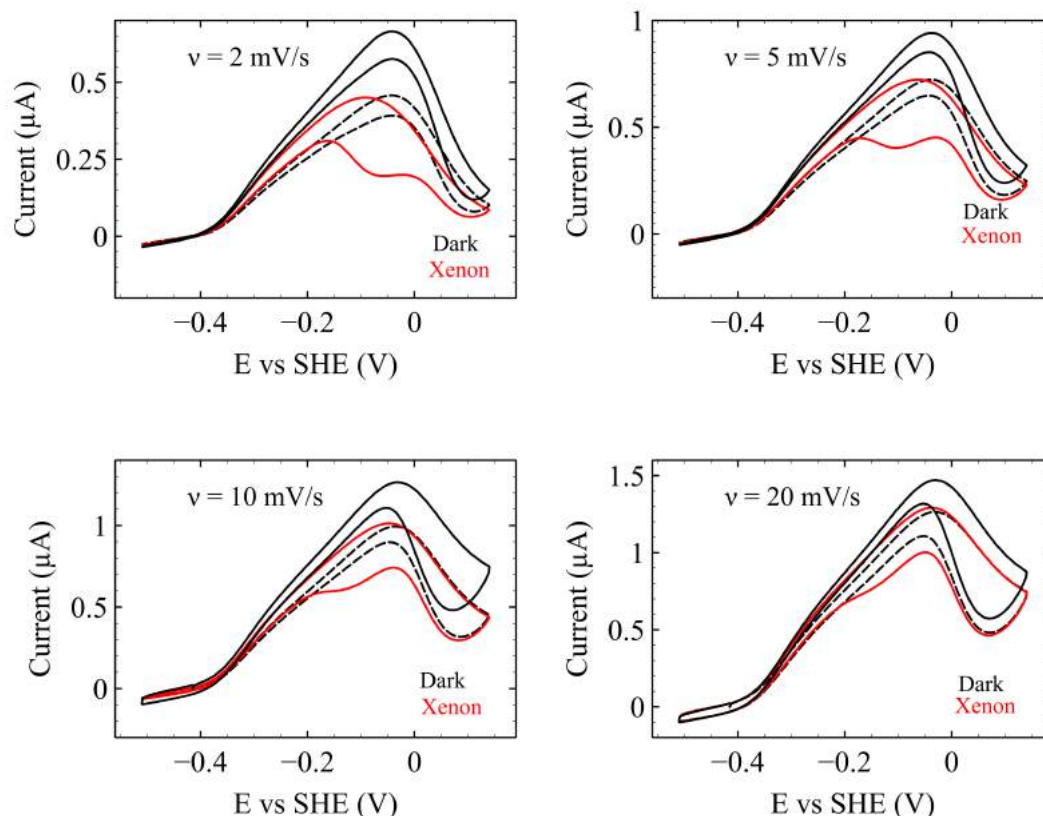


Figure 5.2: Change in the shape of cyclic voltammograms of CrHydA1 exposed to Xenon light in mixed buffer at  $10^\circ\text{C}$ . The black solid line is the first cycle in the dark; the red line is the second cycle under irradiation of a Xenon lamp and the black dashed line is the third cycle in the dark. Conditions: mixed buffer  $\text{pH} = 7$ ,  $\nu = 2, 5, 10, 20$  mV/s,  $\omega = 3000$  rpm, 1 bar  $\text{H}_2$ ,  $T = 10^\circ\text{C}$ .

### 5.5.3 Is UV light responsible of the characteristic shape of the CVs under of irradiation?

Since we know that the UV-B component of the Xenon lamp is responsible for the photoinhibition observed in phosphate buffer (as shown previously in this chapter), we verified if the effect observed on the CVs is caused by a specific wavelength. The left part of figure 5.3 shows in red a CV recorded under irradiation of a Xenon lamp in the presence of a glass that filters all the UV light. The UV-filtered light of the Xenon lamp has no effect on the CV, which has exactly the same shape as that observed without irradiation in black. The right part of figure 5.3 shows in

blue a CV recorded under irradiation of a Halogen lamp, which has almost no UV component. The irradiation by Halogen lamp has no effect on the shape of the CV, which is the same as that recorded in the dark (in black). These observations confirm that the UV component of the Xenon lamp is responsible for the appearance of the new local minimum in the reverse scan of the CVs in mixed buffer.

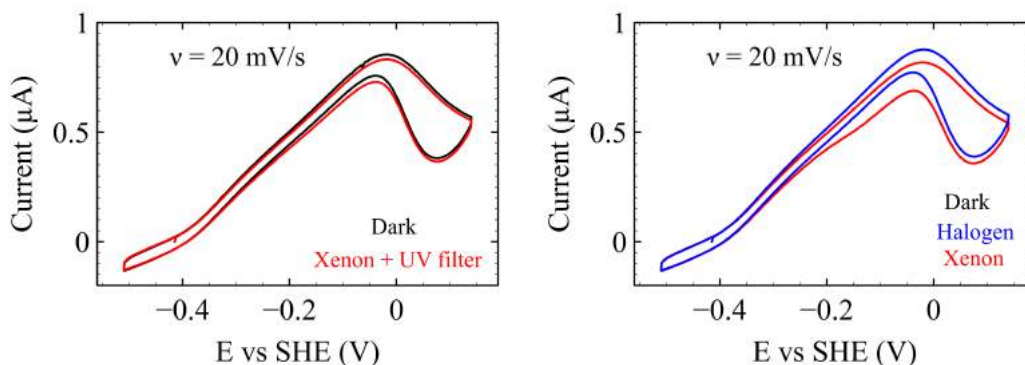


Figure 5.3: Experimental evidence that UV induces the change of the CV shape. On the left, the black solid line is a CV in the dark, the red line is a CV recorded under irradiation by a Xenon lamp in presence of a UV-filter. On the right, the black solid line is a CV recorded in the dark, the red line is a CV recorded under irradiation of a Xenon lamp and the blue line is a CV recorded under irradiation of a Halogen lamp. Conditions: enzyme = CrHydA1, mixed buffer pH = 7,  $\nu = 20$  mV/s,  $\omega = 3000$  rpm, 1 bar  $H_2$ ,  $T = 10^\circ C$ .

#### 5.5.4 Effect of temperature and scan rate on the CV shape in mixed buffer

We tested the effect of changing temperature and scan rate on the shape of CVs recorded with CrHydA1 with or without exposure to the light of a Xenon lamp. As observed before in figure 5.2, in presence of light the CVs (on the right in fig. 5.4) present a new local minimum in the reverse scan (from high to low potential), which is more prominent at lower scan rates.

We repeated the same experiment, with and without irradiation, but setting the temperature of the solution in the electrochemical cell to 1.5, 30 and 40°C (Fig. 5.5). In the CVs in figure 5.5 we observed that:



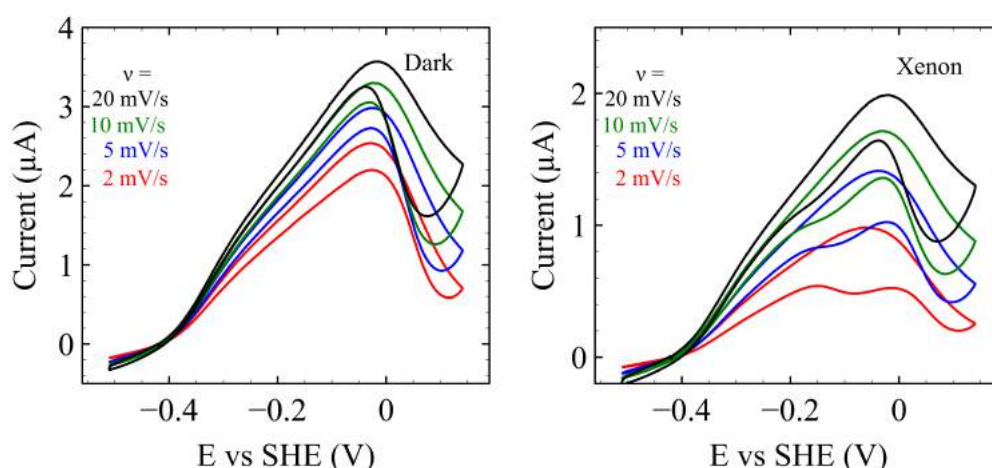


Figure 5.4: Evidence that the new feature in CVs is dependent on scan rate. On the left are shown four CVs recorded with scan rates 2, 5, 10 and 20 mV/s. On the right the same CVs are recorded but under irradiation of a Xenon lamp. Conditions: enzyme = CrHydA1, mixed buffer pH = 7,  $\omega = 3000$  rpm, 1 bar  $\text{H}_2$ ,  $T = 10^\circ\text{C}$ .

- in the dark, the local minimum in the reverse scan appears only at high temperatures ( $30^\circ\text{C}$  or  $40^\circ\text{C}$ ) when the CV is recorded at low scan rates (5 mV/s and 2 mV/s);
- in the dark, the new minimum is localized in the same range of potentials (-0.2 to 0 mV vs SHE) where we observed it upon irradiation;
- under irradiation, the local minimum is more prominent than in the dark;
- under irradiation, the local minimum becomes prominent when we increase the temperature and/or decrease the scan rate
- under irradiation, the local minimum is absent only in CVs recorded at  $1.5^\circ\text{C}$  with scan rates higher than 10 mV/s.

We fitted the same kinetic model as that employed in ref. 96 to the data in figures 5.4 and 5.5. The kinetic model takes into account the formation of three inactive species at high potential, one irreversibly formed and two reversibly formed (1H and 2H in fig. 1.13).

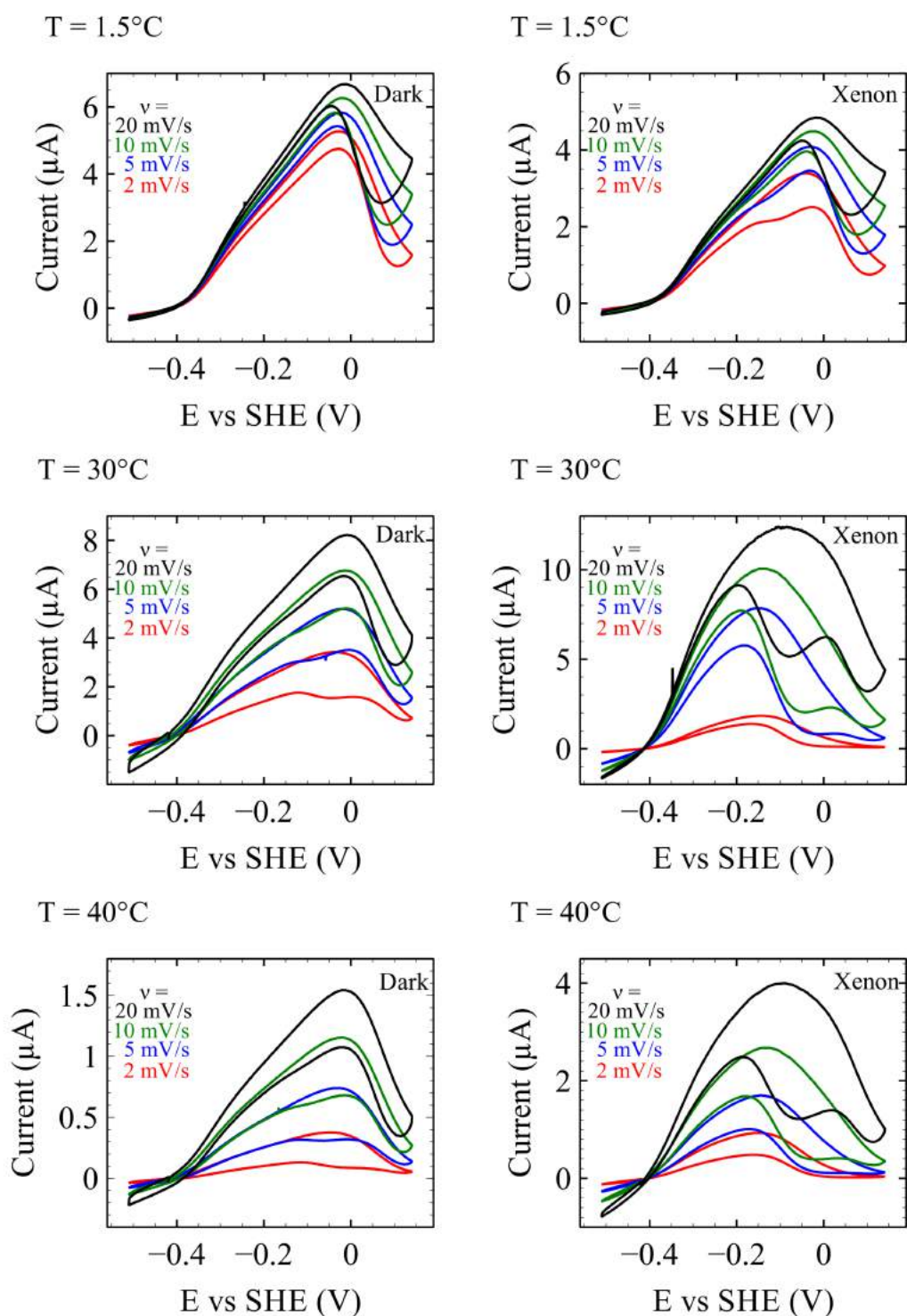


Figure 5.5: Evidence that the new feature in CVs is dependent on scan rate, temperature and is present also in the dark. Cyclic voltammograms of CrHydA1 recorded at 1.5, 30 and 40°C. At each temperature, on the left are shown four CVs recorded with scan rates 2, 5, 10 and 20 mV/s. On the right the same CVs as those on the left have been recorded but under irradiation of a Xenon lamp. Conditions: mixed buffer pH = 7,  $\omega$  = 3000 rpm, 1 bar H<sub>2</sub>.

Figure 5.6 shows an example of the curves obtained from the fitting. Under irradiation the values obtained from the fitting procedure indicate a decrease of the two rate constants involved in the reactivation of one of the two reversibly formed over-oxidized states reported in the scheme in fig. 5.7 ( $k_a^{direct}$  and instead of the  $k_a^{redox}$ , we calculated the  $k_a^0$ , which is the rate constant of reactivation at 0 V). This decrease is more pronounced at lower temperatures. These results suggest that in presence of light one of the two reversibly formed inactive species reactivates more slowly than in the dark. This interpretation is counter-intuitive because we expect that light increases the rate of reactions.

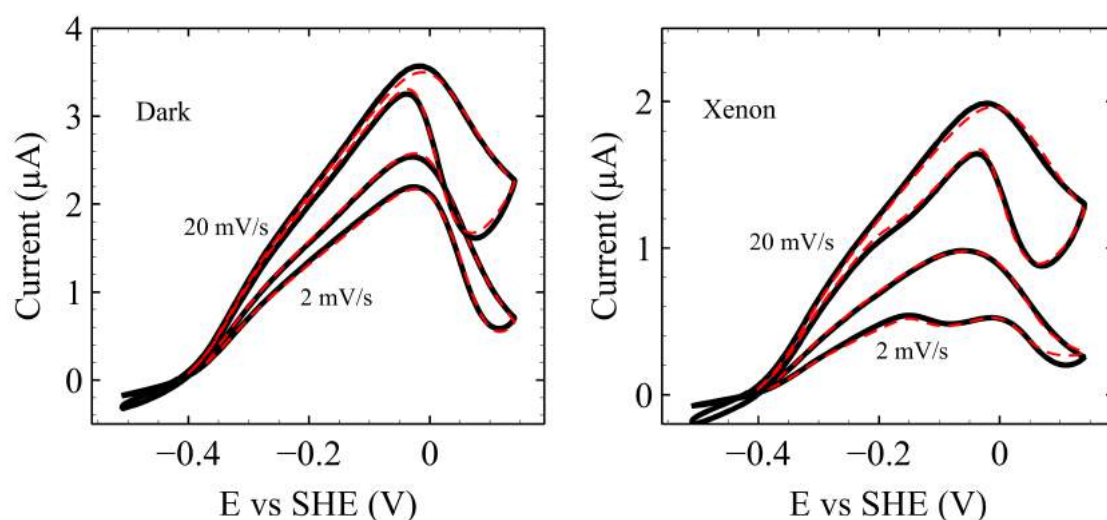


Figure 5.6: Result of the fitting of the kinetic model to CVs recorded in the dark or under irradiation with a Xenon lamp. The black curves are the experimental data. The dashed red lines have been obtained from the fitting procedure. The scan rates are reported near the corresponding curve. Conditions: enzyme = CrHydA1, mixed buffer pH = 7,  $\omega = 3000$  rpm, 1 bar  $\text{H}_2$ ,  $T = 10^\circ\text{C}$ .

The results of the fit are obviously model-dependent and we used a model where only three inactive species are included, while new species could be formed upon irradiation. We conclude that we need more data and that the model cannot represent the data because probably it takes into account less species than that involved in the process.

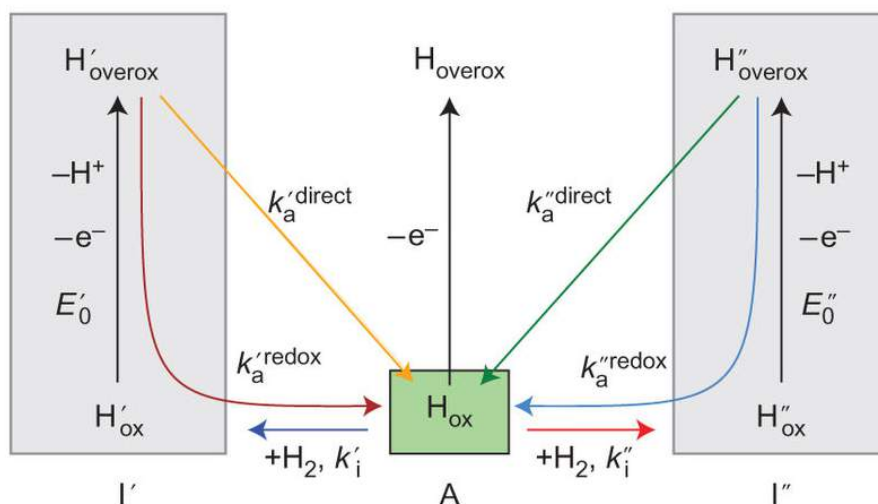


Figure 5.7: Scheme of the kinetic model for the anaerobic oxidative inactivation fitted to the data. Figure from ref 96

### 5.5.5 Chronoamperograms recorded in mixed buffer

We recorded chronoamperograms of CrHydA1 in mixed buffer, in presence of irradiation of a Xenon lamp and using UV filters, as done previously in this chapter in potassium phosphate buffer. As shown in figure 5.8, UVB light induces the photoinhibition, as observed in potassium phosphate buffer, both a high and at low potential. At  $E = -158$  mV vs SHE when light is turned off we can observe a small increase in current. This reactivation is present only at high potential, in agreement with the existence of reversibly formed inactive species observed in the CVs. This explains also why in mixed buffer the reactivation and the photoinhibition look dependent on potential, in contrast with the experiments performed in potassium phosphate buffer. Indeed, in mixed buffer with chloride the decrease in current observed upon irradiation of Xenon lamp at high potential is due to the irreversible photoinhibition but also to the reversible formation of an inactive species that reactivates when light is switched off.

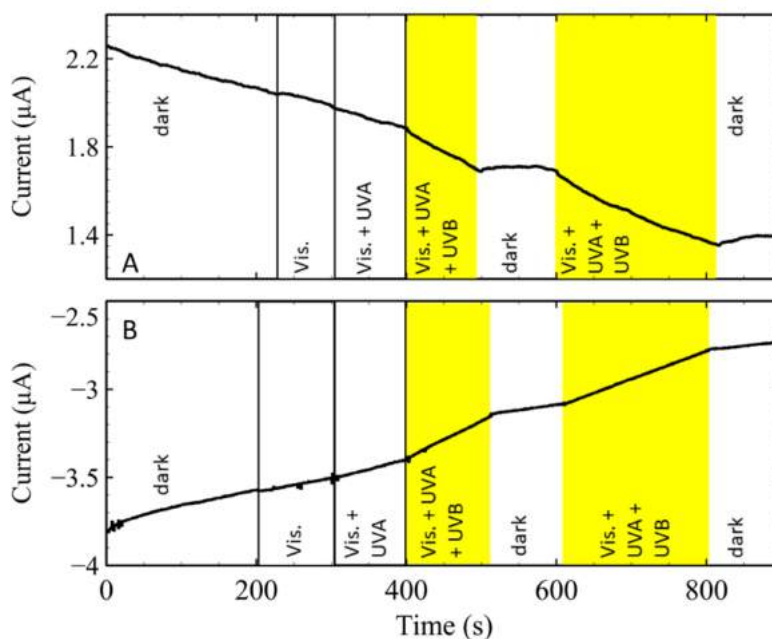


Figure 5.8: The photoinhibition is induced by UVB and at high potential we can observe a reactivation upon removal of the irradiation. Chronoamperograms of CrHydA1 in mixed buffer with chloride in presence of irradiation of a Xenon lamp with or without glass filters at A)  $E = -0.158$  mV and B)  $E = -508$  mV. Conditions: mixed buffer with NaCl  $\text{pH} = 7$ ,  $\omega = 3000$  rpm, 1 bar  $\text{H}_2$ ,  $T = 30^\circ\text{C}$ .

### 5.5.6 Discussion

The preliminary results about the effect of light on the activity of FeFe-hydrogenase from *C. reinhardtii* show the appearance of a new local minimum at  $\text{H}_2$  oxidation potential in the reverse scan of CVs recorded with a mixed buffer with chloride. This local minimum becomes more prominent by increasing the temperature and decreasing the scan rate. We suggest that light induces the formation of new species at high potential or a change in the kinetics of reactivation of the known inactive species. We observed that a new local minimum appears also in the reverse scan of CVs recorded in the dark at high temperatures when we used scan rates lower than 10 mV/s. At the present time we cannot say if the feature observed upon irradiation arises from the same process as that observed at high temperatures in the dark. Furthermore the unclear role of chloride in the dark complicates also the interpretation of the data obtained under irradiation. For this reason we used a potassium phosphate buffer to study the photoinhibition in the previous article. In

## CHAPTER 5. EFFECT OF LIGHT ON THE ACTIVE FORMS OF FEFE HYDROGENASES

---

conclusion, from the preliminary data we can suggest that the effect of light on CVs in presence of chloride is due to the UV component and it affects species formed at high potential.

## Chapter 6

### Effect of light on other metalloenzymes

## 6.1 Summary

We performed preliminary direct photo-electrochemistry experiments with *Df* NiFe-hydrogenase and *Dv* CODH.

NiFe-hydrogenases catalyze the evolution and oxidation of H<sub>2</sub>. The oxidation of O<sub>2</sub>-tolerant NiFe-hydrogenase forms the inactive Ni-B state, which is reactivated upon irradiation and reduction. Upon oxidation O<sub>2</sub>-sensitive NiFe-hydrogenases form two inactive states called Ni-A and Ni-B,<sup>140</sup> which are reactivated upon reduction. We demonstrated for the first time that irradiation by violet or white light reactivates the O<sub>2</sub>-sensitive NiFe-hydrogenase from *D. fructosovorans*. The photo-reactivation is absent when the enzyme is previously activated by reduction at low potential. Further information could be obtained by performing direct photo-electrochemistry experiments on the photo-reactivation as a function of the power of light and DFT calculations on the photo-sensitivity of Ni-A and Ni-B.

CO-dehydrogenases are enzymes that reversibly catalyze the reduction of CO<sub>2</sub> and protons to CO and water. Many structural and catalytic properties of these enzymes are still unknown. CODHs are partially inactivated by exposure to oxygen and some of them, like *Dv*CODH, are more resistant than those from other microorganisms.<sup>141</sup> We showed that the irradiation by a Xenon lamp increases the reactivation of the inactive states formed upon exposure to oxygen. We also observed that the reactivation is faster when the enzyme has not been previously reduced at low potential. These preliminary results pave the way for the investigation of the photo-sensitivity of CODH by direct photo-electrochemistry and also suggest the need for DFT and MD studies of the aerobic inactivation of CODHs.



## 6.2 Résumé

Nous avons réalisé des expériences préliminaires de photo-électrochimie directe avec *Df*NiFe-hydrogenase et *Dv* CODH.

Les hydrogenases NiFe catalysent l'évolution et l'oxydation de H<sub>2</sub>. Leur site actif se compose d'un ion Ni coordonné par deux thiolates de cystéines et un ion Fe qui lie deux CN<sup>-</sup> et un CO, les deux métaux sont reliés par deux thiolates de cystéines. L'oxydation des hydrogenases NiFe O<sub>2</sub>-tolérante forme l'état inactif Ni-B, qui est réactivé par irradiation et par réduction. Lors de l'oxydation, l'hydrogénase-NiFe O<sub>2</sub>-sensitive forme deux états inactifs appelés Ni-A et Ni-B,<sup>140</sup> qui sont réactivés par réduction. Nous avons démontré, pour la première fois, que l'irradiation par la lumière violette ou blanche réactive la hydrogénase NiFe O<sub>2</sub>-sensible de *D. Fructosovorans*. La photo-réactivation est absente si l'enzyme est précédemment réactivée par réduction à bas potentiel. D'autres informations pourraient être obtenues en effectuant des expériences de photo-électrochimie directe sur la photo-réactivation en fonction de la puissance de la lumière et des calculs DFT sur la photo-sensibilité des Ni-A et Ni-B.

Les CO-déshydrogénases sont des enzymes qui catalysent de manière réversible la réduction du CO<sub>2</sub> et des protons aux CO et eau. De nombreuses propriétés structurales et catalytiques de ces enzymes sont encore inconnues. Les CODH sont partiellement inactivés par l'exposition à l'oxygène et certains, comme la *Dv* CODH, sont plus résistantes que celles d'autres microorganismes.<sup>141</sup> Nous avons montré que l'irradiation par une lampe au xénon augmente la réactivation des états inactifs formés lors de l'exposition à l'oxygène. Nous avons également observé que la vitesse de réactivation est plus rapide lorsque l'enzyme n'a pas été précédemment réduite à bas potentiel. Ces résultats préliminaires ouvrent la voie à la recherche de la photo-sensibilité de CODH par photo-électrochimie directe et suggèrent également la nécessité d'études par DFT et MD sur l'inactivation aérobie des CODH.

## 6.3 NiFe hydrogenases photo-activation

In this section we will show and discuss my preliminary results about the effect of light on NiFe-hydrogenases obtained with direct photo-electrochemistry. In particular, we shall demonstrate that an inactive oxidized state of the enzyme is reactivated by irradiation with light at specific wavelengths.

### 6.3.1 Introduction

NiFe-hydrogenases are enzymes widespread in bacteria and archaea, where they are localized in the cytosol, in the periplasm or bound to the membrane. NiFe-hydrogenase can perform  $H_2$  uptake,  $H_2$  evolution or both reactions. The active site consists of a dinuclear Ni-Fe site, where the Fe is coordinated by one CO, two  $CN^-$  and two thiolates of cysteine residues that bridge the two metals. The nickel atom is coordinated also by two further thiolates of cysteine residues. The Fe ion is generally considered in the 2+ oxidation state and redox inactive through the cycle, while the oxidation state of Ni ion changes.<sup>142</sup> There are  $O_2$ -tolerant and  $O_2$ -sensitive NiFe-hydrogenases. As shown in figure 6.1, more forms of the active site of the oxygen-sensitive NiFe-hydrogenases than of the  $O_2$ -tolerant enzymes have been characterized by spectroscopy. we will focus on the reactivation of the oxidized species of  $O_2$  sensitive NiFe-hydrogenases by light. The aerobic or anaerobic oxidation of the  $O_2$ -sensitive NiFe-hydrogenases leads to the formation of two inactive species called Ni-A and Ni-B. The enzyme can be reactivated by chemical<sup>143</sup> or electrochemical reduction.<sup>144</sup> The kinetics of reactivation for Ni-B is faster than that of Ni-A. In  $O_2$ -tolerant NiFe-hydrogenases only Ni-B is formed upon aerobic and anaerobic oxidation. There is a general agreement that Ni-B presents an hydroxide in bridging position between  $Ni^{III}$  and  $Fe^{II}$ . The nature of Ni-A is still matter of debate but recently crystallography<sup>145</sup> and DFT calculations<sup>146</sup> converged on the definition of this state as a  $Ni^{III}$ ,  $Fe^{II}$  with a bridging hydroxide ligand and an oxidized sulfur atom of a bridging cysteine.

In 2013 Ciaccava et al.<sup>147</sup> showed, using direct electrochemistry, that the  $O_2$ -tolerant NiFe-hydrogenase from *Aquifex aeolicus* (MbH1) is activated by irradiation

### 6.3. NIFE HYDROGENASES PHOTO-ACTIVATION

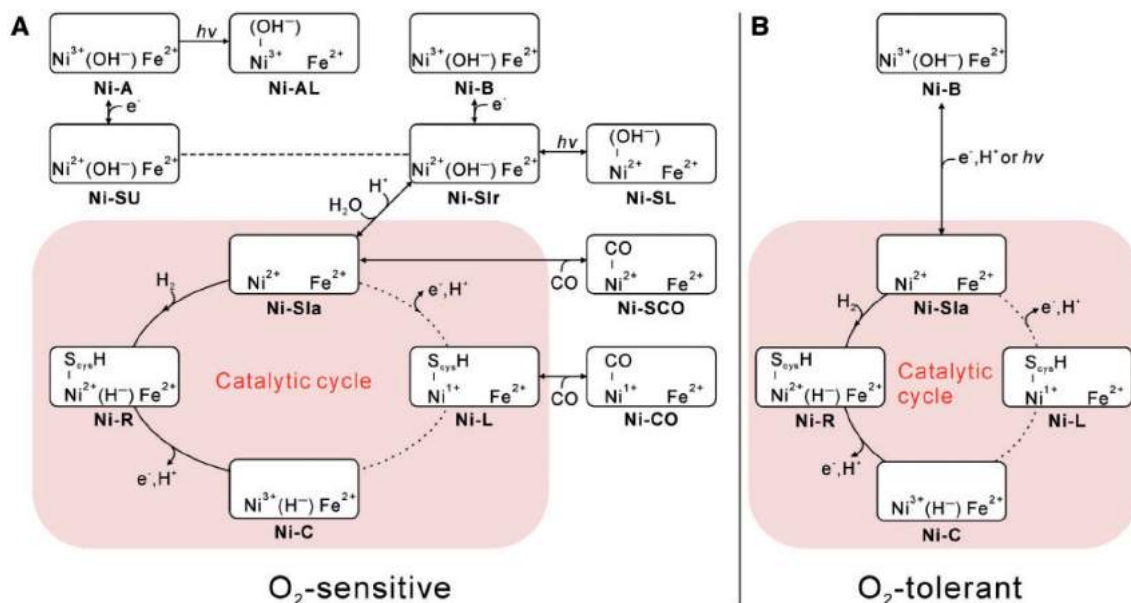


Figure 6.1: Summary of the states of the active site of  $\text{O}_2$ -sensitive and  $\text{O}_2$ -tolerant NiFe-hydrogenases. Figure from ref. 142.

with a 405 nm light, in a potential-dependent process (see figure 6.2). Ciaccafava et al.<sup>147</sup> proposed that irradiation of the  $\text{O}_2$ -tolerant NiFe-hydrogenases in the Ni-B state induces the movement of the hydroxide on the  $\text{Ni}^{\text{III}}$  atom, which is reduced to  $\text{Ni}^{\text{II}}$ . Then the hydroxide is released as water and the Ni-SI<sub>a</sub> active state is formed. The study of the inactive states of NiFe-hydrogenases, and their photo-reactivation, could be helpful to better understand the differences between the  $\text{O}_2$ -sensitive and  $\text{O}_2$ -tolerant enzymes.

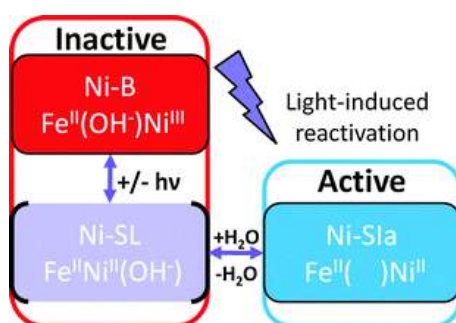


Figure 6.2: Proposed mechanism of the photo-reactivation of the oxygen tolerant NiFe-hydrogenase from *A. aeolicus*. Figure from ref. 147.



reaches a plateau, the reactivation stops and a second irradiation does not produce a further reactivation. This suggests that all the enzymes of the film have been fully reactivated or that the irradiation with this power and wavelength reactivates only a specific amount or state of the enzyme. This also demonstrates that the increase of current is not due to heating. We can notice in the violet trace that when light is switched off, the film seems less stable than the film in the dark before the first irradiation. Starting from the data available for the O<sub>2</sub>-tolerant NiFe-hydrogenases,<sup>147</sup> we can speculate that the effect of light is to reactivate the inactive states, Ni-A and/or Ni-B, since the effect of light is absent when the irradiation is preceded by a reductive step. Indeed, when we reduce the film at low potential (-508 mV) to reactivate the enzyme before recording the chronoamperogram, no photo-induced reactivation is present. We tested also the reactivation induced by a Xenon lamp

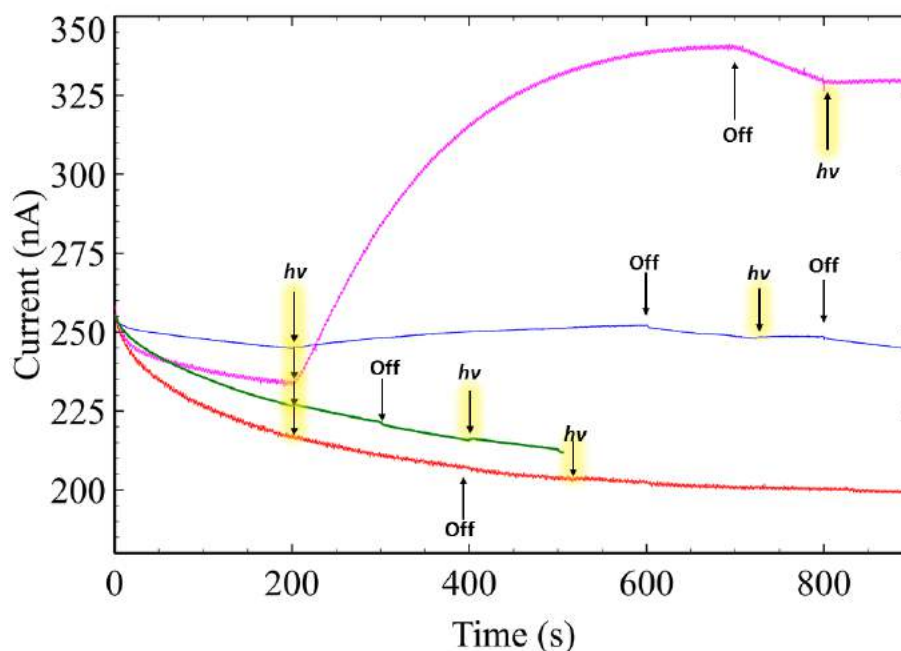


Figure 6.4: Reactivation of *Df* NiFe-hydrogenases exposed to laser at 405 (violet line, current  $\times 2$ ), 450 (blue line, current  $\times 1.2$ ), 532 (green line) and 635 nm (red line, current  $\times 1.05$ ). The arrow evidenced in yellow indicate the instant of the beginning of illumination, while the black arrows indicate the time at which light was turned off. Conditions: T= 40 °C, Mixed buffer (with NaCl) pH=5.5, 1 bar H<sub>2</sub>, E = -158 mV vs SHE, 3 krpm.

with UV-vis components and we observed a faster photo-reactivation compared to

the monochromatic lasers, with a time constant around 86 s (fig. 6.5). For both photo-reactivations induced by laser and Xenon lamp the plateau is reached more slowly than for the O<sub>2</sub>-tolerant *Ae* NiFe-hydrogenases.<sup>147</sup> Ciaccafava et al. observed that the plateau was reached in 30 s when the potential is lower than -101 mV vs SHE, while in my experiments at -158 mV vs SHE we need hundreds of seconds. This difference could be related to the use of different temperatures (40°C vs 60°C), light sources (LED vs laser/Xenon lamp) or could be an intrinsic property of the enzyme.

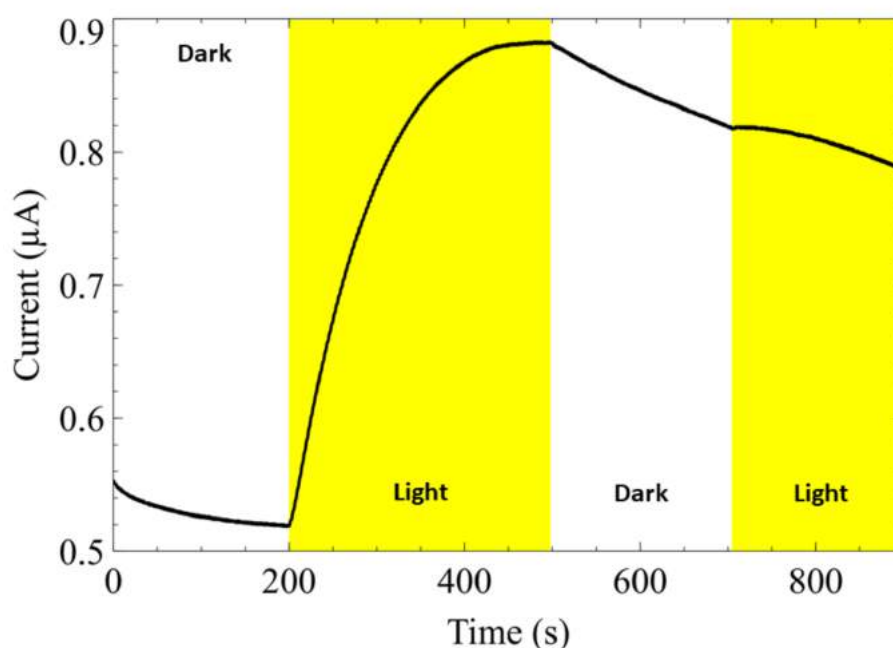


Figure 6.5: Reactivation of *Df* NiFe-hydrogenase by irradiation with a Xenon light. The yellow background indicates that the film was illuminated. Conditions: T= 40 °C, Mixed buffer (with NaCl) pH=5.5, 1 bar H<sub>2</sub>, E = -158 mV vs SHE, 3 krpm.

### 6.3.3 Discussion

We showed for the first time that O<sub>2</sub>-sensitive NiFe-hydrogenases in oxidized inactive state are reactivated by light, like O<sub>2</sub>-tolerant NiFe-hydrogenases.<sup>147</sup> We observed that the enzyme reactivates when it is irradiated by violet/blue light and by the UV-visible light of a Xenon lamp. Irradiation by light at longer wavelengths has no effect. In O<sub>2</sub>-sensitive NiFe-hydrogenases oxidation generates two inactive state

Ni-A and Ni-B and they could be both affected by irradiation. The reactivation of Ni-B could follow the same mechanism as that proposed in figure 6.2 for O<sub>2</sub>-tolerant FeFe-hydrogenases, whereas we do not know if Ni-A can be also photo-reactivated. The results showed above could be combined with the characterization of the the excited states of Ni-A by TDDFT to give mechanistic information about the feasibility of its photo-reactivation. A combination of direct electrochemistry and EPR experiments, as done in ref.,<sup>140</sup> could also be used to study the photo-reactivation of Ni-A and/or Ni-B state under aerobic and anaerobic conditions, to investigate a possible contribution of O<sub>2</sub> in the inactivation and photo-reactivation of the enzyme. This could help to clarify the differences between O<sub>2</sub>-tolerant and O<sub>2</sub>-sensitive NiFe-hydrogenases.

## 6.4 Effect of light on Ni-CODH

In this section we present preliminary data about the effect of light on the enzyme carbon monoxide dehydrogenases (CODH). Few mechanistic and kinetic data are available for this enzyme. The response of CODH to the irradiation by light could give hints to better understand their active site geometry, electronic structure and catalytic properties, as showed for NiFe and FeFe-hydrogenases in the literature and in this thesis. We studied the consequences of irradiation by a Xenon lamp on the active form of the enzyme and also on the CODH inhibited by oxygen. The study that we shall present has never been performed before and it is an important first step to obtain information about the reactivity and the possible forms of the active site of this enzyme, in active and inhibited states.

### 6.4.1 Introduction

Carbon monoxide dehydrogenases (CODH) are enzymes found in anaerobic and aerobic bacteria and archaea that grow using CO as source of carbon and energy.<sup>151,152</sup> CODH catalyze reversibly the oxidation of CO to CO<sub>2</sub> according to the following reaction:



Two types of CODHs have been identified: Ni-CODHs, which harbors a Ni and Fe containing active site and are found in anaerobic microorganisms, and Mo-CODHs, which embed a Mo and Cu containing active site and are found in aerobic bacteria. We shall describe the effect of light on Ni-CODH. This enzyme is a homodimer that harbors two [4Fe4S] clusters (B-clusters), a further FeS cluster, [4Fe4S] or [2Fe2S], at the interface between the two monomers (D-cluster) and an unusual [4Fe4S] cluster that contain also a nickel atom (C-cluster). The C-cluster, shown in figure 6.6, is the active site of the enzyme and is characterized by a structure resembling a [4Fe4S] cluster where one iron atom is replaced by a nickel and the fourth iron atom (called unique iron, Fe<sub>u</sub>) is displaced. Some Ni-CODH form a complex with acetyl-



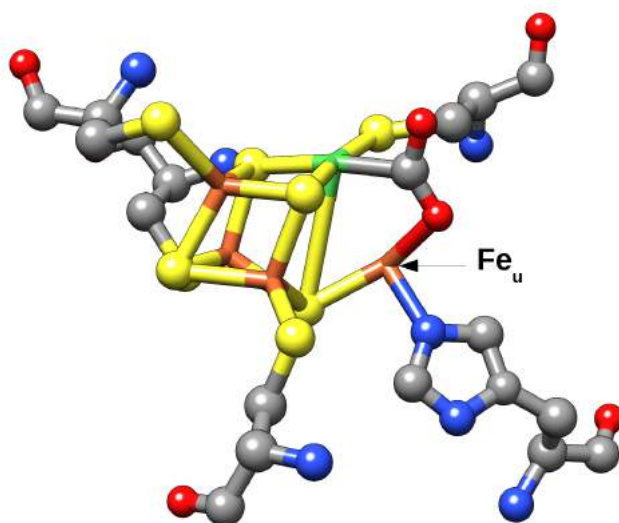


Figure 6.6: C-cluster of CODH from the bacterium *Carboxydotherrmus hydrogenoformans* (PDB code: 3B52).Color code: gray C, red O, blue N, brown Fe, green Ni, yellow S.

CoA synthase (ACS), coupling  $\text{CO}_2$  reduction by CODH to Acetyl-CoA synthesis by ACS. Three states of the C-cluster have been characterized with spectroscopic methods:<sup>153,154</sup>  $\text{C}_{\text{red1}}$  is an active, reduced state that can be reduced by two electrons to form  $\text{C}_{\text{red2}}$ , or oxidized to the inactive state  $\text{C}_{\text{ox}}$ . The oxidized inactive form of the enzyme can be reactivated by reduction.<sup>141,155</sup> In direct electrochemistry, this can be achieved by performing a low potential step (-560 mV vs SHE) before the injection of the substrate CO. CO-dehydrogenase are sensitive to  $\text{O}_2$  but some of them, like the CODH from *Desulfovibrio vulgaris*, are resistant and can be reductively fully reactivated.<sup>141</sup>

## 6.4.2 Results

Meriem Merrouch and we performed direct photoelectrochemistry experiments to observe the effects of the irradiation of *Dv*CODH under catalytic conditions and after exposure to oxygen. In panel A of figure 6.7 a *Dv*CODH film activated at low potential (-560 mV vs SHE), is exposed to the substrate CO (at  $t = 140$  s), at -360 mV vs SHE. This induces an increase of current due to the oxidation of CO. At  $t = 160$  s the film is exposed to the direct irradiation of a Xenon lamp. Light has no detectable effects. To test the aerobic inactivation, we performed an experiment

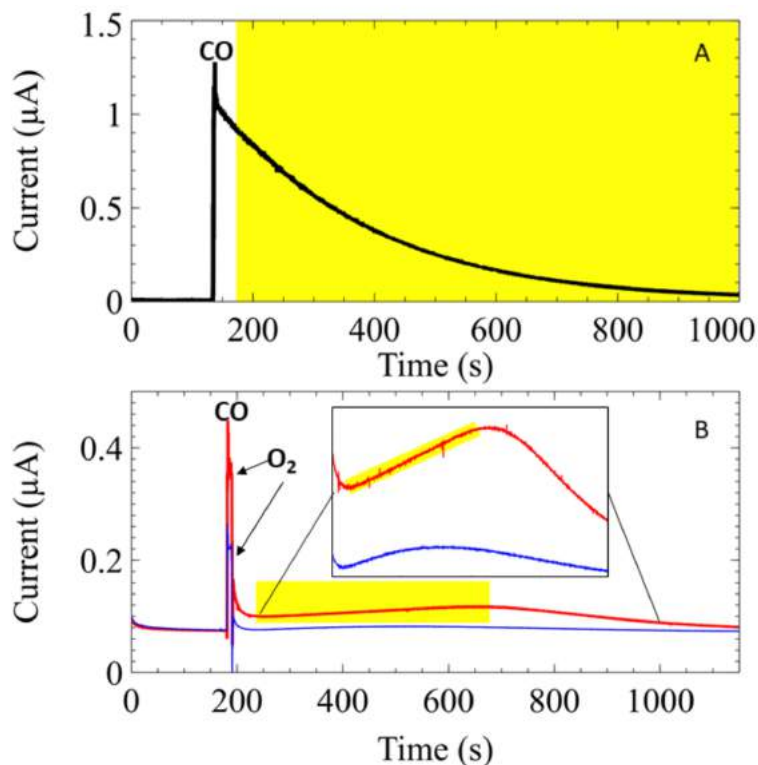


Figure 6.7: Experimental evidence that irradiation with a Xe lamp accelerates the reactivation of *Dv*CODH exposed to O<sub>2</sub>. A) The film was exposed to Xenon light from  $t = 160$  s. B) After the injection of CO, at 195 s O<sub>2</sub> (0.25 μM concentration in the cell, indicated by arrows) was injected. The red trace represents an experiment where the film was irradiated by Xenon light (yellow rectangle) after the inhibition by O<sub>2</sub>. The blue trace is the same experiment as that described before but recorded in the dark. In all the experiments we performed an initial reductive step at -506 mV vs SHE to fully reactivate the enzyme. Conditions: T = 25°C, pH = 7, E = -360 mV vs SHE, 3000 krpm, [CO] = 50 μM.

where 10 s after the injection of CO (50 μM concentration in the cell), we injected an oxygen saturated solution in the cell (to reach 0.25 μM concentration in the cell at the time of injection). After the drop of current due to the inhibition by oxygen, there is a small reactivation, as shown by the blue trace in panel B of figure 6.7. In panel B is also shown, in red, the same experiment as that described above but in this case the enzyme film was exposed to irradiation with a Xenon lamp 20 seconds after the injection of O<sub>2</sub>. We can see that during the illumination more current is recovered than in the experiment in the dark. But this recovery is transient because current decreases after the end of the illumination.

In panel C and D of figure 6.8 we show the results of the same experiments as

that shown in panel A and B of figure 6.7 but performed without the reactivating reductive step. The irradiation by a Xenon lamp, in panel C, induces a small increase of current, which is absent in the experiments where the film is previously reactivated at low potential. In panel D the reactivation after inhibition by oxygen is faster in presence of light than in the dark, as observed previously in panel B. The experiment reported in panel E is the same as that shown in panel D but light irradiates the film constantly (red trace). In this case no significant effect of light is detectable.

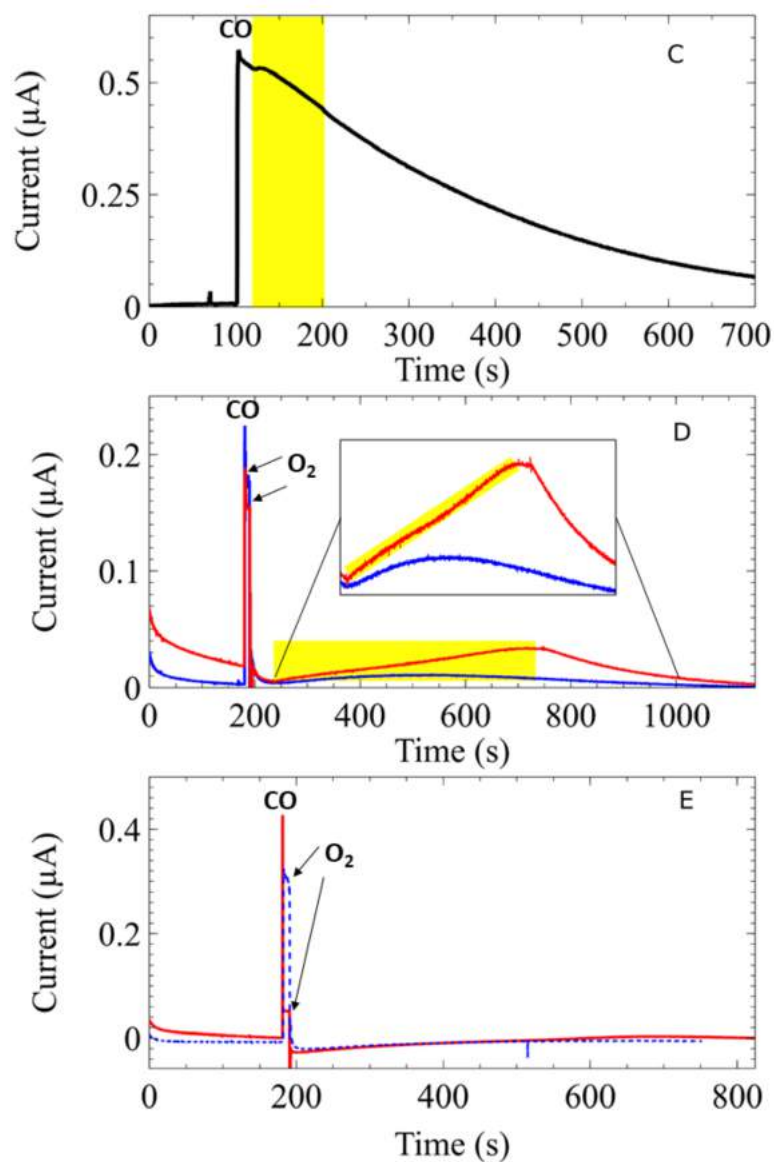


Figure 6.8: Acceleration by light of the reactivation of *Dv*CODH exposed to O<sub>2</sub> without an initial reductive step. C) The film was exposed to Xenon light from  $t = 120$  s to  $t = 200$  s. D) After the injection of CO, at 200 s O<sub>2</sub> (0.25 μM concentration in the cell) was injected. The red trace represents an experiment where the film was irradiated by Xenon light (yellow rectangle) after the inhibition by oxygen. E) The film was constantly irradiated by Xenon light before and after the injection of CO and oxygen (red trace). The blue trace is the same experiment as that shown in red but without irradiation. Conditions:  $T = 25^{\circ}\text{C}$ ,  $\text{pH} = 7$ ,  $E = -360$  mV vs SHE, 3000 krpm,  $[\text{CO}] = 50$  μM.

### 6.4.3 Discussion

Many aspects of CODH reactivity are still obscure. Furthermore, the study of this enzyme with direct electrochemistry is challenging. For example Meriem Merrouch observed heterogeneity of the response to CO of different films made from the same CODH sample. The main conclusion that we can draw is that we observed for the first time that light increases the rate of reactivation after aerobic inactivation. The concentration of CO decreases over time because the electrochemical cell that we used is not gas-tight and CO diffuses away from the enzyme and from the solution. This means that current decreases over time also in absence of an inhibitor and this explain why photo-reactivation induces only the recover of a small amount of current. We also observed that when the enzyme is reduced at low potential before the exposure to CO and O<sub>2</sub> the photo-reactivation is smaller. We can speculate that this small difference could be related to what we observed in NiFe-hydrogenases under the same conditions (section 6.3). Reactivation of CODH inhibited by oxygen could involve the reduction of O<sub>2</sub> to water, as observed in NiFe-hydrogenases<sup>156</sup> and FeFe-hydrogenases (chapter 3), with the formation of an intermediate with a bridging hydroxide between Ni and the Fe<sub>u</sub>. This geometry resembles that observed in the Ni-B state of NiFe-hydrogenases, which is reactivated upon irradiation, as shown in section 6.3. We do not know the redox state of Ni and Fe<sub>u</sub> in this hypothetical bridging-hydroxide state, but we know that an hydroxide is bound terminally on Fe<sub>u</sub> in the C<sub>red1</sub> state. The Ni state (II) does not change during the catalytic cycle (as we also observed in unpublished DFT calculations during my master thesis), in contrast with the behavior of Ni in NiFe-hydrogenases. The study of the inhibition of CODH by oxygen with DFT would be useful to clarify the electronic structure of the inhibited active site and possible photosensitive intermediates.



# Chapter 7

## Conclusions and perspectives

The main objective of this thesis was to investigate the reactivity and the photochemistry of the active site of FeFe-hydrogenases. For this study we used a combination of protein film voltammetry and time-dependent density functional theory. We employed PFV to study the kinetic properties of FeFe-hydrogenases and other metalloenzymes, in their active or inhibited form. We performed DFT and TDDFT calculations to study the structural and electronic properties of the active site of FeFe-hydrogenases at QM level in the ground or excited states. Chapter 2 is an introduction to protein film voltammetry and computational methods.

We performed PFV experiments to study the inhibition by CO and O<sub>2</sub> in mutants of the gas channels of FeFe hydrogenase from *C. reinhardtii*. This work was part of an article, presented in chapter 3, realized in collaboration with two theoretical groups. The aim of this project was to study the inactivation of the enzyme by O<sub>2</sub> and to obtain mutants resistant to anaerobic inactivation, one of the main topics in hydrogenase research. We simulated the diffusion of oxygen from the surface to the active site of the enzyme and we demonstrated with experiments that the mutation of specific residues in the gas channels slows the diffusion of CO and O<sub>2</sub>. We studied also the reactions of oxygen at the active site and we showed that the partial reversibility of the inhibition of FeFe-hydrogenases by O<sub>2</sub> is due to the four-electron reduction of oxygen to water. The results of this work suggest the possibility to realize other mutants more resistant to aerobic inactivation.

In Chapter 4 we presented the first part of the study of the photochemistry of the active site of FeFe-hydrogenases. The interest about the photochemistry of FeFe-hydrogenases has been growing in the last years for two reasons. First, spectroscopy and electrochemistry experiments showed that visible light damages FeFe-hydrogenases in a still unclear process and this could be a limit to the use of these enzymes for hydrogen photo-production *in vitro*. Second, the study of the excited states and the photochemical processes of FeFe-hydrogenases is important to have more information about the electronic structure of the active site and the intermediates involved in the catalytic cycle, which is not fully established. We developed a new methodology that we call direct photo-electrochemistry, which consists of direct electrochemistry measurements in presence of irradiation by various



---

light sources. Using this methodology we can observe how the absorption of light at specific wavelengths and power affects the catalysis and the inactivation processes of the enzyme. We tested this methodology combined with TDDFT calculations to investigate the photodissociation of the inhibitor CO from FeFe-hydrogenases from different microorganisms. Changing the power and the wavelength of irradiation, we determined the action spectra of the CO photodissociation, which showed that violet-blue light increases the rate of release of CO from the active site. We performed for the first time TDDFT calculations of the excited states of the active site inhibited by CO. We showed that in agreement with the experimental results only high energy visible light induces the photodissociation of the CO in apical position in the active site. We also described the process of deactivation of the excited states involved in the photodissociation of this specific CO. Direct photo-electrochemistry provides new findings compared to classical spectroscopy because we irradiate the enzyme under catalytic conditions. Furthermore, the combination with TDDFT allows the interpretation of the data at QM level. This approach could be employed to study the photochemistry of other metalloenzymes.

We used the same methodological approach to study the effect of irradiation on the active form of the enzyme. We demonstrated in chapter 5 that UVB is responsible for the photoinhibition of the FeFe hydrogenases from *C. acetobutylicum* and *C. reinhardtii*. We performed DFT and TDDFT calculations and we showed that the photoinhibition begins with the photodissociation of one of the intrinsic CO ligands bound to the active site. Then the active site forms a stable inactive species. This study showed that the FeFe-hydrogenases of *C. acetobutylicum* and *C. reinhardtii* are not damaged by visible light and are more resistant to photoinhibition than that from *D. desulfuricans*, making them a good candidate for the employment in dyad systems for the photoproduction of H<sub>2</sub> *in vitro* using the energy of sunlight. We need further studies on FeFe-hydrogenase from other microorganisms to understand the factors that determine the different sensitivity to light. In the same chapter we also showed that the presence of Cl<sup>-</sup> in the buffer changes the response of the FeFe-hydrogenases at high potential both in the dark and under irradiation. This observation opens many questions and new experiments must be performed to verify

the dependence of the  $\text{Cl}^-$  effect on the experimental conditions (temperature, pH,  $\text{H}_2$  concentration) in the dark and under irradiation. DFT calculations and MD simulations could exclude or support the hypothesis that chloride anions reach and modify the active site.

In the final chapter (6), we showed preliminary direct photo-electrochemistry results using NiFe-hydrogenase and CODH.  $\text{O}_2$ -tolerant NiFe-hydrogenases are inactivated by oxidation and form an inactive state called Ni-B. This state can be reactivated by reduction or irradiation by light. This process is important to understand the mechanism of oxygen resistance. In the first section of chapter 6 we demonstrated that the  $\text{O}_2$ -sensitive NiFe-hydrogenase from *D. fructosovorans* can be also reactivated by violet and white light. The oxidation of this enzyme forms two inactive states Ni-A and Ni-B. Further studies with PFV, DFT and EPR could reveal if this state can be also photo-activated. This would help to clarify the nature of Ni-A and its link with oxygen sensitivity. In the second section of chapter 6 we showed the first preliminary photo-electrochemistry study of the effect of irradiation of CODH. Many aspects of CO-dehydrogenase are still unknown and the studies on this field are growing because of the interest in  $\text{CO}_2$  reduction. The experiments showed that white light increases the rate of reactivation of the enzyme exposed to oxygen. We observed this process for the first time. The study of the photo-activation of CODH exposed to oxygen could help to understand the differences in sensitivity to oxygen in CODHs from different microorganisms. We also observed that if the exposure to oxygen and light is preceded by a reductive step, the rate of photo-activation decreases. This project is just at the beginning and a deep investigation is still necessary. For example, we could reproduce the same experiments using CODH more sensitive to oxygen or irradiating with monochromatic lasers changing wavelength and power, to obtain an action spectra. We could also perform DFT studies to elucidate the process of inhibition of CODH by  $\text{O}_2$ .

The study of metalloenzymes is important for many reasons: from the research about the evolution of life to the applications in energy industry and biotechnologies. In this thesis we focused on hydrogenases which are very promising catalysts to use in

---

"green" production of energy. But, many processes and properties of these enzymes are still obscure. We showed that we can find some pieces of the puzzle by combining protein electrochemistry experiments and computational chemistry calculations.



# Bibliography

- [1] Stephenson, M.; Stickland, L. H. *The Biochemical journal* **1931**, *25*, 205–214.
- [2] Lubitz, W.; Ogata, H.; Rudiger, O.; Reijerse, E. *Chemical reviews* **2014**, *114*, 4081–4148.
- [3] Peters, J. W.; Schut, G. J.; Boyd, E. S.; Mulder, D. W.; Shepard, E. M.; Broderick, J. B.; King, P. W.; Adams, M. W. *Biochimica et Biophysica Acta (BBA) - Molecular Cell Research* **2014**,
- [4] Fontecilla-Camps, J. C.; Volbeda, A.; Cavazza, C.; Nicolet, Y. *Chemical Reviews* **2007**, *107*, 4273–4303.
- [5] Schut, G. J.; Adams, M. W. W. *Journal of Bacteriology* **2009**, *191*, 4451–4457.
- [6] Madden, C.; Vaughn, M. D.; Díez-p, I.; Brown, K. A.; King, P. W.; Gust, D.; Moore, A. L.; Moore, T. A. **2012**, 1577–1582.
- [7] Bressan, L.; Collodi, G.; Ruggeri, F. *Hydrocarbon Engineering* **2009**,
- [8] DePoulpiquet, A.; Ranava, D.; Monsalve, K.; Giudici-Ortoni, M. T.; Lojou, E. *ChemElectroChem* **2014**, *1*, 1724–1750.
- [9] Plumeré, N.; Rüdiger, O.; Oughli, A. A.; Williams, R.; Vivekananthan, J.; Pöller, S.; Schuhmann, W.; Lubitz, W. *Nature chemistry* **2014**, *6*, 822–7.
- [10] Lalaoui, N.; de Poulpiquet, A.; Haddad, R.; Le Goff, A.; Holzinger, M.; Gounel, S.; Mermoux, M.; Infossi, P.; Mano, N.; Lojou, E.; Cosnier, S. *Chem. Commun.* **2015**, *51*, 7447–7450.
- [11] Vignais, P. M.; Billoud, B. *Chemical Reviews* **2007**, *107*, 4206–4272.

## BIBLIOGRAPHY

---

- [12] Pierik, A. J.; Hulstein, M.; Hagen, W. R.; Albracht, S. P. J. *European Journal of Biochemistry* **1998**, *258*, 572–578.
- [13] Nicolet, Y.; De Lacey, A. L.; Vernède, X.; Fernandez, V. M.; Hatchikian, E. C.; Fontecilla-Camps, J. C. *Journal of the American Chemical Society* **2001**, *123*, 1596–1601.
- [14] Fan, H. J.; Hall, M. B. *Journal of the American Chemical Society* **2001**, *123*, 3828–3829.
- [15] Silakov, A.; Wenk, B.; Reijerse, E.; Albracht, S. P. J.; Lubitz, W. *Journal of Biological Inorganic Chemistry* **2009**, *14*, 301–313.
- [16] Berggren, G.; Adamska, A.; Lambertz, C.; Simmons, T. R.; Esselborn, J.; Atta, M.; Gambarelli, S.; Mouesca, J.-M.; Reijerse, E. J.; Lubitz, W.; Happe, T.; Artero, V.; Fontecave, M. *Nature* **2013**, *499*, 66–69.
- [17] Lemon, B. J.; Peters, J. W. *Biochemistry* **1999**, *38*, 12969–12973.
- [18] Kubas, A.; Orain, C.; De Sancho, D.; Saujet, L.; Sensi, M.; Gauquelin, C.; Meynial-Salles, I.; Soucaille, P.; Bottin, H.; Baffert, C.; Fourmond, V.; Best, R. B.; Blumberger, J.; Léger, C. *Nature Chemistry* **2017**, *9*, 88–95.
- [19] Cohen, J.; Kim, K.; Posewitz, M. C.; Ghirardi, M. L.; Schulten, K.; Seibert, M.; King, P. *Biochemical Society Transactions* **2005**, *33*, 80–82.
- [20] Cohen, J.; Kim, K.; King, P.; Seibert, M.; Schulten, K. *Structure* **2005**, *13*, 1321–1329.
- [21] Peters, J. W.; Lanzilotta, W. N.; Lemon, B. J.; Seefeldt, L. C. *Science* **1998**, *282*, 1853–1858.
- [22] Nicolet, Y.; Piras, C.; Legrand, P.; Hatchikian, C. E.; Fontecilla-Camps, J. C. *Structure* **1999**, *7*, 13–23.
- [23] Happe, T.; Naber, J. D. *European journal of biochemistry / FEBS* **1993**, *214*, 475–81.

- [24] Mulder, D. W.; Boyd, E. S.; Sarma, R.; Lange, R. K.; Endrizzi, J. A.; Broderick, J. B.; Peters, J. W. *Nature* **2010**, *465*, 248–251.
- [25] Swanson, K. D.; Ratzloff, M. W.; Mulder, D. W.; Artz, J. H.; Ghose, S.; Hoffman, A.; White, S.; Zadovnyy, O. A.; Broderick, J. B.; Bothner, B.; King, P. W.; Peters, J. W. *Journal of the American Chemical Society* **2015**, *137*, 1809–1816.
- [26] Glick, B. R.; Martin, W. G.; Martin, S. M. *Can.J.Microbiol.* **1980**, *26*, 1214–1223.
- [27] Happe, T.; Mosler, B.; Naber, J. D. *European Journal of Biochemistry* **1994**, *222*, 769–774.
- [28] Greening, C.; Biswas, A.; Carere, C. R.; Jackson, C. J.; Taylor, M. C.; Stott, M. B.; Cook, G. M.; Morales, S. E. *The ISME Journal* **2015**, In press.
- [29] Ghirardi, M. L.; Zhang, L.; Lee, J. W.; Flynn, T.; Seibert, M.; Greenbaum, E. **2000**, *18*, 506–511.
- [30] Peters, J. W. *Current Opinion in Structural Biology* **1999**, *9*, 670–676.
- [31] Pandey, A. S.; Harris, T. V.; Giles, L. J.; Peters, J. W.; Szilagyi, R. K. *Journal of the American Chemical Society* **2008**, *130*, 4533–4540.
- [32] Caserta, G.; Adamska-Venkatesh, A.; Pecqueur, L.; Atta, M.; Artero, V.; Roy, S.; Reijerse, E.; Lubitz, W.; Fontecave, M. *Biochimica et Biophysica Acta - Bioenergetics* **2016**, *1857*, 1734–1740.
- [33] Foster, C. E.; Krämer, T.; Wait, A. F.; Parkin, A.; Jennings, D. P.; Happe, T.; McGrady, J. E.; Armstrong, F. A. *Journal of the American Chemical Society* **2012**, *134*, 7553–7557.
- [34] Lautier, T.; Ezanno, P.; Baffert, C.; Fourmond, V.; Cournac, L.; Fontecilla-Camps, J. C.; Soucaille, P.; Bertrand, P.; Meynial-Salles, I.; Léger, C. *Faraday Discussions* **2011**, *148*, 385.

- [35] Cornish, A. J.; Gärtner, K.; Yang, H.; Peters, J. W.; Hegg, E. L. *Journal of Biological Chemistry* **2011**, *286*, 38341–38347.
- [36] Knörzer, P.; Silakov, A.; Foster, C. E.; Armstrong, F. A.; Lubitz, W.; Happe, T. *Journal of Biological Chemistry* **2012**, *287*, 1489–1499.
- [37] Morra, S.; Giraudo, A.; Di Nardo, G.; King, P. W.; Gilardi, G.; Valetti, F. *PLoS ONE* **2012**, *7*, e48400.
- [38] Cornish, A. J.; Ginovska, B.; Thelen, A.; Da Silva, J. C. S.; Soares, T. A.; Raugei, S.; Dupuis, M.; Shaw, W. J.; Hegg, E. L. *Biochemistry* **2016**, *55*, 3165–3173.
- [39] Morra, S.; Maurelli, S.; Chiesa, M.; Mulder, D. W.; Ratzloff, M. W.; Giannello, E.; King, P. W.; Gilardi, G.; Valetti, F. *Biochimica et Biophysica Acta - Bioenergetics* **2016**, *1857*, 98–106.
- [40] Hong, G.; Cornish, A. J.; Hegg, E. L.; Pachter, R. *Biochimica et Biophysica Acta - Bioenergetics* **2011**, *1807*, 510–517.
- [41] Ginovska-Pangovska, B.; Ho, M.-H.; Linehan, J. C.; Cheng, Y.; Dupuis, M.; Raugei, S.; Shaw, W. J. *Biochimica et Biophysica Acta (BBA) - Bioenergetics* **2014**, *1837*, 131–138.
- [42] Mulder, D. W.; Ratzloff, M. W.; Bruschi, M.; Greco, C.; Koonce, E.; Peters, J. W.; King, P. W. *Journal of the American Chemical Society* **2014**, *136*, 15394–15402.
- [43] Greco, C.; Fourmond, V.; Baffert, C.; Wang, P.-h.; Dementin, S.; Bertrand, P.; Bruschi, M.; Blumberger, J.; de Gioia, L.; Léger, C. *Energy Environ. Sci.* **2014**, *7*, 3543–3573.
- [44] Erbes, D. L.; Burris, R. H.; Johnson, W. H. O. *Proc. Nat. Acad. Sci.* **1975**, *72*, 4795–4799.
- [45] Rusnak, F. M.; Adams, M. W. W.; Mortenson, L. E.; Munck, E. *Journal of Biological Chemistry* **1987**, *262*, 38–41.



- [46] Popescu, C.; Münck, E. *Journal of the American Chemical Society* **1999**, 15054–15061.
- [47] Chen, Z.; Lemon, B. J.; Huang, S.; Swartz, D. J.; Peters, J. W.; Bagley, K. A. *Biochemistry* **2002**, 41, 2036–2043.
- [48] Roseboom, W.; De Lacey, A. L.; Fernandez, V. M.; Hatchikian, E. C.; Albracht, S. P. *Journal of Biological Inorganic Chemistry* **2006**, 11, 102–118.
- [49] Mulder, D. W.; Ratzloff, M. W.; Shepard, E. M.; Byer, A. S.; Noone, S. M.; Peters, J. W.; Broderick, J. B.; King, P. W. *Journal of the American Chemical Society* **2013**, 135, 6921–6929.
- [50] Fiedler, A. T.; Brunold, T. C. *Inorganic chemistry* **2005**, 44, 9322–9334.
- [51] Silakov, A.; Reijerse, E. J.; Albracht, S. P. J.; Hatchikian, E. C.; Lubitz, W. *Journal of the American Chemical Society* **2007**, 129, 11447–11458.
- [52] Adamska, A.; Silakov, A.; Lambertz, C.; Rüdiger, O.; Happe, T.; Reijerse, E.; Lubitz, W. *Angewandte Chemie (International ed. in English)* **2012**, 51, 11458–62.
- [53] Adamska-Venkatesh, A.; Krawietz, D.; Siebel, J.; Weber, K.; Happe, T.; Reijerse, E.; Lubitz, W. *Journal of the American Chemical Society* **2014**, 136, 11339–11346.
- [54] Happe, R. P.; Roseboom, W.; Pierik, A. J.; Albracht, S. P. J. *Nature* **1997**, 385, 126.
- [55] Greco, C.; Bruschi, M.; Fantucci, P.; Ryde, U.; Dea Gioia, L. *Chemistry - A European Journal* **2011**, 17, 1954–1965.
- [56] Bruschi, M.; Greco, C.; Bertini, L.; Fantucci, P.; Ryde, U.; De Gioia, L. *Journal of the American Chemical Society* **2010**, 132, 4992–4993.
- [57] Silakov, A.; Kamp, C.; Reijerse, E.; Happe, T.; Lubitz, W. *Biochemistry* **2009**, 48, 7780–7786.

## BIBLIOGRAPHY

---

- [58] Cao, Z.; Hall, M. B. *Journal of the American Chemical Society* **2001**, *123*, 3734–3742.
- [59] Dijk, C. v.; Berkel-Arts, A. v.; Veeger, C. *FEBS Letters* **1983**, *156*, 340–344.
- [60] Morra, S.; Arizzi, M.; Valetti, F.; Gilardi, G. *Biochemistry* **2016**, *55*, 5897–5900.
- [61] Pereira, A. S.; Tavares, P.; Moura, I.; Moura, J. J. G.; Huynh, B. H. *Journal of the American Chemical Society* **2001**, *123*, 2771–2782.
- [62] Albracht, S. P. J.; Roseboom, W.; Hatchikian, E. C. *Journal of biological inorganic chemistry : JBIC : a publication of the Society of Biological Inorganic Chemistry* **2006**, *11*, 88–101.
- [63] Albracht, S. P.; Roseboom, W.; Hatchikian, E. C. *Journal of Biological Inorganic Chemistry* **2006**, *11*, 88–101.
- [64] Liu, Z.-p.; Hu, P. *Journal of the American Chemical Society* **2002**, *124*, 5175–5182.
- [65] Van Dijk, C.; Mayhew, S. G.; Grande, H. J.; Veeger, C. *Eur. J. Biochem* **1979**, *102*, 317–330.
- [66] Filipiak, M.; Hagen, W. R.; Veeger, C. *European journal of biochemistry / FEBS* **1989**, *185*, 547–53.
- [67] Butt, J. N.; Filipiak, M.; Hagen, W. R. *European journal of biochemistry / FEBS* **1997**, *245*, 116–122.
- [68] Silakov, A.; Wenk, B.; Reijerse, E.; Lubitz, W. *Physical Chemistry Chemical Physics* **2009**, *11*, 6553.
- [69] Bruschi, M.; Greco, C.; Fantucci, P.; De Gioia, L. *Inorganic Chemistry* **2008**, *47*, 6056–6071.
- [70] Siegbahn, P. E. M.; Tye, J. W.; Hall, M. B. *Chemical reviews* **2007**, *107*, 4414–4435.

- [71] Zampella, G.; Greco, C.; Fantucci, P.; De Gioia, L. *Inorganic Chemistry* **2006**, *45*, 4109–4118.
- [72] Mulder, D. W.; Guo, Y.; Ratzloff, M. W.; King, P. W. *Journal of the American Chemical Society* **2017**, *139*, 83–86.
- [73] Katz, S.; Noth, J.; Horch, M.; Shafaat, H. S.; Happe, T.; Hildebrandt, P.; Zebger, I. *Chem. Sci.* **2016**, *7*, 6746–6752.
- [74] Reijerse, E. J.; Pham, C. C.; Pelmeshnikov, V.; Gilbert-Wilson, R.; Adamska-Venkatesh, A.; Siebel, J. F.; Gee, L. B.; Yoda, Y.; Tamasaku, K.; Lubitz, W.; Rauchfuss, T. B.; Cramer, S. P. *Journal of the American Chemical Society* **2017**, *139*, 4306–4309.
- [75] Pierik, A. J.; Hagen, W. R.; Redeker, J. S.; Wolbert, R. B. G.; Boersma, M.; Verhagen, M. F. J. M.; Grande, H.; Veeger, C.; Mutsaers, P. H. A.; Sands, R. H.; Dunham, W. R. *European Journal of Biochemistry* **1992**, *209*, 63–72.
- [76] Liu, C.; Liu, T.; Hall, M. B. *Journal of Chemical Theory and Computation* **2015**, *11*, 205–214.
- [77] Bruschi, M.; Fantucci, P.; De Gioia, L. *Inorganic Chemistry* **2002**, *41*, 1421–1429.
- [78] Schmidt, M.; Contakes, S. M.; Rauchfuss, T. B. First generation analogues of the binuclear site in the Fe-only hydrogenases:  $\text{Fe}_2(\mu\text{-SR})_2(\text{CO})_4(\text{CN})_2/2$ -1999.
- [79] Cloirec, A. L.; Davies, S. C.; Evans, D. J.; Hughes, D. L.; Pickett, C. J.; Best, S. P.; Borg, S. *Chemical Communications* **1999**, *1*, 2285–2286.
- [80] Lyon, E. J.; Georgakaki, I. P.; Reibenspies, J. H.; Darensbourg, M. Y. *Angewandte Chemie - International Edition* **1999**, *38*, 3178–3180.
- [81] Noodleman, L.; Norman, J. G. *J. Phys. Chem.* **1979**, *70*, 4903.

- [82] Noodleman, L. *The Journal of Chemical Physics* **1981**, *74*, 5737–5743.
- [83] Greco, C.; Bruschi, M.; Fantucci, P.; Ryde, U.; De Gioia, L. *Journal of the American Chemical Society* **2011**, *133*, 18742–18749.
- [84] Kowal, A. T. **1989**, *264*, 4342–4348.
- [85] Adams, M. W. W. *Biochimica et Biophysica Acta - Bioenergetics* **1990**, *1020*, 115–145.
- [86] Vincent, K. A.; Parkin, A.; Armstrong, F. A. *Chemical Reviews* **2007**, *107*, 4366–4413.
- [87] Rodríguez-Maciá, P.; Birrell, J. A.; Lubitz, W.; Rüdiger, O. *ChemPlusChem* **2016**, *81*, 1–6.
- [88] Baffert, C.; Demuez, M.; Cournac, L.; Burlat, B.; Guigliarelli, B.; Bertrand, P.; Girbal, L.; Léger, C. *Angewandte Chemie - International Edition* **2008**, *47*, 2052–2054.
- [89] Armstrong, F. a.; Belsey, N. a.; Cracknell, J. a.; Goldet, G.; Parkin, A.; Reiser, E.; Vincent, K. a.; Wait, A. F. *Chemical Society reviews* **2009**, *38*, 36–51.
- [90] Stripp, S. T.; Goldet, G.; Brandmayr, C.; Sanganas, O.; Vincent, K. A.; Haumann, M.; Armstrong, F. A.; Happe, T. *Proceedings of the National Academy of Sciences of the United States of America* **2009**, *106*, 17331–6.
- [91] Lambertz, C.; Leidel, N.; Havelius, K. G. V.; Noth, J.; Chernev, P.; Winkler, M.; Happe, T.; Haumann, M. *Journal of Biological Chemistry* **2011**, *286*, 40614–40623.
- [92] Orain, C.; Saujet, L.; Gauquelin, C.; Soucaille, P.; Meynial-Salles, I.; Baffert, C.; Fourmond, V.; Bottin, H.; Léger, C. *Journal of the American Chemical Society* **2015**, *137*, 12580–12587.
- [93] Stiebritz, M. T.; Reiher, M. *Inorganic Chemistry* **2009**, *48*, 7127–7140.

- [94] Finkelmann, A. R.; Stiebritz, M. T.; Reiher, M. *Inorganic Chemistry* **2014**, *53*, 11890–11902.
- [95] Parkin, A.; Cavazza, C.; Fontecilla-Camps, J. C.; Armstrong, F. A. *Journal of the American Chemical Society* **2006**, *128*, 16808–16815.
- [96] Fourmond, V.; Greco, C.; Sybirna, K.; Baffert, C.; Wang, P.-h.; Ezanno, P.; Montefiori, M.; Bruschi, M.; Meynial-Salles, I.; Soucaille, P.; Blumberger, J.; Bottin, H.; De Gioia, L.; Léger, C. *Nature chemistry* **2014**, *6*, 336–342.
- [97] Senger, M.; Mebs, S.; Duan, J.; Wittkamp, F.; Apfel, U.-P.; Heberle, J.; Haumann, M.; Stripp, S. T. *Proceedings of the National Academy of Sciences* **2016**, *113*, 8454–8459.
- [98] Fernandez, V. M.; Munilla, R.; Ballesteros, A. *Archives of Biochemistry and Biophysics* **1982**, *215*, 129–135.
- [99] Hajj, V.; Baffert, C.; Sybirna, K.; Meynial-Salles, I.; Soucaille, P.; Bottin, H.; Fourmond, V.; Léger, C. *Energy & Environmental Science* **2014**, *7*, 715.
- [100] Baffert, C.; Sybirna, K.; Ezanno, P.; Lautier, T.; Hajj, V.; Meynial-Salles, I.; Soucaille, P.; Bottin, H.; Léger, C. *Analytical chemistry* **2012**, *84*, 7999–8005.
- [101] Tard, C.; Pickett, C. J. *Chemical Reviews* **2009**, *109*, 2245.
- [102] Sommer, C.; Adamska-Venkatesh, A.; Pawlak, K.; Birrell, J. A.; Rüdiger, O.; Reijerse, E. J.; Lubitz, W. *Journal of the American Chemical Society* **2017**, jacs.6b12636.
- [103] Kempner, W.; Kubowitz, F. *Biochem. Z.* **1933**, *265*, 245–252.
- [104] Thauer, R. K.; Kaufer, B.; Jungermann, K.; Zahringer, M. *European Journal of Biochemistry* **1974**, *42*, 447–452.
- [105] Bertini, L.; Greco, C.; Bruschi, M.; Fantucci, P.; De Gioia, L. *Organometallics* **2010**, *29*, 2013–2025.

## BIBLIOGRAPHY

---

- [106] Goldet, G.; Brandmayr, C.; Stripp, S. T.; Happe, T.; Cavazza, C.; Fontecilla-Camps, J. C.; Armstrong, F. A. *Journal of the American Chemical Society* **2009**, *131*, 14979–14989.
- [107] Baffert, C.; Bertini, L.; Lautier, T.; Greco, C.; Sybirna, K.; Ezanno, P.; Etienne, E.; Soucaille, P.; Bertrand, P.; Meynial-salles, I.; De Gioia, L.; Léger, C. *Journal of the American Chemical Society* **2011**, *133*, 2096–2099.
- [108] Hartridge, H.; Roughton, F. J. W. *Proc. Roy. Soc. London* **1932**, *94*, 337–365.
- [109] Gibson, Q. H. *J. Physiol.* **1956**, *134*, 112–122.
- [110] Purec, L.; Krasna, A. I.; Rittenberg, D. *Biochemistry* **1962**, *1*, 270–275.
- [111] Purec, L.; Krasna, A. I. *Biochemistry* **1967**, *57*, 1416–1421.
- [112] Pureci, L.; Krasna, A. I. *Biochemistry* **1968**, *7*, 51–55.
- [113] Sadana, J. C.; Rittenberg, D. *Proc. Nat. Acad. Sci.* **1963**, *50*, 900–904.
- [114] Peck, H. D.; Pietro, A. S.; Gest, H. *Proceedings of the National Academy of Sciences of the United States of America* **1956**, *42*, 13–19.
- [115] Patil, D. S.; Czechowski, M. H.; Huynh, B. H.; Legall, J.; Peck, H. D.; Dervartanian, D. V. *Biochemical and Biophysical Research Communications* **1986**, *137*, 1086–1093.
- [116] Silakov, A.; Reijerse, E. J.; Lubitz, W. *European Journal of Inorganic Chemistry* **2011**, *2011*, 1056–1066.
- [117] Greco, C.; Zampella, G.; Bertini, L.; Bruschi, M.; Fantucci, P.; De Gioia, L. *Inorganic Chemistry* **2007**, *46*, 108–116.
- [118] Finkelmann, A. R.; Stiebritz, M. T.; Reiher, M. *Chem. Sci.* **2014**, *5*, 215–221.
- [119] Bruschi, M.; Greco, C.; Kaukonen, M.; Fantucci, P.; Ryde, U.; De Gioia, L. *Angewandte Chemie - International Edition* **2009**, *48*, 3503–3506.

- [120] Mirmohades, M.; Adamska-Venkatesh, A.; Sommer, C.; Reijerse, E.; Lomoth, R.; Lubitz, W.; Hammarström, L. *Journal of Physical Chemistry Letters* **2016**, *7*, 3290–3293.
- [121] Sensi, M. et al. *Journal of the American Chemical Society* **2016**, *138*, 13612–13618.
- [122] Lemon, B. J.; Peters, J. W. *Journal of the American Chemical Society* **2000**, *122*, 3793–3794.
- [123] Cramer, C. J. *Essentials of Computational Chemistry: Theories and Models, 2nd Edition*; Wiley, 2004; p 618.
- [124] Jensen, F. *Introduction to Computational Chemistry*; Wiley: Chichester, UK, 1999.
- [125] Hohenberg, P.; Kohn, W. *Phys. Rev.* **1964**, *136*, B864–B871.
- [126] Kohn, W.; Sham, L. J. *Phys. Rev.* **1965**, *140*, A1133–A1138.
- [127] Runge, E.; Gross, E. K. U. *Physical Review Letters* **1984**, *52*, 997–1000.
- [128] Furche, F.; Ahlrichs, R. *Journal of Chemical Physics* **2002**, *117*, 7433–7447.
- [129] Balzani, V.; Ceroni, P.; Juris, A. In *Photochemistry and Photophysics: Concepts, Research, Applications*; Vch Verlagsgesellschaft Mbh, Ed.; Wiley-VCH: Weinheim, 2014; p 472.
- [130] Dunietz, B. D.; Dreuw, A.; Head-Gordon, M. *J. Phys. Chem. B* **2003**, *107*, 5623–5629.
- [131] Rappoport, D.; Furche, F. *The Journal of Chemical Physics* **2005**, *122*, 064105–064105.
- [132] Bertini, L.; Greco, C.; De Gioia, L.; Fantucci, P. *J. Phys. Chem. A* **2009**, *113*, 5657–70.
- [133] Bertini, L.; Greco, C.; Fantucci, P.; De Gioia, L. *International Journal of Quantum Chemistry* **2014**, *114*, 851–861.

- [134] Goy, R.; Bertini, L.; Rudolph, T.; Lin, S.; Schulz, M.; Zampella, G.; Dietzek, B.; Schacher, F. H.; De Gioia, L.; Sakai, K.; Weigand, W. *Chemistry - A European Journal* **2017**, *23*, 334–345.
- [135] Schäfer, A.; Huber, C.; Ahlrichs, R.; Schafer, A.; Huber, C.; Ahlrichs, R. *The Journal of Chemical Physics* **1994**, *100*, 5829–5835.
- [136] Becke, A. D. *Physical review A* **1988**, *38*, 3098–3100.
- [137] Perdew, J. P. *Physical review B* **1986**, *33*, 8822–8824.
- [138] Adamo, C.; Scuseria, G. E.; Barone, V. *Journal of Chemical Physics* **1999**, *111*, 2889–2899.
- [139] Eichkorn, K.; Weigend, F.; Treutler, O.; Ahlrichs, R. *Theoretical Chemistry Accounts* **1997**, *97*, 119–124.
- [140] Abou Hamdan, A.; Burlat, B.; Gutiérrez-Sanz, O.; Liebgott, P.-P.; Baffert, C.; De Lacey, A. L.; Rousset, M.; Guigliarelli, B.; Léger, C.; Dementin, S. *Nature chemical biology* **2013**, *9*, 15–7.
- [141] Merrouch, M.; Hadj-Saïd, J.; Domnik, L.; Dobbek, H.; Léger, C.; Dementin, S.; Fourmond, V. *Chemistry - A European Journal* **2015**, *21*, 18934–18938.
- [142] Ogata, H.; Lubitz, W.; Higuchi, Y. *Journal of Biochemistry* **2016**, *160*, 251–258.
- [143] Fernandez, V. M.; Hatchikian, E.; Patil, D. S.; Cammack, R. *Biochimica et Biophysica Acta (BBA) - General Subjects* **1986**, *883*, 145–154.
- [144] Abou Hamdan, A.; Burlat, B.; Gutiérrez-Sanz, O.; Liebgott, P.-P.; Baffert, C.; De Lacey, A. L.; Rousset, M.; Guigliarelli, B.; Léger, C.; Dementin, S. *Nature Chemical Biology* **2012**, *9*, 15–17.
- [145] Volbeda, A.; Martin, L.; Barbier, E.; Gutiérrez-Sanz, O.; De Lacey, A. L.; Liebgott, P. P.; Dementin, S.; Rousset, M.; Fontecilla-Camps, J. C. *Journal of Biological Inorganic Chemistry* **2015**, *20*, 11–22.



- [146] Breglia, R.; Ruiz-Rodriguez, M. A.; Vitriolo, A.; Gonzalez-Laredo, F. R.; De Gioia, L.; Greco, C.; Bruschi, M. *Journal of Biological Inorganic Chemistry* **2017**, *22*, 137–151.
- [147] Ciaccafava, A.; Hamon, C.; Infossi, P.; Marchi, V.; Giudici-Ortoni, M.-T.; Lojou, E. *Physical chemistry chemical physics : PCCP* **2013**, *15*, 16463–7.
- [148] Léger, C.; Dementin, S.; Bertrand, P.; Rousset, M.; Guigliarelli, B. *Journal of the American Chemical Society* **2004**, *126*, 12162–12172.
- [149] Dementin, S.; Belle, V.; Bertrand, P.; Guigliarelli, B.; Adryanczyk-Perrier, G.; De Lacey, A. L.; Fernandez, V. M.; Rousset, M.; Léger, C. *Journal of the American Chemical Society* **2006**, *128*, 5209–5218.
- [150] Leroux, F.; Dementin, S.; Burlat, B.; Cournac, L.; Volbeda, A.; Champ, S.; Martin, L.; Guigliarelli, B.; Bertrand, P.; Fontecilla-Camps, J.; Rousset, M.; Leger, C. *Proceedings of the National Academy of Sciences* **2008**, *105*, 11188–11193.
- [151] Ragsdale, S. W. *Critical Reviews in Biochemistry and Molecular Biology* **2004**, *39*, 165–195.
- [152] Ragsdale, S. W. *Journal of Biological Chemistry* **2009**, *284*, 18571–18575.
- [153] Anderson, M. E.; Lindahl, P. a. *Biochemistry* **1996**, *35*, 8371–80.
- [154] Fraser, D. M.; Lindahl, P. A. *Biochemistry* **1999**, *38*, 15706–15711.
- [155] Wang, S.; Huang, H.; Kahnt, J.; Thauer, R. K. *Journal of bacteriology* **2013**, *195*, 1267–75.
- [156] Evans, R. M.; Parkin, A.; Roessler, M. M.; Murphy, B. J.; Adamson, H.; Lukey, M. J.; Sargent, F.; Volbeda, A.; Fontecilla-Camps, J. C.; Armstrong, F. A. *Journal of the American Chemical Society* **2013**, *135*, 2694–2707.



FeFe hydrogenases are metalloenzymes that catalyze the oxidation and production of H<sub>2</sub>. The catalytic cycle and many aspects of the reactivity of these enzymes, including their aerobic and anaerobic inactivation, are still the subjects of intense investigations. Spectroscopy is commonly used to obtain information on the electronic structure of the active site of FeFe hydrogenases, by determining the absorption of the enzyme at different wavelengths. In contrast, in this thesis, I propose to use in this context a new technique which we have called "direct photoelectrochemistry", whereby the enzyme is directly wired to an electrode which can be irradiated with a light source, and the turnover frequency is measured as a current. We can detect the absorption of the active site as a function of light wavelength and power by monitoring changes in reactivity upon irradiation. Focusing on the variations of turnover rate, we are sure that we are studying the effect of light on catalytic intermediates.

I used direct photo-electrochemistry to study the effect of monochromatic irradiation in the visible range on the kinetics of inhibition by CO of three distinct FeFe hydrogenases. I determined the action spectrum of the photo-dissociation of the inhibitor CO and I described the process at the QM level for the first time, obtaining good agreement between experiments and theory.

I also studied the photoinhibition of the enzyme. I carried out photoelectrochemistry experiments irradiating the protein with monochromatic visible light laser diodes, a halogen lamp or a xenon lamp, and I observed that the FeFe hydrogenases from *C. reinhardtii* and *C. acetobutylicum* are irreversibly inactivated by UVB light. Using DFT and TDDFT, I concluded that the initial steps of photoinhibition consist in the photodissociation of one carbonyl intrinsic ligand of the active site, followed by the formation of a stable inactive species.

I also performed preliminary experiments to examine the effect of light on the activity of two other metalloenzymes: Carbon monoxide dehydrogenase (CODH) and NiFe-hydrogenase. I observed that the turnover rate of CODH is not affected by light, but the reactivation of the enzyme after exposure to oxygen is faster upon irradiation with white light. I also showed that the oxidized, inactive form of NiFe-hydrogenase reactivates more quickly upon irradiation with violet/blue light than in the dark.

My results illustrate the strength of the methodological approach that combines direct electrochemistry and TDDFT, and reveal new insights in the chemical and photochemical properties of several metalloenzymes.

Les hydrogénases FeFe sont des métalloenzymes qui catalysent l'oxydation et la production de H<sub>2</sub>. Le cycle catalytique et de nombreux aspects de la réactivité de ces enzymes, y compris l'inactivation aérobie et anaérobie, ne sont toujours pas complètement compris. Des techniques spectroscopiques sont couramment utilisées pour obtenir des informations sur la structure électronique du site actif des hydrogénases FeFe, en déterminant l'absorption de l'enzyme à différentes longueurs d'onde. Dans cette thèse, je propose d'utiliser dans ce contexte une nouvelle technique que nous avons appelée "photoélectrochimie directe", où l'on mesure la fréquence de turnover d'une enzyme en contact direct avec une électrode et irradiée par une source lumineuse. Je montre qu'il est possible de détecter l'absorption de la lumière par le site actif en fonction de la longueur d'onde et de la puissance de la lumière incidente, en enregistrant des changements de fréquence de turnover induites par l'irradiation. En mettant l'accent sur ces changements d'activité, nous sommes sûrs d'étudier l'effet de la lumière sur des intermédiaires catalytiques.

J'ai utilisé la photo-électrochimie directe pour étudier l'effet de l'irradiation sur la cinétique d'inhibition par le CO de trois hydrogénases FeFe distinctes. J'ai déterminé le spectre d'action de la photo-dissociation de l'inhibiteur CO et j'ai décrit le processus au niveau QM pour la première fois, en obtenant un bon accord entre les expériences et la théorie.

J'ai également étudié la photoinhibition de l'enzyme. J'ai effectué des expériences de photoélectrochimiques en irradiant la protéine avec des diodes laser monochromatiques dans le domaine de la lumière visible, une lampe halogène ou une lampe au xénon et j'ai observé que les hydrogénases FeFe de *C. reinhardtii* et *C. acetobutylicum* sont irréversiblement inactivées par la lumière UVB. En utilisant la DFT et la TDDFT, j'ai conclu que les étapes initiales de la photoinhibition consistent en la photodissociation d'un ligand carbonyle intrinsèque du site actif, suivie de la formation d'une espèce inactive stable.

J'ai aussi effectué des expériences préliminaires pour examiner l'effet de la lumière sur l'activité de deux autres métalloenzymes: la CO déshydrogénase (CODH) et la hydrogénase NiFe. J'ai observé que l'activité du CODH n'est pas affectée par la lumière, mais la réactivation de l'enzyme, après exposition à l'oxygène, est plus rapide lors de l'irradiation avec la lumière. J'ai également montré que la forme oxydée et inactive de NiFe-hydrogénase se réactive plus rapidement lors de l'irradiation avec une lumière violette/bleue que dans l'obscurité.

Mes résultats illustrent la force de l'approche méthodologique qui combine électrochimie directe et TDDFT, et apportent de nouvelles connaissances sur les propriétés chimiques et photochimiques de plusieurs métalloenzymes.